OUKA
The University of Osaka
Institutional Knowledge Archive

Title	Formation Mechanisms of Cliff-Front Dunes and Their Impact on Coastal Sediment Transport
Author(s)	Hsin, Hsiang
Citation	大阪大学, 2026, 博士論文
Version Type	VoR
URL	https://doi.org/10.18910/105478
rights	
Note	

The University of Osaka Institutional Knowledge Archive : OUKA

https://ir.library.osaka-u.ac.jp/

The University of Osaka

Doctoral Dissertation

Formation Mechanisms of Cliff-Front Dunes and Their Impact on Coastal Sediment Transport

HSIN, HSIANG

December 2025

Graduate School of Engineering,
The University of Osaka

Formation Mechanisms of Cliff-Front Dunes and Their Impact on Coastal Sediment Transport

by

Hsiang Hsin

A Doctoral Thesis

Submitted to
the Graduate School of the University of Osaka
on December 16, 2025
in Partial Fulfillment of the Requirements
for the Degree of Doctor of Engineering
in Civil Engineering

Thesis Supervisor: Susumu Araki
Professor of Civil Engineering

ABSTRACT

The Omotehama Coast, located on the Pacific side of the Atsumi Peninsula in Aichi Prefecture, has long experienced shoreline retreat due to reduced sediment supply from the Tenryu River and sea cliffs. To mitigate coastal erosion, a large scale restoration project involving the relocation and reconstruction of submerged breakwaters was implemented between 2008 and 2021. Although this countermeasure successfully widened the beach near Ikobe Coast, an unanticipated large foredune subsequently developed in front of the modified section, altering the littoral sediment balance. The formation of this dune revealed that the aeolian process previously neglected in coastal sediment management plays a significant role in the sediment dynamics of the region.

This study aims to clarify the mechanisms and impacts of coastal dune formation at Ikobe and along the Omotehama Coast through an integrated analysis of topographic, meteorological, and numerical data. Drone based digital surface models (DSM) and aerial orthophotos were used to quantify morphological changes in five major dunes from 2019 to 2025. Slope and elevation analyses revealed progressive dune accretion at Ikobe and Takatsuka, while smaller dunes such as Mutsure exhibited erosion and vegetation induced stabilization.

Bathymetric and beach survey data from Aichi Prefecture were used to examine the relationships among dune volume, beach width, and submarine sediment volume. The results showed that during the initial dune development stage (2011–2014), increases in nearshore sediment volume coincided with beach widening and dune growth, whereas in later years (after 2014), dune growth corresponded to decreases in submarine sediment volume indicating that the dunes now act as sinks within the littoral sediment transport system.

Wind observations and vertical balloon measurements confirmed that winter northwesterly winds, after flowing over the coastal cliff, generate a wake vortex that reverses near the beach, forming persistent landward winds responsible for dune accretion. Computational fluid dynamics (CFD) simulations using OpenFOAM reproduced these local wind fields and demonstrated that the intensity and spatial extent of the reverse flow are strongly influenced by the cliff height and incident wind angle.

The overall sediment budget analysis, integrating aeolian, beach, and submarine components, revealed that dune formation reduces the westward littoral drift by trapping approximately 10^4–10^5 m³ of sand annually. This finding highlights the importance of incorporating terrestrial aeolian processes into coastal sediment management frameworks. The study concludes that dunes along the Omotehama Coast, particularly the Ikobe dune, function not only as geomorphological features but also as active sediment reservoirs that fundamentally alter coastal sediment circulation.

Acknowledgements

This study was conducted at the Department of Civil Engineering, Graduate School of Engineering, Osaka University.

The author wishes to express his deepest gratitude to **Professor Susumu Araki**, the present academic supervisor, for his continuous guidance, insightful comments, and encouragement throughout the course of this dissertation.

The author is especially indebted to **Professor Shin-ichi Aoki**, the former academic advisor, for his invaluable mentorship, which included initiating the research topic, guiding field surveys, and providing continuous support and direction during the early and middle stages of this study. His enthusiasm and dedication to coastal research have been a lasting inspiration.

The author would also like to extend sincere appreciation to **Professors Takumi Okabe, Takaaki Uda, and Shigeru Kato** for their constructive advice on coastal observations and their valuable suggestions for the preparation of this thesis.

Special thanks are due to **Mr. and Mrs. Tanaka** of the **NPO Omotehama Network**, who kindly provided local guidance and on-site support during the field observations at the Omotehama Coast.

The author is also grateful to **Professors Masayasu Irie, Yusuke Nakatani, and Yuya Sasaki** for their helpful discussions and feedback during laboratory meetings, which helped refine the analytical and interpretative aspects of this study.

Finally, the author wishes to express sincere thanks to all members of the Coastal Engineering Laboratory at Osaka University for their technical assistance, collaboration in drone-based field measurements, and many thoughtful discussions that greatly enriched this research.

Contents

1 Introduction **1**
1.1 Background . . . 1
1.1.1 Recovery of the Takatsuka Coast and dune formation; continued erosion at the Ikobe Coast . . . 1
1.1.2 Recovery of the Ikobe Coast and dune formation; continued erosion at the downstream coast . . . 2
1.2 Problem Definition . . . 2
1.3 Objectives . . . 3
1.3.1 Research Questions . . . 4
1.4 Study Approach and Chapter Organization . . . 4
1.4.1 Conditions for Dune Formation at Ikobe . . . 4
1.4.2 Study Approach . . . 5
1.4.3 Chapter Organization . . . 5
2 Literature Review **6**
2.1 Fundamental Studies on Coastal Dune . . . 6
2.1.1 Aeolian transport processes . . . 6
2.1.2 Cliff-wind interactions and airflow modification . . . 7
2.1.3 Coastal dune typology and growth stages . . . 7
2.2 Regional Studies of Coastal Dunes and Sediment Dynamics in Japan . . . 8
2.2.1 Coastal dune systems in Japan . . . 8
2.2.2 Coastal Sediment Budget and Littoral Drift Systems in Japan . . . 10
2.2.3 Sediment dynamics along the Atsumi Peninsula and Enshunada Coast . . . 11
2.2.4 Evolution of the Ikobe dune system . . . 13
3 Field Survey, Data Processing, and Morphological Evolution of Cliff-Front Dunes **15**
3.1 Field Survey and Data Processing . . . 15
3.1.1 Field Survey . . . 15
3.1.2 Data Processing . . . 18
3.2 Survey Results of the Five Dune Sites in the Atsumi Peninsula . . . 28
3.2.1 Takatsuka Dune . . . 29
3.2.2 Ikobe Dune . . . 35
3.2.3 Ikobenishi Dune . . . 41
3.2.4 Mutsure Dune . . . 46
3.2.5 Koijigahama Dune . . . 48
4 Beach Morphology, Bathymetric Changes, and Their Relationship with Cliff-Front Dunes **50**
4.1 Sandy Beach Morphology . . . 50
4.1.1 Monitoring framework . . . 50
4.1.2 Temporal changes in sandy beach width . . . 51
4.1.3 Shoreline changes along the western sector . . . 51
4.1.4 Discussion . . . 51
4.2 Annual Bathymetric Changes . . . 53

4.3 Relationships among Beach, Dune, and bathymetry 54
4.3.1 Relationship between Beach Width Change and Submarine Sediment Volume Change 54
4.3.2 Relationship between Beach Width Changes and Dune Volume Changes 56
4.3.3 Relationship between Dune Volume Change and Submarine Sediment Volume Change 57
5 Wind Characteristics Relevant to Aeolian Processes 59
5.1 Wind Climate of the Atsumi Peninsula 59
5.2 Nearshore Wind Conditions around Omotehama Beach 60
5.2.1 Field Observations of Nearshore Wind 60
5.2.2 Discussion of Observed Wind Fields 63
5.3 Numerical Calculation of Wind Conditions 64
5.3.1 Calculation Method and Initial Settings 65
5.3.2 Terrain Models 67
5.3.3 2D Model Results 68
5.3.4 3D Model Results 71
5.3.5 Discussion 73
6 Aeolian Sand Transport and Integrated Sediment Budgets within the Dune–Beach–Nearshore System 79
6.1 Observation of Wind-Blown Sand 79
6.2 Relationship between Wind-Blown Sand and Wind Conditions 80
6.3 Relationship between Wind-Blown Sand and Topographic Change . . . 81
6.4 Integrated Sediment Budgets of the Dune–Beach–Nearshore System . . 82
6.4.1 Components of Aeolian Sand Transport 83
6.4.2 Case (1): Deposition on both beach and submarine zones including dune sediment 84
6.4.3 Case (2): Deposition on both beach and submarine zones excluding dune sediment 85
6.4.4 Case (3): Erosion on both beach and submarine zones including dune sediment 85
6.4.5 Case (4): Erosion on both beach and submarine zones excluding dune sediment 85
6.4.6 Discussion of Integrated Sediment Budget Results 86
7 Conclusion and Future Work 90
7.1 Summary of Key Findings 90
7.2 Applicability and Implications for Sediment Management 90
7.3 Limitations of This Study 91
7.4 Future Research Directions 91
Appendix 93
DSM Figures 93
Orthophoto Figures 101
Elevation Change Figures 112
Slope Figures 115

Chapter 1

Introduction

1.1 Background

1.1.1 Recovery of the Takatsuka Coast and dune formation; continued erosion at the Ikobe Coast

The Omotehama Coast, located along the Pacific side of the Atsumi Peninsula (Aichi Prefecture), is a predominantly sandy shoreline shaped by westward littoral drift supplied largely by the Tenryu River. This region forms part of the wider Enshunada coastal system (Omaezaki–Cape Irago, ∼117 km) and has been managed under the Enshunada Coastal Conservation Master Plan Aichi Prefecture [2003, 2011], Aichi Prefecture and Shizuoka Prefecture [2015].

Since the 1960s, shoreline retreat has accelerated across Omotehama due to substantial reductions in sediment supply. These reductions stem from (i) decreased fluvial input associated with extensive watershed development and flood-control projects, and (ii) diminished sediment release from coastal cliffs [Kawata and Uemoto, 1998, Hattori et al., 1974]. In response, a variety of countermeasures have been implemented to increase sediment input and maintain alongshore sediment continuity. These include dam reconfiguration projects [Uda et al., 2007b], the installation of submerged breakwaters [Uda et al., 2007b], and beach nourishment programs [Uda et al., 2006].

Severe erosion was documented at the Takatsuka and Ikobe coasts in the 1970s. To address this, submerged breakwaters were constructed offshore of the Takatsuka Coast beginning in 1993, resulting in progressive beach recovery and, eventually, the formation of the Takatsuka Dunes. However, this recovery induced an unintended downstream effect: erosion intensified along the Ikobe Coast. By 2003, a pronounced difference in beach width had developed between Takatsuka (recovered) and Ikobe (eroding).

These observations suggest that dune formation can disrupt the alongshore sediment continuity. Although the submerged breakwaters effectively trapped sediment and promoted beach recovery at Takatsuka, the newly formed dune system created favorable conditions for aeolian transport. The increased beach width and accumulation of dry fine sand at Takatsuka further enhanced the susceptibility of the recovered beach to aeolian entrainment, accelerating dune formation. As a result, a portion of the sediment that would have continued to drift westward was instead transported landward by wind and deposited as dunes. This reduction in alongshore sediment supply contributed to further erosion on the downstream (western) Ikobe Coast.

1.1.2 Recovery of the Ikobe Coast and dune formation; continued erosion at the downstream coast

In 2006, Aichi Prefecture launched the *Atsumi Peninsula Omotehama Coast Protection Council* Aichi Prefecture and Shizuoka Prefecture [2015], adopting a policy to secure a minimum beach width of 20 m. The project partially removed blocks from up-drift submerged breakwaters and relocated them down-drift to smooth the alongshore sediment distribution. Construction began in 2008 and finished in 2021. The relocation scheme is summarized in Fig. 1.1; monitoring-based beach-width changes are shown in top of Fig. 1.1 (2011−2012 vs. 2022−2023).

The lower panel of Fig. 1.1 illustrates the relocation and installation of these submerged breakwaters. Specifically:

1. A portion of the submerged breakwater between survey lines No. 8 and No. 9 (between Ikobe and Takatsuka coasts) was removed and relocated to the down-drift sections between No. 9−10 and No. 10−11.

2. Similarly, part of the submerged breakwater between No. 7 and No. 8 (off Takatsuka Coast) was removed and relocated offshore of Shiroshita Coast, between No. 13+100 and No. 14.

This modification aimed to reduce sand-trapping in the up-drift section (Takatsuka−Ikobe) and promote smoother sediment transport toward the down-drift side. An evaluation conducted by Sato et al. [2018] confirmed an improvement in the littoral drift balance, demonstrating the effectiveness of the countermeasures in stabilizing the beach around Ikobe. While the structural countermeasures improved local sediment retention, the rapid dune formation altered the alongshore sediment budget, likely intercepting sand that would otherwise have been transported westward. This dune growth was promoted by the wide, dry beach surface created after the structural countermeasures and the strong northwesterly winds characteristic of Ikobe.

Monitoring indicates that beaches widened around Ikobe and Akasawa (lines No. 9−12) and remained $>$60 m at the eastern sector (No. 6−9), whereas farther west (No. 12−14) no clear widening occurred despite structures in place. In several western reaches, sandy beaches have continued to narrow or vanish (see satellite comparisons in Fig. 4.3).

The Ikobe dune itself has rapidly grown over the same period, with its crest rising from $\sim$20 m to nearly $\sim$25 m T.P. by 2025 and accumulating more than 10^5 m^3 of sand. Such large-scale aeolian storage is not currently accounted for in Aichi Prefecture′s sediment management framework, suggesting that conventional littoral drift models underestimate terrestrial sand retention.

This study aims to bridge that gap by quantifying the mechanisms and impacts of dune development on the regional sediment budget.

1.2 Problem Definition

The preceding section highlighted that recent coastal recovery along the Takatsuka and Ikobe coasts has been strongly influenced by structural countermeasures designed to modify littoral drift pathways. However, despite localized shoreline improvements, erosion has persisted in downstream areas. This indicates that conventional evaluations of sediment continuity typically based on shoreline position, beach width, and nearshore bathymetry may not fully capture the underlying sediment dynamics.

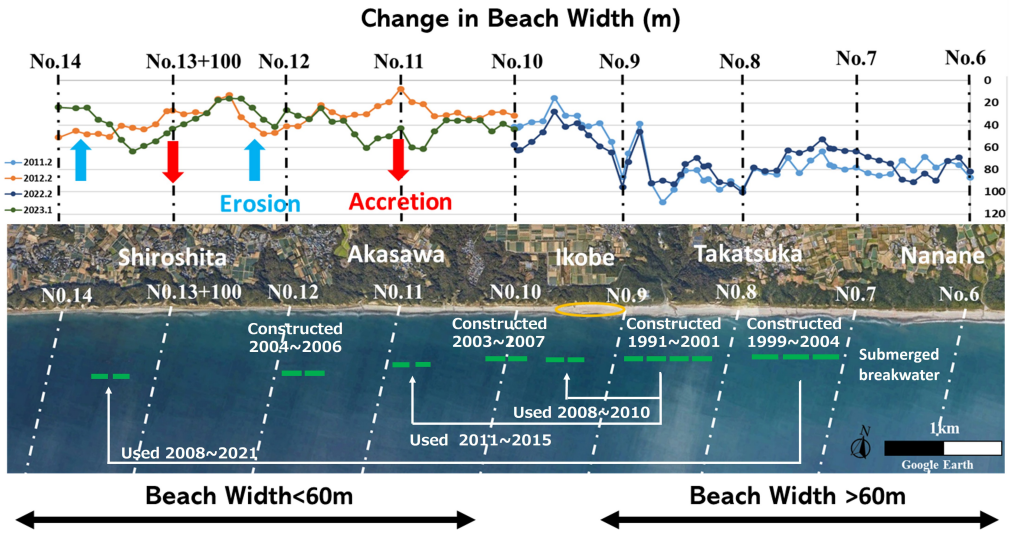

Figure 1.1: Relocation of submerged breakwaters.

A key limitation is that aeolian sand transport and dune accumulation are not incorporated into current sediment budget assessments within the Omotehama coastal management framework. Rapid dune growth at Takatsuka and Ikobe has resulted in substantial landward sediment sequestration that effectively removes material from the alongshore transport system. As a result, the apparent sediment deficit observed in downstream reaches may be partly attributable to unaccounted terrestrial storage rather than solely to littoral drift imbalance.

This gap leads to two critical problems:

1. **Misinterpretation of erosion mechanisms:** shoreline retreat may be incorrectly attributed solely to offshore losses or structural impacts, while the contribution of aeolian removal of beach sediment remains overlooked.
2. **Underestimation of regional sediment budgets:** dune-stored sand volumes are omitted from calculations, creating inaccuracies in sediment-flux estimates and leading to suboptimal coastal-management decisions.

Therefore, this study aims to quantify the role of dune formation in modifying the regional sediment budget, clarify the mechanisms by which aeolian transport intercepts or redirects littoral sediment, and evaluate the implications for long-term coastal management along the downstream Omotehama coast.

1.3 Objectives

The overarching objective of this study is to quantify and explain how dune formation modifies the coastal sediment system at Ikobe and adjacent coasts by explicitly incorporating the aeolian pathway. Specifically, we aim to:

1. Characterize dune morphology and recent evolution at five sites along Omotehama, including volumetric changes, slope development, and seasonal to interannual variability.

2. Reconstruct beach and nearshore bathymetric evolution to analyze coupled dune, beach, and seabed interactions.
3. Clarify the wind field responsible for onshore aeolian transport using in-situ observations and OpenFOAM simulations to resolve flow separation, wake vortex structure, and wind reversal height.
4. Quantify aeolian sand transport through trap observations and directional decomposition, and evaluate its controlling meteorological and geomorphological factors.
5. Close an integrated sediment budget (dune, beach, and nearshore seabed) across contrasting periods (net deposition versus erosion) to assess how dune growth alters alongshore (littoral) sediment flux.

1.3.1 Research Questions

This study seeks to address the following key scientific questions:

1. To what extent does dune growth function as a landward sediment sink that reduces net westward littoral drift?
2. What wind and topography interactions (such as cliff induced flow separation, incidence angle, and wind reversal height) govern aeolian sand transport toward the foredune?
3. How does the inclusion of dune storage change the interpretation of regional sediment budgets and coastal management strategies along Omotehama?

1.4 Study Approach and Chapter Organization

1.4.1 Conditions for Dune Formation at Ikobe

The formation of a coastal dune generally requires three essential conditions:

1. A sufficient sediment supply.
2. Adequate space for dune development.
3. An onshore directed wind capable of transporting sand landward.

At Ikobe, these conditions are satisfied as follows. First, the reconfiguration of submerged breakwaters increased nearshore sediment retention, leaving abundant sand available on the beach as the aeolian source. Second, the coastal plain in front of the cliff provides ample accommodation space for dune accumulation. Third, strong winter northwesterly winds descending along the cliff, forming wake vortices, and turning landward at the beach serve as the principal driver of onshore sand transport. These winds frequently exceed the threshold friction velocity required for sand entrainment, ensuring continuous onshore aeolian transport.

These three factors explain the rapid expansion of the Ikobe dune after 2009. The following chapters detail how these processes relate to dune morphology, beach change, wind modification, and sediment budgets along the Atsumi Peninsula.

1.4.2 Study Approach

This thesis integrates multi-source datasets and methods:

- **Topography:** RTK-GNSS and drone SfM surveys ($\rightarrow$ DSM/ orthophoto), combined with Aichi Prefecture beach profiles and nearshore bathymetry.
- **Wind:** AMeDAS statistics, offshore reanalysis, ground-based observation points, and pilot-balloon vertical soundings.
- **Aeolian Transport:** Alongshore arrays of box-type sand traps with vector decomposition of transport direction.
- **Modeling:** OpenFOAM RANS (2D/ 3D) over observed terrain to examine cliff-induced flow separation, incidence angle effects, and wind-reversal heights.
- **Sediment Budgeting:** Partitioning into dune (T.P. $>$ 3 m), beach (0–3 m), and submarine (−7–0 m) zones; assembling annualized volume and flux terms for contrasting depositional and erosional periods.

1.4.3 Chapter Organization

The remainder of this thesis is organized as follows.

Chapter 2 *Literature Review* —A synthesis of fundamental and regional studies relevant to this research. The first part reviews foundational work on coastal dunes, including aeolian transport processes, cliff wind interactions, and dune typology and growth. The second part summarizes regional studies on sediment dynamics in Japan, with emphasis on coastal dune systems, littoral drift and sediment budget frameworks, and previous investigations along the Atsumi Peninsula and Enshunada Coast, including the evolution of the Ikobe dune system.

Chapter 3 *Field Survey, Data Processing, and Morphological Evolution of Cliff-Front Dunes* —Field survey methods, data processing, and detailed descriptions of the five dune sites along the Atsumi Peninsula (Takatsuka, Ikobe, Ikobenishi, Mutsure, Koijigahama), including recent volumetric change.

Chapter 4 *Beach Morphology, Bathymetric Changes, and Their Relationship with Cliff-Front Dunes* —Monitoring framework, shoreline and nearshore morphological changes, temporal beach-width variations, and relationships between beach width, dune volume, and bathymetric changes.

Chapter 5 *Wind Characteristics Relevant to Aeolian Processes* —Regional and local wind environment, observations near the beach, vertical profiles and reversal layers, and OpenFOAM simulations of cliff-induced flow dynamics.

Chapter 6 *Aeolian Sand Transport and Integrated Sediment Budgets within the Dune–Beach–Nearshore System* —Trap based flux measurements, spatial patterns of aeolian transport, relationships between wind, topography, and sand movement, and integrated sediment budgets for dune, beach, and seabed.

Chapter 7 *Conclusion and Future Work* —Summary of findings, implications for coastal sediment management, and directions for future research.

Chapter 2

Literature Review

2.1 Fundamental Studies on Coastal Dune

Coastal dune systems develop through the interaction of sediment supply, wind regimes, beach morphology, and inland boundary conditions. Understanding these processes is essential for interpreting dune formation at Ikobe, where a steep coastal cliff strongly modifies near-surface winds and influences aeolian sediment delivery from the beach. This section reviews foundational knowledge on dune typology, aeolian sediment transport, and the aerodynamic effects of cliffs, highlighting the mechanisms most relevant to the dune examined in this study.

2.1.1 Aeolian transport processes

Wind-blown sand transport is one of the fundamental processes shaping coastal dunes. The physics of aeolian entrainment and transport has been established through a long tradition of work beginning with the foundational studies of Bagnold [1941] and later synthesised by Pye and Tsoar [1990]. Sand movement occurs in three principal modes: *saltation*, *surface creep*, and *suspension*. Saltation dominates the overall mass flux. Grains are lifted by aerodynamic drag and lift forces, accelerated along ballistic trajectories, and upon impact eject other grains from the bed. Surface creep is driven by the impacts of saltating grains and by the direct action of fluid drag on coarser particles. Suspension occurs when fine particles remain aloft within turbulent eddies, although this mode is generally limited for typical dune sands ($d \approx 0.1$–0.3 mm) Pye and Tsoar [1990].

The initiation of transport depends on the aerodynamic entrainment threshold. The classic description of threshold shear velocity was provided by Bagnold [1941] and later refined by Shao and Lu [2000]. Two thresholds are commonly distinguished: the *fluid threshold*, above which grains are directly entrained by wind, and the lower *impact threshold*, which allows sustained saltation once grain–bed collisions begin Bagnold [1937]. For typical beach sands, the impact threshold is the more relevant parameter.

Moisture plays a critical role in controlling sand availability. Laboratory and field observations Hotta et al. [1984], Horikawa et al. [1982] demonstrate that increasing surface moisture significantly elevates the fluid threshold and restricts the development of an effectively dry fetch. Grain-size effects are also well documented. Coarser grains require higher threshold velocities but may still produce substantial near-surface flux during high-wind events Nakajima and Suekatsu [1978], Horita et al. [1995, 2004].

For the Ikobe dune, aeolian transport is controlled almost entirely by beach conditions

because there is essentially no inland sediment source. The combination of an open beach, dry winter conditions, and strong seasonal northwesterlies implies that fetch length and threshold conditions are key determinants of the observed dune growth.

2.1.2 Cliff-wind interactions and airflow modification

According to Sweet and Kocurek [1990], airflow over the lee side of a dune can be categorised into three regimes: separated flow, attached deflected flow, and attached undeflected flow. The occurrence of each regime is controlled by dune slope, dune geometry, wind incident angle relative to the dune, and atmospheric stability. Steep dunes with high height-to-length ratios are most prone to developing separated flow under oblique winds or unstable atmospheric conditions, generating an extensive lee-side recirculation zone. In contrast, gentle slopes or winds approaching more parallel to the dune crest tend to produce attached flows. Attached flow is typically associated with higher wind speeds that promote ripple formation and surface transport processes, whereas separated flow zones commonly correspond to grainflow and grainfall driven largely by gravity.

Based on the terrain-forced airflow framework proposed by Walker and Nickling [2002], dunes and other large topographic obstacles induce characteristic lee-side vortex structures, including roller vortices and helical vortices, which strongly shape the spatial pattern of erosion and deposition. The airflow classification developed by Bauer et al. [2012] for foredune systems further indicates that, under varying wind-approach angles, the lee slope commonly exhibits flow separation and the development of recirculation cells. These recirculation zones can generate localized wind reversals and substantially alter sediment-transport pathways. Together with later findings from Bauer et al. [2013], these studies emphasise the key roles of flow separation, lee-side reverse flow, crest steering, and localized wind acceleration in controlling dune morphodynamics.

Gabarrou et al. [2018] also highlighted that dune mobility is highly sensitive to changes in wind conditions, such as shifts in mean wind speed or storm duration, and that its variability is more strongly influenced by model parameterisation than by stochastic wind time series alone. Similarly, Henrico et al. [2020] demonstrated that wind-driven processes constitute the primary control on dune mobility in coastal environments.

2.1.3 Coastal dune typology and growth stages

Coastal dunes are widely recognised as dynamic landforms created through the interaction of wind, beach morphology, sediment supply, and vegetation. Classic dune studies commonly divide coastal dunes into two major categories: primary dunes and secondary dunes Masselink et al. [2014], Davies and Clayton [1972]. Primary dunes form directly from sand transported landward from the beach and therefore occupy the position closest to the shoreline. Because of their proximity to marine processes, primary dunes are more exposed to wave attack, storm overwash, and seasonal erosion. Davies and Clayton [1972] further subdivided primary dunes into free dunes, which develop without significant vegetation influence, and impeded dunes, which form when vegetation traps saltating sand and promotes vertical accretion. Foredunes, the dominant dune type along many sandy coasts, belong to this impeded category because vegetation plays an essential role in trapping sand and stabilising the dune surface.

Secondary dunes, by contrast, develop farther inland and depend partly on the

presence of pre-existing primary dunes. These landward dune types may evolve as the coastline shifts seaward or landward over long timescales or as erosional notches in primary dunes expand into blowouts. Common forms include parabolic dunes, blowout dunes, and transgressive dunes Davies and Clayton [1972], Hesp and Hyde [2008]. Although parabolic and transgressive dunes are often considered secondary, they may also originate directly from beach-sourced sand when vegetation is sparse. This demonstrates that dune classification is not strictly binary; coastal dune systems typically represent a continuum of forms reflecting sediment supply, wind regime, and vegetation cover.

The dune examined in this study is best described as a foredune, as it forms immediately landward of the beach and receives nearly all its sediment from onshore winds. Foredunes generally follow a characteristic sequence of development, typically divided into three growth stages: incipient foredunes, established foredunes, and relict foredunes Hesp [2002]. Incipient foredunes form when obstacles, most commonly vegetation but also driftwood or irregular beach microtopography, create zones of reduced wind velocity and promote the deposition of saltating sand. These initial mounds are small, mobile, and easily eroded by storm waves or strong winds. Nevertheless, they play an essential role in triggering dune initiation because they anchor the location of future dune growth.

Established foredunes represent the stage at which vegetation becomes sufficiently dense to stabilise the dune surface, allowing the dune to grow vertically and horizontally. During this stage, the dune profile becomes smoother and more continuous, rainfall and compaction contribute to greater stability, and the foredune ridge becomes a more permanent landscape feature.

The Ikobe dune corresponds most closely to this established stage: its crest has increased in height over the past decade, its volume continues to grow, and vegetation has spread across the slope, indicating progressive stabilisation under persistent aeolian supply. Relict foredunes represent the remnants of formerly active dunes that have been cut off from direct sand supply or overridden by inland dune migration. They may occur when secondary dunes migrate across the landscape or when shoreline retreat changes the spatial relationship between dune and beach. However, at Ikobe the landward boundary is a steep cliff, leaving no room for inland dune migration. As a result, the evolutionary trajectory differs from that of classical coastal plains, and the foredune cannot transition into a relict phase through dune-over-dune replacement. Instead, its eventual transition into a relict or erosional state would depend on a reduction of aeolian sand supply or on beach narrowing driven by longshore sediment deficits.

Overall, the morphological characteristics of the Ikobe dune reflect the general principles of foredune evolution described in the literature, but the cliff-backed setting imposes unique constraints on its development. This makes the site a valuable natural example for examining how boundary conditions, especially steep inland barriers, shape the initiation and long-term growth of coastal dunes.

2.2 Regional Studies of Coastal Dunes and Sediment Dynamics in Japan

2.2.1 Coastal dune systems in Japan

Previous studies have examined the classification and formation of coastal dunes across Japan. Tanabe [1941] presented one of the earliest morphological classifications of Japanese coastal dunes, while Miie [1965] further investigated their formative

processes. In addition, Naruse [1989] reported that dune forming coasts account for approximately 7% of Japan's shoreline, with a total length of around 1,900 km, and broadly categorized these dune systems into three major regions: the Sea of Japan, the Pacific Ocean, and the Izu Islands.

Research on Japanese coastal dunes can be broadly divided into four fields: (1) Agricultural and environmental utilization of dune landscapes, (2) Disaster mitigation roles of dunes, (3) Geological investigations of paleo-dunes, (4) Geomorphological and morphodynamic studies of modern dune formation. Although the present dissertation is primarily concerned with modern dune development (category 4), the other three fields are briefly reviewed to provide the broader scientific and geomorphic context.

Environmental and Agricultural Utilization of Dunes Representative studies include early work such as Kawasaki [1942]. More recently, numerous studies led by the Arid Land Research Center, Tottori University have addressed dune environments and their sustainable use Matsuda [1990], Inoue [2024]. As these topics lie outside the scope of the present study, they are not discussed in detail here.

Coastal Dunes and Disaster Mitigation Following the 2011 Tohoku Earthquake and Tsunami, research on the disaster prevention function of coastal dunes has expanded rapidly. Yanagisawa et al. [2012] demonstrated that coastal dunes can reduce tsunami overflow and that reinforcing dunes with geogrids and concrete panels enhances their erosion resistance. Subsequently, Maekawa et al. [2013] analyzed inundation depths and structural damage in Chiba Prefecture, concluding that sufficiently high dunes significantly reduce tsunami inundation and damage. Nikaido et al. [2015] investigated dune erosion caused by tsunami overflow using hydraulic experiments and aerial survey data, showing that wide dune crests are particularly effective in resisting erosion, as demonstrated in Natori City. Nikaido et al. [2016] further combined hydraulic tests and numerical simulations, revealing that erosion tends to initiate from the seaward slope and later progresses landward depending on the flow conditions. Their simulations for a potential Nankai Trough megathrust tsunami showed that, although dunes would undergo substantial erosion, dune bodies with greater width maintain high erosion resistance. Hamaguchi et al. [2017] emphasized the role of vegetation in mitigating inland tsunami impacts, particularly under conditions where dune width alone is insufficient. Okutani and Hiraishi [2020] showed, through hydraulic experiments using solitary waves, that dune erosion occurs in two stages and that dune presence and cross-sectional shape significantly affect the maximum run-up depth landward of the dune. Ho et al. [2022] validated a 2D–3D hybrid tsunami model against hydraulic experiments to further analyze dune erosion processes.

Geological Studies on Paleo-Dunes Geological research has documented paleo-dune sequences across Japan, including studies of Tanegashima Naruse [1971], the San'in region Toyoshima [1975], the Hokuriku coast Fuji [1975], western Honshu Ono [1963], and the coasts along the Japan Sea and East China Sea Kakuda [1975]. Other examples include dune studies in Tottori Toyoshima and Akagi [1965], Tamura et al. [2011], Aomori Tanino [2000], and Niigata Tanaka et al. [1996]. These paleo-dune studies provide the geological background for understanding long-term dune evolution in Japan.

Modern Coastal Dune Studies in Japan Modern dune formation has been examined at several major sites: Kujukuri Beach Yokota et al. [2017, 2019], Fukiagehama Dune Naruse [1969], Nishi et al. [1998], Udo and Takewaka [2001], Hamamatsu–Shinohara Coast Sato [2008], Yokota et al. [2020a,b], Nakatajima Dune Uda et al. [2007a], Wakae et al. [2008]. Studies related to the Hamamatsu–Shinohara coast and the Nakatajima dune both located within the same littoral drift system as the Atsumi Peninsula will

be presented in detail in the following subsection. Research on the Tottori dunes was addressed earlier in this section.

2.2.2 Coastal Sediment Budget and Littoral Drift Systems in Japan

Sorimachi [1999] argued that coastal erosion does not occur in isolation along the shoreline; rather, it is a consequence of disruptions throughout the entire sediment-supply chain within a river basin. Therefore, maintaining the integrity of the sediment transport system must therefore serve as the fundamental basis for coastal management. Through international comparison, Naruse and Ooka [2000] highlighted two major challenges facing coastal management in Japan: institutional fragmentation across multiple agencies and an overreliance on hard engineering structures. In contrast, Western countries generally adopt long-term monitoring, ecosystem-based approaches (e.g., beach nourishment, nature-based coastal protection), and integrated coastal zone management (ICZM), suggesting valuable lessons for Japan. Studies by Isobe [2008] and Tomita et al. [2011] further emphasized that Japan's severe shortage of coastal sediment is fundamentally caused by human disturbances to the sediment system linking mountains, rivers, and coasts—such as dams, forest-road development, sabo structures, and channel modifications. To restore a healthy sediment cycle, they proposed comprehensive sediment management that includes upstream forest management, sediment flushing at dams, maintaining river-mouth morphology, and implementing nourishment measures aligned with littoral drift directions. Sediment management must therefore be conducted at a basinwide scale rather than through isolated engineering works; such integrated approaches are crucial for national land conservation and long-term shoreline stability. Onuma [2015] noted that Japan's declining population has intensified the dual pressures of limited financial and human resources, coupled with rising disaster risks. Traditional, structure-heavy coastal protection is no longer sustainable. A shift toward selective management of priority areas, along with nature-based, flexible disaster-mitigation strategies and ecosystem restoration, is essential. Future coastal policy must therefore strengthen long-term monitoring, multi-stakeholder collaboration, and the strategic use of natural processes to achieve sustainable shoreline management.

To illustrate how sediment budget disruptions manifest in different geomorphic settings, several representative cases from around Japan are reviewed.

A typical example of erosion caused by sediment depletion and interrupted littoral drift can be found along the Shonan Coast. Uda et al. [2016] demonstrated that erosion is driven by "insufficient sediment supply" and "drift blockage by coastal structures." Aerial photographs and surveys revealed accelerated seabed erosion after 2005, particularly in the central region (Tsujido to Chigasaki). Near the Sagami River mouth, reduction of river terraces caused river-borne sediment to be removed by waves before reaching the coast. Although localized accretion was observed on the western side of Chigasaki due to headlands and detached breakwaters, this formed a closed littoral system and did not improve the overall sediment budget. Effective mitigation requires integrated monitoring of seabed and shoreline morphology, sediment budget assessment, and measures to restore sediment continuity. Ishikawa et al. [2021] further demonstrated that reduced riverine supply and drift interruption are the primary causes of erosion, and identified wind-driven sand transport and backshore sand storage as key sediment sources. Their modeling improved predictive accuracy and showed that reusing backshore sand for nourishment is both effective and sustainable.

A similar situation is found along the Tottori Coast. Yasumoto et al. [2006b] proposed a comprehensive sediment management guideline for Tottori Prefecture based on basin−

coast sediment budget principles, emphasizing sand recycling, flexible soft-engineering methods, and a PDCA monitoring cycle. The guideline highlights collaboration among government, residents, and researchers, representing one of Japan's leading examples of nature-based coastal management. Using the Chiyo River right-bank system as a case study, Yasumoto et al. [2006a] demonstrated that erosion on the Tottori Coast results from reduced riverine sediment supply and littoral drift blockage. Aerial-photo analysis showed long-term retreat of dunes and the shoreline. Comprehensive sediment measures—sand recycling, nourishment, soft structures, and systematic monitoring —were proposed to restore the sediment budget. Shibuya et al. [2012] evaluated nourishment and sand-recycling measures implemented since 2005, showing significant increases in beach width, stabilization of seabed materials, and recovery of the natural northward littoral drift pathway. These results verified the effectiveness of nourishment and recycling, while also highlighting the need for ongoing monitoring. Shibuya et al. [2015] further confirmed long-term shoreline advancement and stable beach width following nourishment. Sediment migrated northward along the dominant drift direction, consistent with the natural sediment-transport system. Although seasonal erosion–accretion cycles persisted, large-scale nourishment successfully reduced chronic erosion and strengthened coastal stability, benefiting both dune conservation and coastal protection. Based on shoreline data from 1974–2013, Tsujimoto and Shibuya [2019] used EOF analysis and a one-line model to examine spatiotemporal shoreline variability. They found that shoreline fluctuations are primarily driven by seasonal wave climate, showing a clear winter-erosion and summer-recovery cycle. Some areas exhibited nodal behavior caused by coastal structures. Long-term trends indicated overall erosion due to decreased riverine supply and drift interruption. After nourishment and sand recycling, shoreline positions gradually stabilized. Both EOF and one-line models effectively reproduced observed shoreline changes, demonstrating their suitability for future shoreline prediction. Tsujimoto and Shibuya [2024] analyzed shoreline and cross-shore profile changes following the construction of offshore reefs. EOF results again confirmed clear seasonal cycles. The reefs successfully mitigated local erosion, particularly on the eastern side. Seasonal bar migration followed a Storm–Calm pattern, and the CSHORE model accurately reproduced morphological responses, confirming its applicability for future forecasting. Overall, artificial reefs combined with comprehensive sediment management have contributed to shoreline stabilization, though spatial differences in response remain.

A detailed analysis of the Atsumi Peninsula and Enshū-nada sediment system will be presented in the following section.

2.2.3 Sediment dynamics along the Atsumi Peninsula and Enshunada Coast

The Enshunada coast extends approximately 117 km from Cape Omaezaki to Cape Irago and includes both the eastern and western sectors of the broader coastal system. The Omotehama coast and the Atsumi Peninsula, which form the western portion of this system, are of particular relevance to the present study because they encompass the primary zones of sediment transport influenced by the Tenryu River.

A large body of research has examined long-term coastal change along the Enshunada coast and the Atsumi Peninsula, with particular attention to the role of sediment supply from the Tenryu River. Early analyses of shoreline behavior, beginning with Kawata and Uemoto [1998], demonstrated a strong correspondence between regional erosion and reductions in river-derived sediment. Subsequent studies by Aoki et al. [1999, 2003] quantified the westward littoral drift along the sector west of the river mouth and showed

that shoreline retreat intensified after the 1970s as the westward sediment flux became insufficient to maintain beach width. Nagashima et al. [2005] further documented that erosion was particularly severe along the 40 km stretch from the river mouth to Kosai, with notable sediment coarsening around the Hamamatsu coast.

More recent sediment budget reconstructions provide refined estimates of the magnitude and temporal evolution of sediment supply. Kainuma et al. [2019] estimated that sediment discharge at the Tenryu River mouth was approximately 570,000 m^3/yr between 1946 and 1965, declining sharply to around 70,000 m^3/yr between 1965 and 2005 due to watershed development and dam construction. Their analysis also indicated that the regional sediment deficit persisted despite post-2004 countermeasures such as submerged breakwaters and coarse-material nourishment. Uda et al. [2006, 2007b] similarly noted that although evenly spaced submerged breakwaters can promote local retention, the overall erosional trend along the Enshunada coast continues to be governed primarily by the reduced sediment supply at the river mouth and the prevailing westward littoral drift. Research on basin-scale sediment management, such as Sato et al. [2004], has reinforced the view that maintaining stable coastal conditions requires a continuous sediment supply from the Tenryu River. Building on this perspective, Yoshii and Sato [2010] indicates that coastal and river-mouth erosion in the Tenryu River system will continue to intensify unless sediment is managed comprehensively at the watershed scale. The study therefore recommends implementing measures such as sediment flushing, sediment reuse, upstream forest management, and riverbank erosion control as components of an integrated watershed sediment management strategy. Such an approach is essential for restoring a healthy sediment cycle and mitigating erosion risks in downstream and coastal areas.

A particularly well-studied example of nourishment-based intervention is the Shinohara coast, located west of the Tenryu River mouth and extending toward the Imagire Inlet. Uda et al. [2014a,b] demonstrated that following the reduction in sediment discharge from the river, this area experienced localized and short-term shoreline advance after the implementation of coarse-grained beach nourishment. However, the overall sediment budget continued to reflect offshore loss of fine sediments and a persistent system-wide deficit. The apparent shoreline recovery after 2005 was caused primarily by coarse material accumulating on the upper beach rather than an actual increase in total sediment volume within the coastal system. This creates an apparent shoreline advance that does not correspond to true system-wide accretion, leading to potential misinterpretation of nourishment effectiveness if changes in the offshore bathymetry are not simultaneously evaluated. Endo et al. [2015] reproduced these observations using the BG model, showing that shoreline advance and offshore erosion can occur simultaneously due to onshore trapping of coarse sediment combined with continued offshore transport of finer fractions. Kainuma et al. [2016] further reported that approximately 3.0×10^5 m^3/yr of westward longshore transport persists at the western boundary of the nourishment area. Although this flux is comparable to the natural sediment supply of the pre-dam Tenryu River, it now represents ongoing sediment loss under a sediment-deficit regime.

Studies on the eastern Enshunada coast, between the Tenryu River mouth and Cape Omaezaki, have documented similarly persistent sediment-deficit conditions. Uda et al. [2013] examined shoreline change near Omaezaki for 1997–2008 and showed that erosion in this region was strongly influenced by the reduced sediment supply from the Tenryu River, with additional modification by tectonic land-level changes. More recent analyses by Kainuma et al. [2018], covering the years 2008 and 2016, identified a continued decline in longshore sediment transport and further reduction in sediment

availability along the eastern sector. Together, these studies indicate that both the eastern and western portions of the Enshunada coast exhibit erosion patterns driven primarily by the long-term decline in sediment discharge from the Tenryu River.

These regional findings provide the broader geomorphic and sedimentary context in which dune formation and aeolian processes at Ikobe must be understood.

2.2.4 Evolution of the Ikobe dune system

The geomorphic development of the Ikobe dune on the southern Atsumi Peninsula has been described in several earlier studies. Historical records indicate that the Ikobe coast once possessed extensive dune bodies. An Edo–Meiji era votive painting documented by Fujishiro Fujishiro [2021] depicts a prominent dune ridge along this shoreline, suggesting that the area had long provided favorable conditions for dune formation. However, severe coastal erosion that progressed from the 1970s onward led to the complete disappearance of the dune, with photographs from 2003 showing no remaining dune body.

In response to the ongoing erosion, Aichi Prefecture implemented coastal management measures beginning in 2008, including the partial removal and relocation of blocks from the submerged breakwaters at Takatsuka to reduce their sand-trapping effect, while simultaneously improving the down-drift submerged structures. As reported by Sato et al. Sato et al. [2018], these measures resulted in notable shoreline recovery around Ikobe. Following this recovery, a new dune began to form around 2009 and, within approximately ten years, developed into a large foredune exceeding 20 m in height.

In addition to these regional management efforts, a series of studies by the present author has examined the physical conditions governing dune initiation and subsequent growth at Ikobe. Hsin et al. [2022] investigated the essential prerequisites for dune initiation in front of a coastal cliff by analyzing long-term shoreline changes together with wind observations and CFD simulations. Their results demonstrated that the reappearance of a sufficiently wide beach due to coastal management was the primary factor enabling dune re-formation. Despite prevailing northwesterly winter monsoon winds, near-surface winds on the beach were consistently directed landward from the southwest. CFD analysis confirmed that this pattern arose from a reverse-flow vortex generated by the cliff topography, providing the dominant aeolian forcing for dune development.

Subsequent work by Hsin et al. [2023] quantified the aeolian sand flux and multi-year dune volume changes using UAV SfM surveys, sand-trap observations, and topographic analysis. By dividing the dune into three sectors, the study demonstrated that cross-shore aeolian flux contributed more to dune growth than alongshore flux, highlighting the importance of landward-directed sand transport in shaping the dune system.

Most recently, Hsin et al. [2024] analyzed the relationship between dune development and nearshore bathymetric changes using terrestrial and submarine topographic datasets together with satellite imagery. A negative correlation was found between dune-volume increase and nearshore sediment volume, suggesting that enhanced aeolian delivery to the dune reduced the sediment available for longshore transport. These findings imply that the development of a large dune body modifies the regional sediment budget and may intensify erosion along the down-drift coastline.

Taken together, previous studies show that the Ikobe dune has undergone substantial morphological transitions over recent decades, driven by interactions among shoreline recovery, wind forcing, and sediment redistribution. Importantly, recent rapid dune growth indicates that the dune itself acts as an active sediment sink within the littoral

system, altering the balance of alongshore sediment transport. These insights provide the foundation for Chapter 3, which examines the detailed morphological evolution and aeolian sediment delivery processes at Ikobe.

Chapter 3

Field Survey, Data Processing, and Morphological Evolution of Cliff-Front Dunes

This chapter describes the field survey methods, data processing procedures, and topographic analyses used to quantify dune morphology. It also presents the observed temporal changes in the five major dune systems along the Atsumi Peninsula. Section 3.1 describes the observation methods, including handheld RTK measurements, drone-based RTK photogrammetry, and post-processing procedures for terrain data generation. Section 3.2 discusses the topographic changes identified from the Digital Surface Models (DSMs) generated for each survey period.

3.1 Field Survey and Data Processing

This section describes the field survey methods and data processing procedures. Three types of data sources were utilized: RTK-GNSS measurements, drone-based point data provided by collaborators, and drone imagery acquired by the author. Since these datasets differ in their format and resolution, their processing workflows also varied accordingly.

In the RTK-GNSS surveys, measurements were conducted at regular intervals along the dune surface to obtain discrete elevation points. The collected point data were then interpolated using ArcMap to generate a Digital Surface Model (DSM).

For the drone-based data, two approaches were applied: (1) Point-based datasets obtained from external drone observations were processed similarly to the RTK data using ArcMap interpolation to generate DSMs from the discrete points; and (2) Drone imagery captured in the visible spectrum was processed using Agisoft Metashape. Through the Structure from Motion (SfM) method, dense point clouds were reconstructed and subsequently converted into DSMs.

Finally, all DSMs whether derived from RTK measurements or drone-based datasets were subjected to geometric and vertical correction in ArcMap, ensuring consistency and accuracy across all survey periods.

3.1.1 Field Survey

Overview of the dune survey campaign across the Atsumi Peninsula

Field surveys were conducted between 2019 and 2025, with one to three campaigns per year. At least one survey was carried out each winter, corresponding to the season of dominant northwesterly monsoon winds that strongly influence dune development.

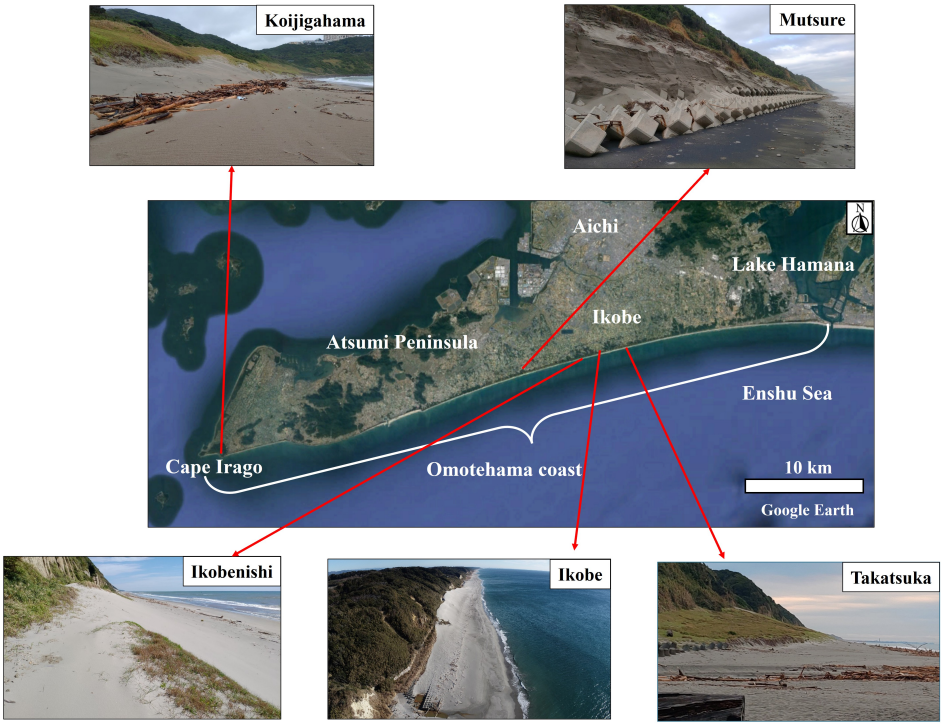

Figure 3.1: Dunes in Atsumi Peninsula

The primary focus of these surveys was the Ikobe dune, while additional measurements were occasionally conducted at other dunes along the Omotehama Coast, including Takatsuka, Ikobe-nishi, Mutsure, and Koijigahama (Fig. 3.1).

Table. 3.1 summarizes the survey datasets, classified by survey date, observation method, and target dune site.

Table 3.1: Summary of field survey data from 2019 to 2025.

Survey date	Observation method	Target dune
2019/01	RTK-GNSS	Ikobe、Takatsuka
2019/06	RTK-GNSS	Ikobe、Takatsuka
2019/11	Drone-based	Ikobe
2020/02	Drone-based	Ikobe
2021/02	Drone-based	Ikobe
2022/01	Drone-based	Ikobe
2022/06	Drone-based	All 5 dunes
2022/10	Drone-based	All 5 dunes
2023/01	Drone-based	Ikobe、Ikobenishi、Takatsuka
2023/07	Drone-based	Ikobe、Ikobenishi、Takatsuka
2024/01	Drone-based	Ikobe、Ikobenishi、Takatsuka
2025/01	Drone-based	Ikobe、Ikobenishi、Takatsuka

RTK-GNSS Observation

RTK (Real-Time Kinematic) Fig. 3.2 positioning determines the GNSS coordinates of both a reference station and a rover (mobile station). By reading the differential

corrections between the two stations, positional accuracy is greatly improved through the elimination of common satellite and atmospheric errors.

In this study, Network RTK was employed. The mobile station consisted of a handheld RTK receiver, while the reference station was a virtual reference point generated by Japan's VRS (Virtual Reference Station) system. Positional data were processed via NetSurv's RTK analysis service, which provides real-time correction information.

Handheld RTK measurements were conducted on the dunes at approximately 10 m intervals along predefined survey lines.The recorded point data were later interpolated using ArcMap to generate Digital Surface Models (DSM) representing dune topography.

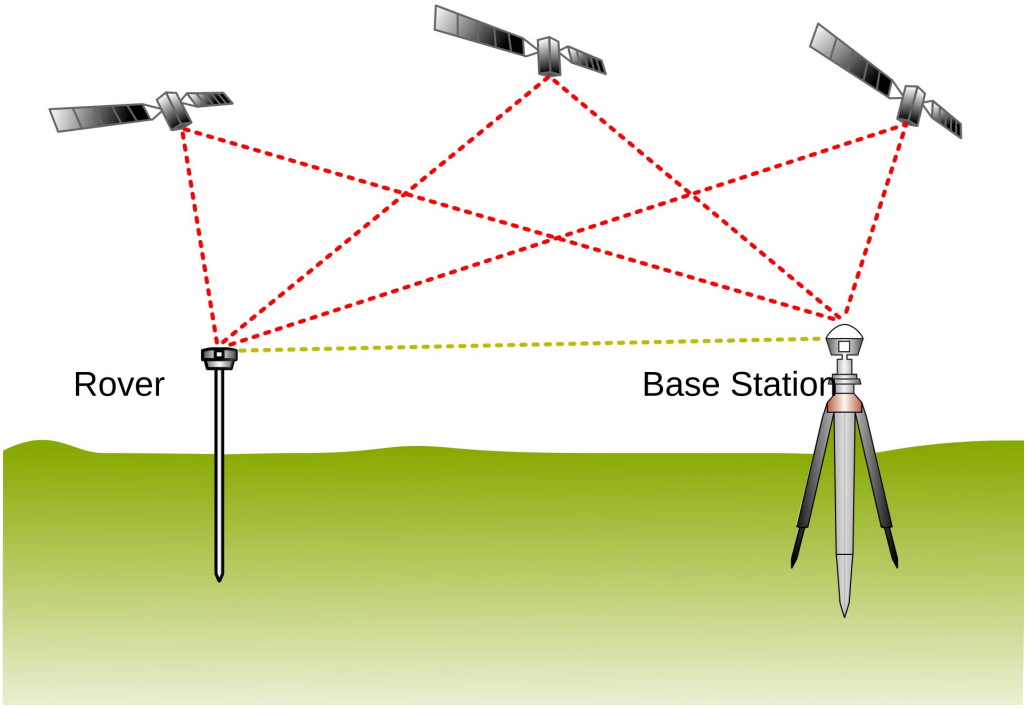

Figure 3.2: RTK-GNSS (Source:`https://sv.wikipedia.org/wiki/Real_time_kinematic`)

Drone-based Photogrammetry (Drone-RTK)

The mobile station (rover) of the Drone-RTK system (Fig. 3.3) is the drone itself, while the reference station is a GNSS receiver temporarily installed near the survey site. The receiver's positioning results were manually corrected using the measurement data obtained from the handheld RTK, thereby improving the overall positional accuracy.

The Drone-RTK measurements were conducted by flying the drone along a pre-defined flight path while continuously capturing overlapping images. The drone used in this study was a Phantom 4 RTK (DJI Co., Ltd.).A combination of nadir (90°) and oblique (60°) camera angles was applied during image acquisition to ensure sufficient surface coverage and geometric accuracy. The image overlap ratio was set to 80% for forward overlap and 70% for side overlap, which allowed for high-quality image alignment and 3D reconstruction in subsequent photogrammetric processing.

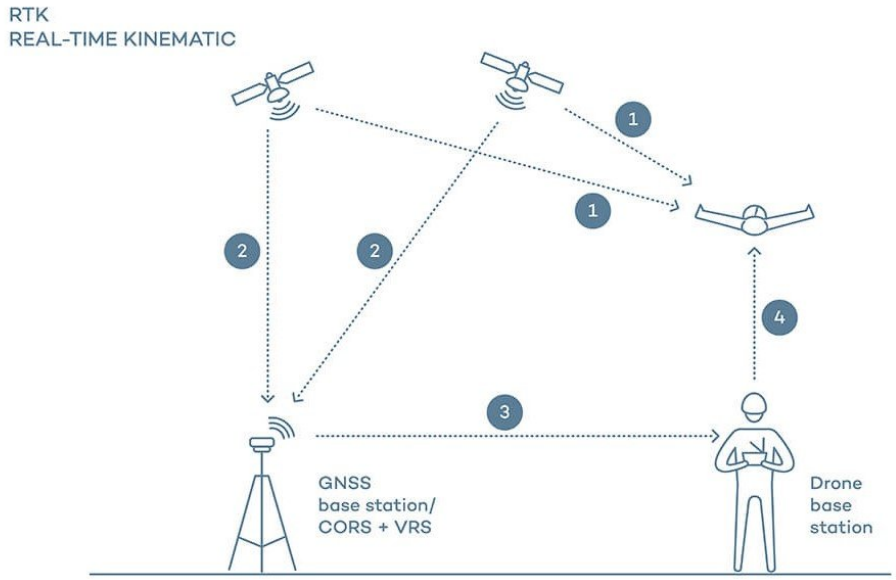

Figure 3.3: RTK-Drone (Source:`https://www.flyeye.io/drone-acronym-rtk`)

3.1.2 Data Processing

This section describes the data processing workflow used to construct digital terrain datasets from both RTK-GNSS and drone-based observations. The overall process consists of three major stages: (1) photogrammetric reconstruction using the Structure from Motion (SfM) method, (2) integration of RTK-GNSS and drone-derived point data to generate Digital Surface Models (DSM), and (3) geometric and vertical correction of the resulting terrain datasets.

SfM Processing and Generation of Digital Surface Models (DSM)

The photogrammetric workflow was performed using *Agisoft Metashape Professional*, following a standardized batch process applied individually to each dune. The overall procedure is summarized below.

Workspace preparation and image import. A dedicated workspace was created for each dune, and all aerial photographs were imported accordingly.

Batch execution setup. A pre-defined batch configuration (*"*Batch for Dune*"*) was used to automate the major photogrammetric operations, ensuring consistent processing parameters among all datasets.

Photo alignment. The Align Photos function was executed to detect and match feature points across overlapping images, reconstructing an initial sparse point cloud.

Alignment optimization. After alignment, the point cloud was refined through iterative optimization and noise reduction. Images with large reprojection errors were removed, and the camera parameters were re-optimized (Optimize Cameras → Advanced settings).

To further reduce noise, the Gradual Selection tool was applied to filter points with high *Reconstruction Uncertainty*, *Reprojection Error*, and *Projection Accuracy*. The order and intensity of these filters were adjusted adaptively for each dataset to minimize noise and improve geometric stability, rather than following a fixed sequence.

Dense reconstruction and DSM generation. After optimization, a dense point cloud was reconstructed using multi-view stereo (MVS) processing. A 3D mesh surface and texture were then generated, and the resulting Digital Surface Model (DSM) and orthophoto were exported in GeoTIFF format for further analysis.

Gradual Selection and Noise Reduction To enhance the geometric reliability of the reconstructed point clouds, the Gradual Selection process in Agisoft Metashape was applied using three filtering parameters: Reconstruction Uncertainty, Reprojection Error, and Projection Accuracy. The threshold values of these parameters were adaptively adjusted for each dataset according to variations in surface conditions, lighting, and image overlap.

The Reconstruction Uncertainty parameter primarily controls the removal of points with unstable triangulation geometry, while the Reprojection Error filter eliminates points exhibiting large residuals between the measured and projected image coordinates. Finally, the Projection Accuracy filter refines the dataset by excluding points with low projection reliability.

By combining these three filters, noise and outliers were effectively reduced while preserving the overall dune morphology. The final thresholds were empirically determined through iterative testing to achieve the minimum total alignment error.

The tables (Table. 3.2、Table. 3.3、Table. 3.4、Table. 3.5、Table. 3.6) below summarize the number of photographs and the threshold parameters used for noise reduction in each survey.

Table 3.2: Processing parameters for the Takatsuka dune.

Survey date	No.of photos	Reconstruction Uncertainty	Reprojection Error (pix)	Projection Accuracy
2022/06	502	X	0.4	3
2022/10	609	10	0.1	2
2023/01	86	8.4	0.7	2.1
2023/07	294	10	0.2	2
2024/01	280	10	0.3	2
2025/01	379	10	0.25	2

Integration of RTK-GNSS Point Data and Drone-derived Point Data for DSM Construction

Two types of topographic point data were used in this study: (1) sparse point data acquired by handheld RTK-GNSS measurements, and (2) dense point data derived from drone-based photogrammetry. Because these datasets differ in spatial density and measurement accuracy, they were processed separately prior to DSM generation.

Table 3.3: Processing parameters for the Ikobe dune.

Survey date	No.of photos	Reconstruction Uncertainty	Reprojection Error (pix)	Projection Accuracy
2021/02	241	X	0.4	X
2022/01	754	10	0.1	2
2022/06	639	X	0.6	X
2022/10	641	10	0.1	2
2023/01	643	X	0.8	1.9
2023/07	338	10	0.2	2
2024/01	394	10	0.3	2
2025/01	504	10	0.3	10

Table 3.4: Processing parameters for the Ikobe-nishi dune.

Survey date	No.of photos	Reconstruction Uncertainty	Reprojection Error (pix)	Projection Accuracy
2022/06	689	X	0.4	5
2022/10	214	10	0.1	2
2023/01	109	X	0.6	2.1
2023/07	187	10	0.2	2
2024/01	212	10	0.5	2
2025/01	241	10	0.3	2

Table 3.5: Processing parameters for the Mutsure dune.

Survey date	No.of photos	Reconstruction Uncertainty	Reprojection Error (pix)	Projection Accuracy
2022/06	594	X	0.4	5
2022/10	680	8	0.8	2

Table 3.6: Processing parameters for the Koijigahama dune.

Survey date	No.of photos	Reconstruction Uncertainty	Reprojection Error (pix)	Projection Accuracy
2022/10	524	10	0.1	2

RTK-GNSS point data. The RTK-GNSS surveys provided discrete elevation points measured at regular intervals along the dune surface. During the January 2019 survey, a total of 579 observation points were collected at the Ikobe dune and 715 points at the Takatsuka dune. In June 2019, the number of observation points increased to 816 at Ikobe and 635 at Takatsuka.

These point datasets were converted into continuous terrain surfaces (DSM) through spatial interpolation. Four interpolation techniques available in *ArcGIS Spatial Analyst* were examined: Inverse Distance Weighted (IDW), Kriging, Natural Neighbor, and Spline.

Interpolation methods:

(1) Inverse Distance Weighted (IDW):

This deterministic method estimates unknown cell values as a weighted average of known sample points, where weights decrease linearly with distance. It assumes spatial autocorrelation—nearby points have greater influence than distant ones and is effective for smoothly varying surfaces but may produce circular "bullseye" patterns around dense point clusters. (Reference: [Esri, n.d.a])

(2) Kriging: Kriging is a geostatistical interpolation method that incorporates both distance and spatial correlation between points. It uses a variogram model to describe spatial dependence and provides both predicted values and estimation variances. Although Kriging is theoretically robust, it requires extensive parameterization and is computationally intensive. It is best suited for datasets exhibiting strong directional or spatial correlation, such as geological or soil properties. (Reference: [Esri, n.d.b])

(3) Natural Neighbor: Natural Neighbor interpolation (Sibson, 1981) identifies the nearest subset of sample points around a query location and computes weighted averages based on the relative areas of Voronoi (Thiessen) polygons. The method is local, non-extrapolating, and guarantees that output values remain within the range of input samples. It preserves surface continuity without creating artificial peaks or pits, making it well suited for dune topography. (Reference: [Esri, n.d.c])

(4) Spline: Spline interpolation fits a minimum-curvature surface through the input points, producing a smooth continuous surface. It tends to over-smooth small topographic variations (e.g., dune crests) and is therefore less suitable for detailed dune morphology. (Reference: [Esri, n.d.d])

Comparison and selection of interpolation method. A qualitative comparison of the four interpolation methods is summarized in Table 3.7. Considering that the observed dune surfaces exhibit small-scale elevation variations and irregular microtopography, the **Natural Neighbor** method was selected as the most appropriate approach. This method provides accurate local interpolation without extrapolation and better preserves the natural relief of dune ridges and troughs.

For the interpolation, the cell size was set to 1 m, consistent with the survey point spacing of approximately 3–5 m. Given the millimeter-level measurement accuracy of the RTK data, the interpolation results adequately represent detailed dune morphology.

Table 3.7: Comparison of interpolation methods for dune surface generation.

Method	**Advantages**	**Disadvantages**	**Suitability for dunes**
IDW	Simple, fast, adjustable smoothness	May produce bullseye artifacts near peaks	Moderate (adequate for coarse terrain)
Spline	Produces smooth continuous surfaces	Over-smooths local dune ridges	Limited (suitable only for sparse data)
Natural Neighbor	High accuracy, preserves local variations, no extrapolation	Slightly slower than IDW but faster than Kriging	**Best** (most realistic dune surface)
Kriging	Statistically rigorous, models spatial variability	Complex setup, long computation, may overfit	High (for large-scale modeling)

Drone-derived point data. In addition to the RTK-GNSS surveys, high-density point clouds were generated from drone-based photogrammetry. The drone-derived point cloud data used in this study were provided by Dr. Takumi Okabe (currently Associate Professor at Mie University), who conducted the original UAV photogrammetry surveys during his tenure at Toyohashi University of Technology. The datasets were subsequently processed by the author for Digital Surface Model (DSM) generation and analysis.

In the November 2019 survey, a total of approximately 4090354 points were obtained over the Ikobe dune. In the February 2020 survey, this increased to approximately 6 381614 points over the same dune area. Compared with the RTK-GNSS measurements, which consist of sparsely sampled elevation points at discrete intervals, the drone-derived datasets provide a spatially continuous, high-resolution representation of the dune surface.

Because the point density was sufficiently high, the drone-derived point clouds were directly converted to raster surfaces using the *Point to Raster* tool in ArcGIS rather than interpolated using a surface-fitting method. The output raster cell size was set to 0.1 m in both the x and y directions, consistent with the spatial resolution adopted for the UAV photogrammetry products.

For the *Cell assignment type* parameter, the *MAXIMUM* option was selected. This option assigns to each raster cell the maximum elevation value among all input points falling within that cell. This choice is appropriate for coastal dune morphology, because the objective is to capture the upper dune surface (crest and outer envelope), rather than to average or smooth local micro-topography. In contrast, using an average (MEAN) or minimum (MINIMUM) assignment would tend to flatten the dune crest or artificially lower steep dune faces.

The resulting 0.1 m raster generated from the UAV point cloud was then treated as the drone-derived DSM and used in subsequent analysis together with the RTK-GNSS−derived surfaces.

Geometric and Vertical Correction of Terrain Datasets

Before integrating the DSM and orthophoto data into ArcGIS for further analysis, geometric and vertical corrections were applied to ensure spatial consistency among all datasets.

(1) **Coordinate system verification.** All terrain datasets were verified to use the *Japan Geodetic Datum 2011 (JGD2011)* with the *Zone 7* projected coordinate system, as Aichi Prefecture is located within the 7th zone of Japan's national plane rectangular coordinate system.

(2) **Projection transformation and resampling.** The DSMs and orthophotos generated by *Agisoft Metashape* were initially in the *GCS_WGS1984* coordinate system. Using the *Project Raster* tool in ArcGIS, these datasets were reprojected into the *JGD2011 / Japan Plane Rectangular CS Zone 7* system (Fig. 3.4). Since the original data accuracy was within 0.1 m, the output raster resolution (i.e., pixel size in both x and y directions) was set to 0.1 m.

Regarding the *resampling technique*, four interpolation options are available in ArcGIS:

Resampling methods. When raster data are reprojected or rescaled, the value of each output cell must be derived from nearby cells in the original raster. Because the center

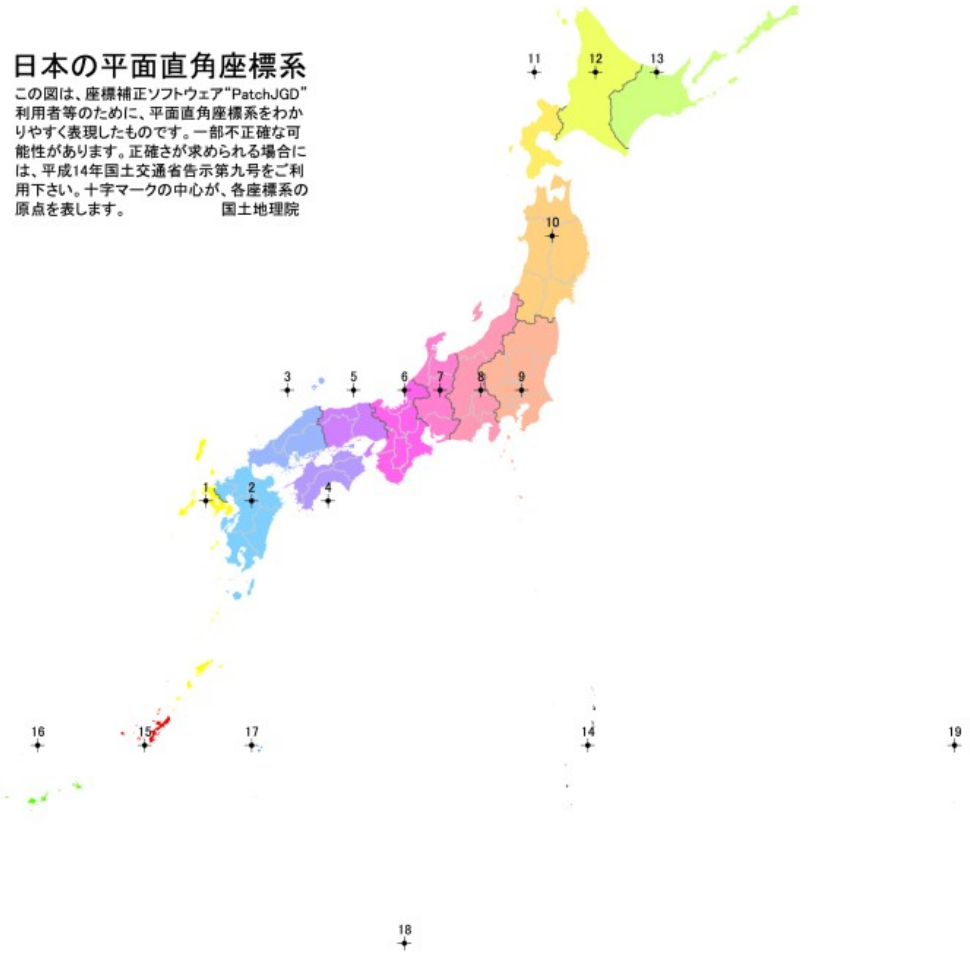

Figure 3.4: Japan Plane Rectangular Coordinate System zones (JGD2011). (Source: `https://www.gsi.go.jp/sokuchikijun/jpc.html`)

of an output cell rarely coincides exactly with that of an input cell, various interpolation methods are used to estimate appropriate values for the output grid. According to the documentation of *ArcGIS Pro* [Esri, 2025a][Esri, 2025b], four primary techniques are commonly employed: nearest neighbor assignment, bilinear interpolation, cubic convolution, and majority resampling.

- **Nearest Neighbor:** Fig. 3.5 assigns the value of the closest input cell to each output cell. It does not modify cell values and is therefore ideal for categorical data, such as land-use or soil type. However, it may produce a blocky or "stepped" appearance in continuous surfaces.
- **Bilinear Interpolation:** Fig. 3.6 computes a weighted average of the four nearest input cells based on their distance from the output cell center. This method generates smoother transitions and is suitable for continuous surfaces, such as elevation or DSM data.
- **Cubic Convolution:** Fig. 3.7 extends bilinear interpolation to the 16 nearest input cells, fitting a smooth cubic surface to estimate the output value. It tends to sharpen edges and is recommended for image data (e.g., orthophotos or visual rendering).
- **Majority:** performs a majority algorithm that determines the new value of

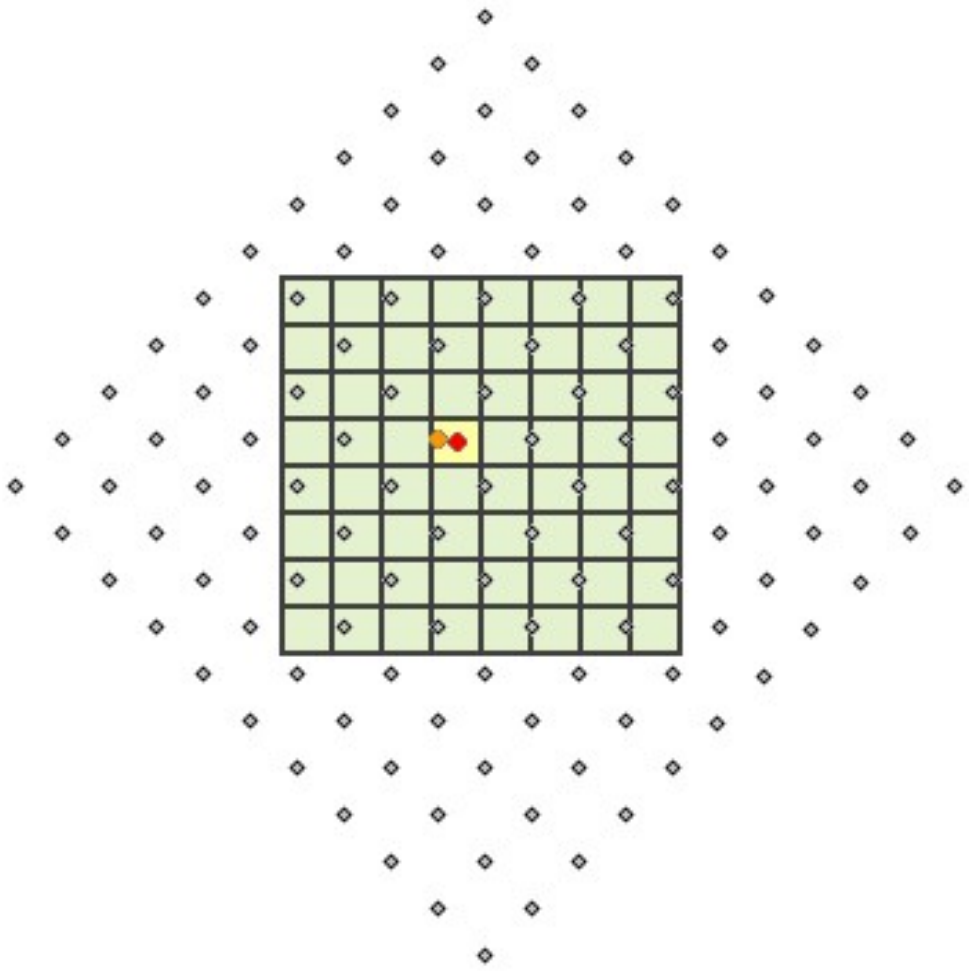

Figure 3.5: Nearest Neighbor

each output cell based on the most frequently occurring values within a 4-by-4 neighborhood window in the input raster. It is mainly used with discrete or classified data, similar to the nearest neighbor method, but tends to produce a smoother overall result.

Among these methods, **Bilinear interpolation** was applied to the DSMs in this study to ensure smooth elevation continuity, while **Cubic convolution** was used for the orthophotos to preserve visual sharpness without introducing pixel artifacts.

(3) **Construction of the geoid raster.** The DSM data obtained from RTK-GNSS and drone photogrammetry initially represent ellipsoidal heights. To convert them into orthometric heights (above mean sea level), the geoid undulation must be subtracted from the ellipsoidal elevation. For this purpose, a geoid raster was created as follows: Geoid point data from the Geospatial Information Authority of Japan (GSI, 2011) were first downloaded and converted to the JGD2011 coordinate system. The point data were then interpolated using the Natural Neighbor method to produce a continuous raster surface representing geoid height. The *Output cell size* was set to 100 m, considering that the original spacing between GSI geoid points is approximately 300 m. The Natural Neighbor method was chosen because it does not extrapolate beyond the range of the input points, thus ensuring stable interpolation within the data coverage.

(4) **Conversion to orthometric elevation.** Using the *Raster Calculator* in ArcGIS,

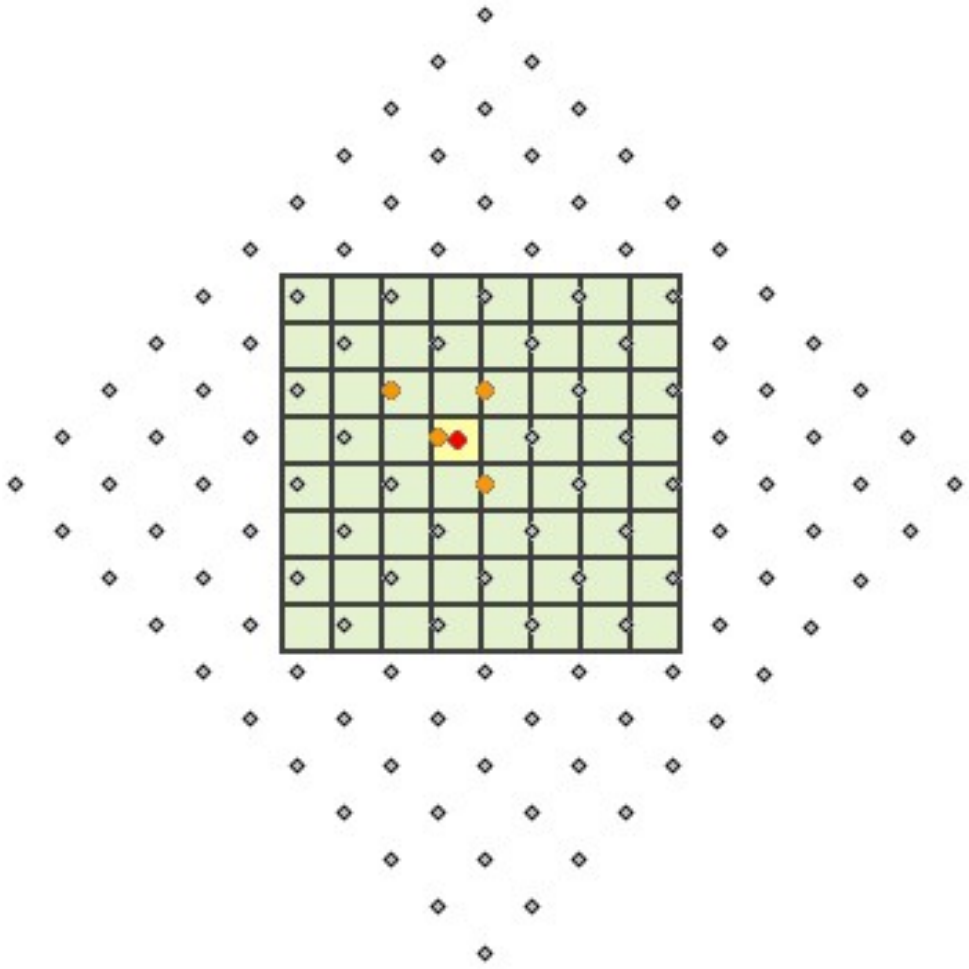

Figure 3.6: Bilinear Interpolation

the orthometric elevation map was obtained by subtracting the geoid raster from the DSM data (`DSM -Geoid = Elevation`). The *mask*, *extent*, and *snap raster* settings were aligned with the DSM, and the *cell size* was standardized to 0.1 m to maintain consistency across all datasets.

(5) **Establishment of a dune elevation reference map.** According to the Geospatial Information Authority of Japan, the elevation of the tidal datum at Akabane (located on the Atsumi Peninsula) is −359.1 mm relative to the national reference plane, and the five-year mean spring high tide level is +438.7 mm. Therefore, the orthometric height of the five-year mean spring high tide corresponds to approximately +0.796 m. Based on this reference, a preliminary raster was generated using the *Raster Calculator* to delineate the potential dune extent, defined as areas with elevations between 0.8 m and 30 m (the maximum dune height is about 25 m).

(6) **Dune boundary delineation.** Using the dune reference raster and ortho-photo images, the actual dune boundaries were manually delineated by visually interpreting the wet line (maximum wave run-up limit) and the cliff base. This polygon was used as the final target area for subsequent analysis.

(7) **Extraction of the dune elevation model.** Finally, the dune region was extracted from the corrected DSM using the *Extract by Mask* tool. The resulting raster represents the final orthometric-elevation DSM of the dune, which was used for all subsequent volumetric and morphological analyses.

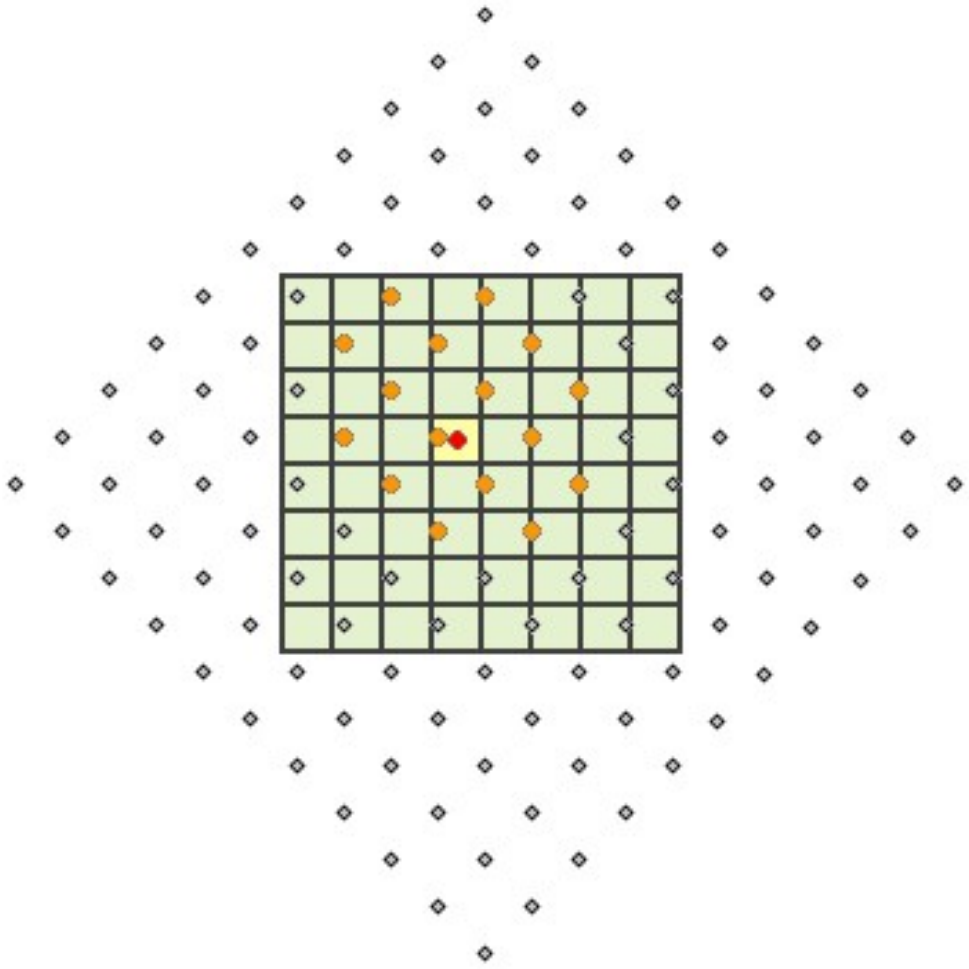

Figure 3.7: Cubic Convolution

(8) **Vertical correction.** Vertical calibration was performed by comparing ground-based RTK-GNSS checkpoints with the drone-derived DSM values. Two reference types were used depending on data availability: fixed parking area reference points and multiple dune checkpoints distributed across the dune surface. The mean elevation difference between the two datasets was calculated and applied as the vertical correction value. When the elevation discrepancy was within ±0.1 m, no additional correction was applied, as the accuracy was considered sufficient for volumetric and morphological analyses. A summary of the vertical correction parameters for each dune dataset is presented in Table 3.8. The table lists the survey dates, correction method used for calibration, and the resulting correction value applied to each dataset.

Slope analysis and dune boundary identification

In this study, dune boundaries were identified using both slope maps and orthomosaic images. When using imagery alone, it is often difficult to distinguish dunes from sandy beaches, and when using DSM or DEM elevation data alone, newly formed low dunes may be overlooked. Therefore, slope analysis provides the most effective method for delineating dune areas. However, artificial structures may locally distort the slope results, so orthomosaic images were used for visual verification and correction.

Vegetation was not removed prior to slope analysis, as there is currently no effective

Table 3.8: Summary of vertical correction parameters for each dune dataset.

Dune name	Survey date	Correction method	Value (m)
Takatsuka	2022/06	Multiple dune checkpoints	-1.403
Takatsuka	2022/10	Parking area reference	-0.345
Takatsuka	2023/01	Not applicable	—
Takatsuka	2023/07	No correction required	—
Takatsuka	2024/01	No correction required	—
Takatsuka	2025/01	No correction required	—
Ikobe	2021/02	No correction required	—
Ikobe	2022/01	Multiple dune checkpoints	-1.365
Ikobe	2022/06	Multiple dune checkpoints	-2.237
Ikobe	2022/10	Parking area reference	-1.541
Ikobe	2023/01	Multiple dune checkpoints	-1.246
Ikobe	2023/07	Parking area reference	-1.414
Ikobe	2024/01	Multiple dune checkpoints	-1.133
Ikobe	2025/01	Multiple dune checkpoints	-1.422
Ikobenishi	2022/06	Not applicable	—
Ikobenishi	2022/10	No correction required	—
Ikobenishi	2023/01	Not applicable	—
Ikobenishi	2023/07	Not applicable	—
Ikobenishi	2024/01	Not applicable	—
Ikobenishi	2025/01	Multiple dune checkpoints	-0.993
Mutsure	2022/06	Multiple dune checkpoints	-1.721
Mutsure	2022/10	Not applicable	—
Koijigahama	2022/10	Not applicable	—

method for complete vegetation filtering in this area. The existing vegetation mainly consists of low grasses, and thus has a limited impact on the accuracy of slope-based dune delineation.

Slope values were then calculated using the *Slope* tool in ArcGIS Spatial Analyst, which computes the maximum rate of elevation change between each cell and its eight neighboring cells within a nine-pixel window.

Based on previous research, the slope classification criteria for coastal sand dunes were defined as follows. According to Shepard [1973], the mean beach slope for sand with grain size between 0.2–0.5 mm is approximately 5°. Al-Hashemi (2018)Al-Hashemi et al. [2018] summarized that the natural angle of repose for sand typically ranges from 30° to 35°. Therefore, in this study, slopes below 5° were classified as sandy beach, 5°–10° as the transition zone between beach and dune, 10°–25° as the gentle slope zone of dunes, and 25°–35° as the steep slope zone of dunes.

To validate the applicability of these thresholds, the Ikobe Dune —the steepest among all survey sites —was analyzed in detail. A one-meter interval profile was extracted from the DSM, extending from the dune crest (defined as 0 m in the horizontal axis) toward the shoreline. The left graph in Fig. 3.8 shows the slope angle variation from crest to toe, and the right graph shows the corresponding elevation profile. The crest area has slopes below 10° at elevations around 20 m, the steepest mid-slope reaches approximately 30° at 15 m elevation (about 20 m horizontally from the crest), and the dune toe exhibits slopes between 10° and 15° at elevations near 5 m. These results confirm that setting the dune boundary threshold at 10° and the upper limit (angle of repose) at 35° provides a reasonable and consistent delineation of dune extent. Although the dune top occasionally

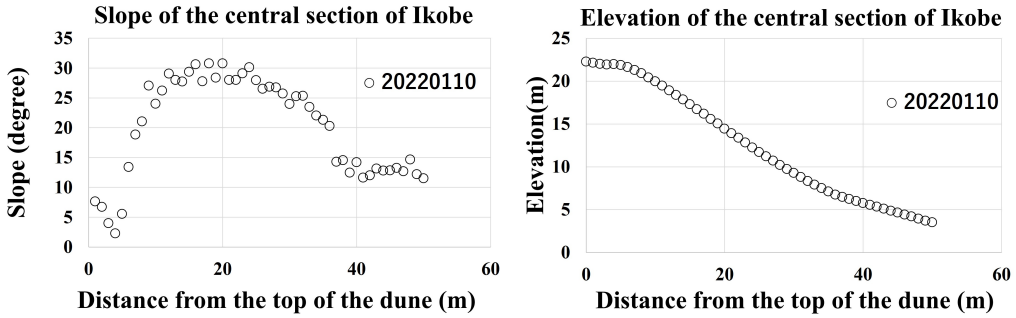

Figure 3.8: Ikobe profile

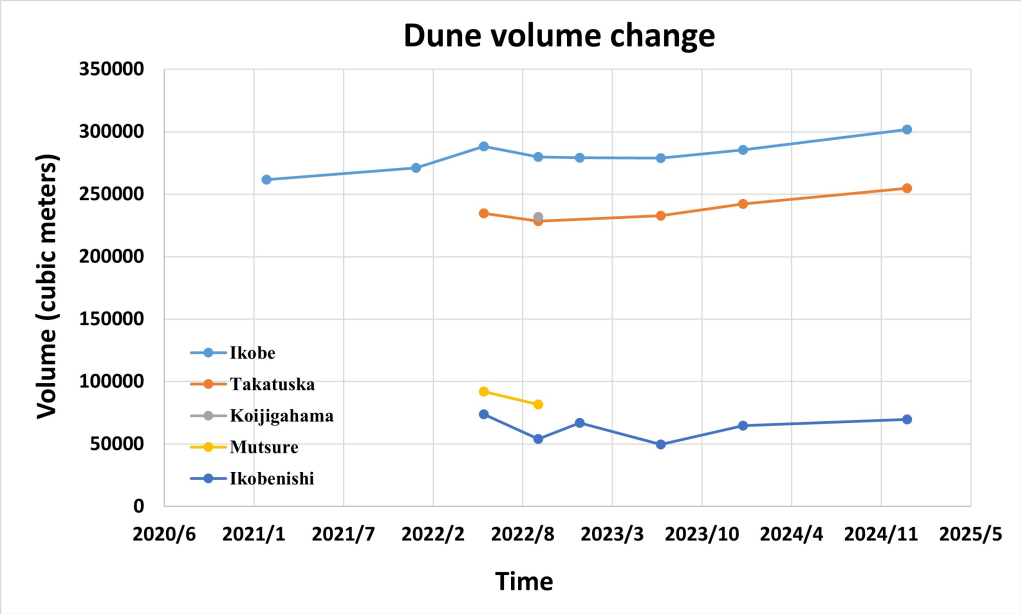

Figure 3.9: Dune change

shows slopes below 10°, its proximity to the sea cliff allows the cliff slope to define the inland boundary.

3.2 Survey Results of the Five Dune Sites in the Atsumi Peninsula

Fig. 3.9 shows the temporal changes in dune volume at the five study sites. Among them, Ikobe and Takatsuka exhibited an overall increasing trend in total volume. Koijigahama Dune was surveyed only once and therefore lacks follow-up data, while Mutsure Dune showed a slight decrease in total volume over the observation period. Ikobenishi Dune remains relatively small in scale and is therefore highly susceptible to fluctuations driven by wave action and weather conditions. As a result, its morphology varies markedly and exhibits considerable temporal instability. The large-scale dunes such as Ikobe, Takatsuka, and Koijigahama have total volumes on the order of approximately 200,000 m^3, whereas Mutsure and Ikobenishi Dunes remain below 100,000 m^3.

In the following sections, detailed results for each dune are presented, including Digital Surface Models (DSMs), orthophoto images, elevation change maps, and slope variation maps.

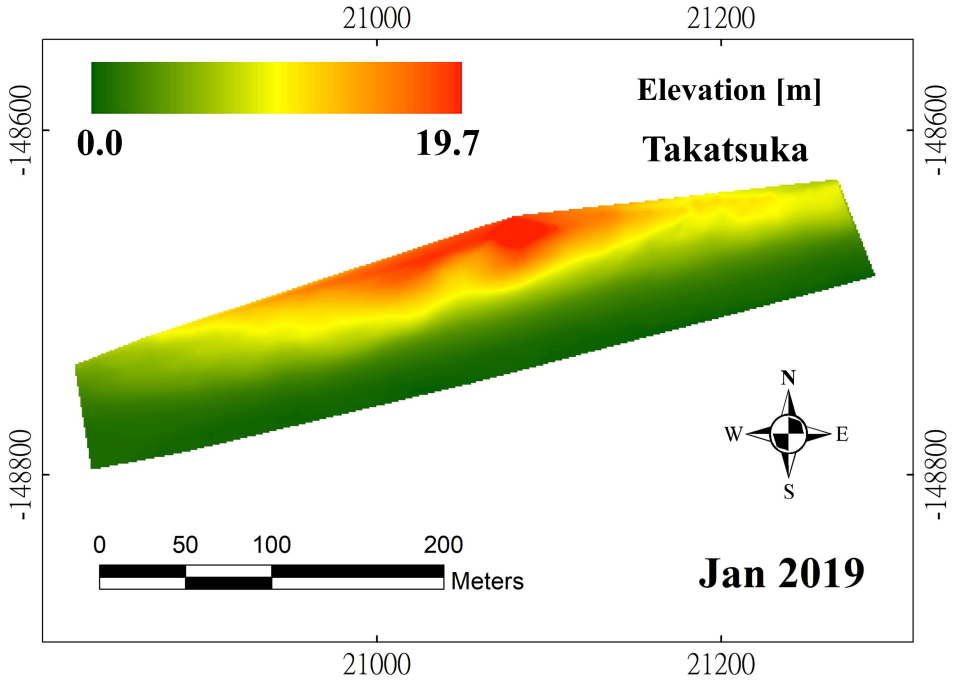

Figure 3.10: Takatsuka DSM 201901

3.2.1 Takatsuka Dune

The elevation of the Takatsuka Dune has remained approximately 20 m in recent years, with a gradual overall increase in total volume.

Fluvial topography. Due to the presence of a small river dividing the dune, sand accumulation mainly occurs on the western side, while the eastern portion remains relatively low in elevation. In 2019 (Fig. 3.10 & 3.11), when DSMs were generated from interpolated RTK points, the river feature was not visible; however, the 2022 dataset (Fig. 3.12 & Fig. 3.13) clearly revealed a small channel through the dune center, which widened in 2023 (Fig. 3.14 & Fig. 3.15) and became shallower again in 2024 (Fig. 3.16)、2025 (Fig. 3.17). The dune's lateral expansion was constrained by both the river and the adjacent parking area. The orthophotos used for visual reference are provided in Appendix 7.4.

Elevation Change

Between June and October 2022 (Fig. 3.18), the dune surface showed dominant bluish colors in the elevation-change map, indicating net erosion. This reflects the summer season when aeolian transport weakens and rainfall or typhoon events cause surface degradation. From July 2023 to January 2024 (Fig. 3.19), deposition resumed, and despite summer erosion, the dune continued to accumulate sand through the following winter. Throughout 2024–2025 (Fig. 3.20), the dune exhibited net accretion, indicating a long-term positive sediment balance.

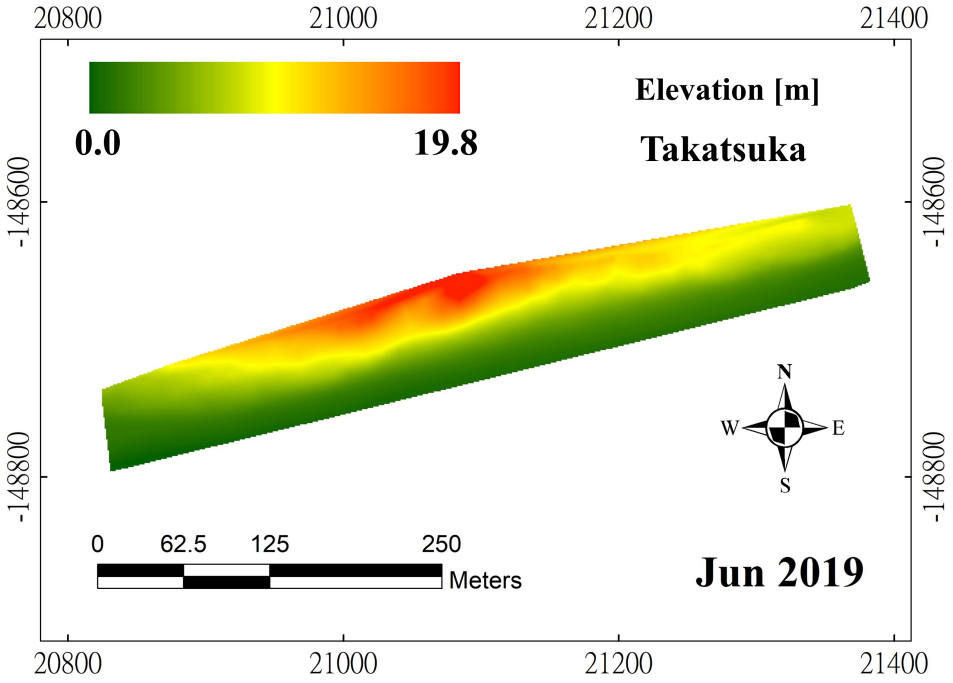

Figure 3.11: Takatsuka DSM 201906

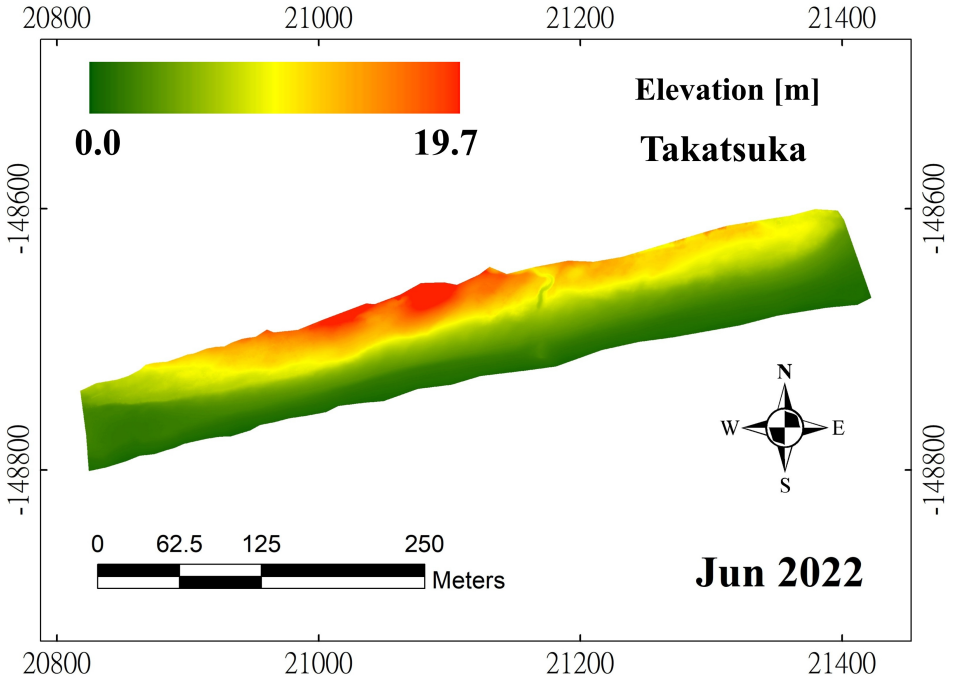

Figure 3.12: Takatsuka DSM 202206

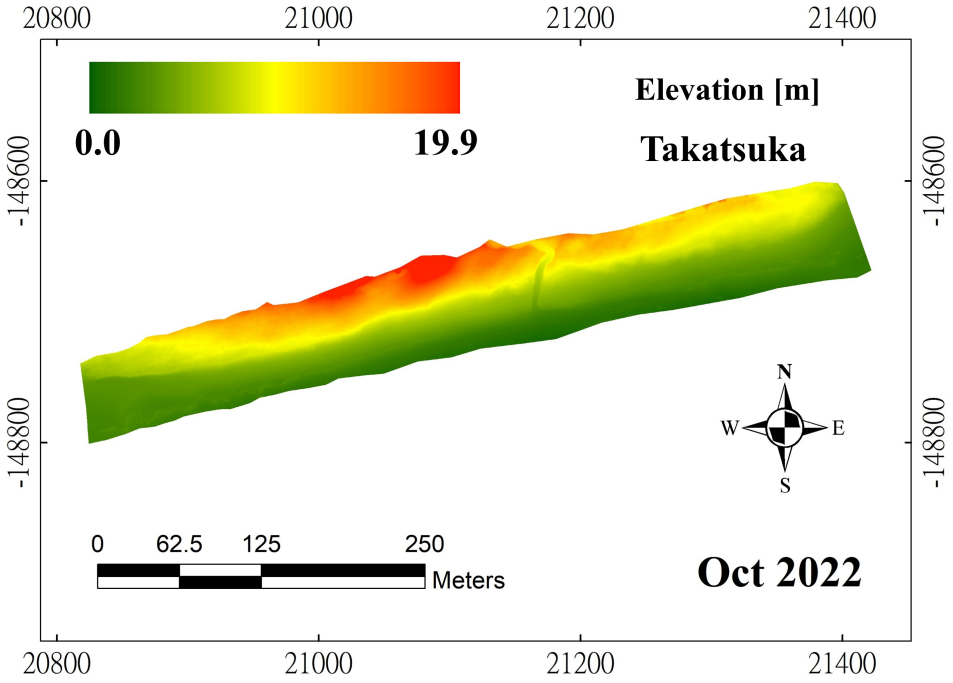

Figure 3.13: Takatsuka DSM 202210

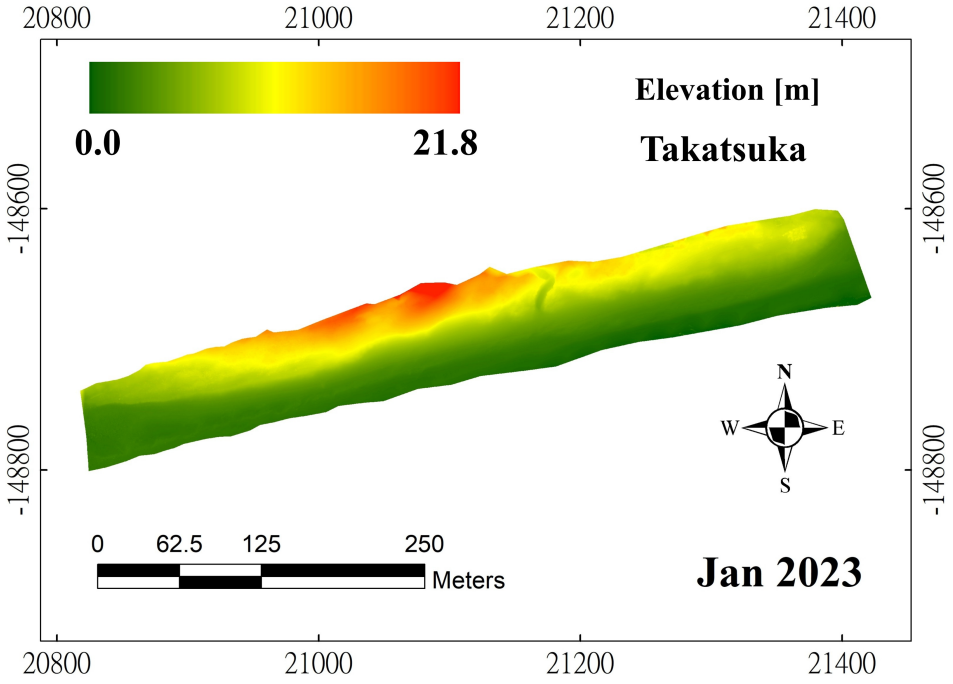

Figure 3.14: Takatsuka DSM 202301

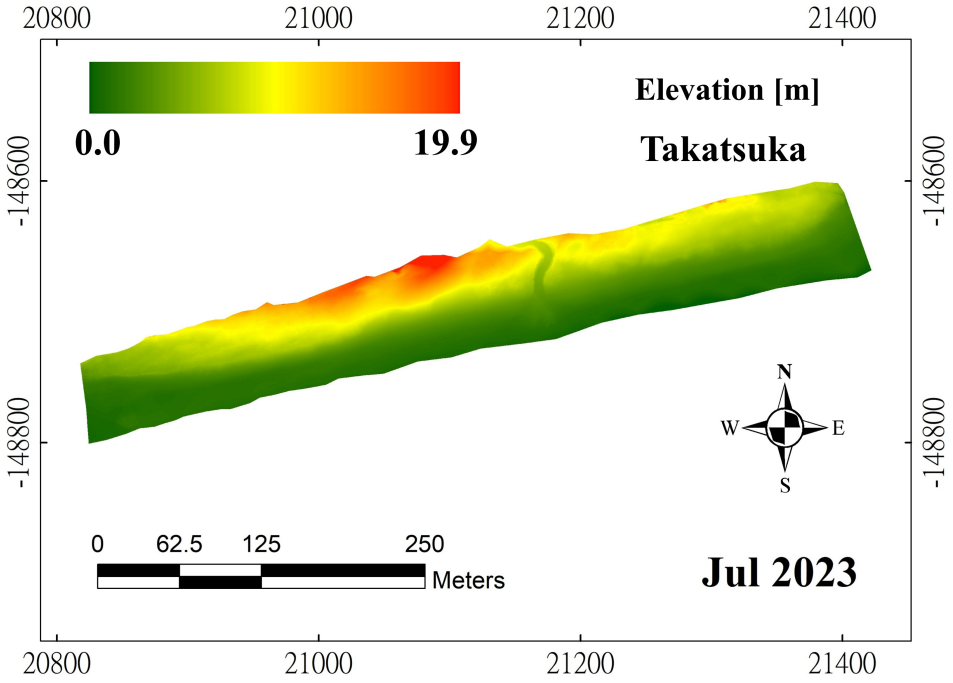

Figure 3.15: Takatsuka DSM 202307

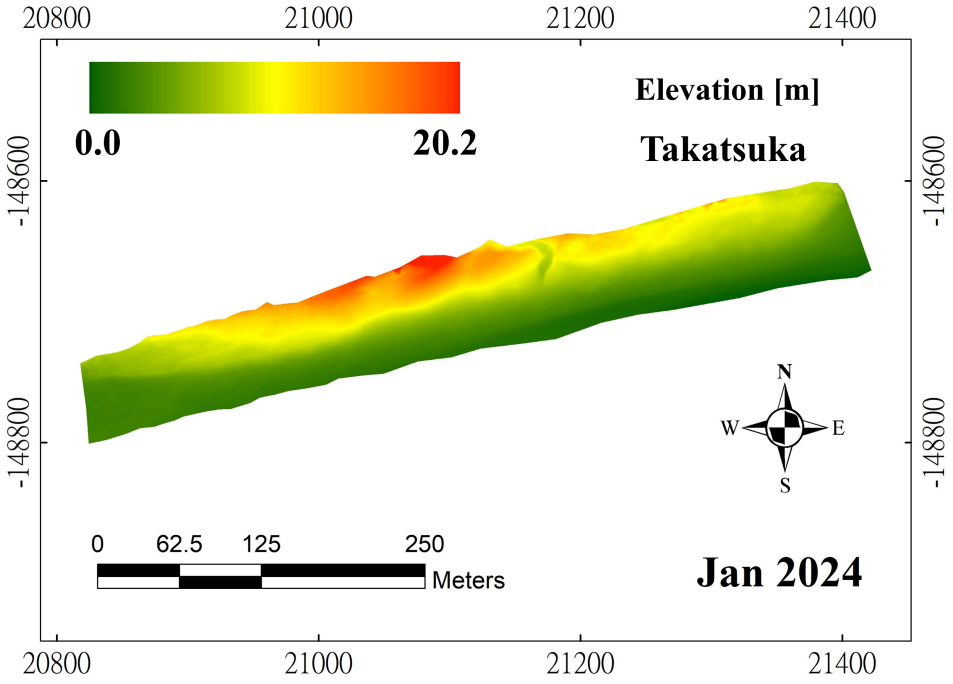

Figure 3.16: Takatsuka DSM 202401

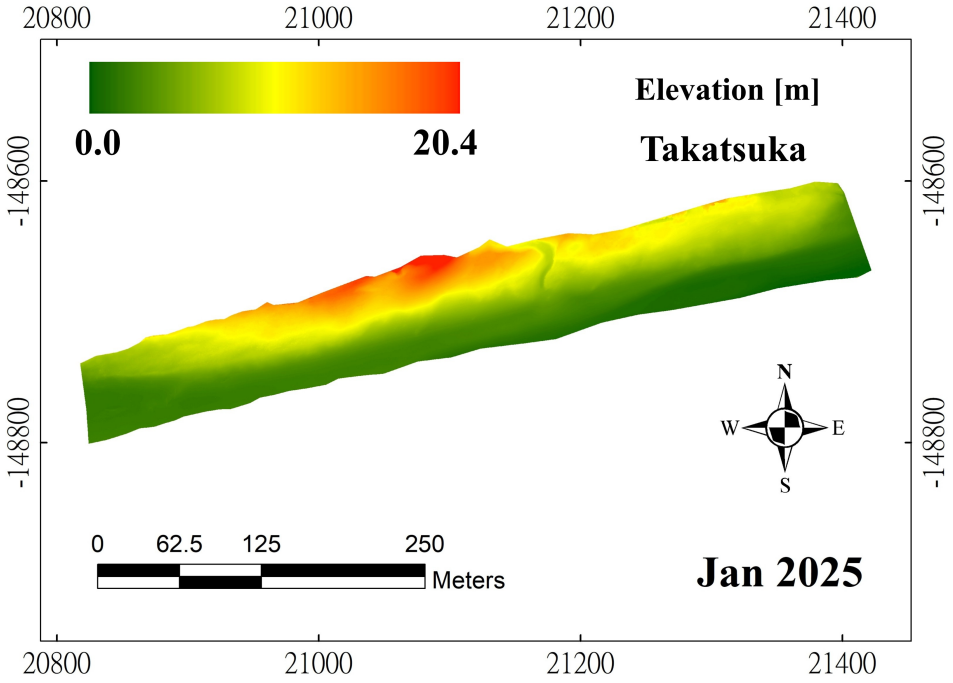

Figure 3.17: Takatsuka DSM 202501

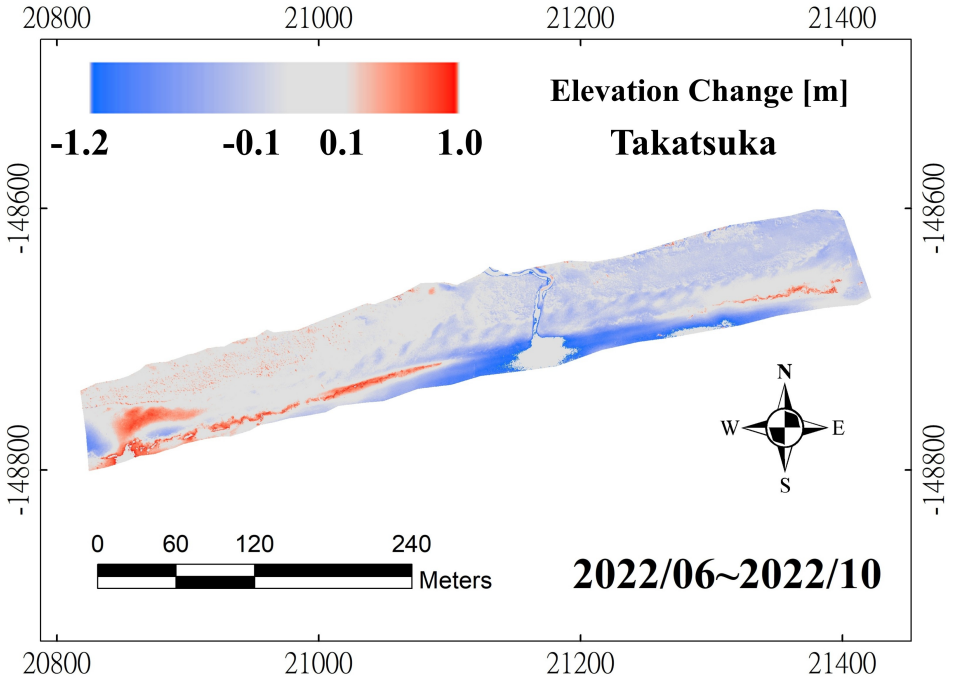

Figure 3.18: Takatsuka Elevation Change 202206-202210

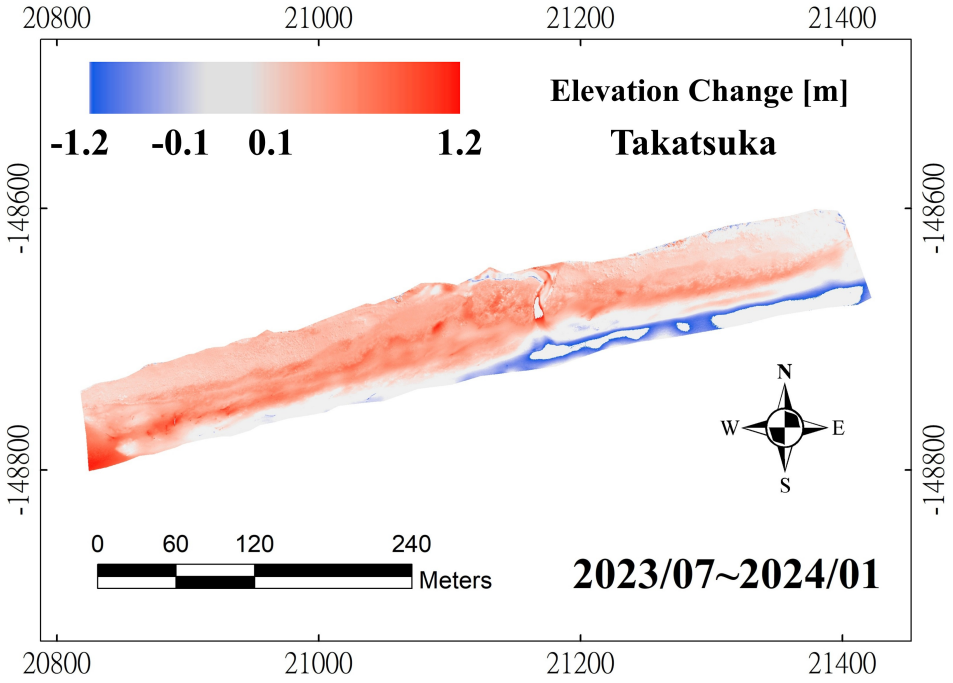

Figure 3.19: Takatsuka Elevation Change 202307-202401

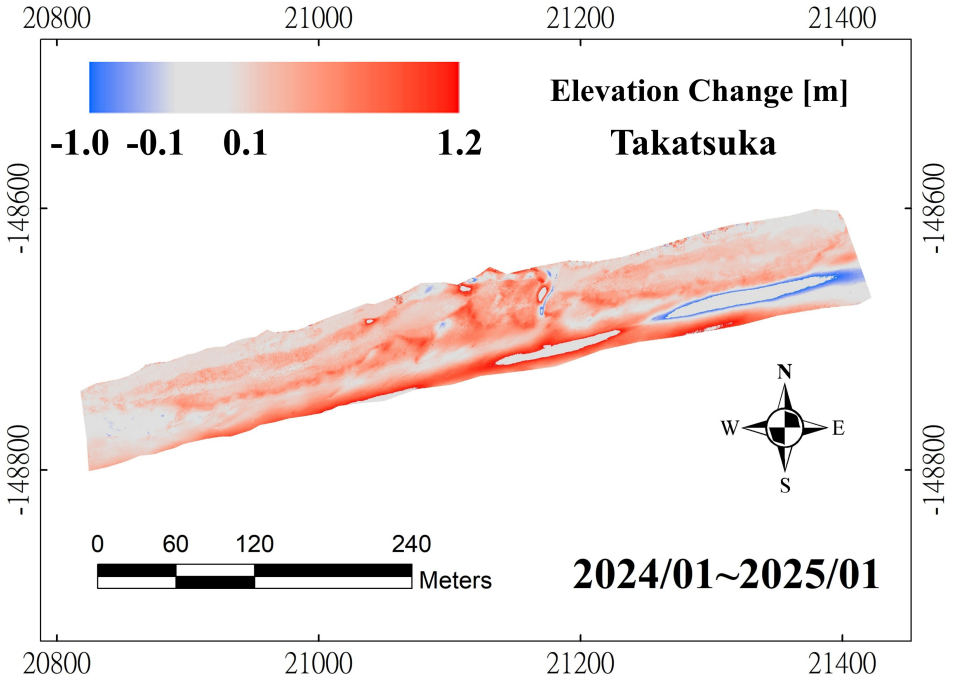

Figure 3.20: Takatsuka Elevation Change 202401-202501

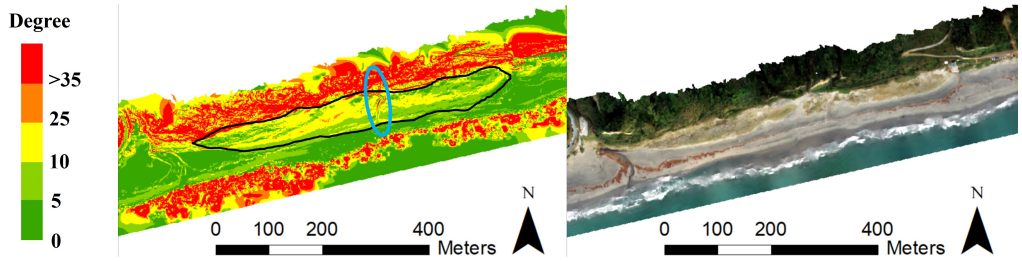

Figure 3.21: Takatsuka Slope 2022

Slope Variation

The topography of the Takatsuka Dune (Fig. 3.21) is more effectively interpreted from the slope map than from the orthophoto image alone. Significant slope variations are observed along the sea cliff at the top of the figure and the water surface at the bottom. These two regions exhibit considerable noise in the DSM generated by the SfM method: the cliff area is densely covered with trees, while the water surface is affected by wave reflection, both of which introduce artifacts during image matching.

Additional noise is also found within the dune area, particularly in the black-circled zone, where vegetation growth has increased in recent years as the dune has entered a mature stage. These vegetation types typically grow in summer and autumn. Furthermore, the slope along both sides of the small river varies sharply, which is difficult to distinguish based on orthophoto imagery alone.

Overall, the slope maps reveal that most dune surfaces have slope angles between 10° and 25°, with locally steeper zones exceeding 35° observed along the dune crest and riverbanks (blue-circled). These results indicate that while the general morphology of the dune remains stable, vegetation and hydrological features introduce local noise that must be accounted for in slope-based analyses. For slope maps of other survey periods, refer to the Slope Figures Appendix 7.4.

3.2.2 Ikobe Dune

The elevation of the Ikobe Dune increased from approximately 20 m in 2019 (Fig. 3.22) to about 25 m by 2021 (Fig. 3.23), after which the crest height stabilized around 25 m (Fig. 3.24). The total dune volume also exhibited a gradual increase over this period, indicating continued sediment accumulation even after the dune height reached equilibrium. Detailed DSM maps and orthophotos for other survey years are provided in the Slope Figures (Appendix 7.4) and (Appendix 7.4).

Elevation Change

Annual elevation-change maps from 2021–2025 all indicate dominant accretion trends. Seasonally, from January to June 2022 ((Fig. 3.25)), deposition occurred mainly at the dune base, likely due to weaker wind speeds. From June to October 2022 ((Fig. 3.26)), aeolian transport weakened and rainfall caused widespread erosion. From October 2022 to January 2023 ((Fig. 3.27)), accretion resumed across most of the dune, particularly near the crest. From January to July 2023 ((Fig. 3.28)), erosion again dominated, probably under weak wind and rainfall influence. From July 2023 to January 2024, accretion recurred, especially near the dune crest. In summary, the dunes show seasonal alternation:

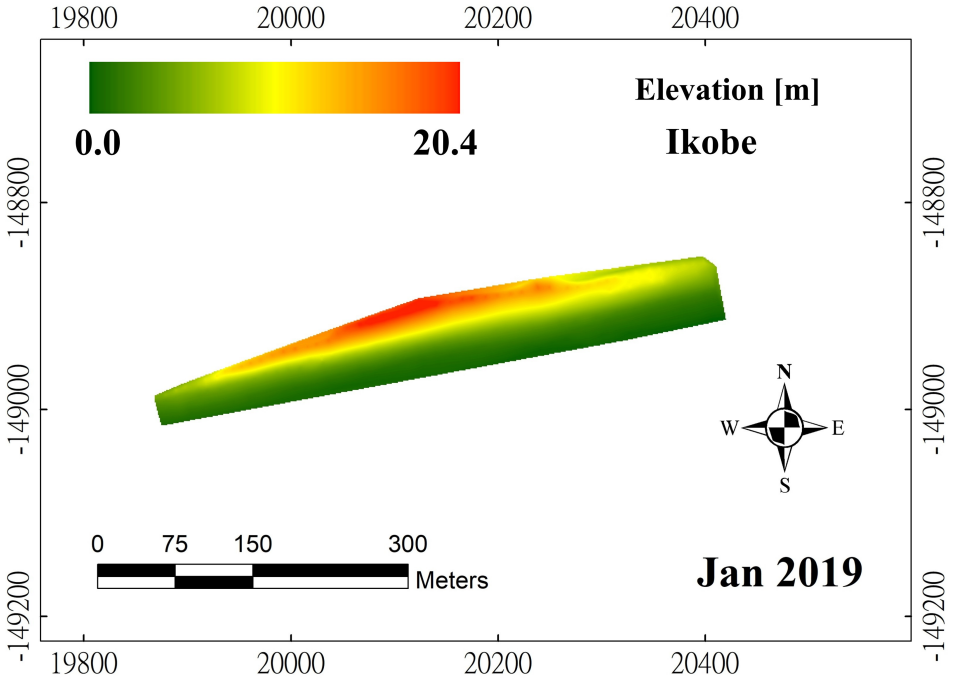

Figure 3.22: Ikobe DSM 201901

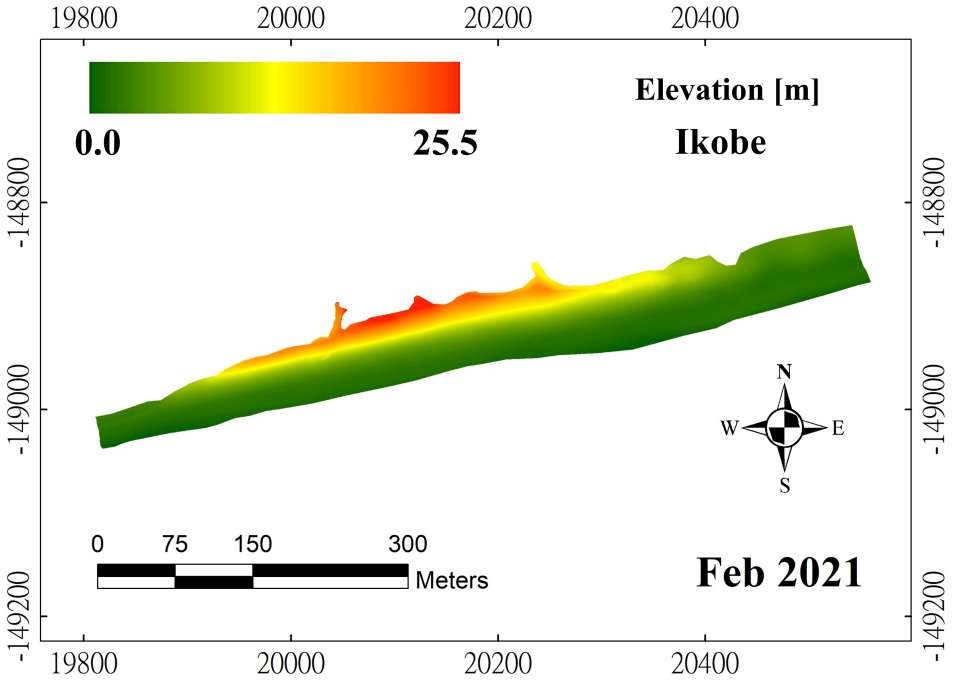

Figure 3.23: Ikobe DSM 202102

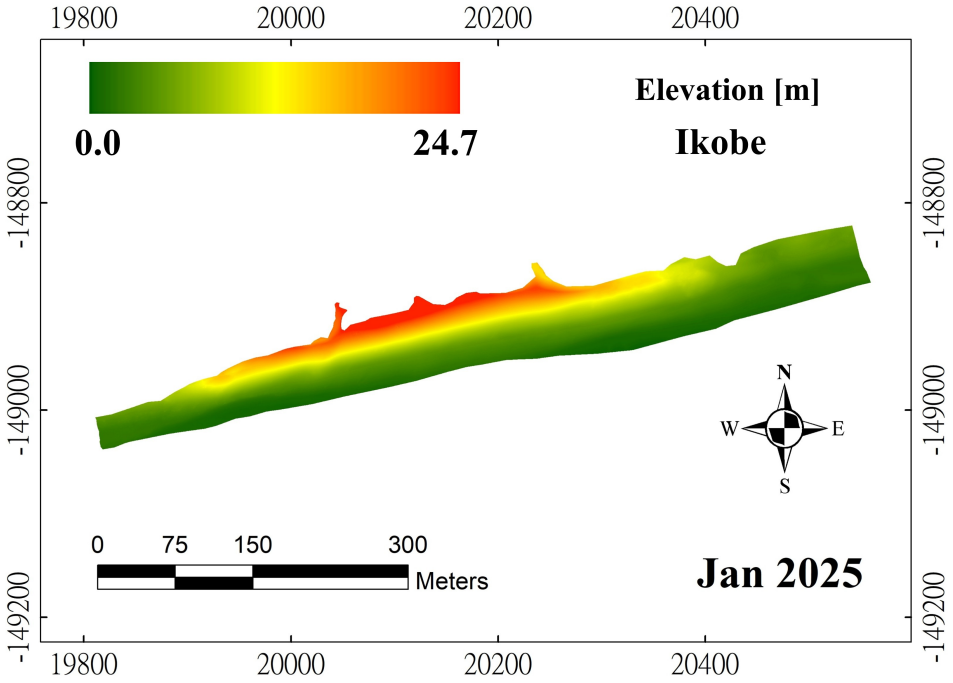

Figure 3.24: Ikobe DSM 202501

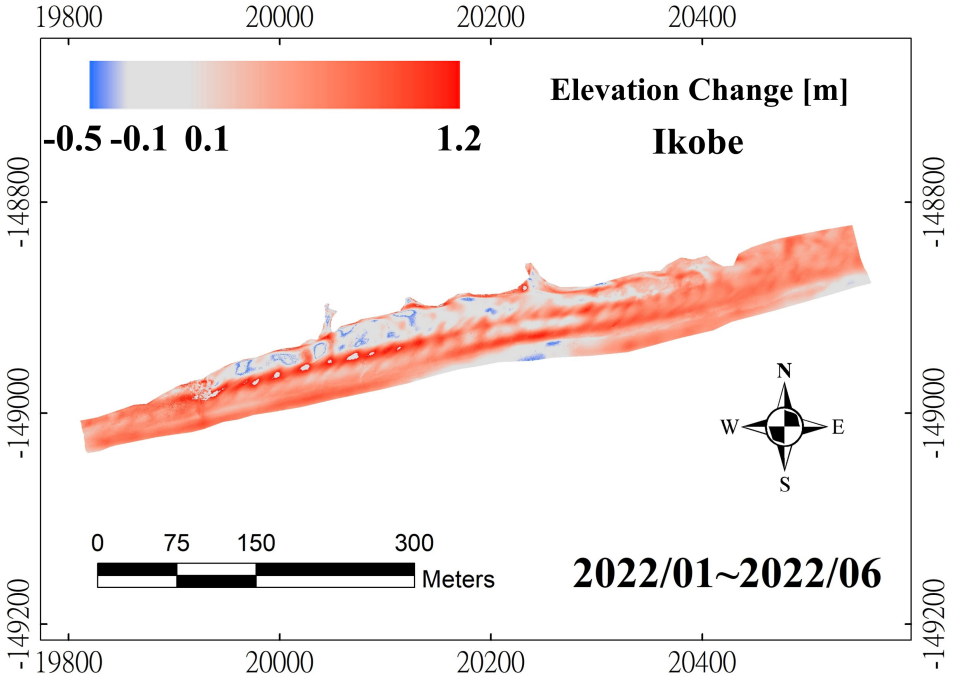

Figure 3.25: Ikobe Elevation Change 202201-202206

deposition during winter–spring when strong winds enhance sand transport, and erosion during summer–autumn when weaker winds and rainfall prevail.

Detailed elevation-change maps for other survey years are provided in the Elevation Change Figures (Appendix 7.4).

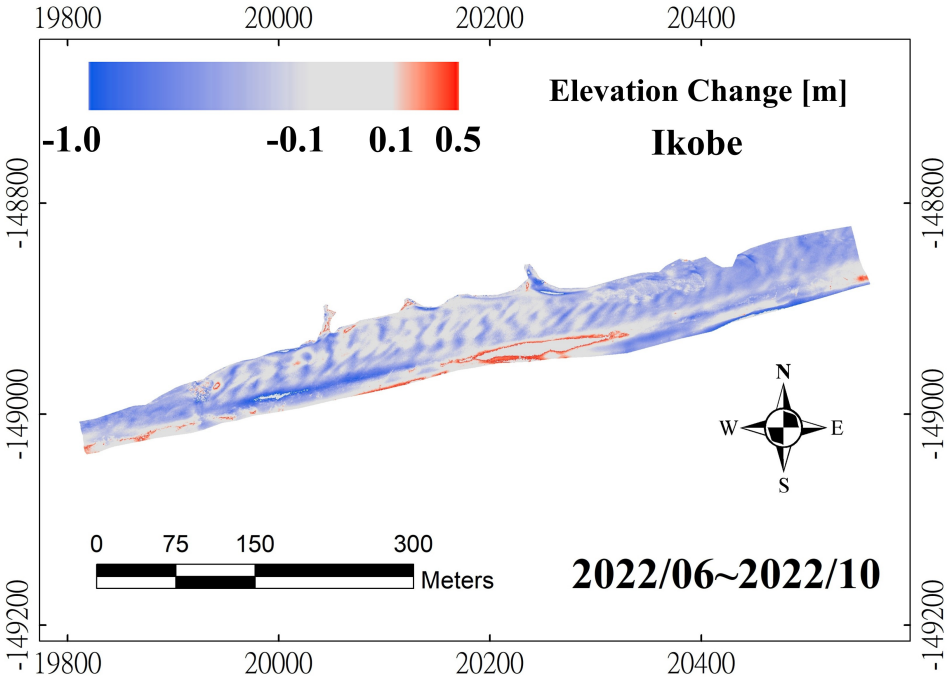

Figure 3.26: Ikobe Elevation Change 202206-202210

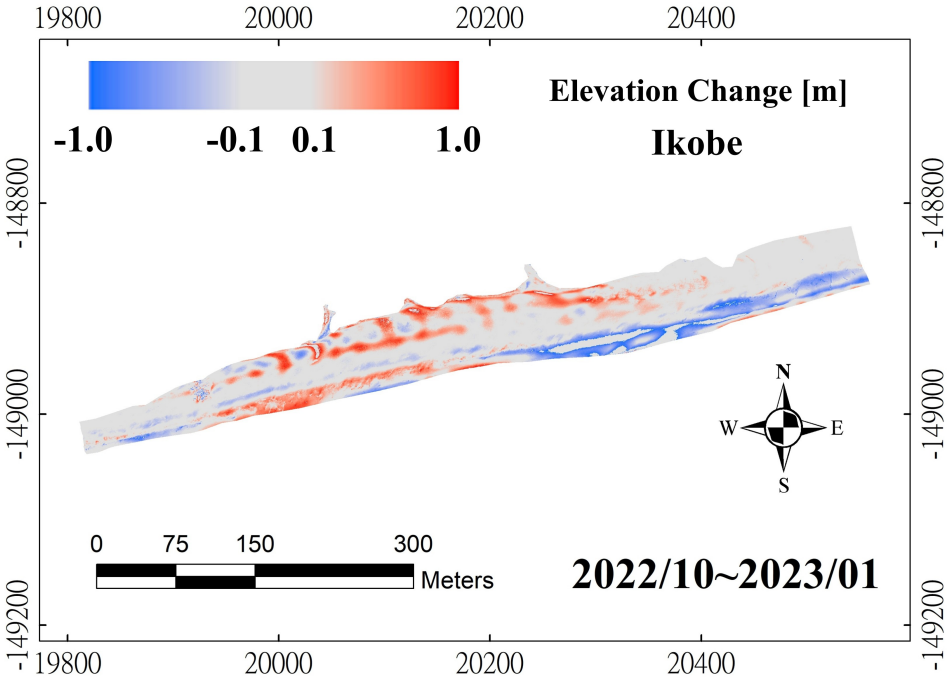

Figure 3.27: Ikobe Elevation Change 202210-202301

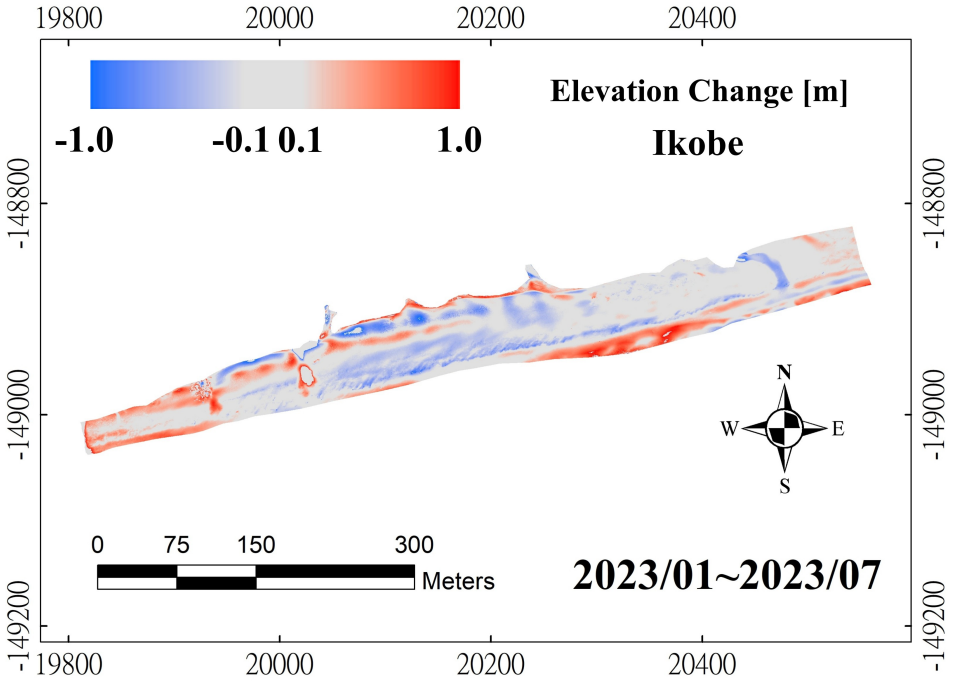

Figure 3.28: Ikobe Elevation Change 202301-202307

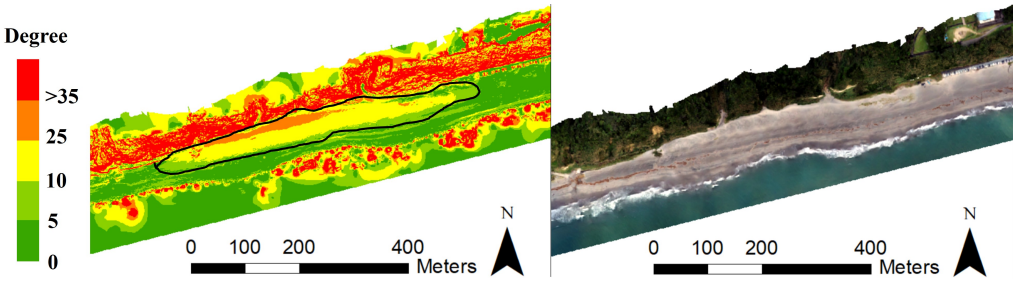

Figure 3.29: Ikobe Slope 2022

Slope Variation

The boundaries of the Ikobe Dune (Figure 3.29) are more clearly defined in the slope map compared to those of the Takatsuka Dune, with less local noise observed in the black-circled areas. This is because the Ikobe Dune is still in an active developmental stage, characterized by strong aeolian sand transport and limited vegetation cover. As a result, the surface morphology is well preserved and less affected by vegetation-induced artifacts.

The central part of the dune consistently maintains slopes greater than 10°, while the western crest exceeds 25°, with similar steepening later observed on the eastern crest. Comparison between the 2021 (Fig. 3.30) and 2025 (Fig. 3.31) slope maps clearly indicates that sand accumulation has progressively shifted from the western to the eastern crest, while the dune boundaries—defined by slopes greater than 10°—have remained stable over time. These findings suggest that the Ikobe Dune continues to grow laterally through active wind-driven sand deposition, with overall morphological stability maintained along its perimeter.

For slope maps of other survey periods, refer to the Slope Figures Appendix 7.4.

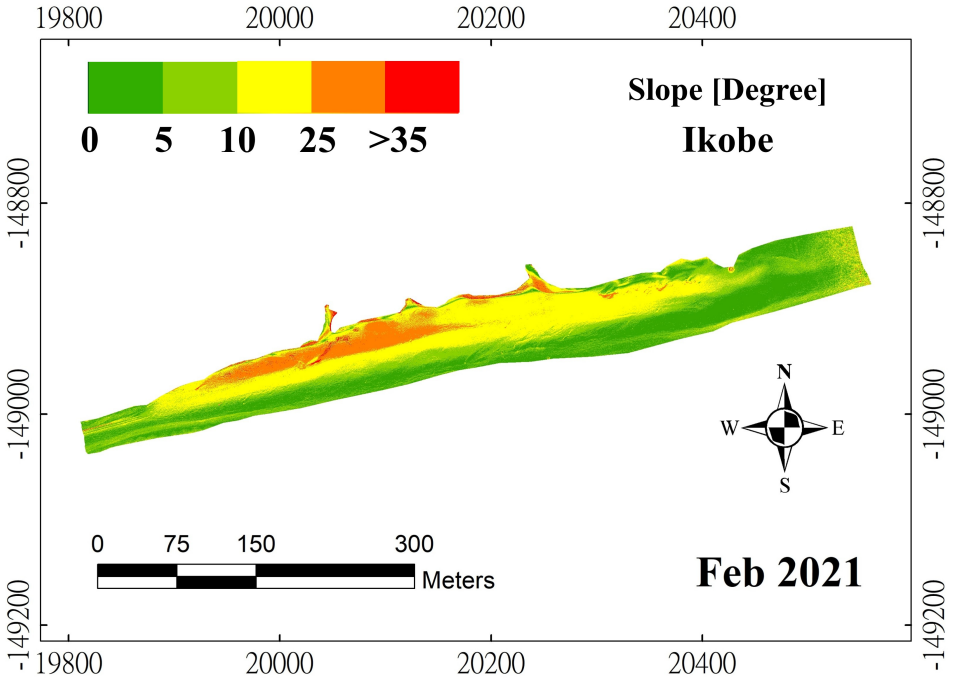

Figure 3.30: Ikobe Slope 202102

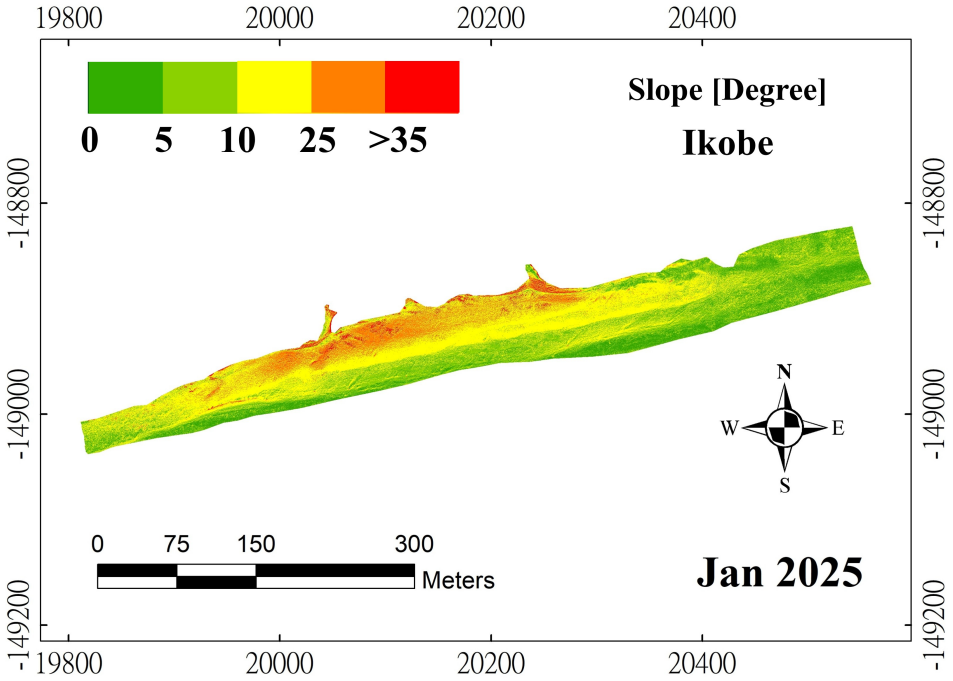

Figure 3.31: Ikobe Slope 202501

3.2.3 Ikobenishi Dune

The Ikobenishi Dune has maintained an elevation of around 12 m in recent years (Fig. 3.32). Its east–west extent remains almost unchanged, likely constrained by small streams on both sides, while in the north–south (cross-shore) direction the dune slightly expanded seaward. Due to its smaller size, this dune shows more pronounced seasonal variability between summer erosion and winter deposition.

Detailed DSM maps and orthophotos for other survey years are provided in the DSM Figures (Appendix 7.4) and Orthophoto Figures (Appendix 7.4).

Elevation Change

Between June and October 2022 (Fig. 3.33), summer erosion dominated, followed by overall deposition during October 2022–January 2023 (Fig. 3.34). From January to July 2023 (Fig. 3.35), erosion reappeared under weaker winds and rainfall. During July 2023–January 2024 (Fig. 3.36), deposition resumed across the entire dune. On an annual scale 2023–2024 (Fig. 3.37), upper dune surfaces showed deposition while the lower flanks experienced minor erosion. Throughout 2024–2025 (Fig. 3.38), the dune again exhibited net accretion.

Slope Variation

The Ikobe Nishi Dune (Fig. 3.39) is relatively small in scale, with a maximum elevation of approximately 12 m and a coastal elevation of around 3 m, resulting in a relative height difference of only about 9 m. Despite its small size, the dune can be clearly identified from both slope and orthophoto maps. Being in an incipient stage of development, the Ikobe Nishi Dune exhibits active aeolian sand transport, limited vegetation cover, and

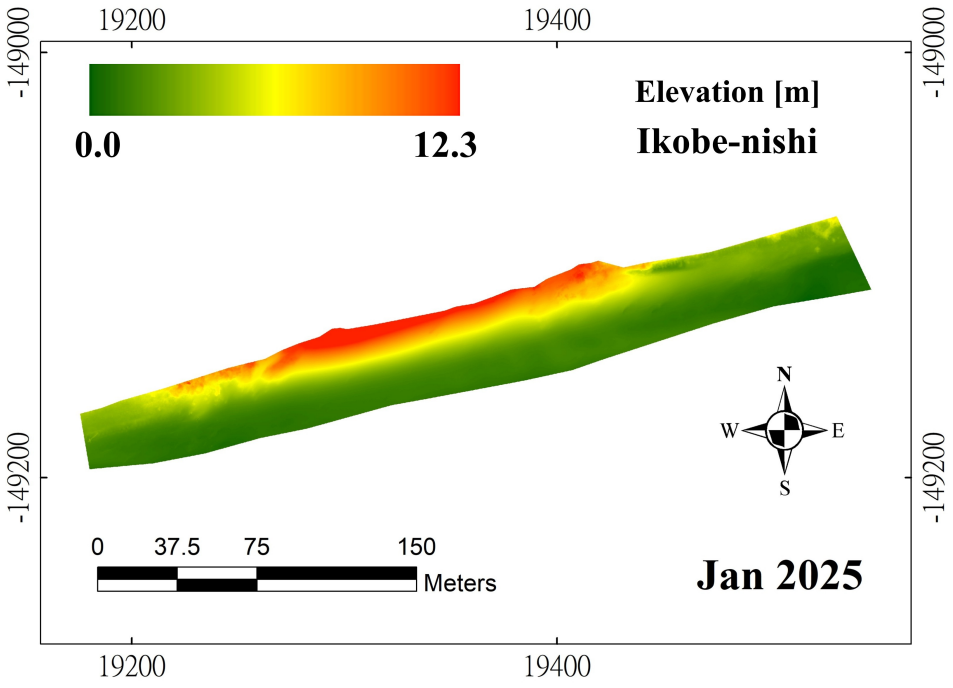

Figure 3.32: Ikobe-nishi DSM 202501

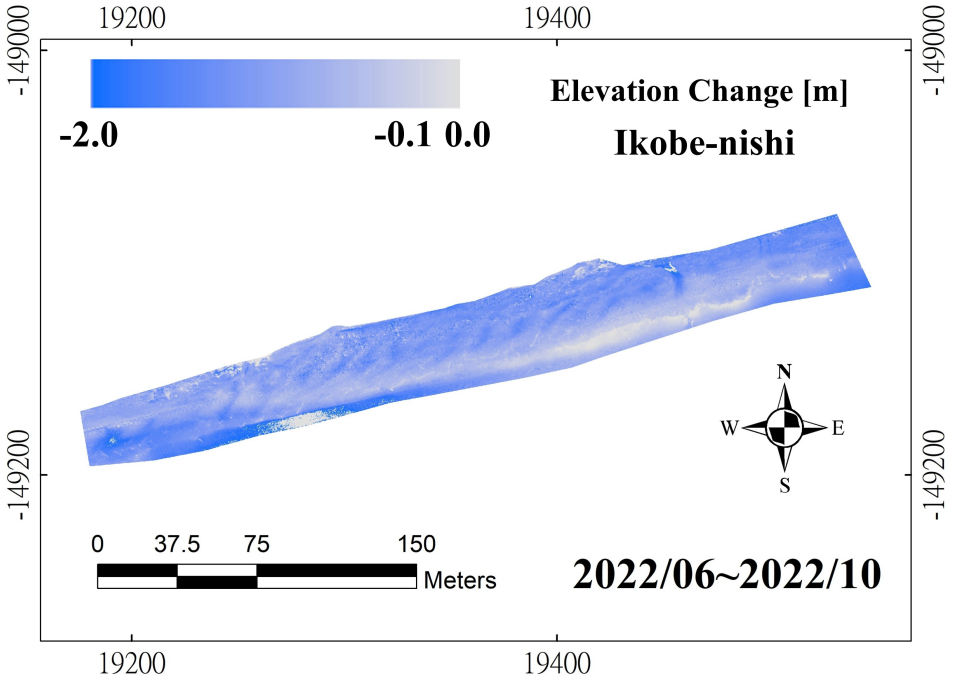

Figure 3.33: Ikobe-nishi Elevation Change 202206-202210

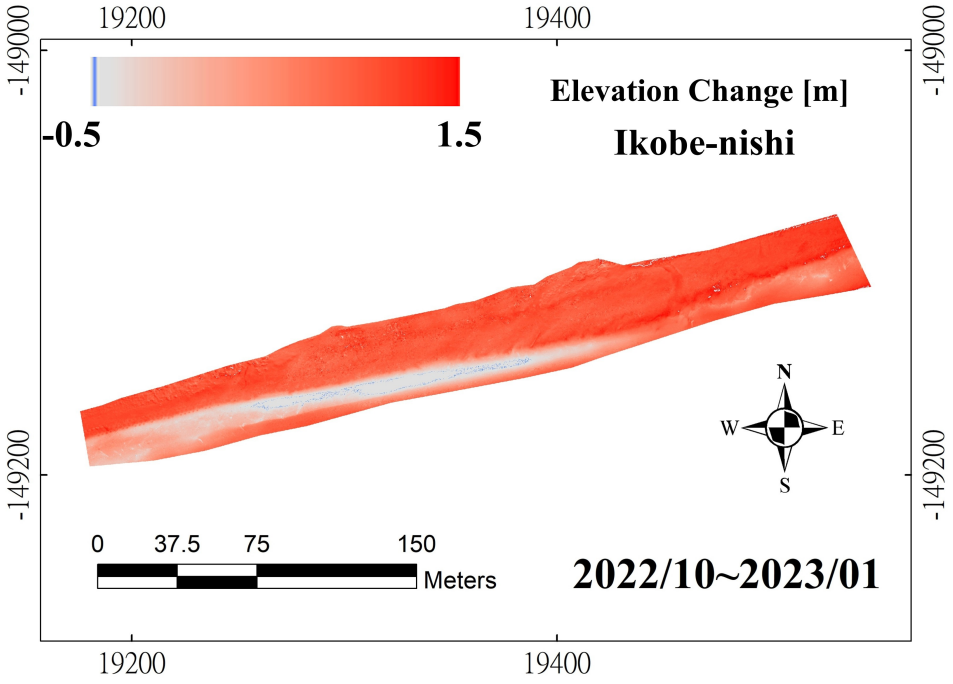

Figure 3.34: Ikobe-nishi Elevation Change 202210-202301

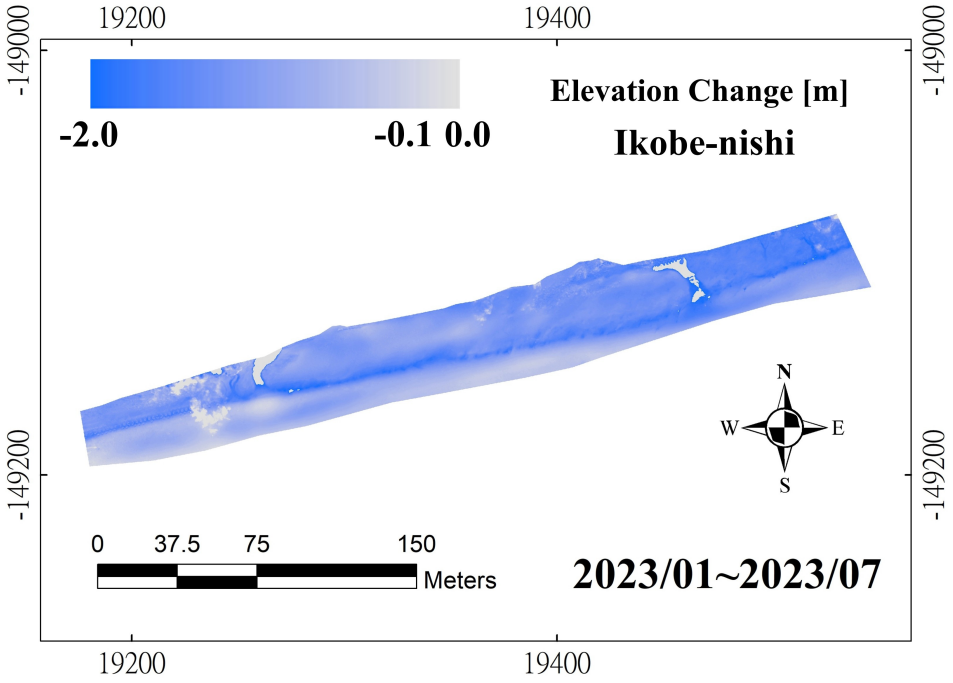

Figure 3.35: Ikobe-nishi Elevation Change 202301-202307

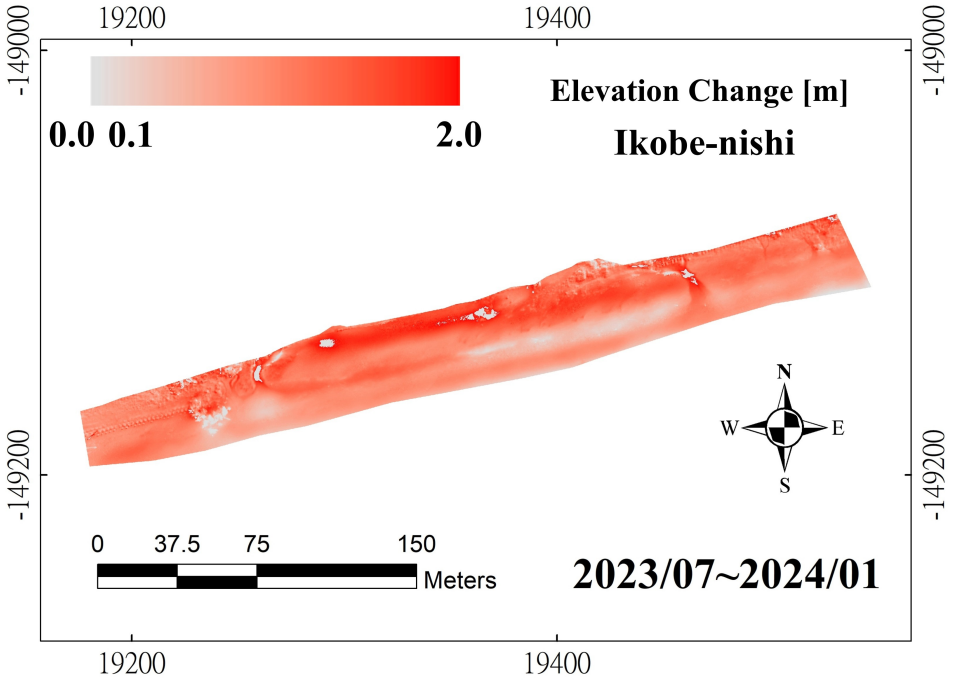

Figure 3.36: Ikobe-nishi Elevation Change 202307-202401

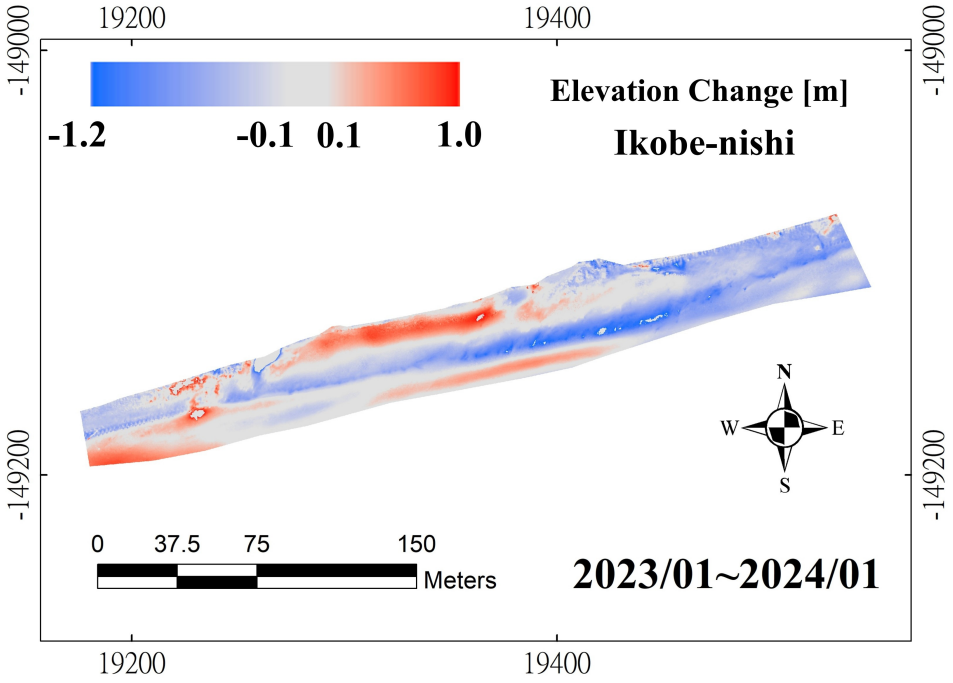

Figure 3.37: Ikobe-nishi Elevation Change 202301-202401

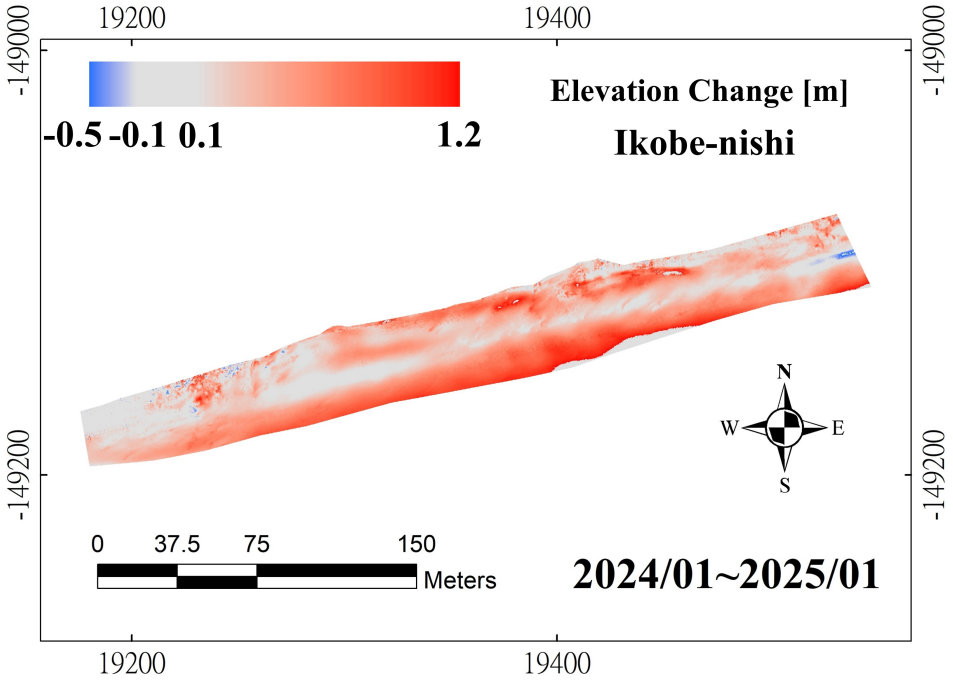

Figure 3.38: Ikobe-nishi Elevation Change 202401-202501

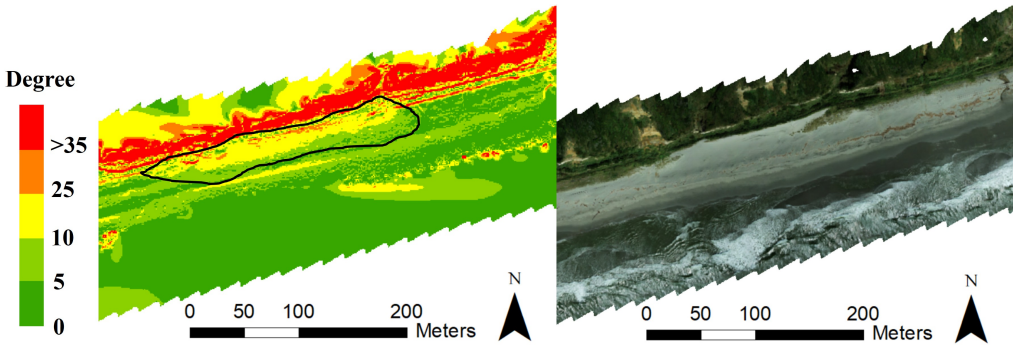

Figure 3.39: Ikobe-nishi Slope 2022

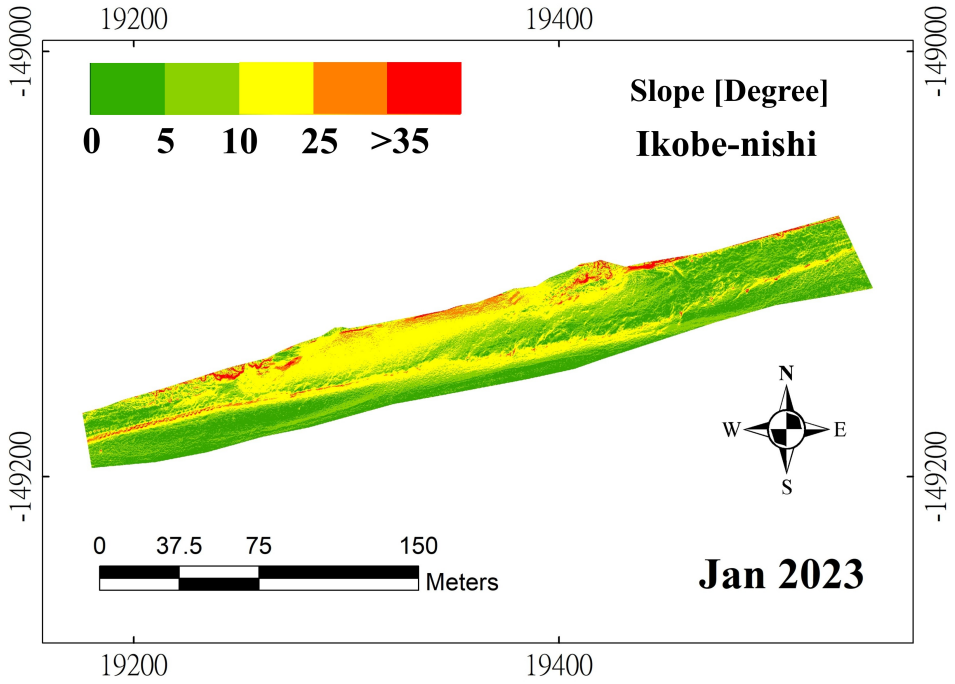

Figure 3.40: Ikobe-nishi Slope 202301

locally steep slopes concentrated in the middle portion of the dune.

Steep slopes exceeding 35° occur only near the dune top, while most of the surface maintains slope angles between 10° and 25°. A comparison of the 2023 (Fig. 3.40) and 2025 (Fig. 3.41) slope maps reveals that initially only the western slope was steep, but both sides gradually became steeper over time, suggesting an eastward progression of sand accumulation. These results indicate that although the dune remains small and sensitive to seasonal environmental changes, its overall morphology continues to evolve dynamically under ongoing aeolian activity. For slope maps of other survey periods, refer to the Slope Figures Appendix 7.4.

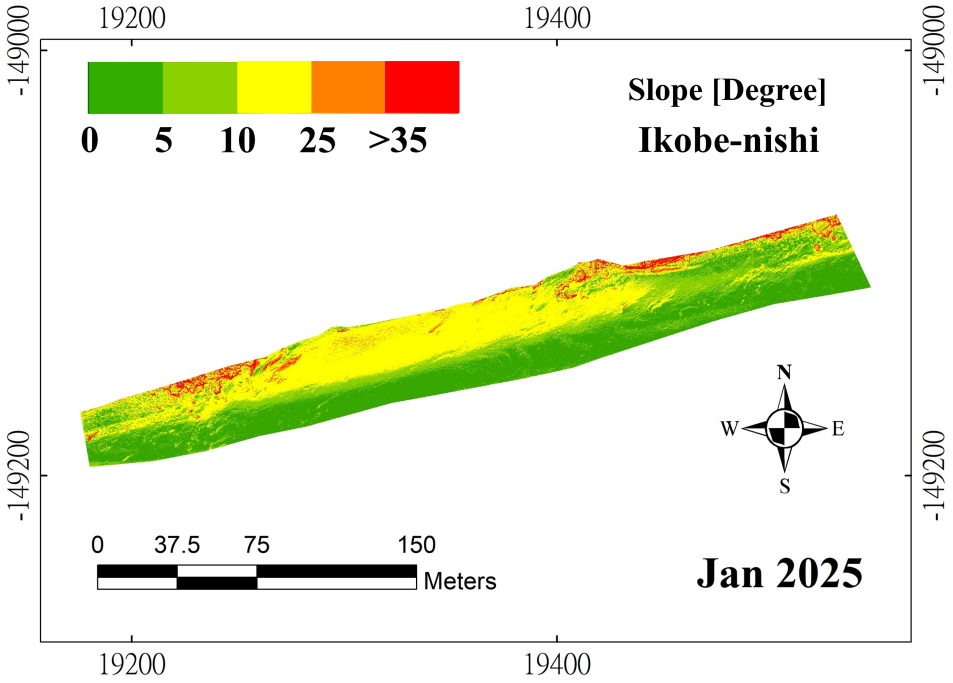

Figure 3.41: Ikobe-nishi Slope 202501

3.2.4 Mutsure Dune

The Mutsure Dune has experienced continuous erosion and is now largely stabilized by vegetation. Only three small remnants of the original dune remain, with the highest crest reaching approximately 17–18 m (Fig. 61).

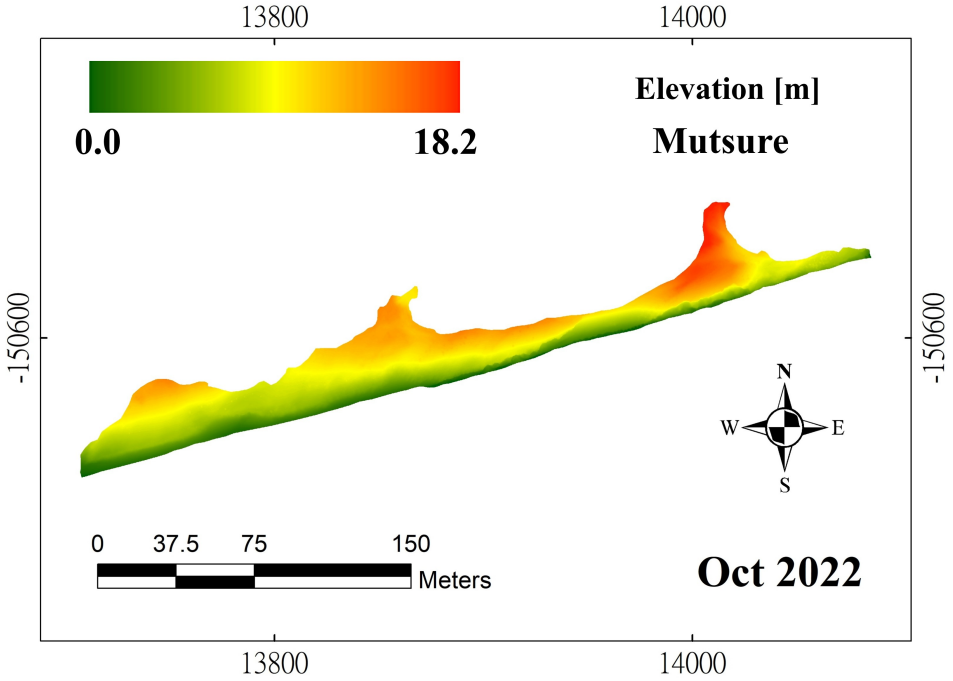

Figure 3.42: Mutsure DSM 202210

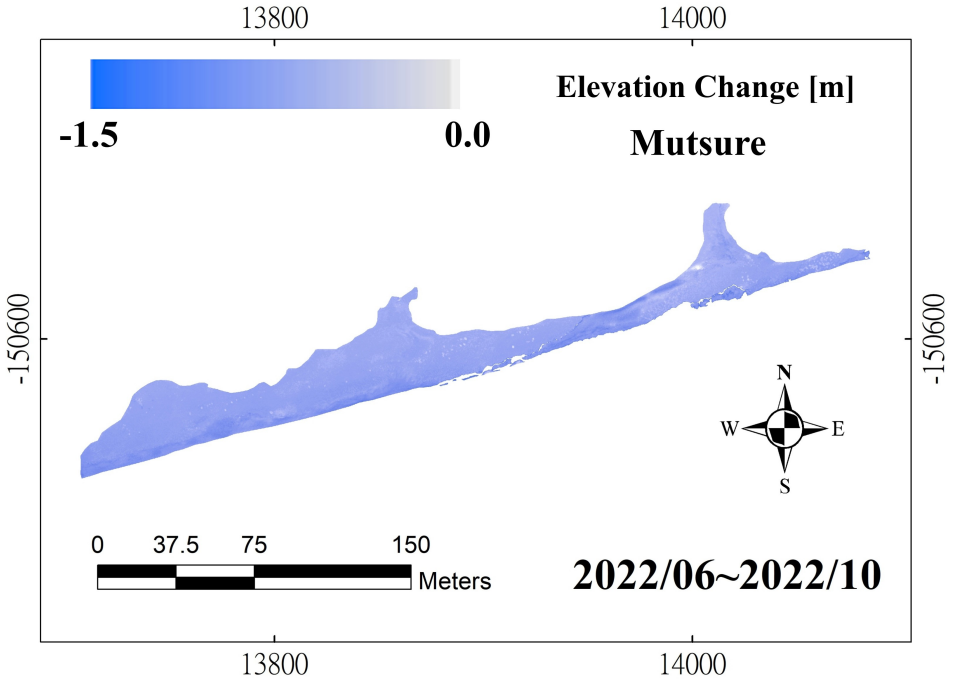

Figure 3.43: Mutsure Elevation Change 202206-202210

Elevation Change

From June to October 2022 (Fig. 3.43), the dune underwent widespread erosion, consistent with weakened wind conditions and seasonal rainfall effects.

Slope Variation

The Mutsure Dune (Fig. 3.44) is currently in an erosional stage, characterized by significant vegetation coverage and reduced aeolian activity. The noise observed in the black-circled areas of the slope map corresponds to dense vegetation that obscures the dune surface. These vegetation types typically grow in summer and autumn. In the white-circle coastal zone, distinct slope discontinuities can be observed, indicating dune collapse caused by wave erosion. As the beach in front of the dune has been severely eroded, sediment supply to the dune has diminished, and in some areas, direct wave undercutting has further accelerated dune retreat.

Steeper slopes are observed along the lateral flanks, while the central portion remains relatively gentle. A small erosional cliff is also present along the southern margin near the shoreline, reflecting continued coastal retreat and the weakened sedimentary stability of the dune system.

For slope maps of other survey periods, refer to the Slope Figures Appendix 7.4.

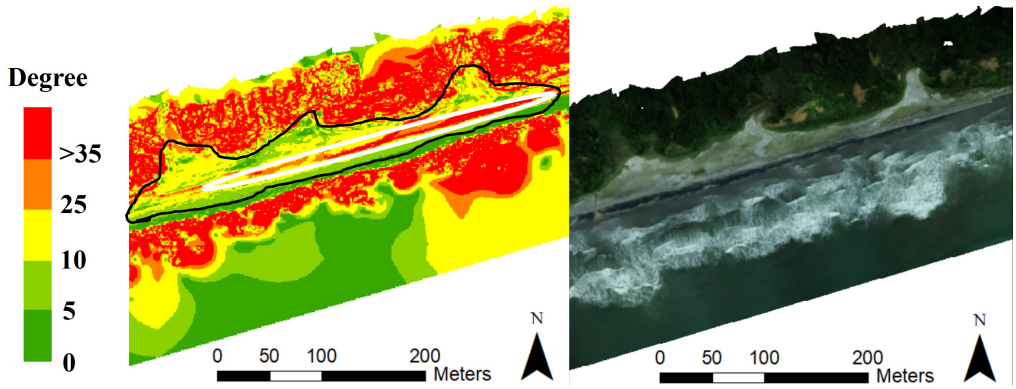

Figure 3.44: Mutsure Slope 2022

3.2.5 Koijigahama Dune

Unlike the other four dunes, Koijigahama was surveyed only once (October 2022). Therefore, temporal elevation change analysis was not possible for this site, and the description below focuses on its geomorphic characteristics based on a single DSM and slope map. The Koijigahama Dune reaches a maximum elevation of about 25 m and is bisected by a small river channel (Fig. 3.45). Detailed orthophoto is provided in the Orthophoto Figures (Appendix 7.4).

Slope Variation

The Koijigahama Dune (Fig. 3.46), like the Mutsure Dune, is currently in an erosional stage. Pronounced slope variations are evident in the white-circle coastal zone, indicating collapse of the dune face due to wave undercutting and shoreline retreat. The significant

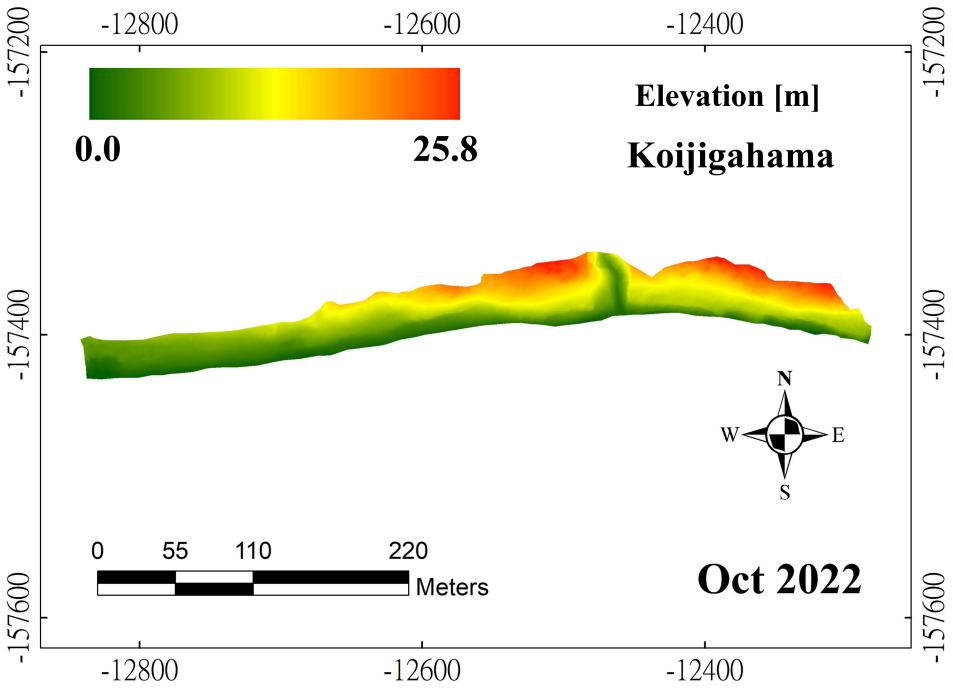

Figure 3.45: Koijigahama DSM 202210

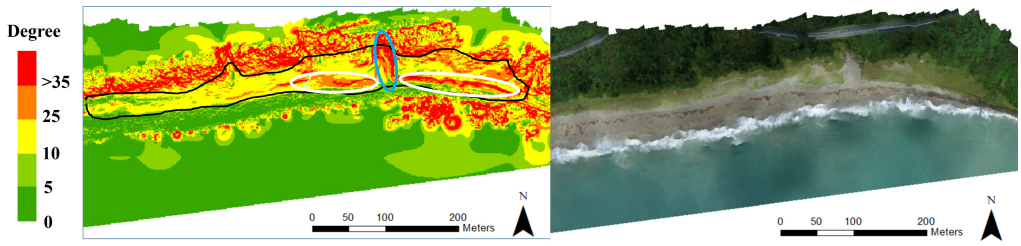

Figure 3.46: Koijigahama Slope 2022

noise observed in the black-circled areas corresponds to dense vegetation coverage, while the blue-circled central zone reveals a fluvial channel cutting through the dune, similar to the geomorphic pattern observed at the Takatsuka Dune.

Steep slopes are concentrated along both riverbanks and the seaward edge, where small erosional scarps have developed under the influence of continuous coastal retreat. These features collectively indicate that the Koijigahama Dune is undergoing active degradation, with vegetation expansion and hydrological incision further accelerating its morphological decay. These vegetation types typically grow in summer and autumn.

Chapter 4

Beach Morphology, Bathymetric Changes, and Their Relationship with Cliff-Front Dunes

This chapter examines the sandy beach and bathymetric characteristics along the Omotehama Coast. Section 4.1 focuses on the sandy beach morphology, Section 4.2 presents bathymetric changes, and Section 4.3 explores the relationship among the sandy beach, bathymetry, and coastal dunes.

4.1 Sandy Beach Morphology

4.1.1 Monitoring framework

To evaluate the effectiveness of coastal protection projects, Aichi Prefecture has been conducting continuous follow-up monitoring since 2010 Aichi Prefecture [2011]. The monitoring program consists of aerial photography every two years and cross-shore topographic surveys, which are alternately conducted every two years for the eastern section (from Ikobe Coast to Nishinanane Coast) and the western section (from Kumihara Coast to Higashi-Akasawa Coast).

In this framework, the coastal zone from Ikobe to Nishinanane corresponds to survey

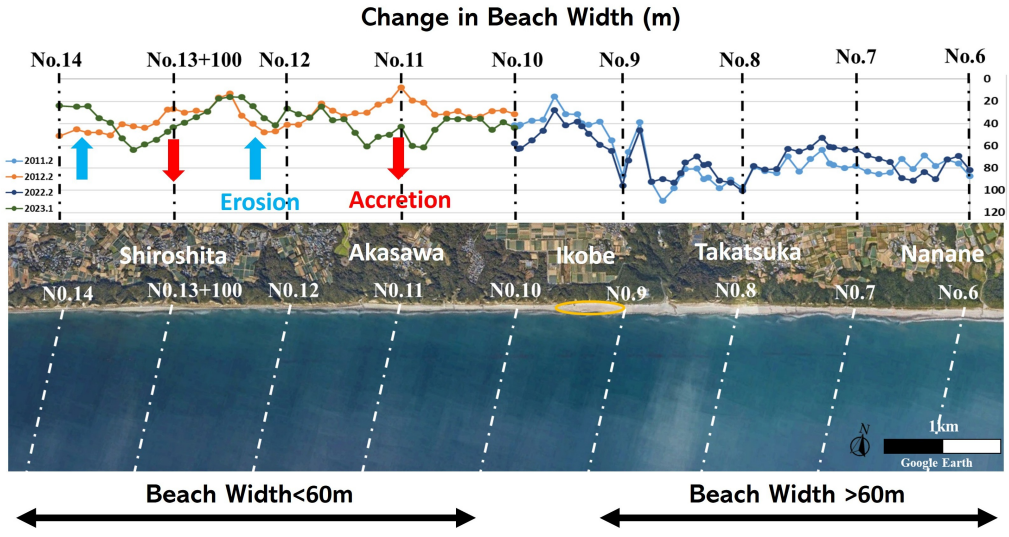

Figure 4.1: Beach width change around Ikobe (upper panel) and survey lines and monitoring framework (lower panel).

lines No. 6−10, while the zone from Kumihara to Higashi-Akasawa corresponds to lines No. 10−14 (see Figure 4.1). The interval between survey lines is approximately 100 m. Each cross-shore survey consists of two parts: (1) a land-based topographic survey conducted at 10 m intervals from the foot of the sea cliff to the shoreline, and (2) a bathymetric (depth) survey conducted at 20 m intervals extending approximately 1 km offshore. In this section, only the subaerial topography (above the mean water level) is analyzed, while the bathymetric data are discussed in Section 3.2.

These periodic surveys provide an extensive and consistent dataset describing the morphological evolution of the Omotehama sandy coast, which serves as the basis for examining changes in beach width, shoreline position, and sediment exchange between the beach and the adjacent dune system over the past decade.

4.1.2 Temporal changes in sandy beach width

Figure 4.1 compares the beach widths observed in 2011−2012 and 2022−2023, based on Aichi Prefecture's topographic survey data. On the eastern side of the Ikobe dune (survey lines No. 6−9), beach widths exceeding 60 m have been maintained for more than a decade. In front of and immediately west of the Ikobe dune (survey lines No. 9~No. 12), a noticeable expansion of the beach has occurred.

Figure 4.2 presents the annual variations in beach width at three representative transects located west of the Ikobe dune. Further west (survey lines No. 12−14), the changes in beach width are less pronounced, showing both slight increases and decreases compared with the previous decade.

4.1.3 Shoreline changes along the western sector

Figure 4.3 shows satellite imagery of the coastal zone between Shiroshita and Mutsure beaches (located west of Ikobe) for the years 2016, 2020, and 2024. The shoreline positions, interpreted from the wet−dry boundary of the beach surface, are plotted in each image.Figure 4.4 display the temporal changes in beach width at Shiroshita and Hamada. Although a slight increase in beach width has been observed in recent years at Shiroshita, the overall trend along this western sector indicates continuing beach narrowing, and in some areas between Kumihara and Hamada, the sandy beach has almost completely disappeared.

4.1.4 Discussion

The results of Figures 4.1−4.3 demonstrate that the sandy beach in the vicinity of Ikobe has experienced noticeable widening over the past decade, whereas erosion persists toward the west. This spatial contrast suggests that sand accumulation near the Ikobe dune may have altered the alongshore sediment transport system. One possible factor is the large-scale dune formation that developed at Ikobe after 2010, which could have influenced the regional sediment budget by trapping wind-blown sand from the beach. This pattern indicates that although the structural modifications improved sediment retention locally around Ikobe, the resulting changes in aeolian transport and dune growth may have reduced the amount of sand available for downstream transport, thereby contributing to continued erosion toward the west. The relationship between the sandy beach, dune growth, and offshore sediment processes will be further discussed in Sections 4.2 and 4.3.

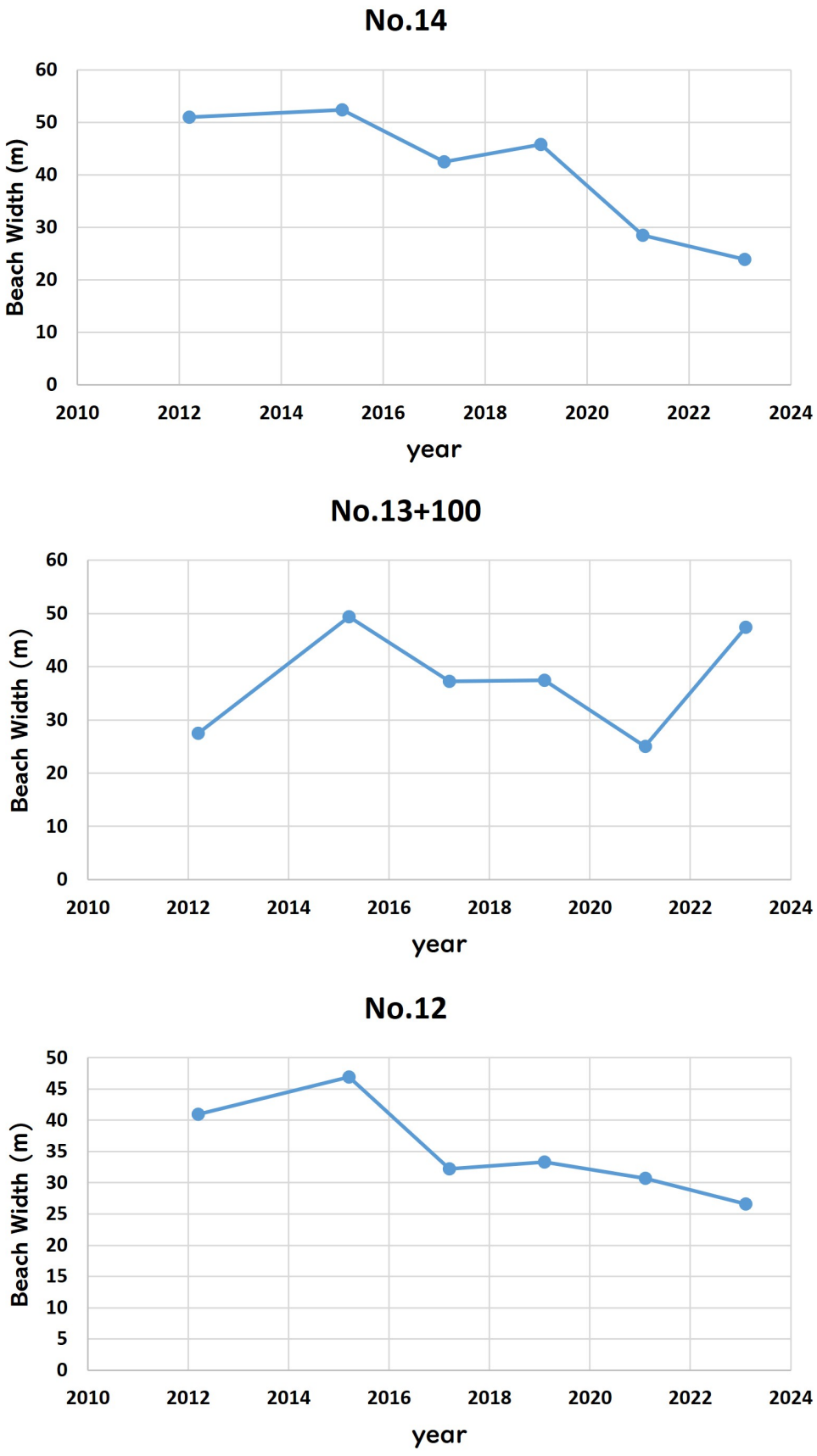

Figure 4.2: Transects located west of the Ikobe

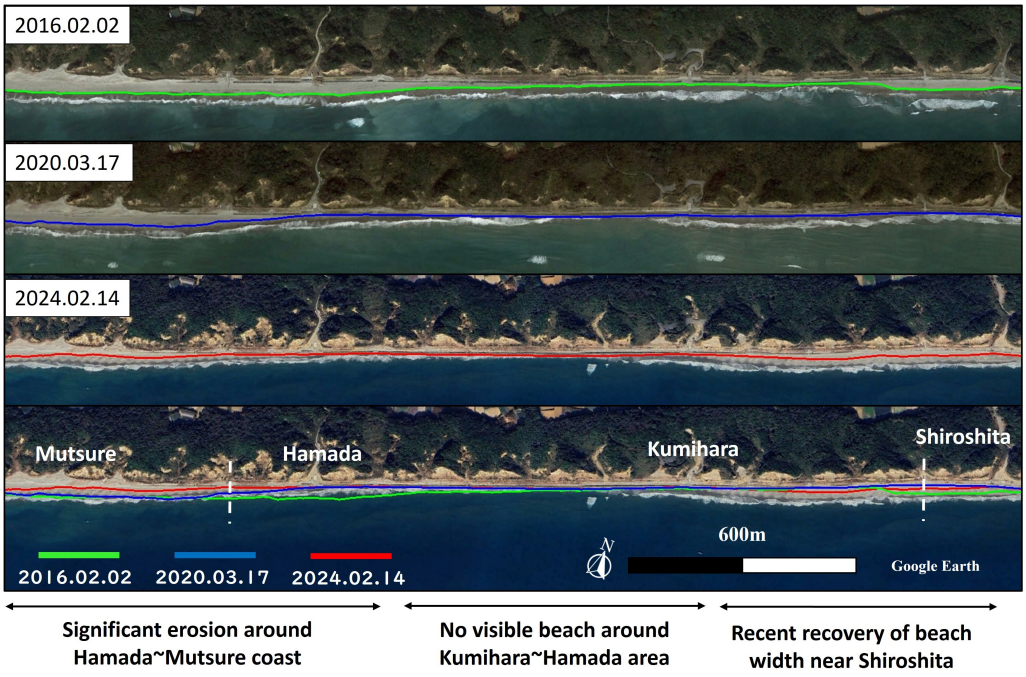

Figure 4.3: Beach width change from Shiroshita to Mutsure

4.2 Annual Bathymetric Changes

Using the cross-sectional survey data provided by Aichi Prefecture, this section analyzes the spatial relationship among the dune, beach, and nearshore bathymetry. To quantify spatial variability in sediment distribution, the study area between cross-shore lines No. 8 and No. 10 (as shown in Fig. 4.2) was divided into 100 m-wide segments.

The area from cross-section No. 8 to No. 8 + 500 m corresponds to the Takatsuka Dune region, while that from No. 9 to No. 9 + 600 m represents the Ikobe Dune region. The intervening zones between No. 8 + 500 m–No. 9 and No. 9 + 600 m–No. 10 were classified as non-dune sandy beaches.

Furthermore, the coastal profile was subdivided into three elevation-based zones according to Tokyo Peil (T.P.) reference levels:

- **Dune zone:** elevations above T.P. +3 m,
- **Beach zone:** elevations between T.P. 0 m and +3 m, and
- **Submarine zone:** elevations between T.P. −7 m and 0 m, corresponding approximately to the crest depth of the submerged breakwaters (T.P. −7 m).

The same elevation thresholds were applied for non-dune beach segments to maintain consistency in classification. The topography around the Ikobe Dune was reconstructed using the Natural Neighbor interpolation method in ArcGIS.

Topographic data from 2014, 2018, 2020, and 2022, including both terrestrial and submarine measurements, were used to assess long-term bathymetric changes (Fig. 4.5).

Between 2014 and 2020 (left side of Fig. 4.6), an expansion of the shoreline was observed, as indicated by the increase in the orange-shaded areas. Simultaneously, the blue regions representing deeper seabed decreased, implying sediment accumulation

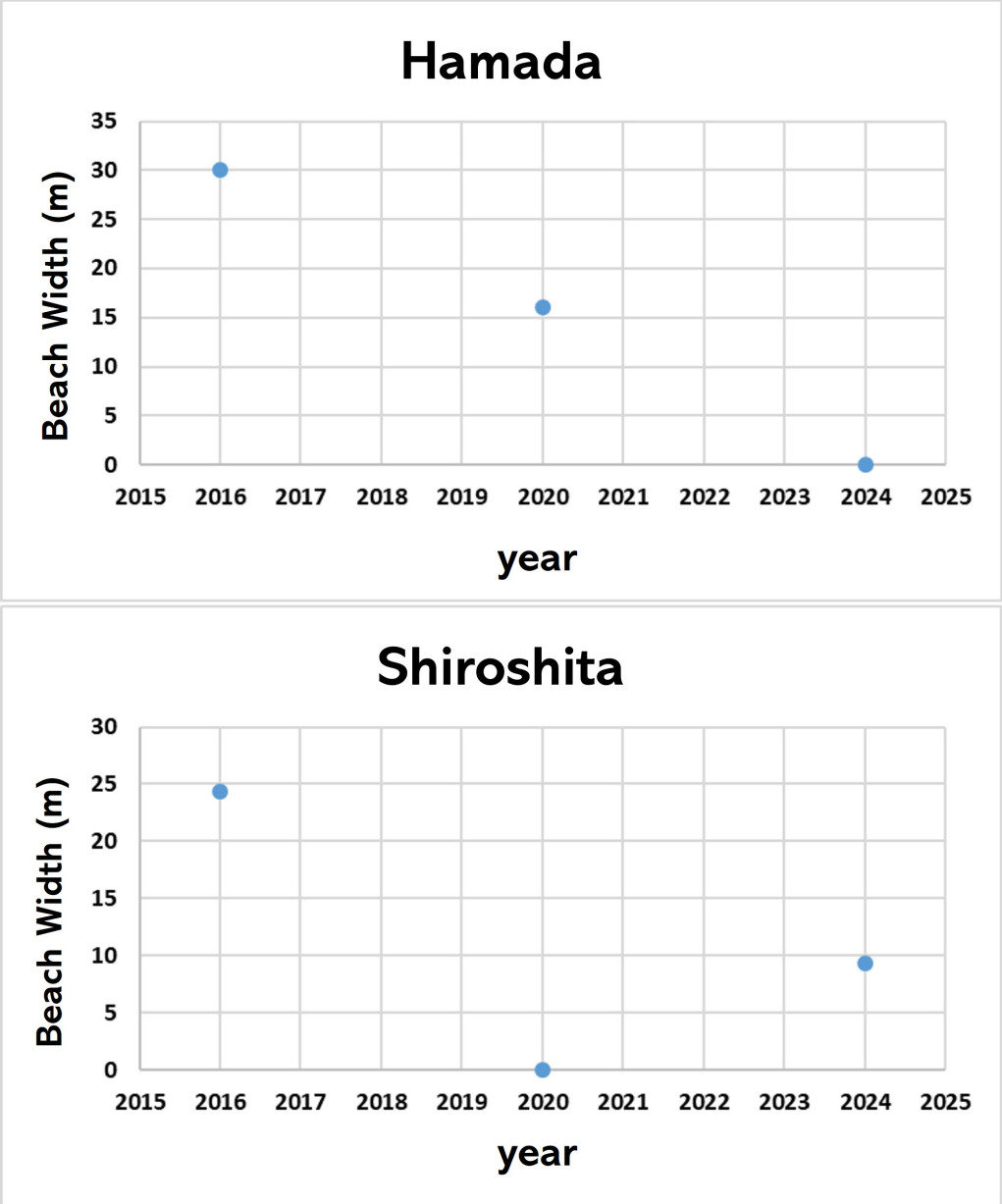

Figure 4.4: Shiroshita and Hamada beach width change

within the nearshore zone. However, between 2020 and 2022 (right side of Fig. 4.6), a slight reduction in nearshore sediment volume was identified, suggesting a decline in total submarine sediment volume and a weakening of sediment supply from offshore. These results highlight a shift from a sediment accretion phase (2014–2020) to erosional condition after 2020.

4.3 Relationships among Beach, Dune, and bathymetry

4.3.1 Relationship between Beach Width Change and Submarine Sediment Volume Change

Figure 4.7 illustrates the relationship between the change in beach width and the corresponding change in submarine sediment volume for each cross-section. Between

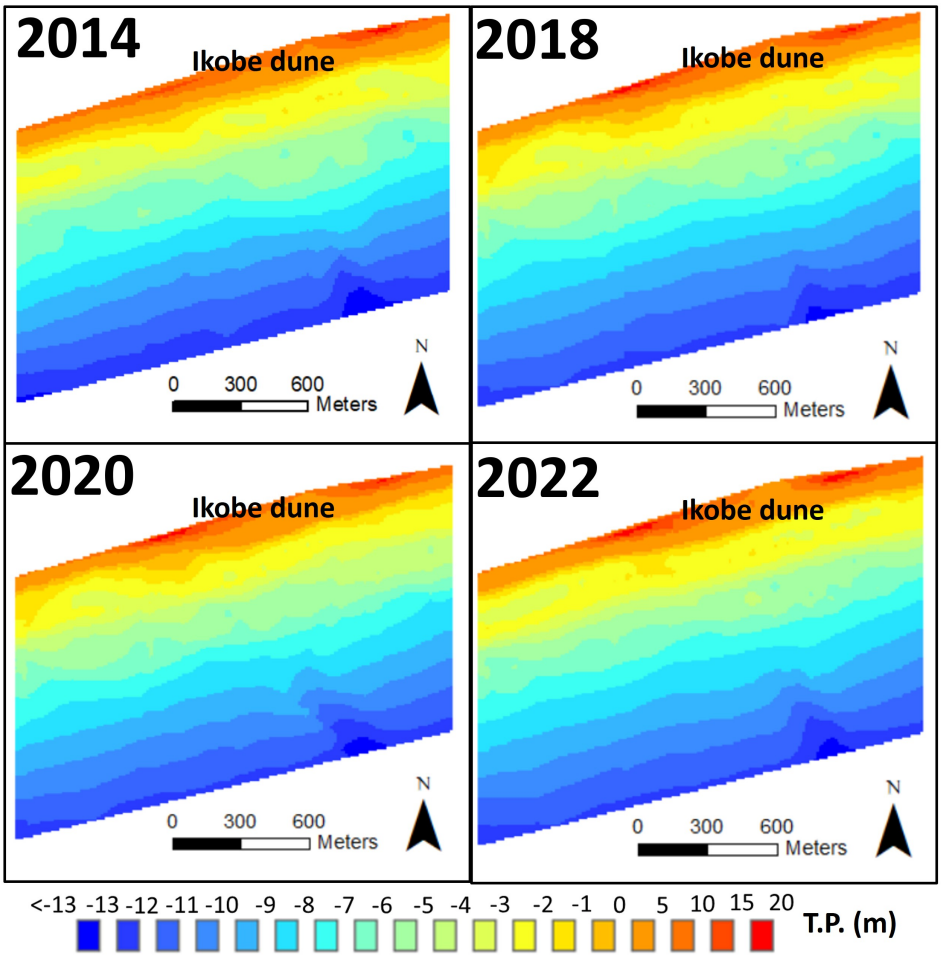

Figure 4.5: Bathymetry

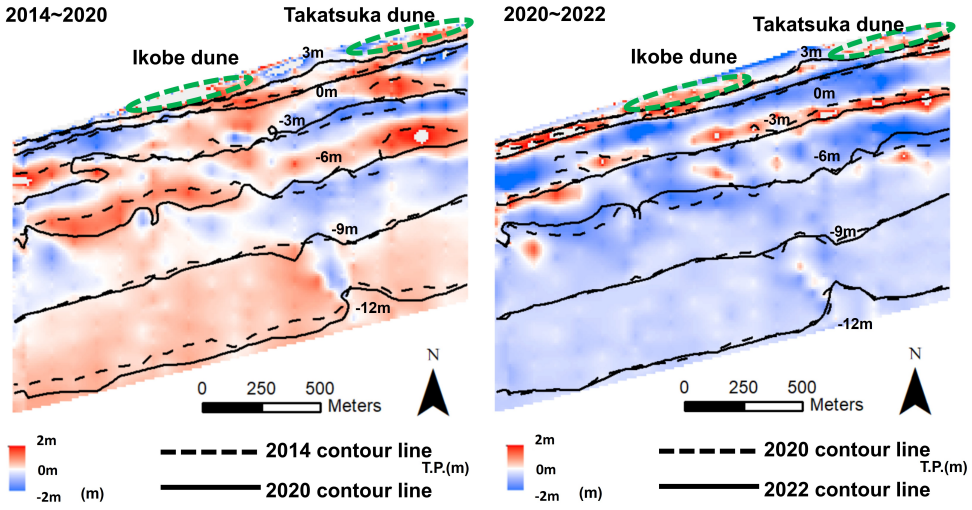

Figure 4.6: Bathymetry change

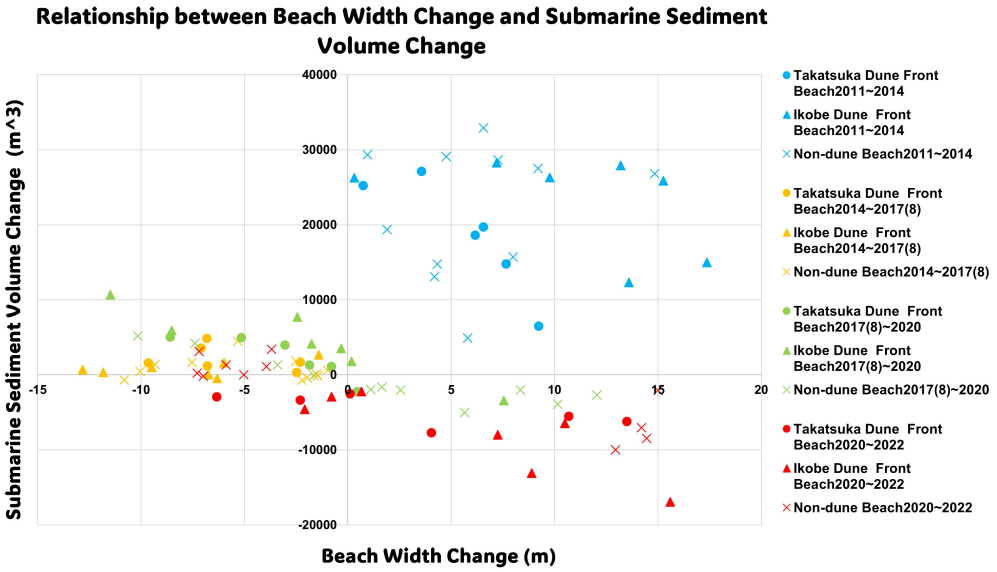

Figure 4.7: Relationship between Beach Width Change and Submarine Sediment Volume Change (per survey period)

2011 and 2014, the beach width increased in all three regions—Ikobe dune, Takatsuka dune, and the non-dune sandy beach. The expansion was most pronounced at the Ikobe dune front, where the shoreline advanced by more than 10 m per year. During the same period, submarine sediment volume also increased across all regions, exceeding 20,000 m³ per year near the Ikobe dune front. This period corresponds to the initial stage of dune development, suggesting that the accumulation of nearshore sediment contributed directly to the widening of the beach.

In contrast, between 2014 and 2020, the beach width in front of both Ikobe and Takatsuka dunes decreased slightly, whereas the submarine sediment volume continued to increase modestly. Subsequently, between 2020 and 2022, the beach width increased again, while the submarine sediment volume declined. Thus, after 2014, a negative correlation emerged between the beach width and submarine sediment volume changes. This shift indicates that the sediment exchange pattern evolved with dune maturity, implying that dune development progressively altered the sediment balance between the nearshore and the beach.

4.3.2 Relationship between Beach Width Changes and Dune Volume Changes

Figure 4.8 shows the relationship between beach width change and dune volume change along each survey line. The results demonstrate that dune volume generally increased regardless of whether the beach width expanded or contracted. Although certain measurement points at the lateral edges of the Takatsuka dune (notably between 2011–2014 and 2017–2020) showed localized decreases, these correspond to dune flanks where erosion or lateral sand redistribution was dominant rather than overall volumetric loss.

During periods of active dune growth, sediment stored temporarily on the beach tends to be transported landward and incorporated into the dune body. As a result, even when offshore sediment input is limited, dune volume may continue to increase while the beach becomes narrower. This indicates that part of the beach sediment is redistributed inland

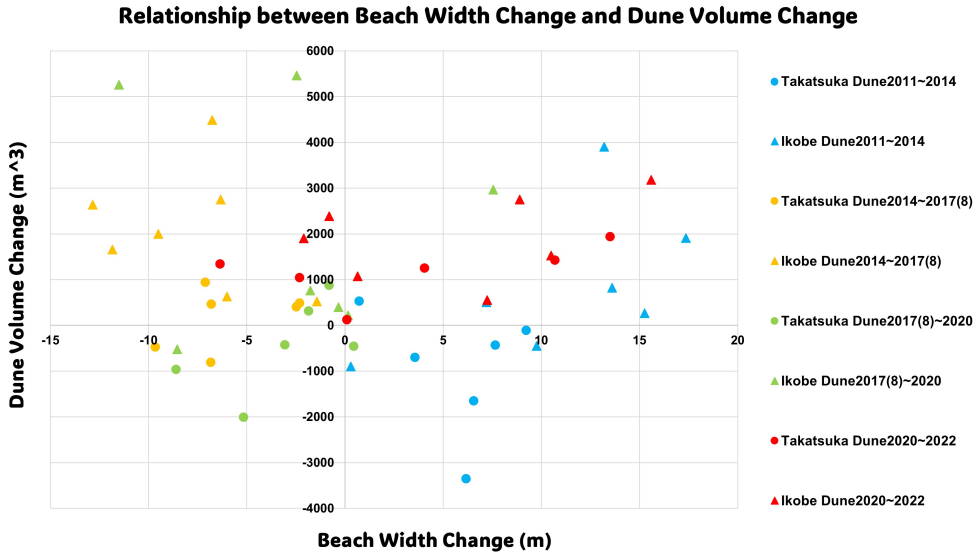

Figure 4.8: Relationship between Beach Width Change and Dune Volume Change (per survey period)

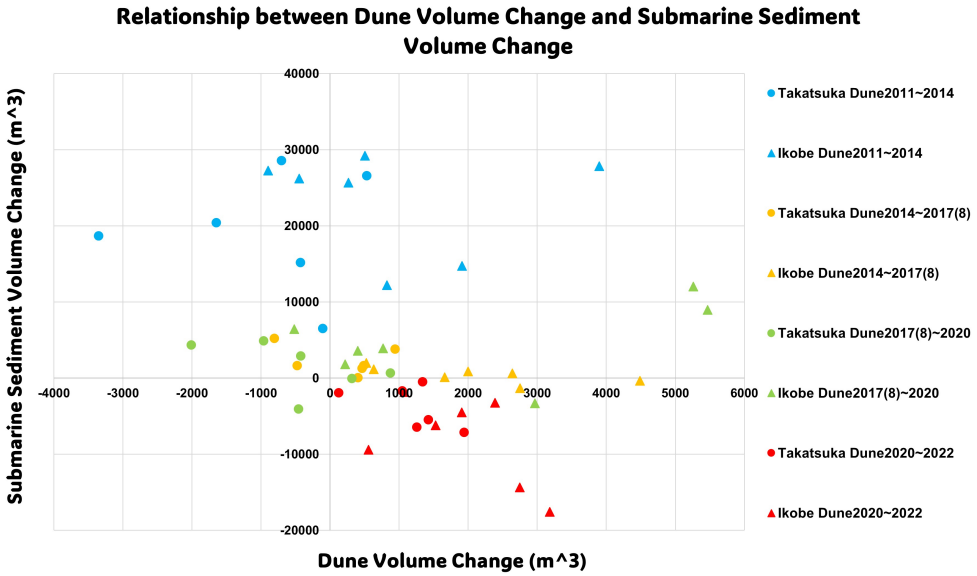

Figure 4.9: Relationship between Dune Volume Change and Submarine Sediment Volume Change (per survey period)

during the dune-accretion phase, producing a temporary reduction in beach width despite ongoing dune expansion.

4.3.3 Relationship between Dune Volume Change and Submarine Sediment Volume Change

Figure 4.9 presents the relationship between dune volume change and submarine sediment volume change. In both the Ikobe and Takatsuka dune regions, a generally negative correlation was observed across most survey periods—that is, when dune

volume increased, submarine sediment volume decreased. This relationship suggests that sand is first transported landward from the seabed to the beach by wave action and subsequently delivered from the beach to the dune via wind-driven transport.

Overall, these observations indicate that the seabed, beach, and dune form an integrated sedimentary system in which material exchange occurs continuously. The development of coastal dunes functions as a sediment sink for nearshore deposits, reflecting the dynamic linkage between marine and terrestrial sediment processes along the Omotehama coast.

Chapter 5

Wind Characteristics Relevant to Aeolian Processes

This chapter examines the wind environment influencing aeolian processes on the Atsumi Peninsula. Section 5.1 presents the long-term inland and offshore wind observations, Section 5.2 describes field measurements near the coastal dunes, and Section 5.3 discusses numerical simulations of the local wind field.

5.1 Wind Climate of the Atsumi Peninsula

According to the Japan Meteorological Agency (JMA) statistics from 2002 to 2021, the prevailing wind direction at Toyohashi is northwesterly from October to May, easterly in June, southeasterly from July to August, and easterly again in September. Throughout the year, northwesterly winds dominate, with the strongest wind speeds typically occurring in winter and spring.

Table 5.1 shows the monthly average wind speed and prevailing wind direction recorded by the Toyohashi AMeDAS (Automated Meteorological Data Acquisition System) in 2021. During winter and spring (December–March), northwesterly winds prevail with an average speed of approximately 4 m/s, which is a key driver of aeolian sand transport and dune formation on the Atsumi Peninsula.

Table 5.1: Wind data from Toyohashi AMeDAS (2021).

Month–Year	Average Wind Speed (m/s)	Main Wind Direction
Jan-21	4.3	NW
Feb-21	4.5	NW
Mar-21	4.4	NW
Apr-21	4.2	WNW
May-21	3.7	WNW
Jun-21	2.9	NE
Jul-21	2.8	NE
Aug-21	3.5	WNW
Sep-21	2.8	E
Oct-21	3.1	NW
Nov-21	3.5	NW
Dec-21	4.0	NW

Figure 5.1 shows the offshore wind directions at 10 m above sea level, derived from ECMWF ERA5 reanalysis data (2010–2017) for an offshore point approximately 10 km south of Ikobe. Most wind vectors fall between azimuths 270° (west) and 360° (north),

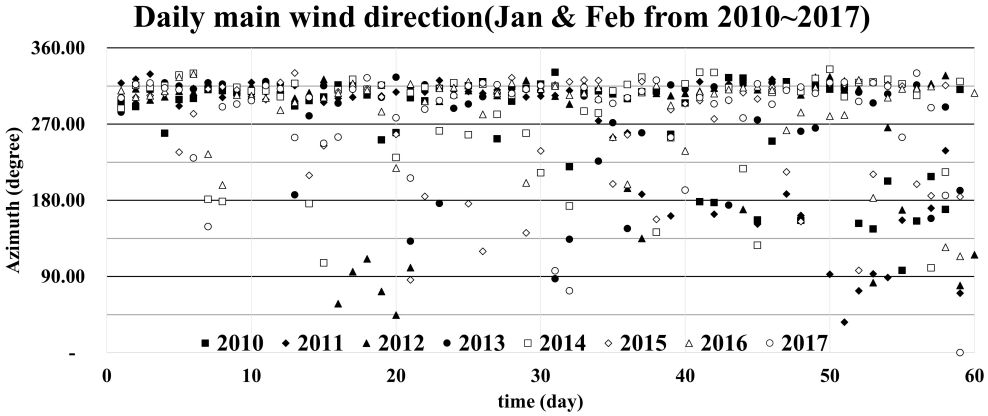

Figure 5.1: Offshore wind direction (January and February, 2010−2017, ECMWF ERA5 data).

indicating a prevailing offshore (land-to-sea) wind direction throughout much of the year.

These results show that both inland (above the coastal cliffs) and offshore, the dominant winter wind generally blows seaward from the northwest. However, this pattern is inconsistent with the observed onshore sand transport and dune accretion during the same season, indicating that the local wind field near the coast is strongly modified by topographic effects, particularly the cliff-induced recirculating eddy below the coastal slope. Large-scale meteorological datasets alone therefore cannot fully explain the actual aeolian transport acting on the coastal dunes of the Atsumi Peninsula.

5.2 Nearshore Wind Conditions around Omotehama Beach

5.2.1 Field Observations of Nearshore Wind

Wind observations were conducted at Ikobe Coast to clarify the local wind field influencing dune formation. Measurements were performed in three campaigns: (1) Horizontal distribution surveys in 2019, 2022 and 2023. (2) Vertical wind profile observation in 2019.

(1) Beach-level observation (January 2019). Four cup anemometers (Davis Instruments) were installed along the sandy beach of Ikobe Coast (Fig. 5.2, red markers) at an elevation of 1−2 m above T.P. and 1.5 m above the sand surface. One sensor was positioned directly in front of a easten valley to investigate the topographic influence of the cliff. The mean wind speeds recorded during the survey were 5.9 m/s on the west side, 3.6 m/s on the east side, 3.1 m/s in front of the easten valley, and 5.3 m/s east of the easten valley. Wind speeds decreased toward the easten valley, showing the lowest value at the valley front. The prevailing wind direction during the observation was south−southwest to southwest, but it shifted to west at the easten valley front, indicating local deflection caused by the terrain.

(2) Simultaneous observation on the dune and the cliff (January 2022). Three cup anemometers were installed: two on the Ikobe dune (upper and lower slopes) and one on the cliff top behind the dune (Fig. 5.3, red markers). The instruments were placed 1.5 m above the ground at each site. Average wind speeds were 4.3 m/s at the cliff top

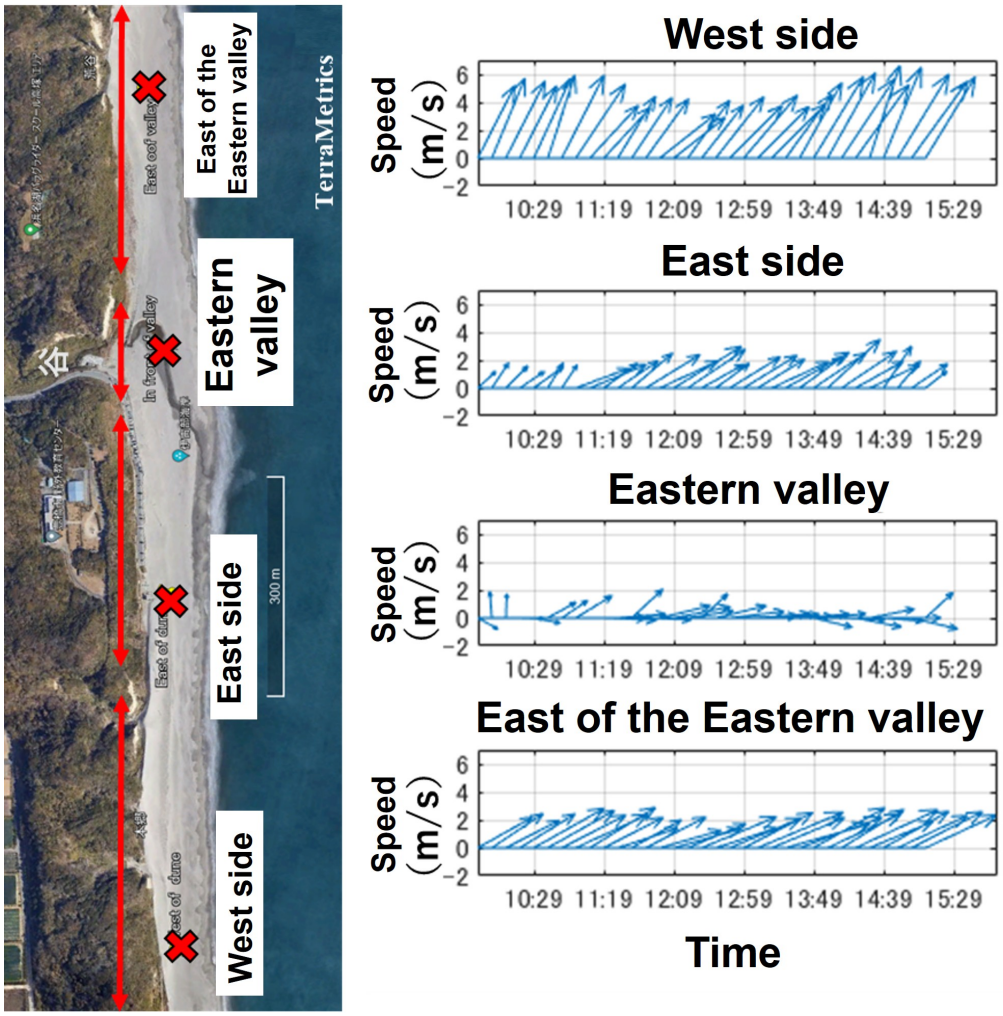

Figure 5.2: Beach-level observation (January 2019).

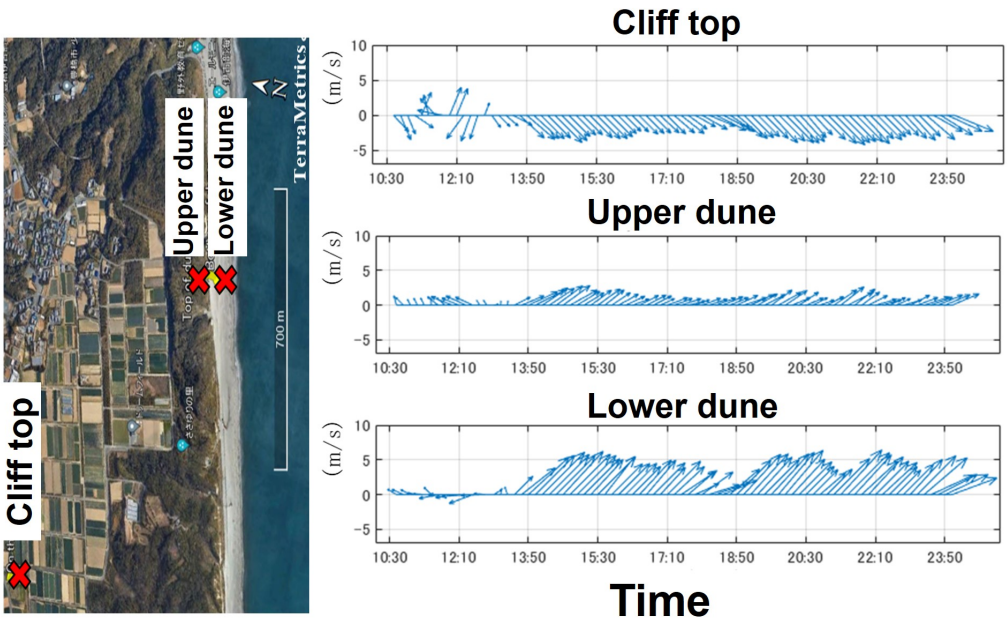

Figure 5.3: Simultaneous observation on the dune and the cliff (January 2022).

(elevation 66.9 m), 3.0 m/s at the upper dune (22.1 m), and 5.8 m/s at the lower dune (1.7 m). Wind direction at the cliff top was northwesterly, whereas both dune stations recorded southwesterly winds demonstrating a complete reversal of flow direction. The cliff-top northwesterly wind was deflected downward and seaward near the beach, producing a stronger southwesterly wind that acts as a primary driving force for winter dune development.

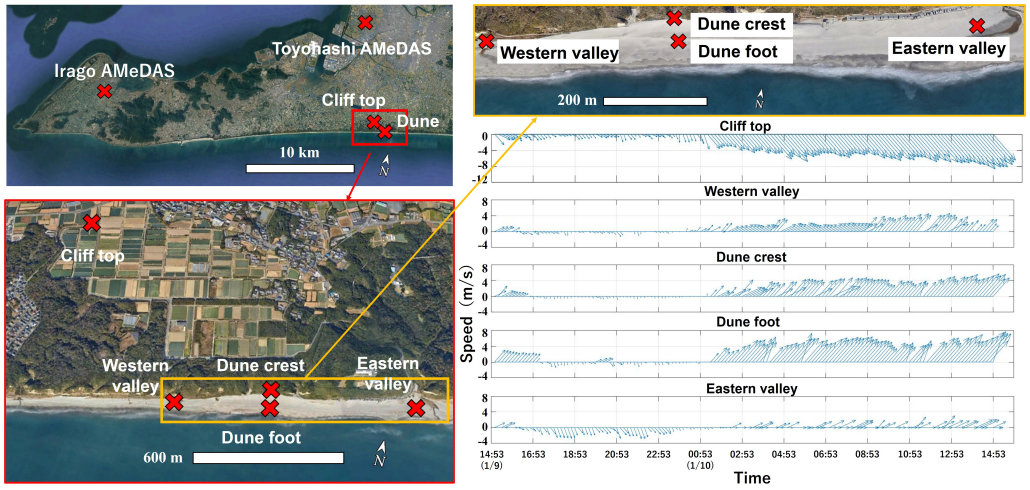

Figure 5.4: Multi-point observation across the dune–cliff system (January 2023).

(3) Multi-point observation across the dune–cliff system (January 2023). A 24-hour simultaneous observation was conducted from 14:53 on January 9 to 14:53 on January 10, 2023 (Fig. 5.4). Five anemometers were installed at the following locations: in front of the western valley, on the central dune crest, on the central dune foot, in front of the eastern valley, and on the cliff top. Cup anemometers were used for the cliff-top and valley stations, and propeller-type anemometers (R.M. Young) were used for the dune stations. The heights above ground were 1.42 m (cliff top), 1.43 m (western valley front), 1.42 m (eastern valley front), 1.38 m (dune crest), and 2.0 m (dune foot). Ten-minute average wind speeds and dominant directions were computed.

The vector plots show that from 3:00 to 15:00, northwesterly winds prevailed at the cliff top, while southwesterly winds dominated near the coast. The 12-hour mean wind speeds and main directions were as follows: WSW 4.61 m/s (western valley front), SW 5.91 m/s (dune crest), SW 7.47 m/s (dune foot), W 3.96 m/s (eastern valley front), and NW 8.51 m/s (cliff top). When strong northwesterly winds occurred over the cliff, the wind velocity increased at the dune center and reversed to a southwesterly direction, while the valley fronts experienced weaker, more westerly flows. This pattern coincides with the development area of the wake vortex behind the cliff, indicating that dune formation occurs within the recirculation zone. Moreover, wind velocity at the dune crest was slightly lower than that at the dune foot, suggesting downward acceleration toward the beach.

(4) Vertical wind profile in front of the cliff (February 2019). To further investigate wind reversal, a pilot-balloon observation was conducted in front of the cliff using a digital theodolite (TD-4, Tamaya Keisoku Systems). Figure 5.5 shows the cross-shore component of wind velocity. Positive values indicate offshore (land-to-sea) flow. Results show that above an elevation of 20 m, the wind blew seaward, while below 20 m, the

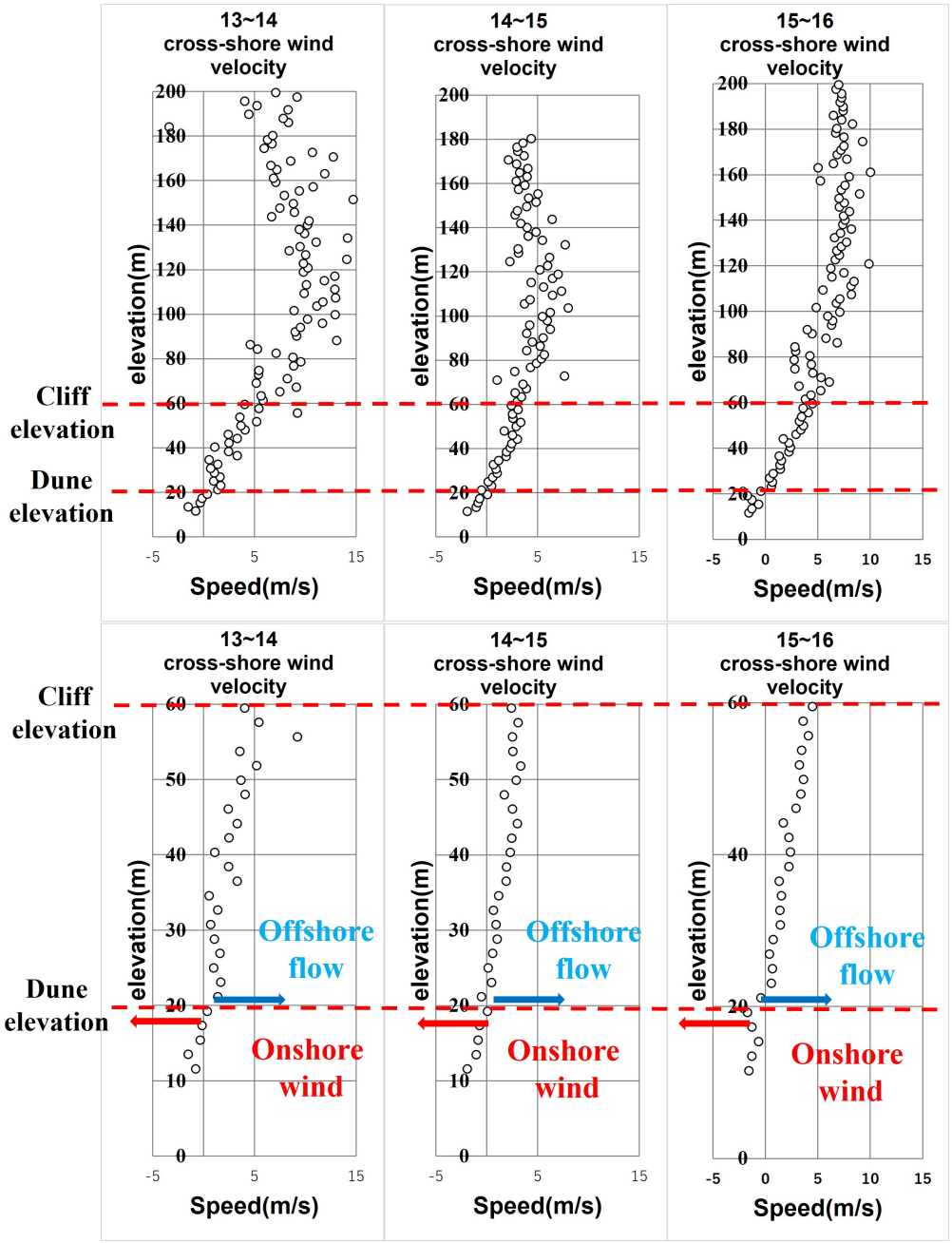

Figure 5.5: Vertical wind profile in front of the cliff (February 2019)

flow reversed toward land at all observation times. This vertical shear corresponds to the observed flow reversal between the cliff and the beach.

5.2.2 Discussion of Observed Wind Fields

(1) Mechanism of the local wind field. Even under dominant northwesterly monsoon conditions during winter, southwesterly winds were consistently observed in front of the cliff. This demonstrates that a local recirculating eddy, generated by the cliff-top flow separation, induces a reverse wind along the beach that drives sand transport toward the dune (Fig. 5.6).

The turning height of the wind reversal, located near 20 m elevation, corresponds

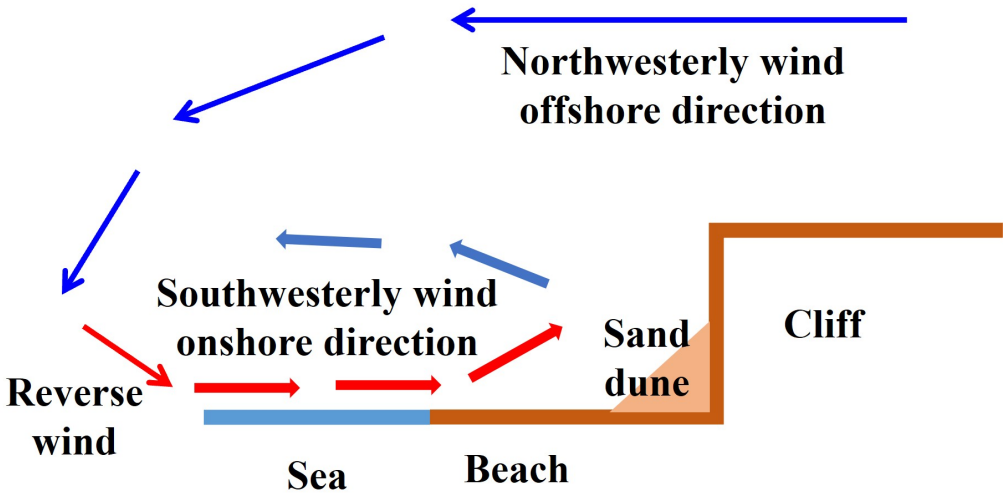

Figure 5.6: Wind mechanism

closely to the maximum dune height, indicating that dune growth is dynamically limited by the structure of the wake vortex. At the time of the observation, the maximum dune elevation was approximately 20 m, whereas it has since increased to nearly 25 m; however, no direct evidence is available to confirm whether the height of the wind reversal has changed accordingly.

In contrast, wind speed reduction and direction change in front of valleys suggest that recirculation weakens in these gaps, which explains why dunes tend to develop between valleys rather than directly in front of them.

(2) Comparison with AMeDAS data. Figures 5.7 and 5.8 compare the local wind observations with Toyohashi and Irago AMeDAS records. When both AMeDAS stations continuously recorded northwesterly winds (e.g., 14:00–24:00 on January 11, 2022, and 01:00–17:00 on January 9–10, 2023), the cliff-top wind remained stably northwesterly, while the dune foot exhibited steady southwesterly winds with higher speeds. The average wind speeds during these intervals were 4.58 m/s (cliff top), 6.76 m/s (dune foot), 5.9 m/s (Irago AMeDAS), and 6.21 m/s (Toyohashi AMeDAS) for 2022, and 8.04 m/s (cliff top), 7.17 m/s (dune foot), 7.36 m/s (Irago AMeDAS), and 7.31 m/s (Toyohashi AMeDAS) for 2023. Conversely, when AMeDAS wind directions deviated from the northwest, the wind field at both cliff top and dune base became unstable and weaker. These results confirm that a sufficiently strong northwesterly wind over the cliff is necessary to generate the wake vortex responsible for the landward sand transport.

5.3 Numerical Calculation of Wind Conditions

Numerical simulations in this chapter were performed using the CFD software *OpenFOAM*. Two main reasons motivated this choice. First, OpenFOAM allows efficient parallel computation, enabling the use of multi-core laboratory computers to accelerate processing. Second, it has a large international user community, providing extensive online discussions and add-on tools, which facilitates troubleshooting and model customization.

Section 5.3.1 introduces the computational methods and initial settings. Section 5.3.2

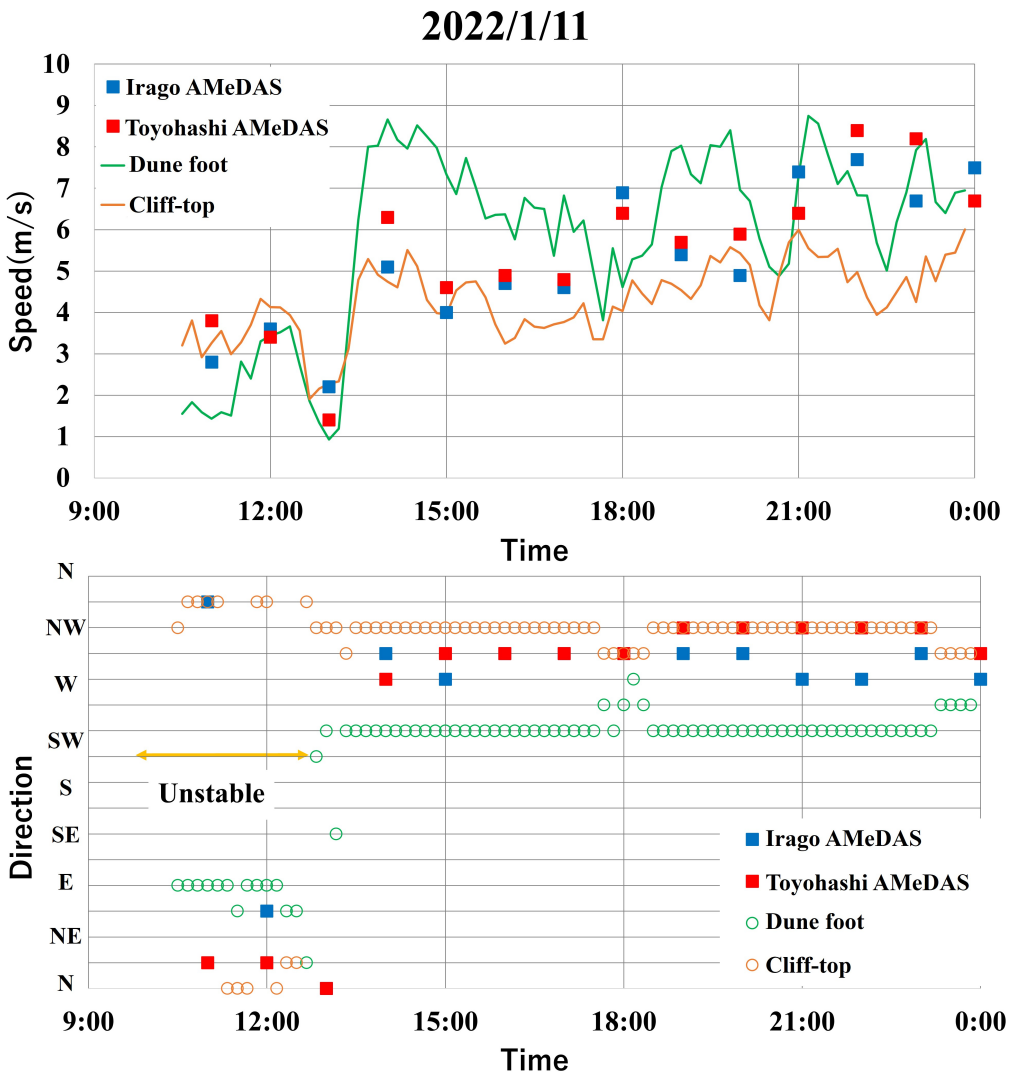

Figure 5.7: Comparison between locally observed winds and AMeDAS data (January 11, 2022)

describes the construction of the terrain models. Section 5.3.3 presents the results of the two-dimensional (2D) simulations, and Section 5.3.4 discusses the results of the three-dimensional (3D) simulations. Finally, Section 5.3.5 provides an integrated discussion on the overall mechanisms and phenomena revealed by the simulations.

5.3.1 Calculation Method and Initial Settings

3D computational domain. The 3D calculation domain (Table 5.2) consisted of a grid spacing of 10 m in the horizontal (x–z) plane and 5 m in the vertical (y) direction. The x-axis represents the east–west direction with 170 cells (1,700 m total length), the z-axis represents the north–south direction with 200 cells (2,000 m total length), and the y-axis represents the vertical direction with 40 cells (200 m height). In total, approximately 1.36 million cells were generated, with additional subdivision applied to the surrounding terrain and upper atmospheric region. The calculation time step was 1 s, and outputs were recorded every 1,000 s. Parallel computation was performed using eight CPU threads.

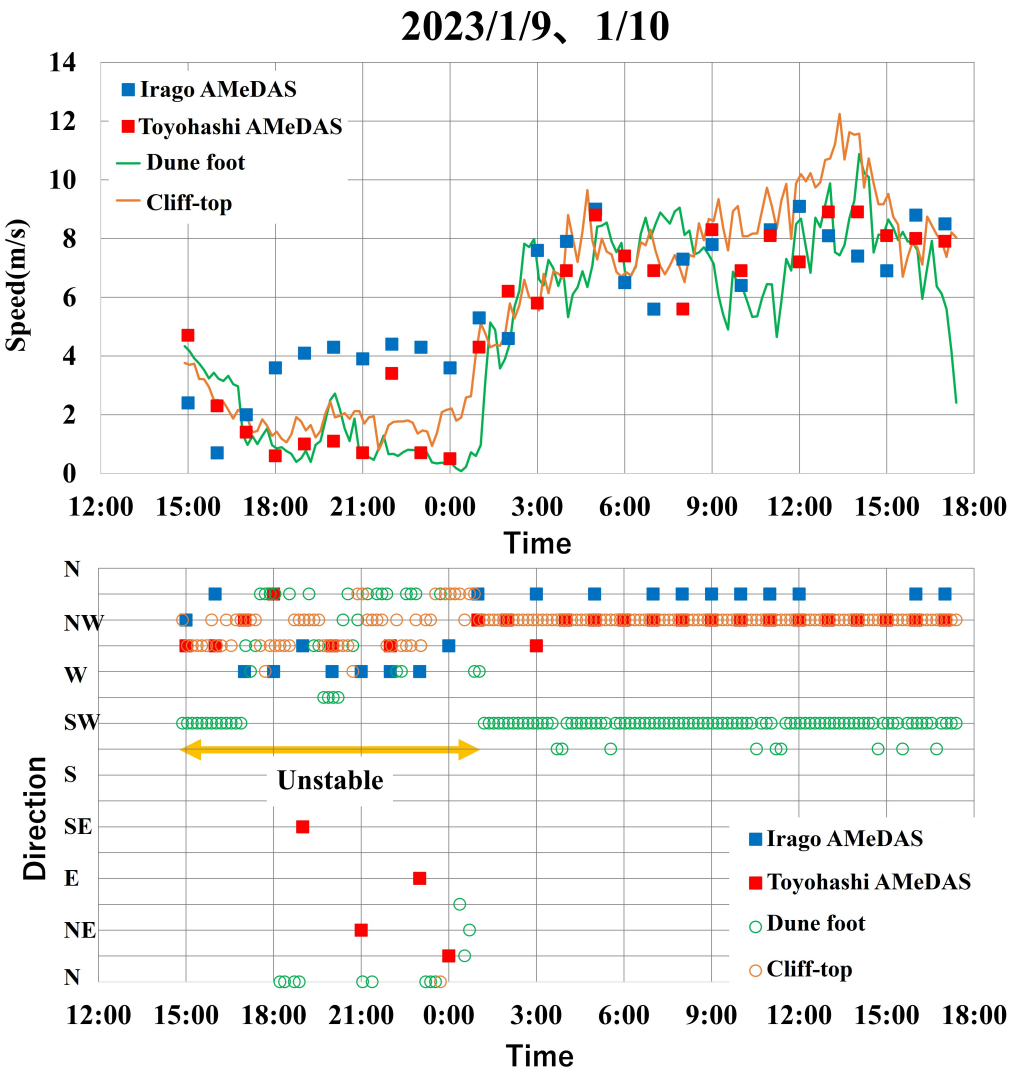

Figure 5.8: Comparison between locally observed winds and AMeDAS data (January 9–10, 2023)

2D computational domain. The 2D model (Table 5.2) used a horizontal grid size of 10 m and a vertical size of 5 m. There were 200 cells in the x-direction (2,000 m length) and 40 in the y-direction (200 m height), with a single cell thickness in the z-direction (8,000 total cells). The calculation time step and output interval were both 1 s, and computations were performed in parallel using eight threads.

Model parameters. For both 2D and 3D simulations (Table 5.3), the air kinematic viscosity was set to 1.5×10^{-5} m^2/s, and the turbulence was modeled using the RANS k–ε model. The RANS model provides a time-averaged representation of flow behavior, capturing general flow patterns but not transient small-scale eddies. Because this study focuses on long-term and large-scale flow behavior over complex terrain, the limitations of RANS were considered acceptable. The k–ε model solves two transport equations for turbulent kinetic energy (k) and its dissipation rate (ε).

Initial wind conditions. The initial inflow velocity was determined based on the average wind speed observed between 150–200 m elevation using pilot balloon data,

Table 5.2: Model configuration and computational domain settings.

Computational setting	**Symbol**	**3D Model**	**2D Model**
Grid size (horizontal)	$\Delta x, \Delta z$ (m)	10	10
Grid size (vertical)	Δy (m)	5	5
Domain size (x)	L_x (m)	1700 (170 cells)	2000 (200 cells)
Domain size (y)	L_y (m)	200 (40 cells)	200 (40 cells)
Domain size (z)	L_z (m)	2000 (200 cells)	Single layer
Total cells	–	1.36 million	8000
Time step	Δt (s)	1	1
Output interval	–	1000 s	1 s
Parallel threads	–	8	8

Table 5.3: Turbulence parameters

Parameter	**Symbol**	**6 m/s Case**	**12 m/s Case**
Reference velocity	u_{ref} (m/s)	6	12
Turbulence intensity	I	0.1	0.1
Turbulent kinetic energy	k (m^2/s^2)	0.54	2.16
Dissipation rate	ε (m^2/s^3)	0.0065	0.0521
Turbulence length scale	L (m)	10	10
Model constant	C_μ	0.09	
Air kinematic viscosity	ν (m^2/s)	1.5×10^{-5}	
Turbulence model	–	RANS k–ε	

since this layer is less affected by surface friction. The three-hour mean wind speed at this height was 9.67 m/s. Specifically, the average speed was 12.52 m/s between 13:00−14:00 and 6.26 m/s between 14:00−15:00. These two values were used as the inflow boundary conditions in the 2D model to represent the maximum and minimum cases. Turbulent parameters k and ε were initialized using OpenFOAM's empirical estimation formulas:

$$k = \frac{3}{2}(I \times u_{\text{ref}})^2 \tag{5.1}$$

$$\varepsilon = C_\mu^{0.75} \frac{k^{1.5}}{L}, \tag{5.2}$$

where I is the turbulence intensity (set to 0.1), u_{ref} is the reference velocity (m/s), $C_\mu = 0.09$, and L is the characteristic length scale (here, the vertical grid size of 5 m).

5.3.2 Terrain Models

2D terrain model. The 2D model geometry (Fig.5.9) was created in *SketchUp*. The modeled cliff extended 600 m from the inflow boundary to the separation point, with its height and slope angle varied in different cases.

3D terrain model. The 3D model was generated using 5 m-resolution DEM data from the Geospatial Information Authority of Japan's aerial laser survey (Fig.5.10). The DEM

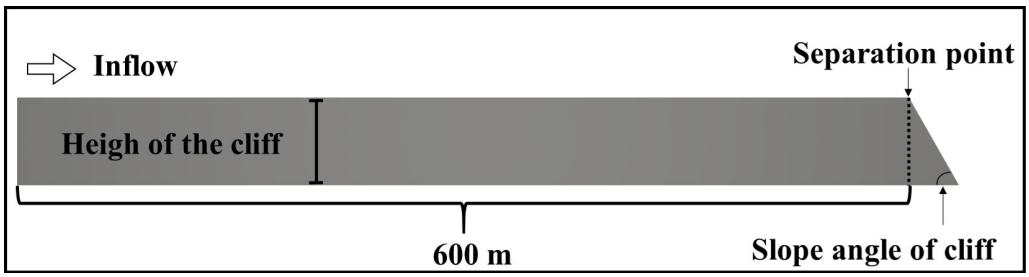

Figure 5.9: 2D terrain model

was converted into an STL mesh of irregular triangles using MATLAB's stlwrite function. The model covers approximately 1,700 m (east–west), 700 m (north–south), and reaches a maximum elevation of about 73 m.

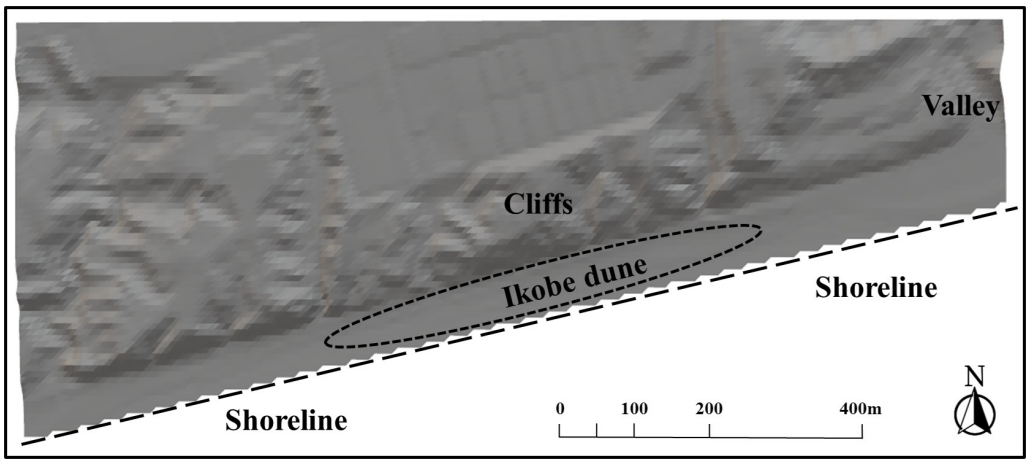

Figure 5.10: 3D terrain model

5.3.3 2D Model Results

The 2D model was used to examine how cliff height and slope angle influence the distance of the reverse (recirculating) flow (Fig.5.11).

Effect of Cliff Height on Reverse Flow Distance

To evaluate the relationship between cliff height and reverse flow length, the cliff height was varied as 30, 60, 90, and 120 m, and two inflow velocities (6 m/s and 12 m/s) were used (Table 5.4). As shown in Fig.5.12, the reverse-flow distance increased with cliff height, while the influence of wind speed was minor. Regression equations and R^2 values are indicated in the figure.

Effect of Slope Angle on Reverse Flow Distance

To investigate the influence of slope angle, the cliff inclination was varied from 15° to 90° (Table 5.5), with inflow speeds of 6 m/s and 12 m/s. As shown in (Fig.5.13), reverse-flow distance increased with slope angle up to about 45°, beyond which the change became negligible. At 30°, the distance increased slightly with velocity, while at 15°, no recirculation formed, and thus no reverse flow was observed.

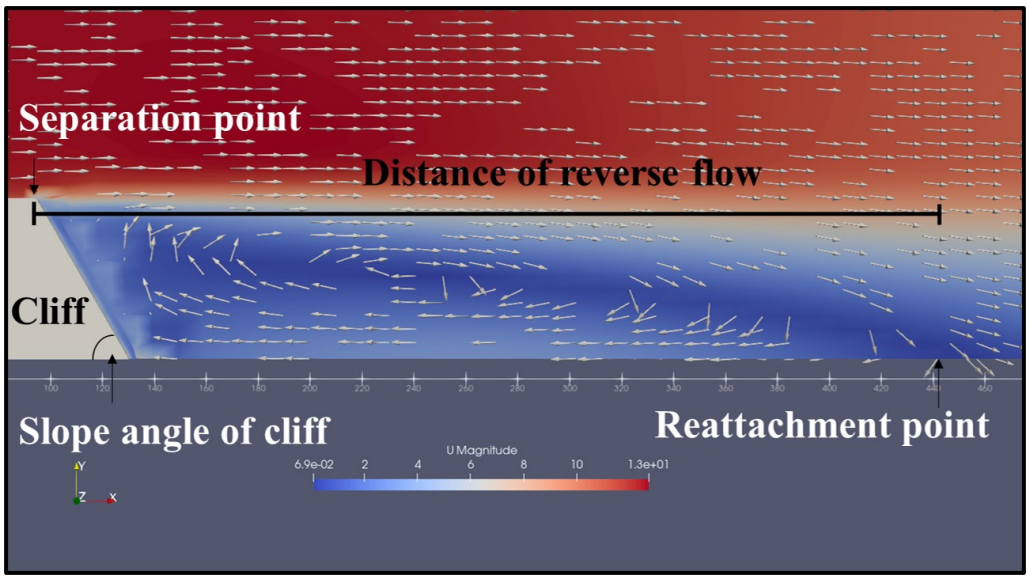

Figure 5.11: Distance of reverse flow in 2D model

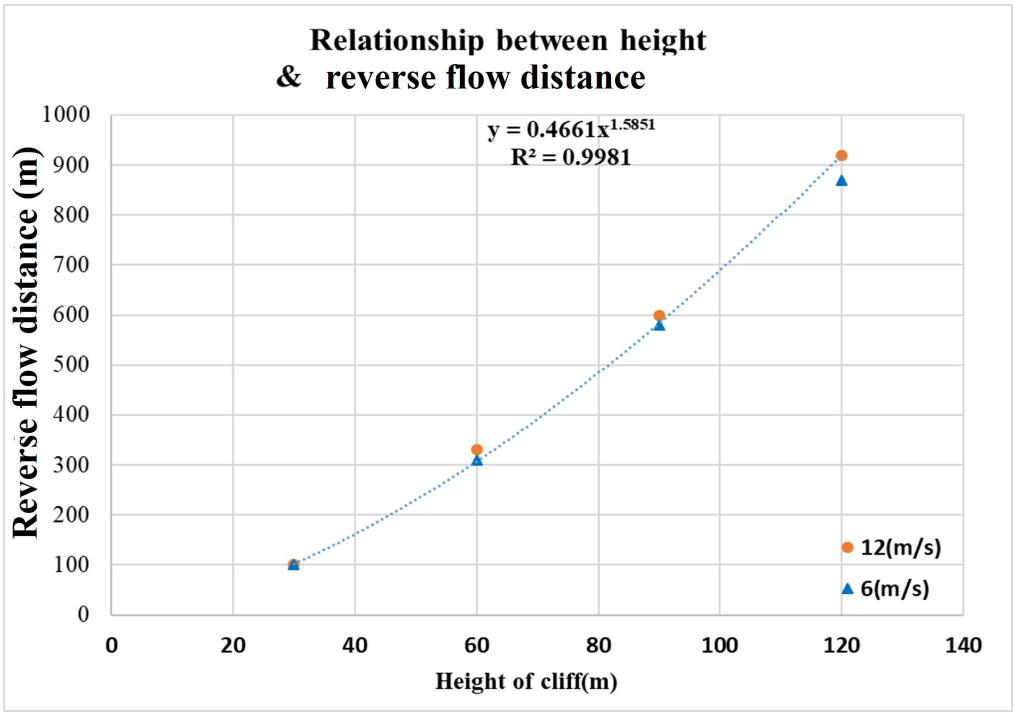

Figure 5.12: Relationship between height and reverse flow distance (cliff angle as 90 degrees)

Table 5.4: Cases for relationship between height and reverse flow distance.

Height of cliff (m)	Speed (m/s)	Angle of slope (°)
120	12	90
120	6	90
90	12	90
90	6	90
60	12	90
60	6	90
30	12	90
30	6	90

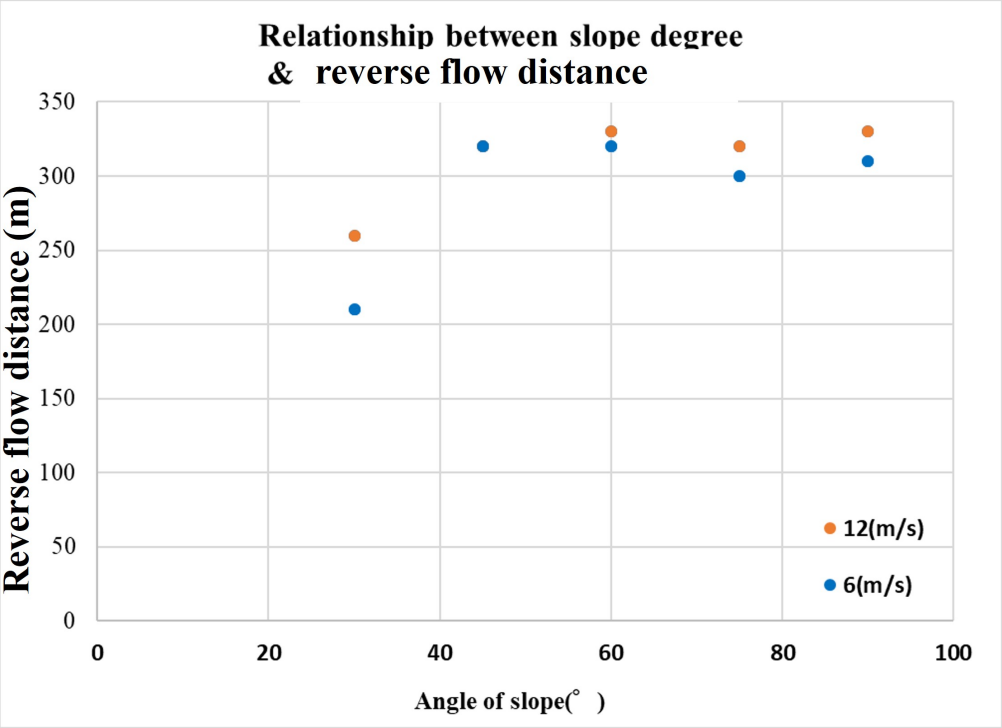

Figure 5.13: Relationship between angle of slope and reverse flow distance(cliff height as 60m)

Table 5.5: Cases for relationship between angle of slope and reverse flow distance.

Height of cliff (m)	Speed (m/s)	Angle of slope (°)
60	12	15
60	6	15
60	12	30
60	6	30
60	12	45
60	6	45
60	12	60
60	6	60
60	12	75
60	6	75
60	12	90
60	6	90

5.3.4 3D Model Results

This section presents three analyses. First, it compares the simulation results with pilot-balloon observations for validation. Second, it examines the effect of the incident wind angle on the wind field beneath the cliff. Finally, it visualizes the recirculating eddies and evaluates how the incident angle influences their structure and extent.

Comparison between Numerical and Observed Results

Fig.5.14 compares the calculated and observed wind-speed profiles. Although real atmospheric flow fluctuates irregularly due to vegetation, sea breeze, and upper-level variability, these effects were omitted to simplify the model. As shown in Fig.5.14, the simulated and observed wind speeds agree reasonably well below 60 m elevation.

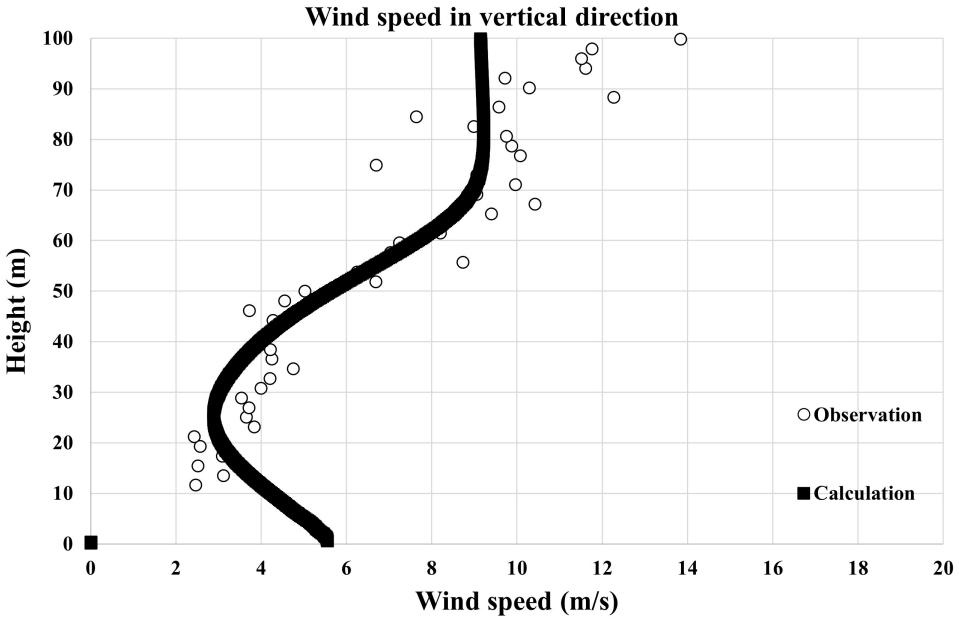

Figure 5.14: Wind speed in vertical direction

In Fig.5.15, wind velocities are projected onto the direction normal to the cliff, with positive values representing offshore (land-to-sea) flow and negative values representing onshore flow. The calculated wind reversal occurs at approximately 15 m elevation, slightly lower than the observed turning height of about 20 m. This difference is likely due to minor deviations in simulated wind direction relative to the observation. Nevertheless, the overall agreement is satisfactory.

Influence of Incident Angle on Wind Direction

To understand how the incidence angle of the approaching wind influences the nearshore wind field, 3D numerical simulations were conducted using the terrain model of the Ikobe coast. By varying the wind direction at the cliff top, the resulting flow patterns over the beach were analyzed.

When the incident angle was small, the wind direction near the beach differed depending on the local topography of the cliff (Fig.5.16 (a) and (b)). At incident angles between 25° and 35°, the wind in front of the cliff (red box) turned southwesterly,

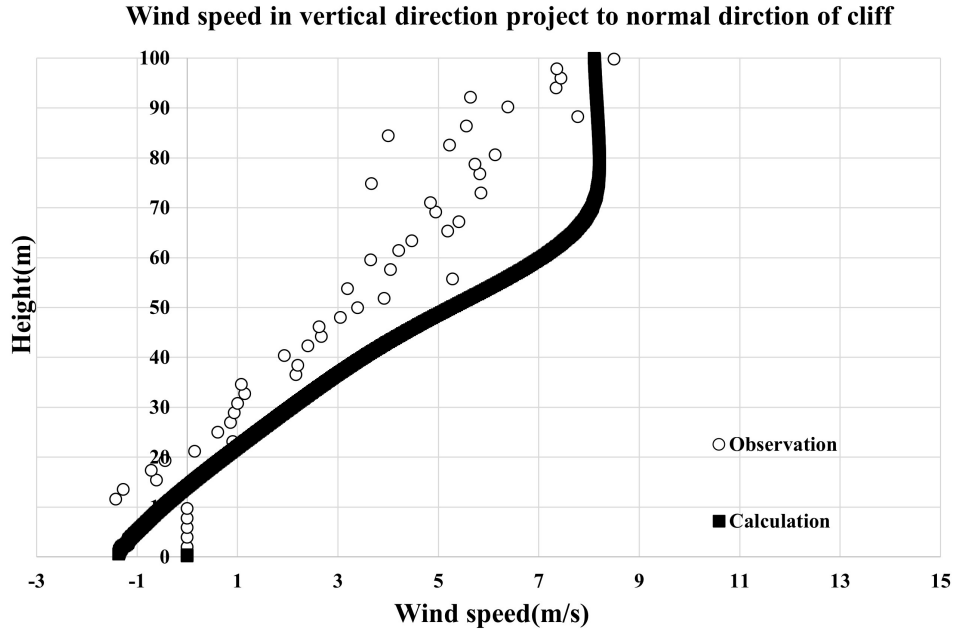

Figure 5.15: Wind speed in vertical direction project to normal direction of the cliff

while the wind in front of the valley (blue box) remained northwesterly (Fig.5.16 (c) and (d)). When the angle increased to 45°, the southwesterly flow in front of the cliff persisted, but the wind in front of the valley shifted westward (Fig.5.16 (e)). At 52.5°, both areas exhibited westerly winds, indicating a transition of the entire nearshore flow field (Fig.5.16(f)).

This progressive shift of wind direction with increasing incident angle corresponds to the development and eventual decay of a cliff-induced vortex, which will be discussed in detail in Section 5.3.5

Influence of Incident Angle on the Eddy

To clarify the airflow pathways over the dune surface, streamline tracing was performed to identify where the passing flow originated and where it was directed, as shown in Fig. 5.17.

When the incident angle is small, the vortex structure varies considerably with local terrain morphology. Its alongshore influence remains limited, and the nearshore wind field becomes highly complex (Fig. 5.17(a), (b)). As the incident angle increases, the alongshore extent of the vortex gradually expands (Fig. 5.17(c)–(e)). During this transition, the vortex elongates horizontally, and the nearshore wind progressively turns southwesterly, becoming more parallel to the cliff line. At large incident angles, the vortex ultimately disappears (Fig. 5.17(f)). Although the cliff-top flow still undergoes some deflection, the resulting wind on the beach becomes predominantly westerly rather than forming a closed recirculating eddy.

To quantify the variation in eddy extent with incident angle, two metrics were analyzed. First, as shown in 5.18, the distance of the reverse flow- defined as the distance from the separation point (where flow detaches from the cliff) to the reattachment point (where flow reverses from landward to seaward)—was measured. In 5.19, it can be seen that the maximum reverse-flow distance remains nearly constant regardless of the incident angle. Second, as illustrated in 5.20, the influence distance of the eddy along

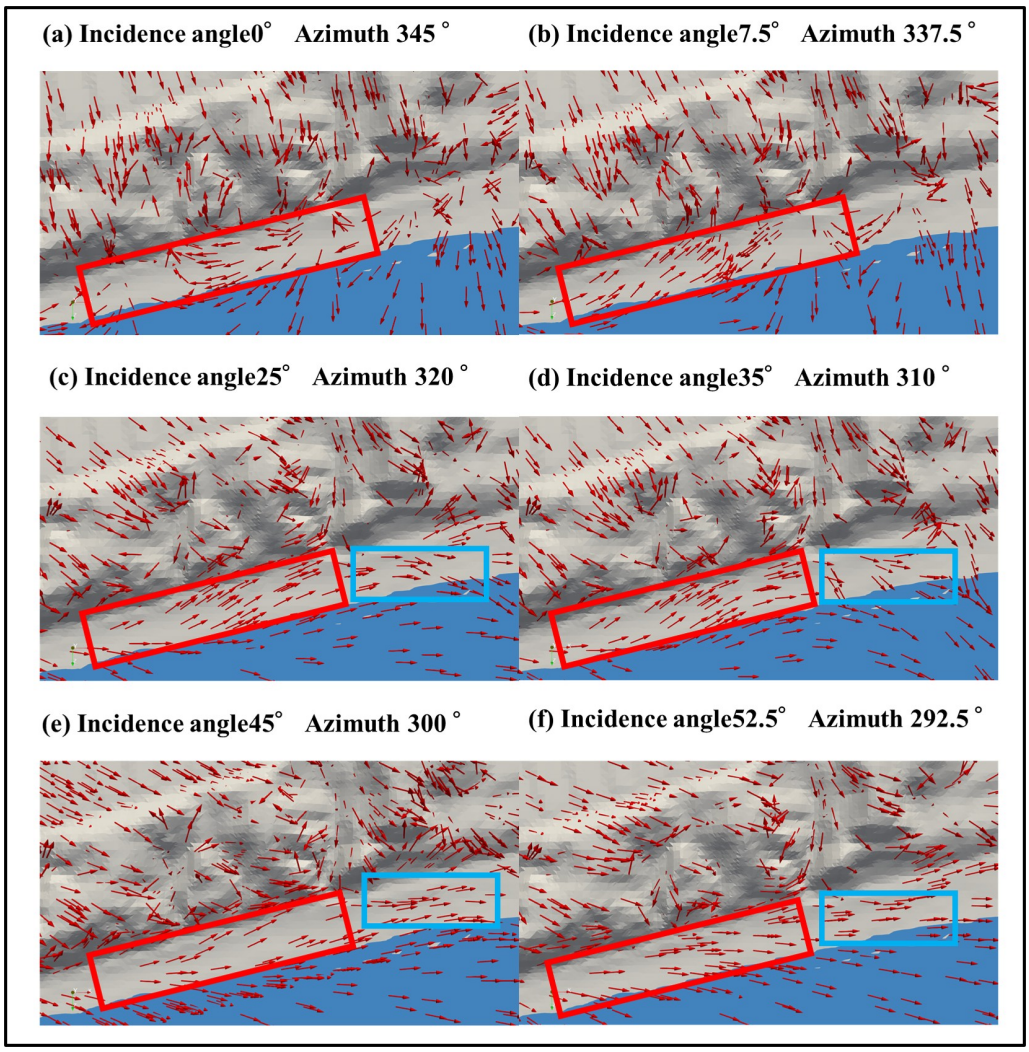

Figure 5.16: The effect of incident angle on the wind direction *(a)–(b)* At small incident angles, the nearshore wind direction varies depending on local cliff topography; *(c)–(d)* at 25°–35°, winds in front of the cliff turn SW while winds in front of the valley remain NW; *(e)* at 45°, the valley wind shifts W; *(f)* at 52.5°, both regions show W winds, marking a full-field transition.

the coastline increases with incident angle until the eddy disappears at 52.5°, as shown in 5.21.

5.3.5 Discussion

Mechanism

As illustrated in 5.22, the formation of coastal dunes can be explained as a three-step wind–terrain interaction process. Sand is first transported landward by wind from the beach and accumulates at the cliff base. Two wind types contribute to dune formation: (1) onshore winds blowing directly from the sea toward the cliff, which cause sand to pile up at the cliff base; and (2) winds blowing parallel to the cliff, which lose momentum due to surface friction, facilitating sand deposition. Because the dune surface is sloped and rougher than flat beaches, it enhances sand entrapment efficiency.

In Step 1, the northwesterly wind blowing over the cliff descends toward the beach,

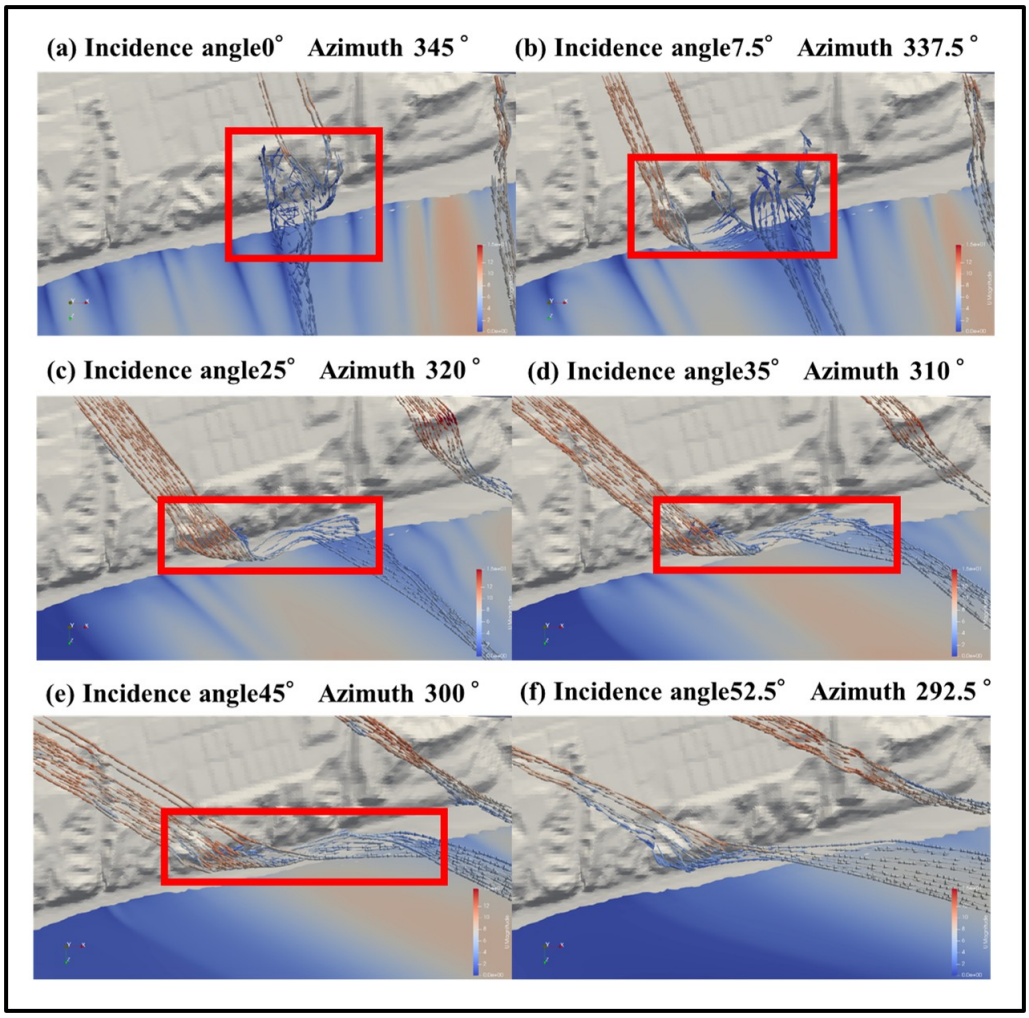

Figure 5.17: Influence of incident angle on eddy *(a)* At 0°, a terrain-dependent small eddy forms; *(b)* at 7.5°, only a weak localized eddy appears; *(c)–(e)* at 25°–45°, the vortex elongates and its alongshore influence expands; *(f)* at 52.5°, the vortex disappears and the nearshore wind becomes predominantly westward.Color shading indicates wind speed (blue = 0 m/s, red = 12 m/s).

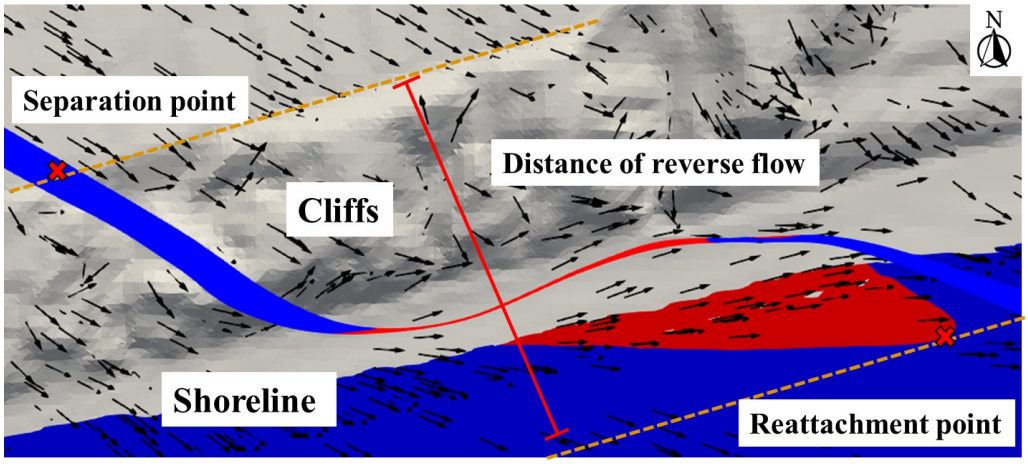

Figure 5.18: Reverse flow distance in the 3D model. The red-shaded area indicates the reverse-flow region.

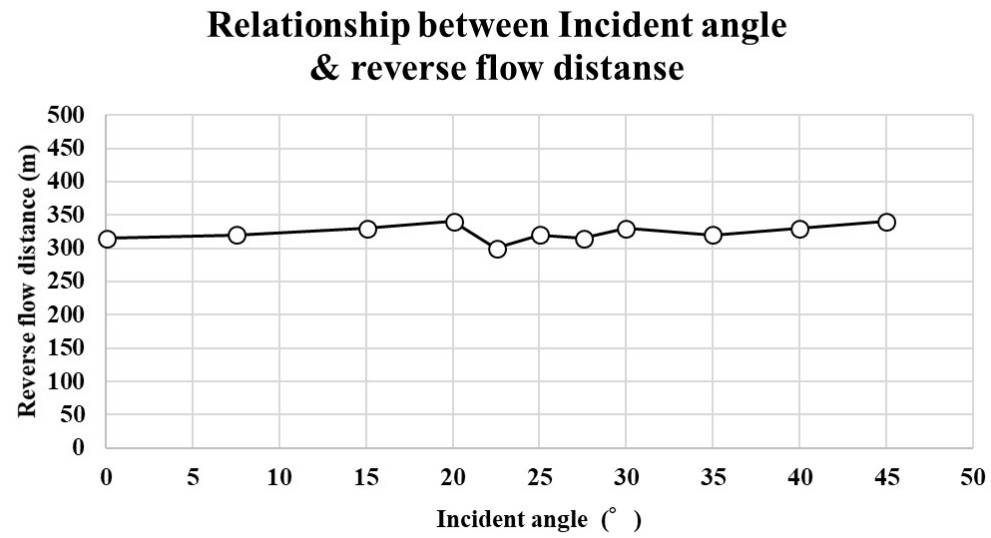

Figure 5.19: Relationship between incident angle and reverse flow distance.

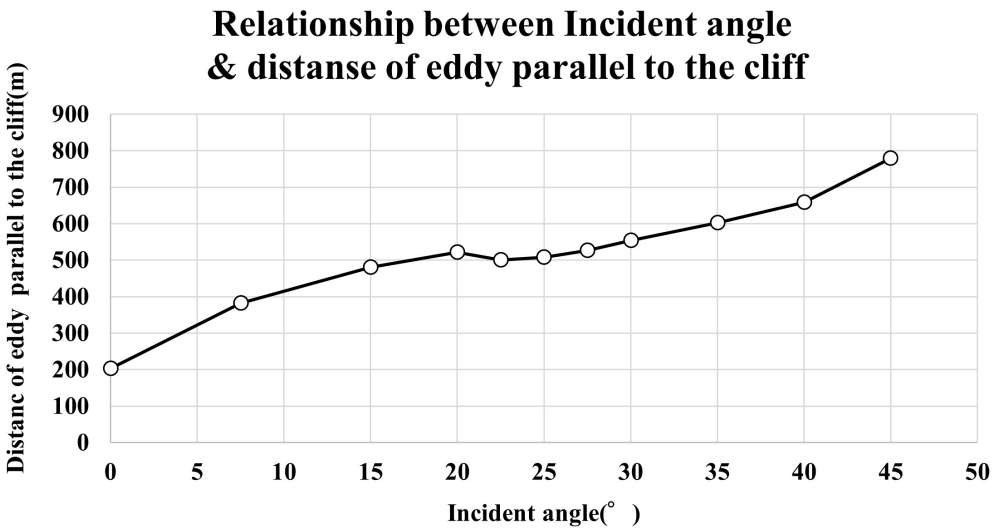

Figure 5.20: Relationship between incident angle and eddy influence distance parallel to the cliff.

deflecting to a southwesterly direction. In Step 2, the southwesterly wind near the beach ascends along the cliff face, providing the main driving force for dune growth. Finally, in Step 3, the wind continues upward and seaward, completing the circulation loop. This mechanism agrees with field observations, confirming the cliff-induced flow reversal and its role in dune accretion.

Characteristics and Evidence of the Eddy

This section discusses the characteristics of the cliff-induced eddy and evidence supporting the mechanism described in Fig. 5.22. The first feature is the reversal from northwesterly winds over the cliff to southwesterly winds beneath it, forming

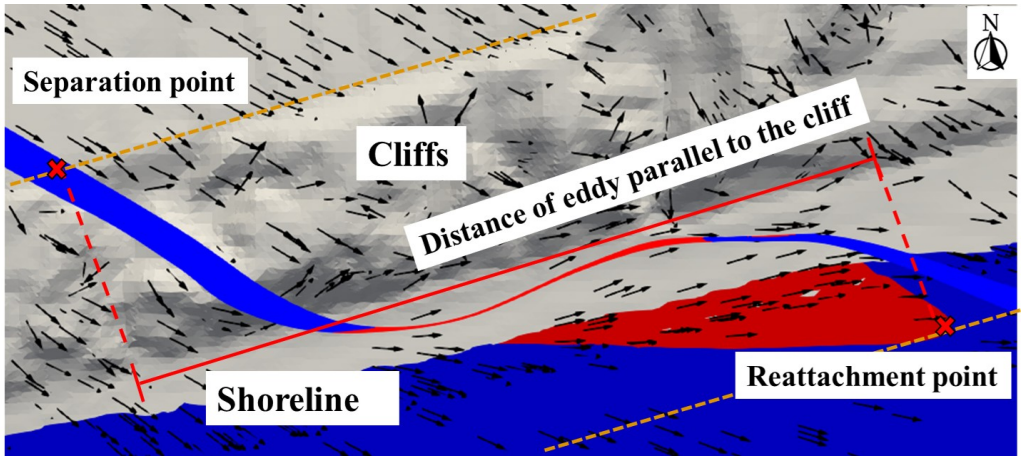

Figure 5.21: Eddy influence distance parallel to the cliff in the 3D model. The red-shaded area indicates the reverse-flow region.

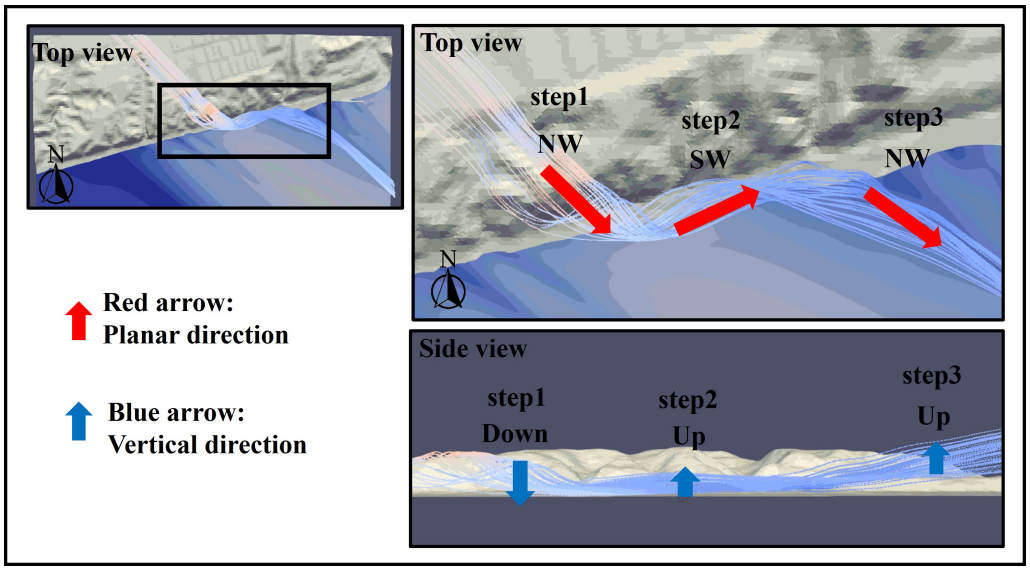

Figure 5.22: Mechanism of dune formation

a recirculating flow. This was verified both from field observations Fig. 5.3-5.4 and numerical simulations Fig. 5.17-5.19.

The second feature is the landward transport of sand by the southwesterly wind from the beach to the dune, confirmed in observations Fig. 5.5 and corresponding simulation results Fig. 5.20. The most notable pattern is the wind-speed reduction and westward turning as air approaches the dune from the beach.

The third feature is the vertical reversal from landward to seaward flow, consistent with both the balloon-based wind profile observations and the model results Fig. 5.18. According to Section 5.2.1, this transition typically occurs at elevations of 15–20 m, coinciding with the observed maximum dune height.

Eddy strength and extent are also influenced by terrain. As shown in the 3D simulation results Fig. 5.20 and field data Fig. 5.4, higher cliffs generate stronger and larger eddies, while lower cliffs (such as east of the Ikobe dune) produce weaker ones. In open areas without cliffs, no eddy forms, and the northwesterly flow persists unobstructed. The effects of inflow speed (6–12 m/s) and slope angle (>45°) were found

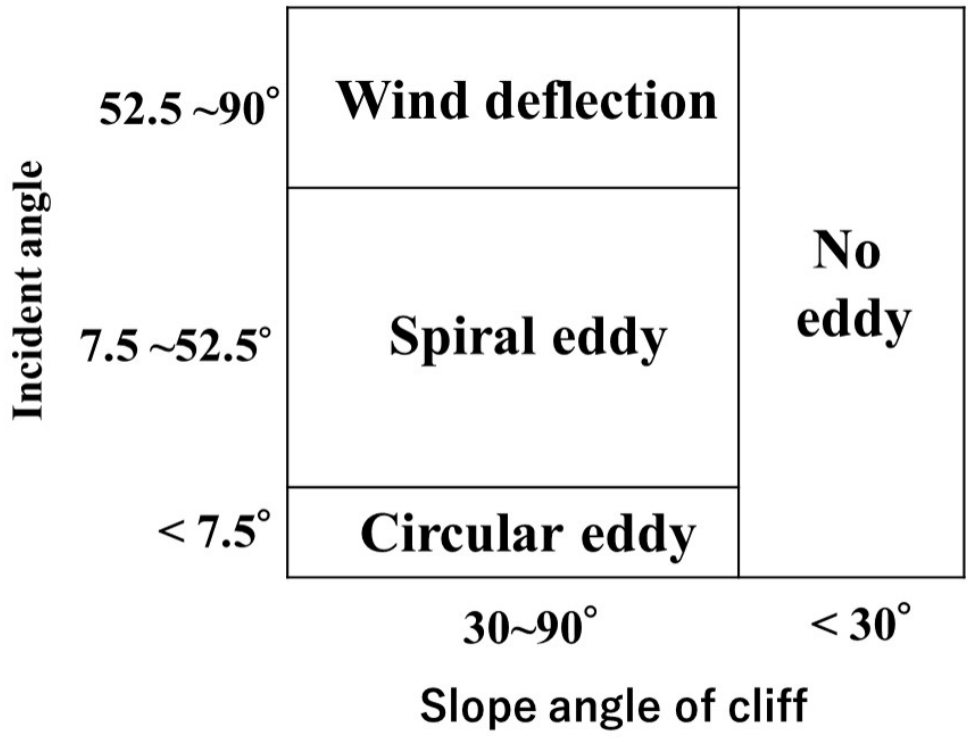

Figure 5.23: Eddy formation regimes under varying incident and slope angles.

to be secondary, consistent with the 2D results of Section 5.3.3.

Finally, the incident angle also influences eddy type and intensity, as discussed in the next section and illustrated in Fig. 5.24.

Types of Eddies and Their Formation Conditions

Figure 5.23 summarizes how the incident and slope angles affect eddy morphology. Eddies fail to form when the cliff slope is below 30°. Above 30°, three regimes are identified: (1) When the incident angle is below 7.5°, a circular eddy forms; (2) Between 7.5° and 52.5°, a spiral-shaped eddy develops; (3) Above 52.5°, the wind merely deflects without forming a closed circulation.

The relationship between these eddy types and incident angles is illustrated in Fig. 5.24. At small incident angles, a compact circular eddy forms, whose deflection direction depends on cliff geometry. At 25°, the circular eddy elongates into a spiral vortex. Interestingly, as confirmed in Section 5.3.4, the reverse-flow distance remains nearly constant, while the alongshore influence range increases with incident angle. At 45°, the eddy elongates further along the coastline, and above 52.5°, it breaks down entirely, producing only directional deflection. The transition from circular to spiral eddy can be imagined as a coiled rope gradually unwinding as it stretches.

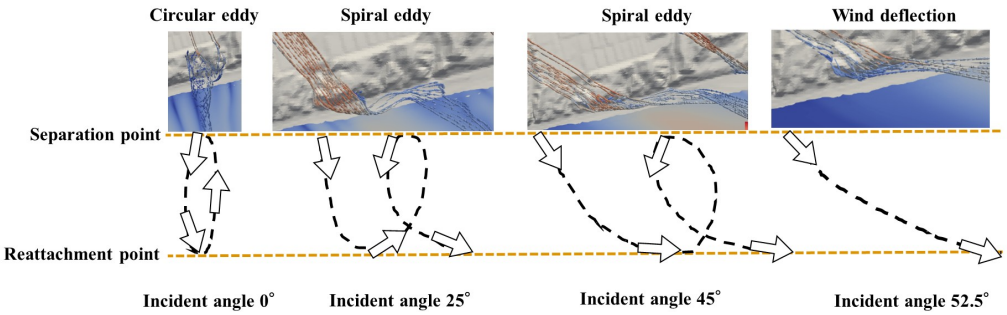

Figure 5.24: Conceptual diagram illustrating the transformation of eddy type with increasing incident angle.

Chapter 6

Aeolian Sand Transport and Integrated Sediment Budgets within the Dune–Beach–Nearshore System

This chapter quantifies aeolian sand transport and examines its characteristics based on field observations, and evaluates integrated sediment budgets within a dune–beach–nearshore system. Section 6.1 describes the wind-blown sand observation methods using sand traps and presents the measured aeolian sand fluxes. Section 6.2 examines the relationship between aeolian sand transport and wind conditions, while Section 6.3 explores the relationship between aeolian sand transport and topographic changes. Finally, Section 6.4 integrates sediment budgets for dunes, beaches, and the nearshore seabed to discuss sediment exchange within the dune–beach–nearshore system.

6.1 Observation of Wind-Blown Sand

Observations of wind-blown sand were conducted along the lower part of the dune, extending from the western valley to the eastern valley. A total of 11 box-type sand traps (No. 0–No. 10) were installed at approximately 100 m intervals along the alongshore direction (see the starting points of arrows in Fig. 6.1). Each sand trap was a rectangular box with internal dimensions of 10 cm (width) × 32 cm (depth) × 12 cm (height).

In addition, at sites located on the dune front (No. 2–No. 6), additional traps were placed near the dune crest and mid-slope to measure the vertical variation in sand transport. The direction of sand movement at each site was determined from the orientation of sand ripples that formed behind a flag marker placed adjacent to each trap.

The trapped sand was collected twice on January 10 at 13:00 and 15:00, respectively. The two measurements were averaged and expressed as vector fluxes (transport rate per minute per centimeter), as shown in the upper panel of Fig. 6.1. At No. 2–No. 5, data from both the lower and upper dune slopes are presented, while at No. 6, data from the lower and mid-slope positions are included. The lower panel of Fig. 6.1 illustrates the decomposition of total sand transport at each lower trap position into alongshore and cross-shore components. The deviation angle between the cross-shore and north–south directions was 14°. Furthermore, Fig. 6.2 shows the trap quantities within the dune area (No. 2–No. 6), categorized into crest, mid-slope, and lower positions.

From the upper panel of Fig. 6.1, the direction of sand transport shifts increasingly westward from the dune toe toward the crest, while the total trapped amount gradually decreases. Similarly, at both valley sites, where the wind direction also shifted westward, the quantity of trapped sand was smaller than at the central dune sites (No. 2–No. 6).

As indicated in the lower panel of Fig. 6.1, the alongshore component of sand

transport was generally greater than the cross-shore component, demonstrating that wind-blown sand movement was predominantly along the coastline. From Fig. 6.2, the sand flux within the dune area decreases from lower → mid-slope → crest, with No. 2 recording the largest transport rate among all observation points.

These results indicate that both wind velocity and sand flux decrease upward along the dune slope, and that local topographic variations—particularly the presence of valleys and dune ridges—strongly influence the spatial distribution of wind-blown sand.

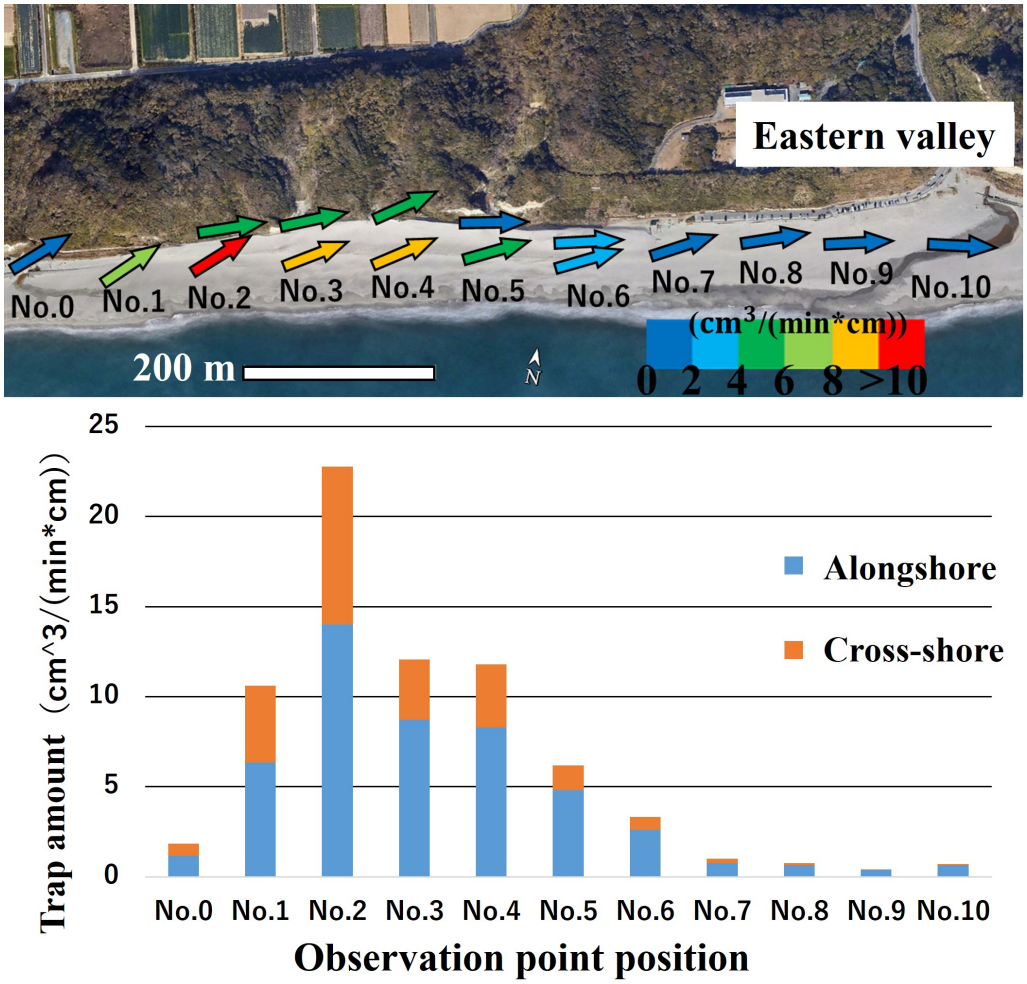

Figure 6.1: Vector distribution of wind-blown sand flux

6.2 Relationship between Wind-Blown Sand and Wind Conditions

Regarding the alongshore variation of wind velocity, as shown in Fig. 5.4, the strongest winds were observed in front of the dune, while the lowest wind speeds occurred at the valleys on both sides. The dominant wind direction was generally southwesterly, except at the eastern valley where it shifted westward.

The distribution of trapped sand (Fig. 6.1) also exhibited the same spatial trend: the largest quantities were recorded in front of the dune, whereas smaller amounts were measured near the flanking valleys. This pattern corresponds closely to the observed variation in wind velocity. Similarly, the direction of sand transport gradually changed from southwest (near the western valley) to west (near the eastern valley), showing strong

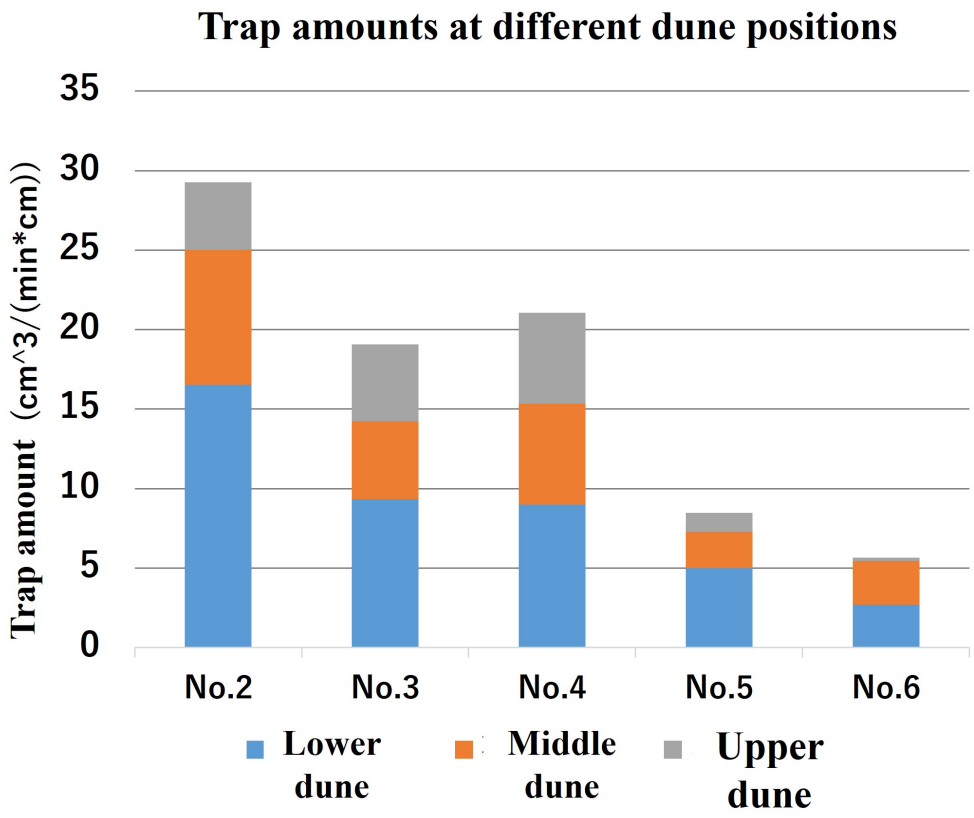

Figure 6.2: Trap amounts at different dune positions

consistency with the alongshore variation in wind direction.

In the cross-shore direction, Fig. 5.4 indicates that wind velocity decreases upward from the dune toe toward the crest. This trend was also confirmed by the sand-trap observations (Fig. 6.1), where the amount of wind-blown sand decreased from the lower to the upper slope, demonstrating a pattern consistent with the wind-speed profile.

These observations indicate that local topography exerts a significant influence on both wind intensity and sand transport. The dune front acts as a zone of wind acceleration and active sand movement, while the valleys on both sides serve as sheltered, depositional areas.

6.3 Relationship between Wind-Blown Sand and Topographic Change

The upper panel of Fig. 6.3 shows the topographic elevation change between January 2022 and January 2023, expressed as a color contour map. The locations of the sand traps and the boundaries of the three subregions (western, central, and eastern parts of the dune) are also indicated.

The lower panel of Fig. 6.3 presents the sediment budget diagram, constructed by treating the observed sand-trap collections as wind-blown sand fluxes. The data from each observation point were weighted and averaged within the three regions, and multiplied by the corresponding boundary length to obtain sand-flux vectors (arrows). The net accumulation (black text) within each region was then estimated from the flux balance.

The alongshore aeolian sand flux was calculated by multiplying the trap quantity at points No. 1, No. 3, No. 5, and No. 7 by the cross-shore distance between traps. The onshore (cross-shore) aeolian flux for the western part of the dune was computed as the weighted mean of trap fluxes at No. 1, No. 2 (×2), and No. 3, multiplied by the alongshore length of that region. The same approach was applied to the central part (No. 3, No. 4 (×2), No. 5) and the eastern part (No. 5, No. 6 (×2), No. 7).

Although these fluxes do not represent the absolute total sand-transport rates, and the single-day observation cannot be directly compared with annual-scale topographic change, the results provide a reasonable indication of the seasonal sediment budget during the winter monsoon period, when dune growth is most active. Therefore, this analysis is considered representative of the dune development phase.

From the sediment budget diagram (Fig. 6.3), it is evident that the western and central parts of the dune experienced larger net sand accumulation than the eastern part. This trend is consistent with the previously discussed topographic-change results. Moreover, the results indicate that direct sand input from the seaward direction contributed more significantly to dune growth than alongshore variations in aeolian flux.

Although the unit flux rates per meter and per hour (Fig. 6.1) suggest that the alongshore flux exceeded the cross-shore flux, when integrated across the entire dune, the total onshore flux was larger. This occurs because, although the alongshore boundaries are longer, the cross-shore flux acts over greater vertical and volumetric distances, resulting in a larger net sediment input from the seaward side.

These findings strongly suggest that dune development at Ikobe is primarily sustained by sand supply from the seaward direction, indicating that the dune effectively captures sediment originating from the nearshore and offshore zones. Thus, the dune acts as a sediment sink within the littoral drift system, highlighting the importance of incorporating aeolian processes into the overall coastal sediment budget for a more comprehensive understanding of sediment dynamics along the Omotehama Coast.

6.4 Integrated Sediment Budgets of the Dune–Beach–Nearshore System

In this section, the relationships among wind-blown sand transport, beach-volume change, dune-volume change, and submarine-sediment-volume change are examined to estimate the overall sediment budget in the study area. Fig. 6.4 shows the locations of the sand-trap observation points and the cross-shore survey lines used for topographic measurements. The calculation domain extends approximately 1 km, from cross-section line No. 8+700 to No. 9+600, of which about 600 m corresponds to the Ikobe dune area, while the remaining 400 m consists of non-dune sandy beach.

Because a small river flows into the sea near line No. 9+600, the inflow of wind-blown sand was assumed to be zero at this boundary. Similarly, sediment input from the sea cliff was also assumed to be negligible. The eastern boundary at No. 8+700 was used to calculate the outflow of wind-blown sand.

Between No. 8+700 and No. 9, the backshore is partly occupied by artificial structures such as parking lots; therefore, only the sand transport (not volumetric change) was considered in that section. In the offshore area, following Sato et al. (2018)Sato et al. [2018], the alongshore littoral drift was assumed to be 53,000 m^3/year, flowing from east to west across the domain.

The topographic changes were calculated separately for three elevation-based zones:

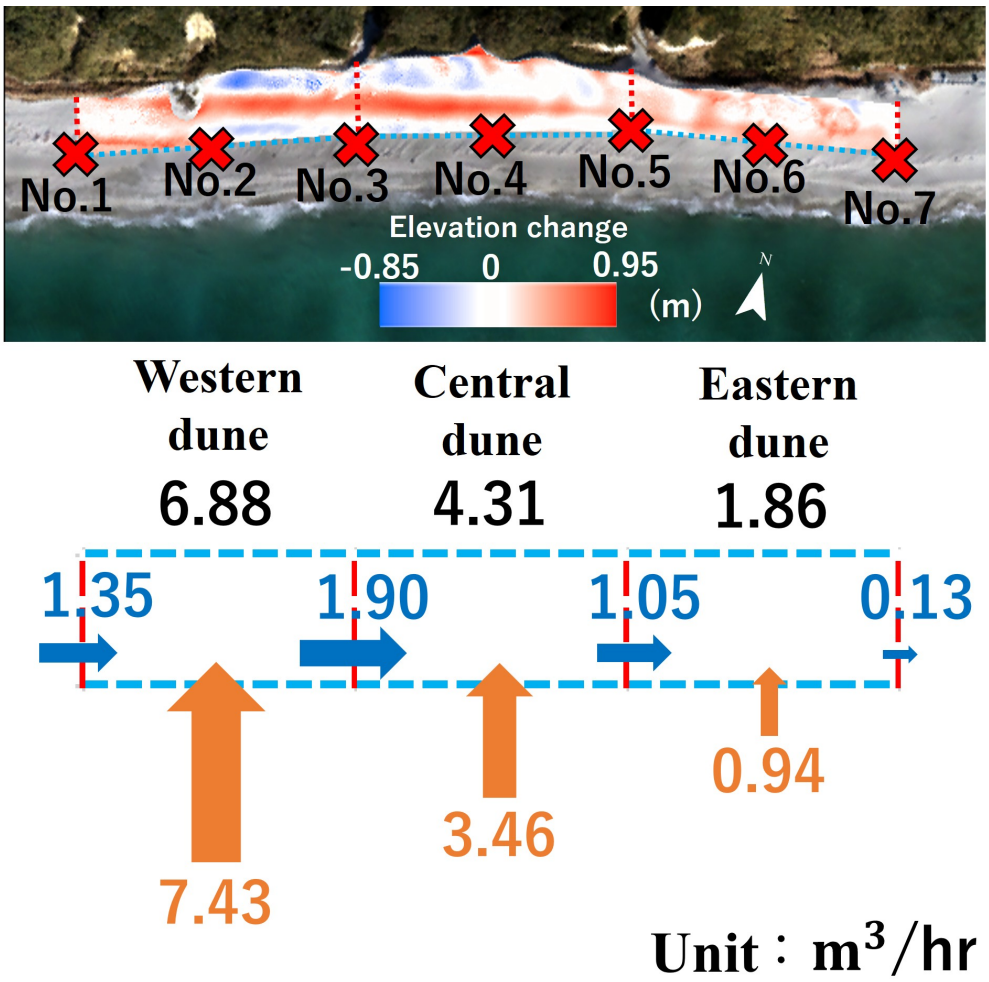

Figure 6.3: Topographic change and sediment budget diagram

1. Dune zone: elevations above T.P. +3 m,
2. Beach zone: elevations between T.P. 0–3 m,
3. Submarine zone: elevations between T.P. −7–0 m, corresponding to the approximate depth of the submerged breakwaters.

An increase in sediment volume was treated as positive, and a decrease as negative. Because the datasets for 2017 and 2018 were combined, the annual mean rate of volume change was calculated as the difference between 2017 (or 2018) and 2020, divided by the number of elapsed years.

6.4.1 Components of Aeolian Sand Transport

Wind-blown sand flux was divided into three main components:

1. Onshore–offshore (cross-shore) transport
2. Alongshore transport on the dune surface
3. Alongshore transport on the beach

The alongshore and cross-shore components of aeolian sand transport were estimated based on the observations. The calculated aeolian fluxes were decomposed as follows:

1. alongshore sand flux on the beach was obtained by multiplying the flux density by the average beach width, and
2. cross-shore sand flux by multiplying the flux density by the cross-shore width between measurement lines (approximately 100 m).

The beach width was defined as the average distance between the T.P. 0 m and +3 m contours for two consecutive survey years. The number of active sand-transport days was assumed to be 95 days per year, with an effective transport duration of 12 hours per day.

The coordinate system was defined as eastward and northward positive, and westward and southward negative. The littoral drift, wave-induced beach sediment change, and alongshore aeolian flux over the dune were computed from sediment-balance equations. In this convention, westward littoral drift was defined as positive, eastward as negative. Deposition on the beach was treated as positive and erosion as negative. Similarly, alongshore aeolian flux over the dune was defined as positive eastward and negative westward.

Four calculation cases were considered, as shown in Fig. 6.5 and in Fig. 6.6. The cases consist of: (1) Deposition on both beach and submarine zones including dune sediment, (2) Deposition on both beach and submarine zones excluding dune sediment, (3) Erosion on both beach and submarine zones including dune sediment, (4) Erosion on both beach and submarine zones excluding dune sediment.

6.4.2 Case (1): Deposition on both beach and submarine zones including dune sediment

This case corresponds to the period 2017(2018)–2020, during which depositional trends were observed across all three zones.

During this period:

1. Dune volume increased by approximately 14,000 m^3/year,
2. Beach volume increased by about 3,700 m^3/year, and
3. Submarine sediment volume increased by around 12,000 m^3/year.

The calculation procedure was as follows:

1. The alongshore aeolian flux over the dune was calculated using the dune-volume change and cross-shore aeolian flux.
2. Using the alongshore flux on the beach, the beach-volume change, and the cross-shore flux, the wave-induced sediment deposition (or erosion) on the beach was estimated.
3. Finally, the littoral drift was derived from the wave-induced beach sediment change and the submarine-volume change.

The results indicated that between 2017(2018) and 2020, approximately 21,000 m^3/year of sediment was transported westward as net littoral drift (Fig. 6.7 left side).

6.4.3 Case (2): Deposition on both beach and submarine zones excluding dune sediment

This case corresponds to the period 2017(2018)–2020, during which depositional trends were observed across all two zones.

During this period:

1. Beach volume increased by about 3,700 m³/year, and
2. Submarine sediment volume increased by around 12,000 m³/year.

The calculation procedure was as follows:

1. Using the alongshore flux on the beach, the beach-volume change, and the cross-shore flux, the wave-induced sediment deposition (or erosion) on the beach was estimated.
2. Finally, the littoral drift was derived from the wave-induced beach sediment change and the submarine-volume change.

The results showed that approximately 35,000 m³/year was transported westward as littoral drift (Fig. 6.8 left side).

6.4.4 Case (3): Erosion on both beach and submarine zones including dune sediment

This case corresponds to the period 2020–2022, when erosional tendencies were dominant.

During this period:

1. Dune volume increased by approximately 11,000 m³/year,
2. Beach volume decreased by about 1,700 m³/year, and
3. Submarine sediment volume decreased by around 38,000 m³/year.

The calculation procedure was identical to Case (1).

The results indicated that between 2020 and 2022, approximately 78,000 m³/year of sediment was transported westward as net littoral drift (Fig. 6.7 right side).

6.4.5 Case (4): Erosion on both beach and submarine zones excluding dune sediment

This case corresponds to the period 2020–2022, when erosional tendencies were dominant.

During this period:

1. Beach volume decreased by approximately 1,700 m³/year, and
2. Submarine sediment volume decreased by around 38,000 m³/year.

The calculation procedure was identical to Case (2).

The results showed that approximately 93,000 m³/year was transported westward as littoral drift (Fig. 6.8 right side).

6.4.6 Discussion of Integrated Sediment Budget Results

The sediment budget calculations for all cases, whether deposition or erosion dominated, consistently indicate that excluding dune sediment from the sediment budget leads to an overestimation of downdrift littoral sediment transport.

The magnitude of this overestimation is on the same order as the littoral sediment flux itself, demonstrating that dune-related sediment represents a substantial component of the coastal sediment system.

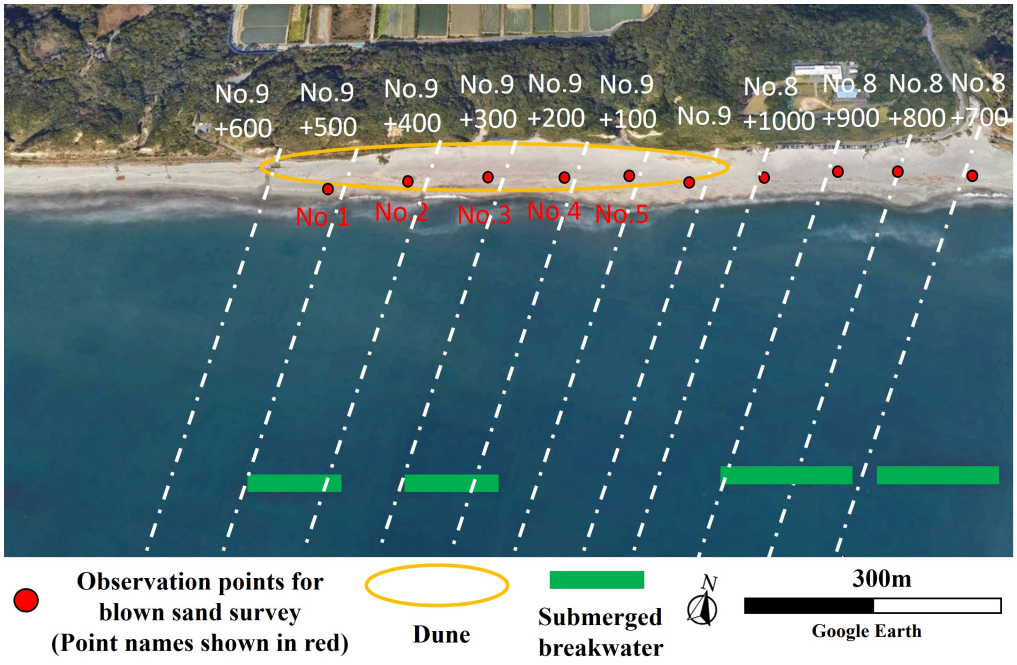

Figure 6.4: Locations of sand-trap observation points

Period when both the beach and seabed accreted

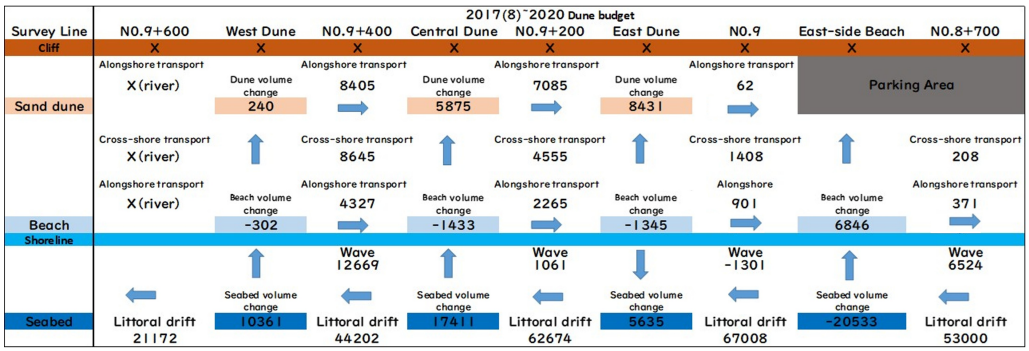

Period when both the beach and seabed eroded

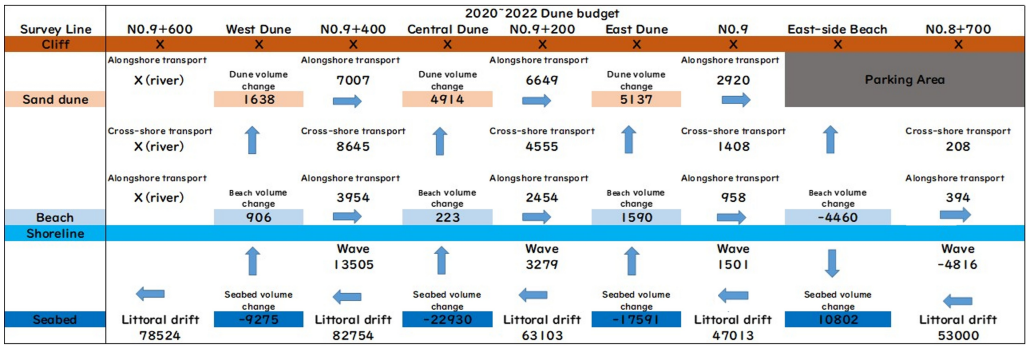

Including Dune

Figure 6.5: Conceptual diagram of sediment-transport calculation cases (Including Dune)

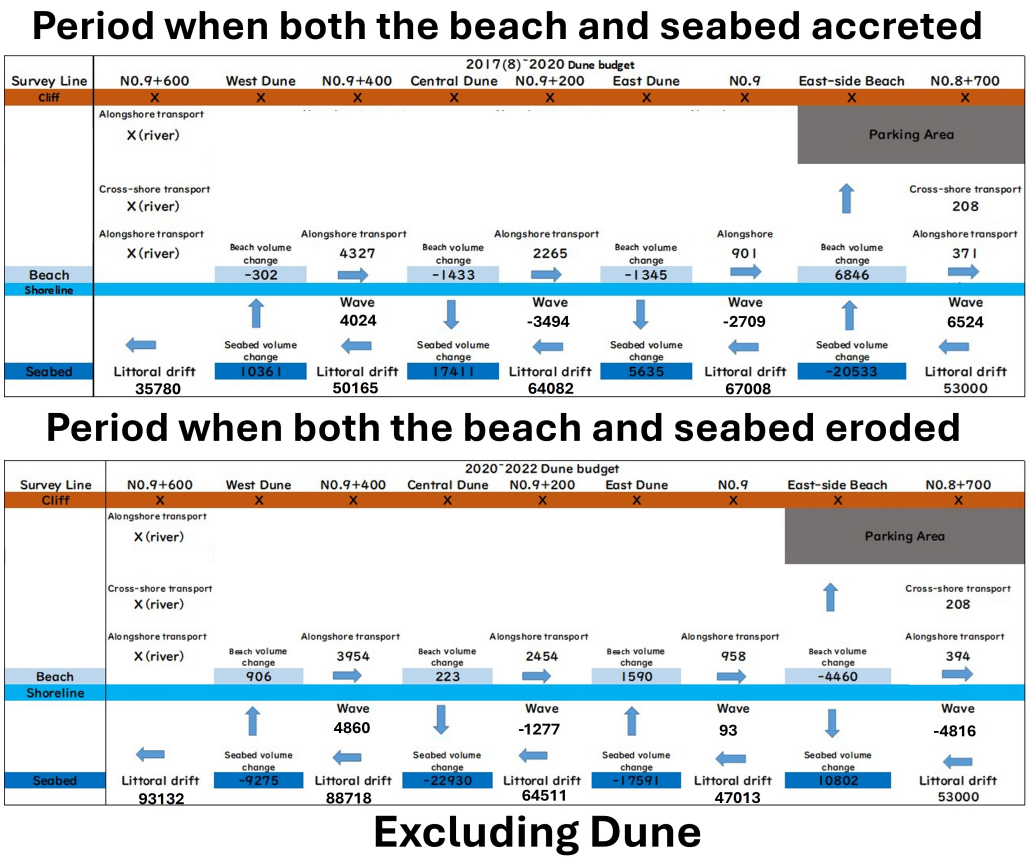

Figure 6.6: Conceptual diagram of sediment-transport calculation cases (Excluding Dune)

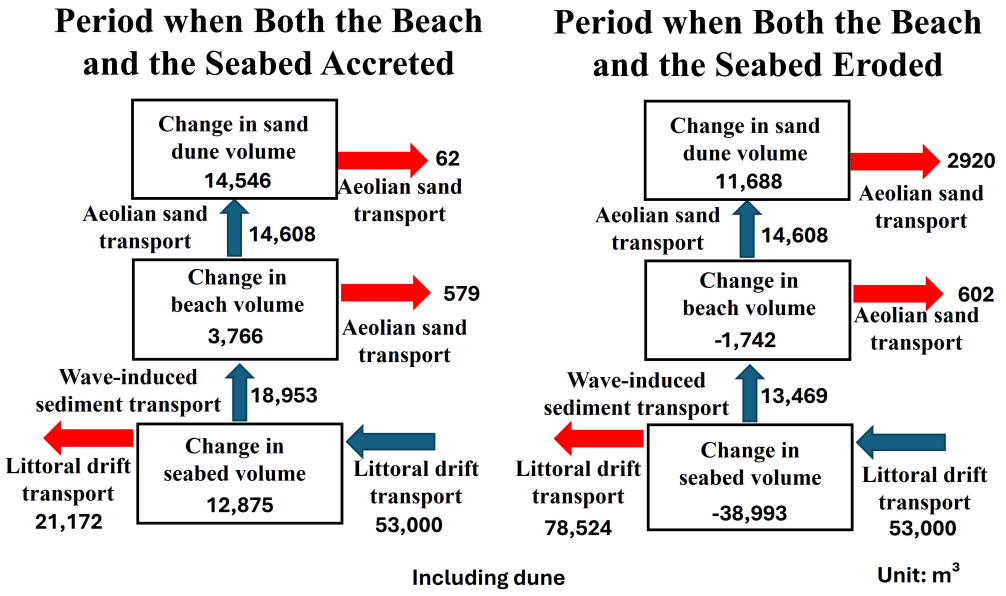

Figure 6.7: Calculated sediment fluxes (Including Dune)

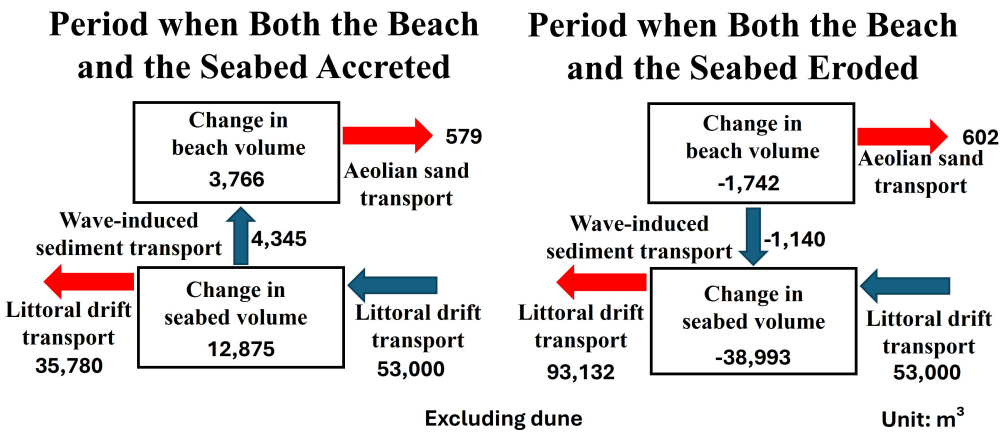

Figure 6.8: Calculated sediment fluxes (Excluding Dune)

Chapter 7

Conclusion and Future Work

7.1 Summary of Key Findings

This study investigated the formation mechanisms, wind characteristics, and sediment budget of coastal dunes along the Omotehama Coast, with a focus on the Ikobe dune system. By integrating field surveys, bathymetric datasets, wind observations, and CFD simulations, the following conclusions were drawn:

1. **Dune formation conditions.** The reappearance and growth of the Ikobe foredune after 2009 were driven by (i) sufficient sediment supply and beach width, (ii) available accommodation space in front of the cliff, and (iii) onshore-directed winds produced within a wake vortex generated by strong northwesterlies over the coastal cliff in winter.

2. **Wind dynamics.** Observations and numerical results consistently show a landward (reversed) flow below the cliff. This reverse flow is the dominant external driver of dune accretion, and its turning height near $\sim$20 m matches the former maximum dune crest, indicating a dynamic limit imposed by the wake structure.

3. **Aeolian–beach interaction.** During the winter monsoon, wind-blown sand transport is most active. Traps and wind situation reveal alongshore gradients controlled by local topography (cliff faces vs. valleys), while cross-shore flux decreases upslope from dune toe to crest.

4. **Sediment budget.** The integrated sediment budget demonstrates that excluding dune sediment from the analysis leads to an overestimation of downdrift littoral sediment transport, with the magnitude of this overestimation being on the same order as the littoral sediment flux itself.

5. **Management issue.** Although structural countermeasures improved beach width locally around Ikobe, the omission of terrestrial aeolian processes in existing management explains the persistence of erosion in the western sector.

7.2 Applicability and Implications for Sediment Management

Although this study focuses on the Omotehama Coast, the proposed framework and findings are not limited to this site. The dune–beach–nearshore system identified in this study represents a class of cliff-backed sandy coasts characterized by strong

sediment transport, seasonally dominant onshore winds, and limited accommodation space controlled by coastal cliffs.

Under such conditions, foredunes can function as dynamic sediment storage nodes that intercept aeolian sand supplied from the beach. Therefore, the mechanisms revealed here, particularly the role of wake-induced landward winds and the integration of aeolian transport into sediment budgets—are applicable to other cliff-backed dune coasts experiencing similar geomorphic and climatic settings.

Based on this broader applicability, the following implications for sediment management can be drawn. Terrestrial aeolian transport must be incorporated into the regional sediment management framework. Recognizing large foredunes as dynamic *storage nodes* in the littoral system will (1) improve evaluations of sand-retention effects, (2) inform adaptive design of submerged breakwaters, and (3) support coordinated objectives of shore protection. Management scenarios should explicitly account for dune growth phases and their feedback on sediment transport.

7.3 Limitations of This Study

Despite the comprehensive integration of field observations, numerical simulations, and sediment budget analysis, several limitations of this study should be acknowledged.

First, the temporal coverage of aeolian transport and wind observations remains limited relative to the long-term evolution of coastal dunes. Although multi-year topographic datasets were used to quantify morphological changes, high-frequency wind and sand-flux measurements were not continuously available, restricting the assessment of interannual variability and extreme-event contributions.

Second, this study focused on a single cliff-backed dune system along the Omotehama Coast. While the Ikobe dune provides a representative example of strong dune–beach–nearshore coupling under winter monsoon conditions, spatial heterogeneity along the coast and differences in cliff geometry, sediment supply, and human interventions may influence the generality of the results.

Third, the numerical simulations employed time-averaged CFD configurations and simplified boundary conditions to resolve wake-induced airflow patterns. Dynamic feedbacks between evolving dune morphology, vegetation growth, and nearshore hydrodynamics were not explicitly modeled, which may affect long-term predictions of dune evolution and sediment.

Finally, the sediment-budget framework assumes partitioning of aeolian and littoral sediment fluxes based on available datasets and geometric thresholds. Uncertainties associated with bathymetric resolution, sediment sorting, and subsurface exchanges could influence quantitative estimates of sediment volumes, particularly in the nearshore zone.

These limitations highlight areas where further investigation is required and provide the basis for the future research directions outlined below.

7.4 Future Research Directions

To advance this work, we propose the following future research directions, corresponding to the limitations identified above.

1. **Long-term monitoring:** Continuous three-dimensional wind profiling and high-frequency aeolian-flux measurements are required to capture interannual variability and quantify the contributions of extreme events to dune growth and sediment.

2. **Spatial extension and comparative studies:** Application of the proposed dune–beach–nearshore framework to other cliff-backed sandy coasts with similar wind climates and sediment transport regimes would help evaluate the generality of the findings and identify site dependent controls.

3. **Coupled morphodynamic modelling with eco-geomorphic feedbacks:** Development of fully coupled CFD–morphodynamic models, incorporating vegetation growth and stabilization effects, is necessary to resolve dynamic feedbacks among airflow, dune evolution, and nearshore morphology.

4. **Refinement and validation of integrated sediment budgets:** Expansion of the sediment-budget domain and scenario-based analyses are needed to reduce uncertainties in aeolian–littoral sediment partitioning and to assess cumulative down-drift impacts under different management strategies.

This integrated perspective strengthens the scientific basis for nature-inclusive, adaptive coastal management on the Omotehama Coast and other cliff-backed dune coasts worldwide.

Appendix

DSM Figures

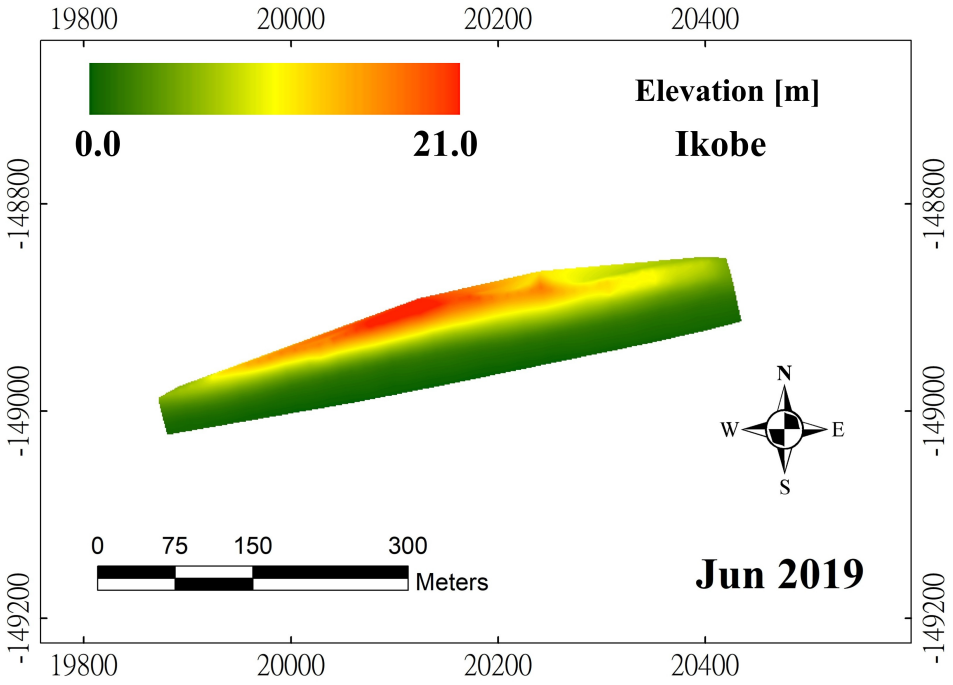

Figure 1: Ikobe DSM 201906

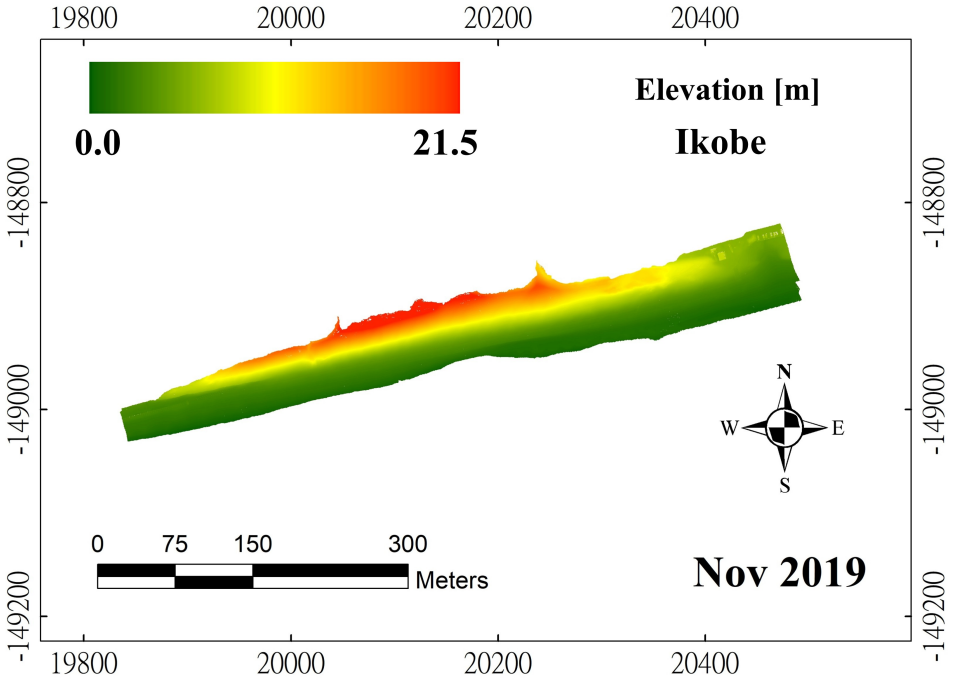

Figure 2: Ikobe DSM 201911

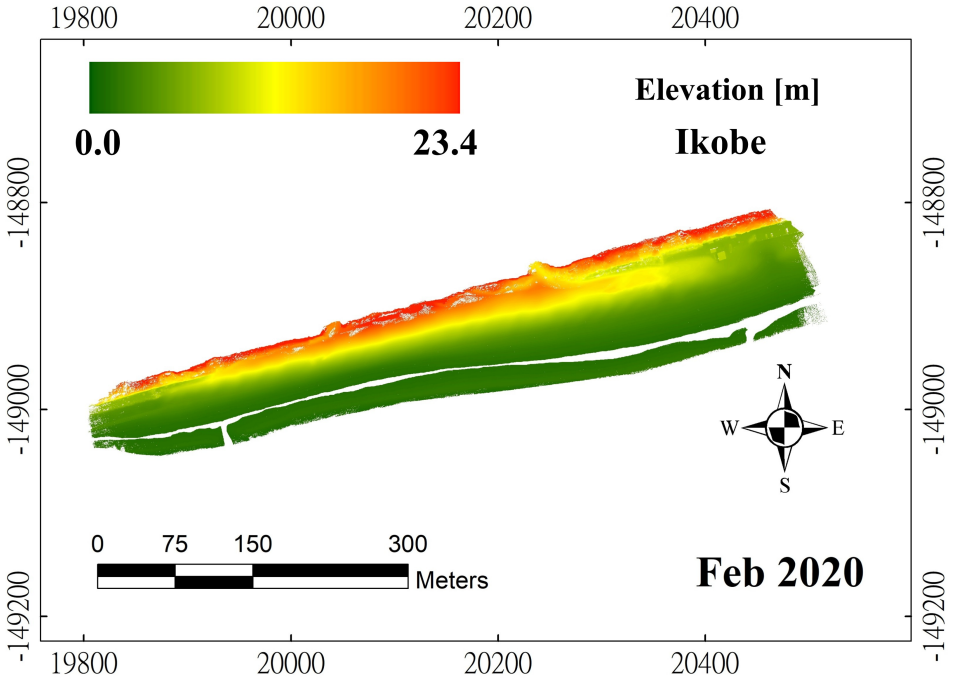

Figure 3: Ikobe DSM 202002

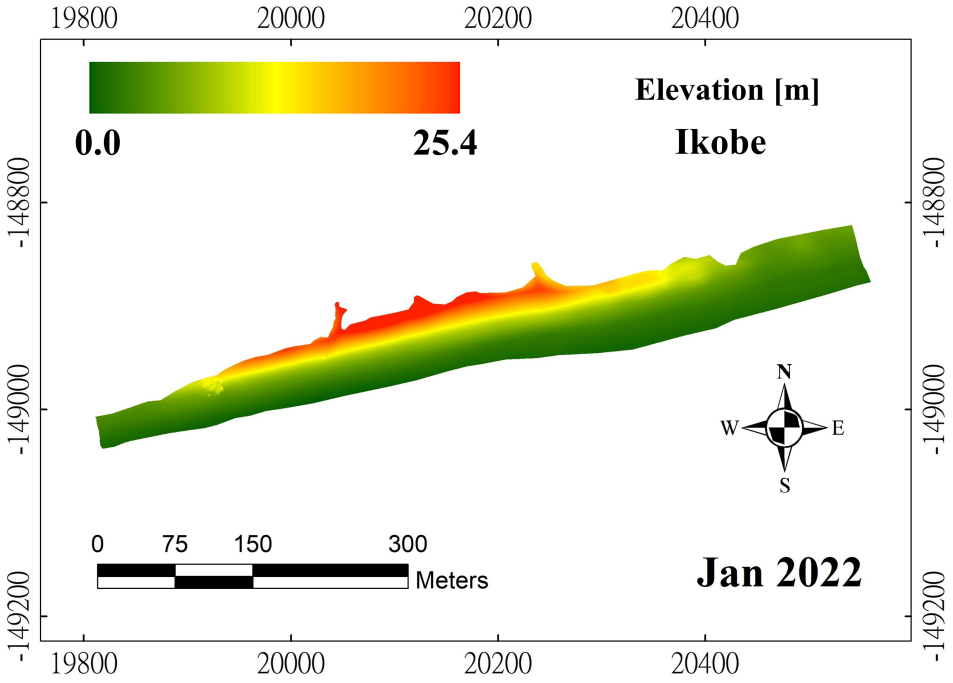

Figure 4: Ikobe DSM 202201

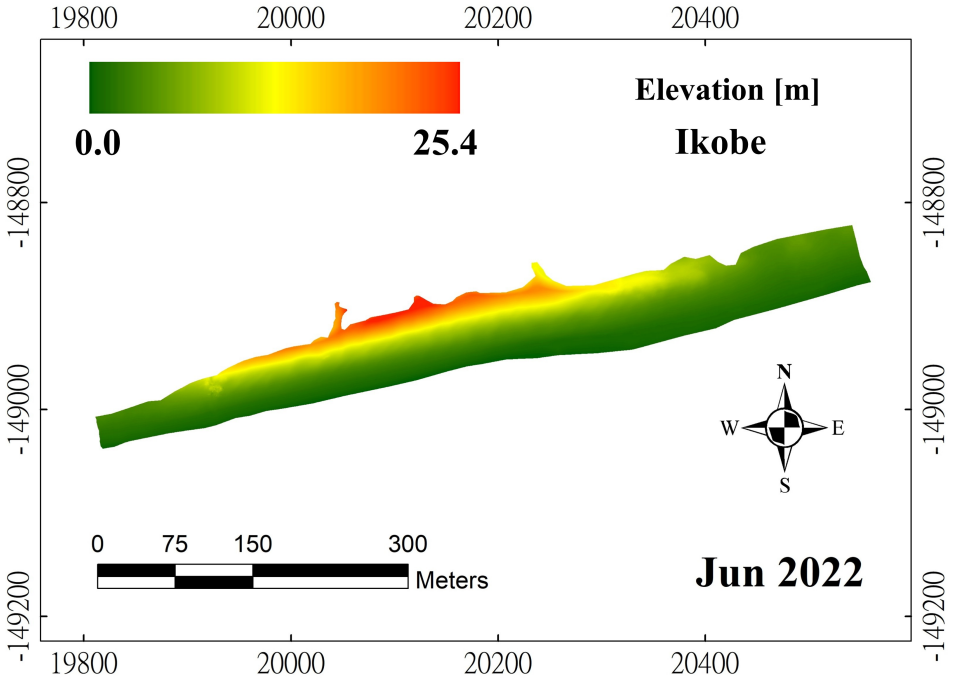

Figure 5: Ikobe DSM 202206

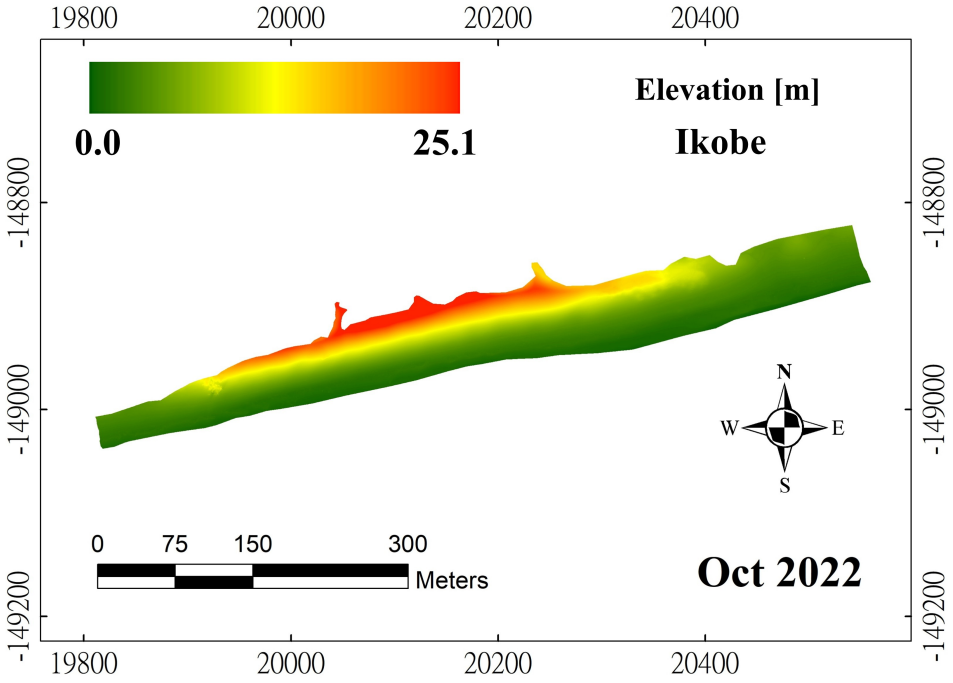

Figure 6: Ikobe DSM 202210

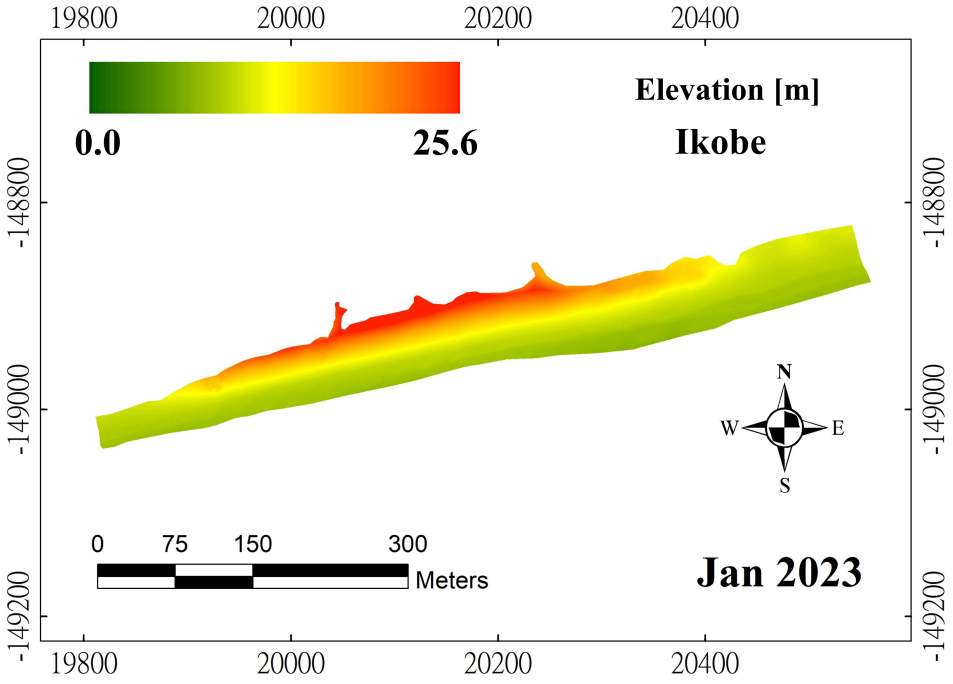

Figure 7: Ikobe DSM 202301

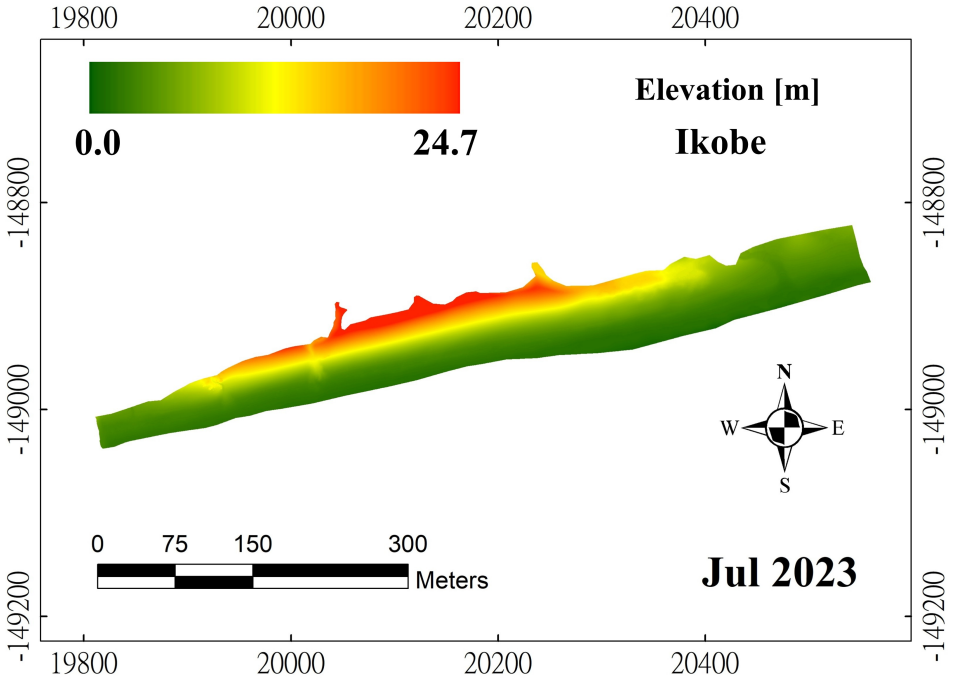

Figure 8: Ikobe DSM 202307

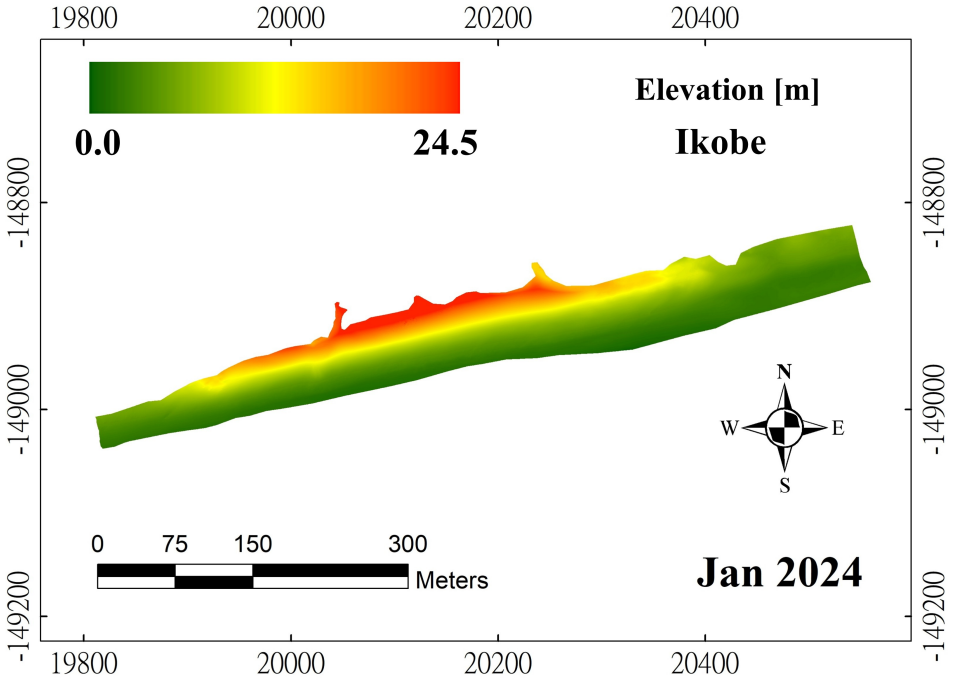

Figure 9: Ikobe DSM 202401

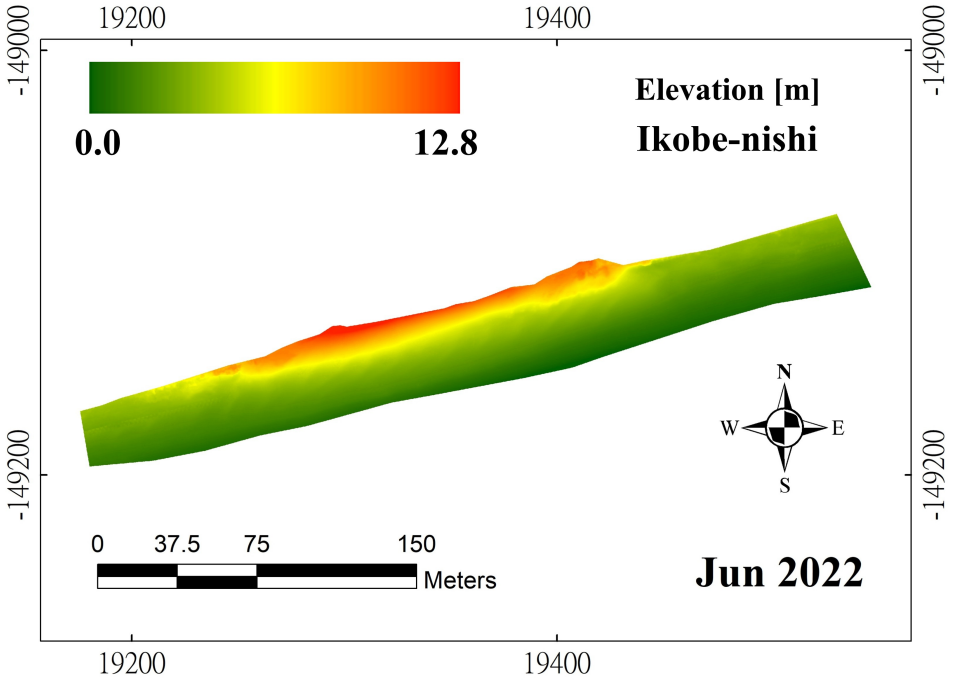

Figure 10: Ikobe-nishi DSM 202206

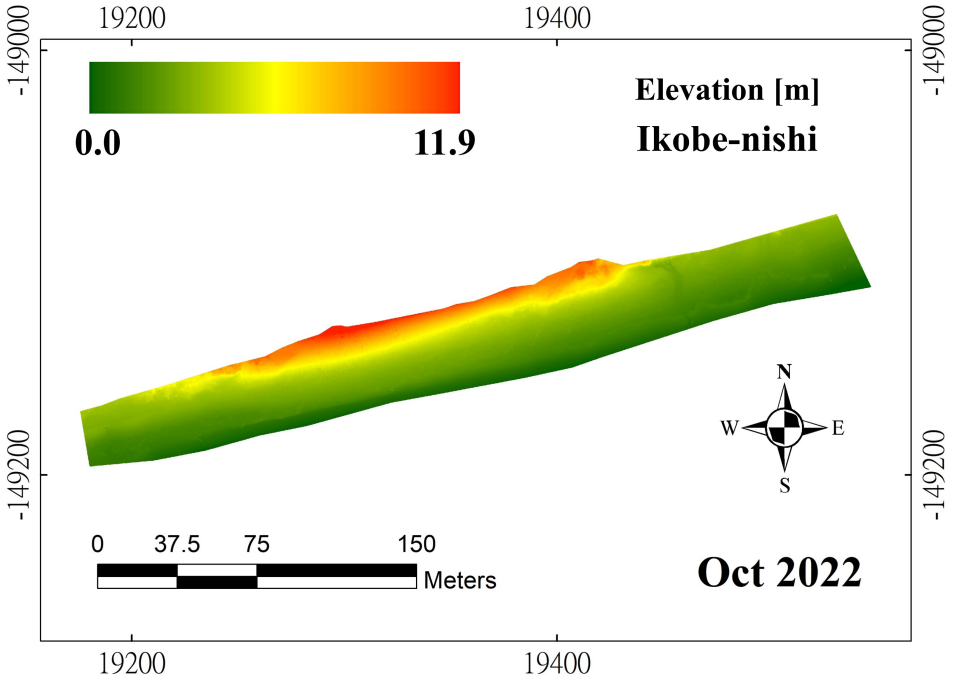

Figure 11: Ikobe-nishi DSM 202210

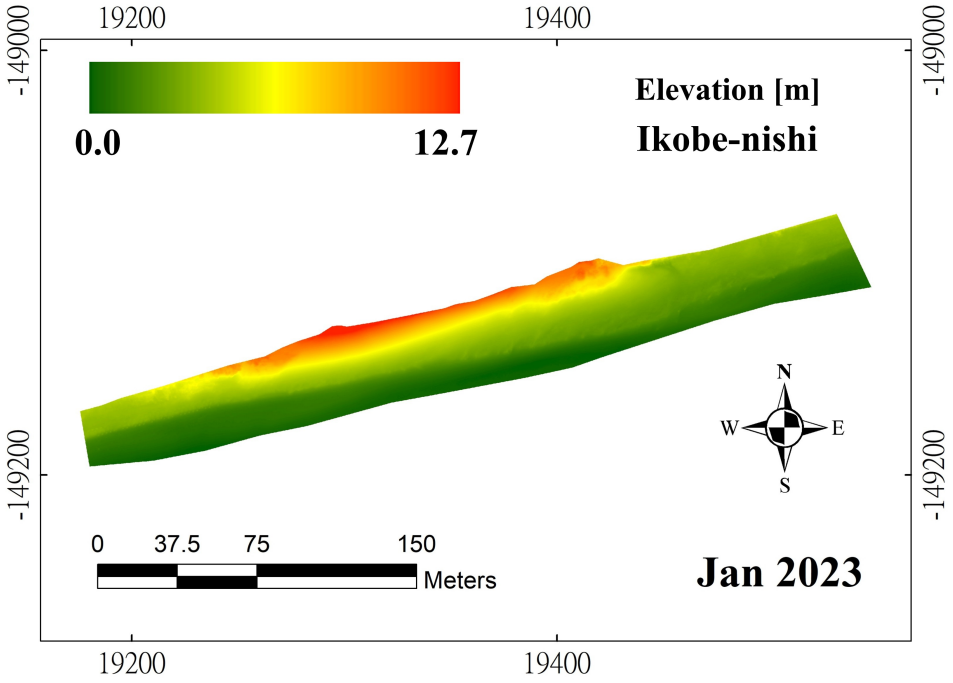

Figure 12: Ikobe-nishi DSM 202301

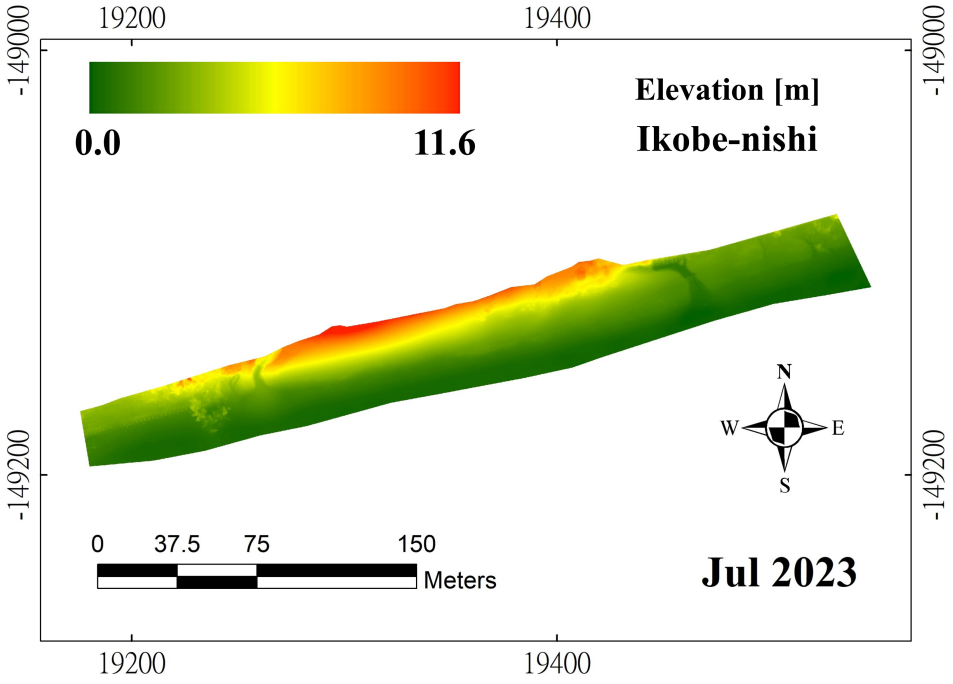

Figure 13: Ikobe-nishi DSM 202307

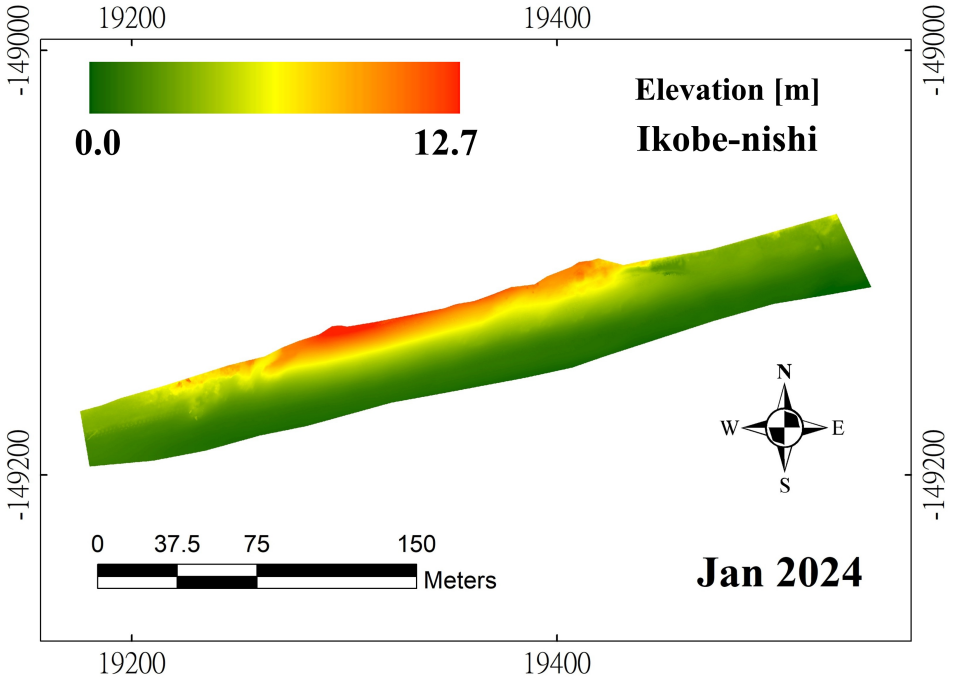

Figure 14: Ikobe-nishi DSM 202401

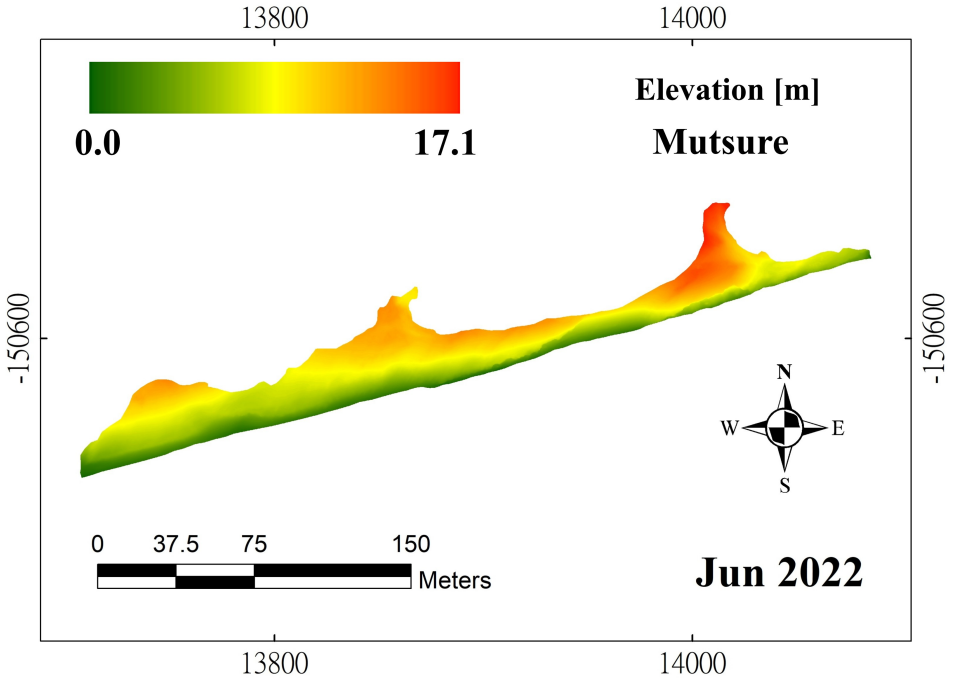

Figure 15: Mutsure DSM 202206

Orthophoto Figures

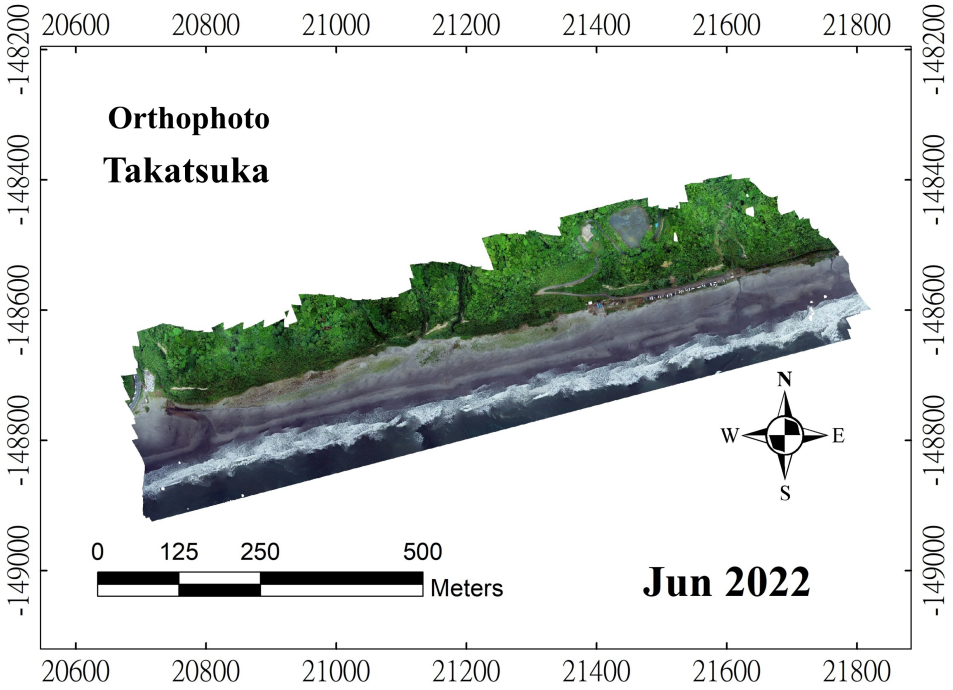

Figure 16: Takatsuka Orthophoto 202206

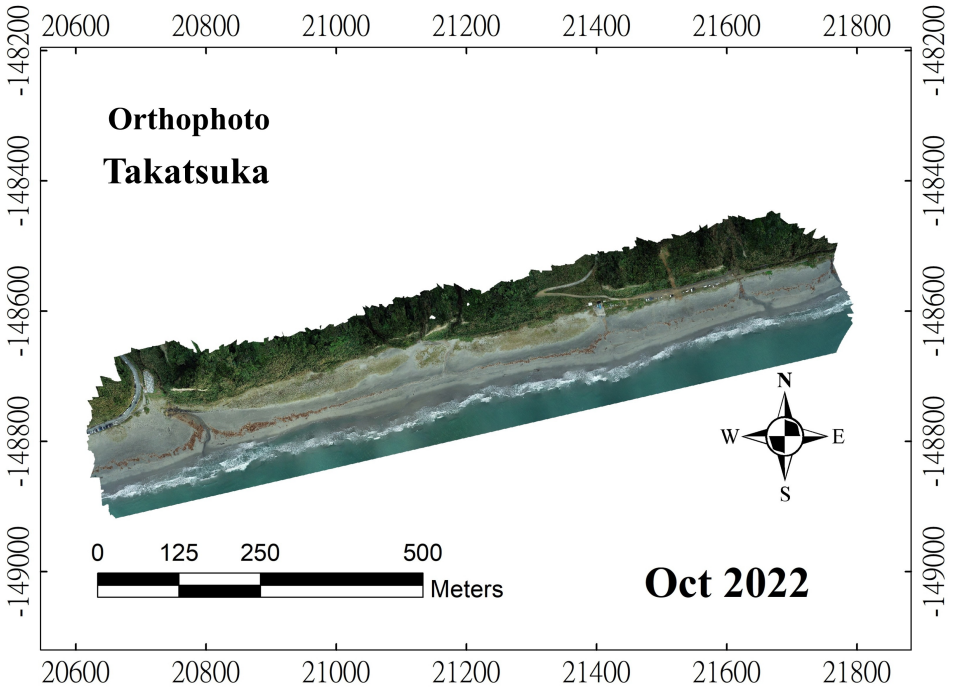

Figure 17: Takatsuka Orthophoto 202210

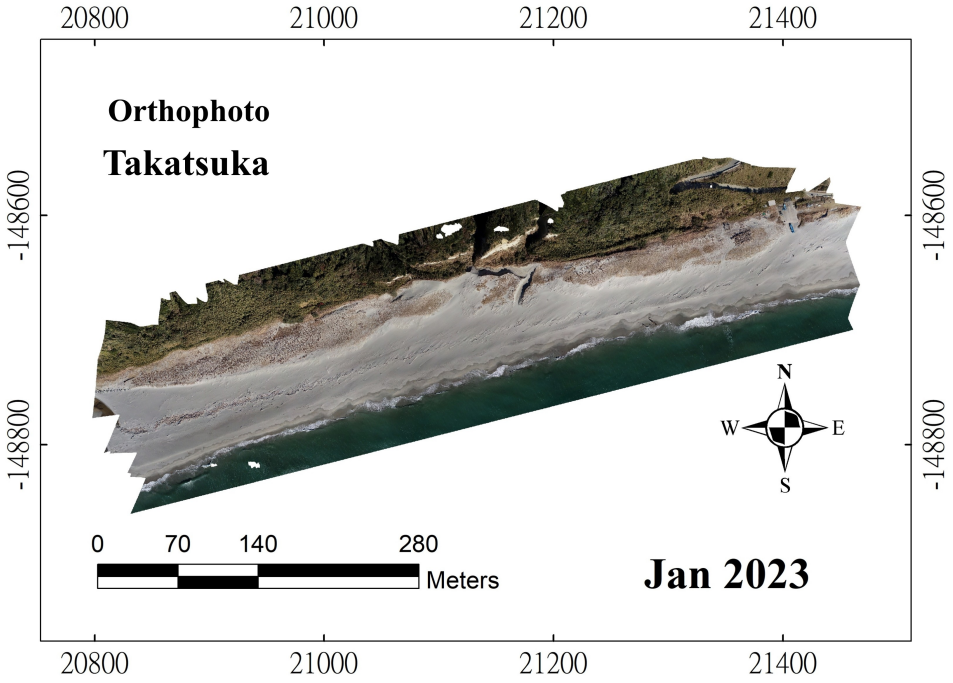

Figure 18: Takatsuka Orthophoto 202301

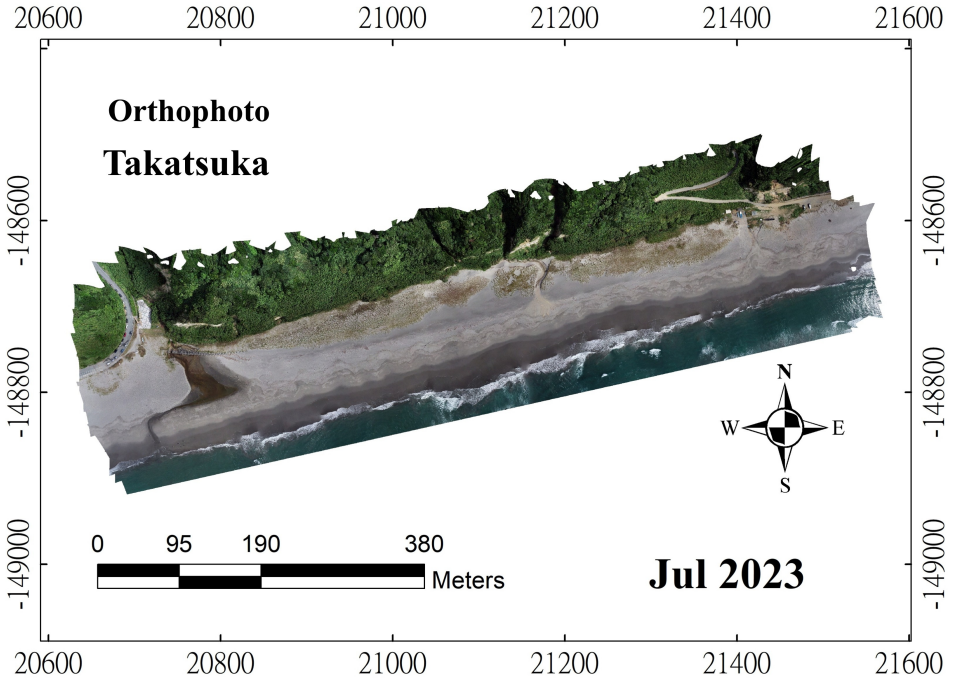

Figure 19: Takatsuka Orthophoto 202307

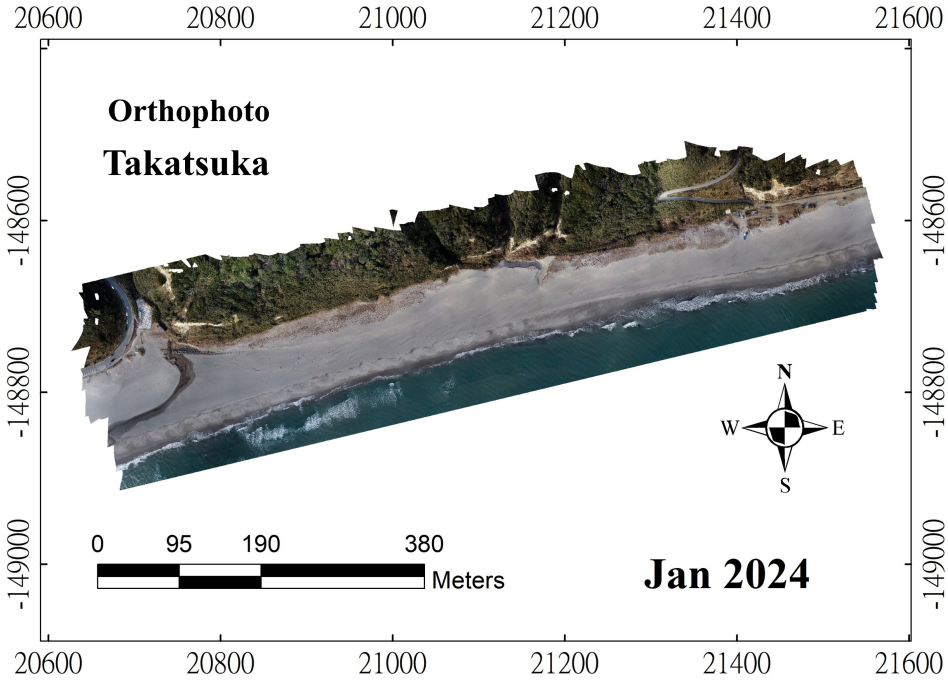

Figure 20: Takatsuka Orthophoto 202401

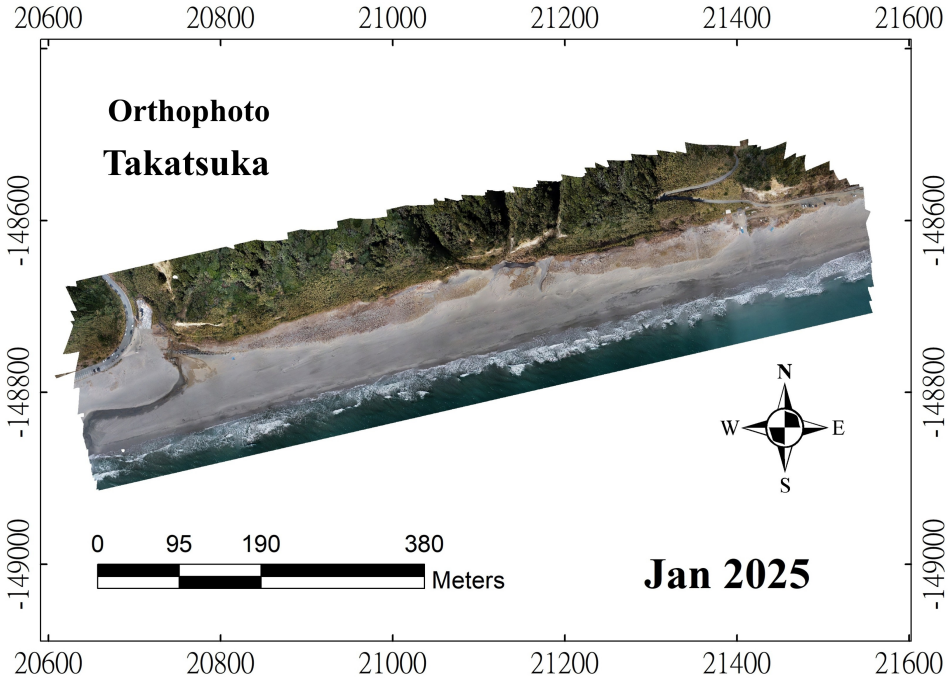

Figure 21: Takatsuka Orthophoto 202501

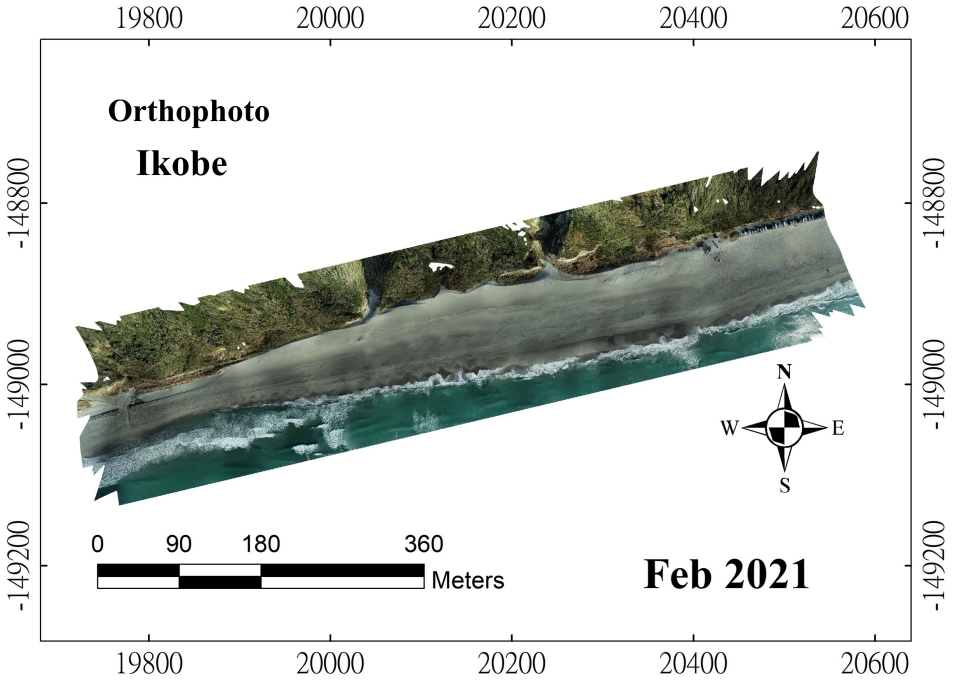

Figure 22: Ikobe Orthophoto 202102

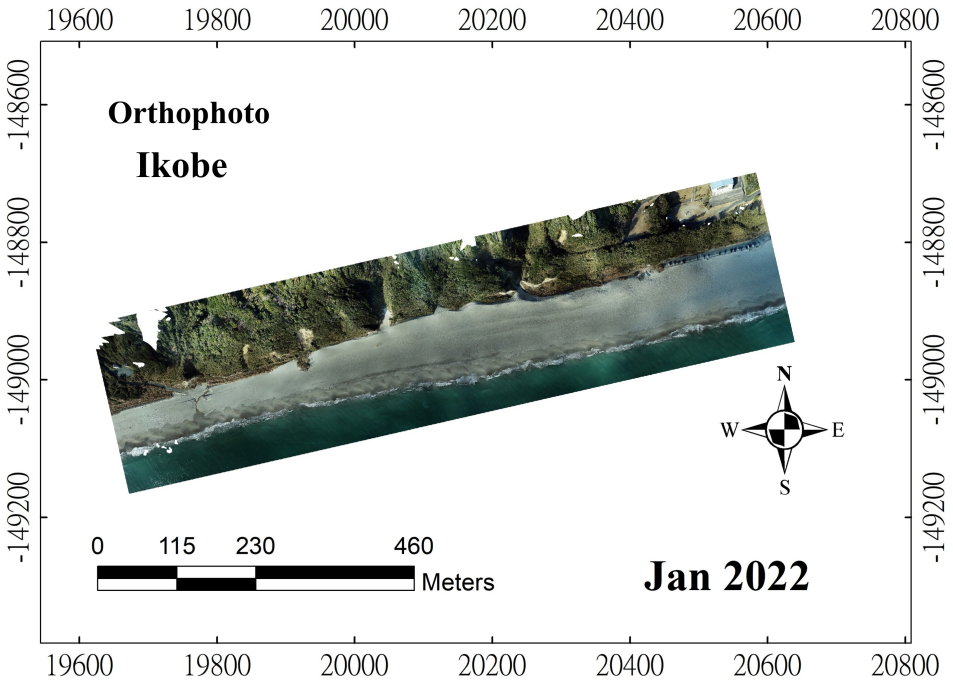

Figure 23: Ikobe Orthophoto 202201

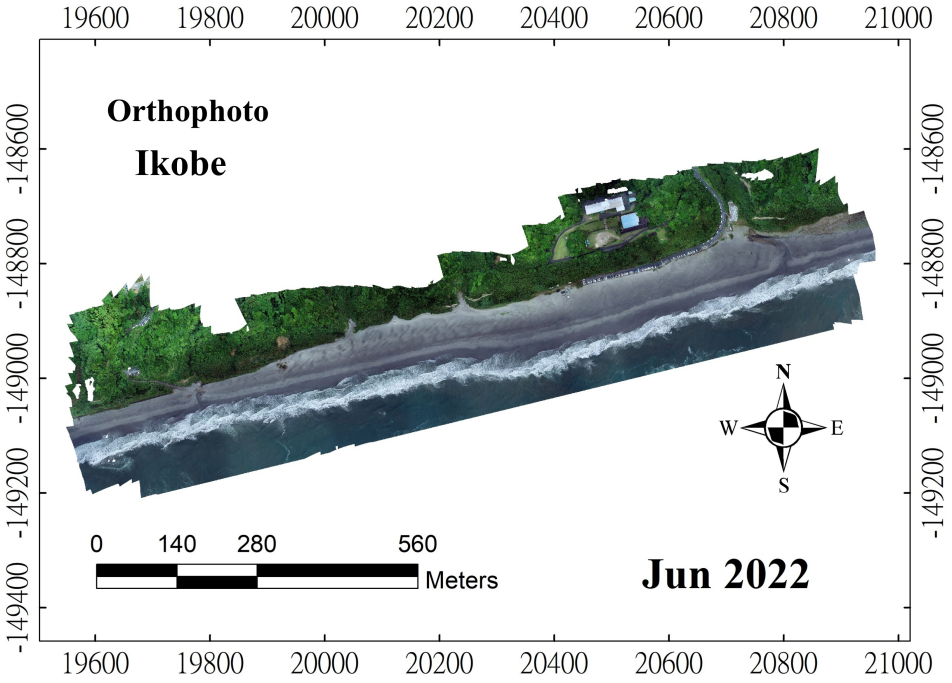

Figure 24: Ikobe Orthophoto 202206

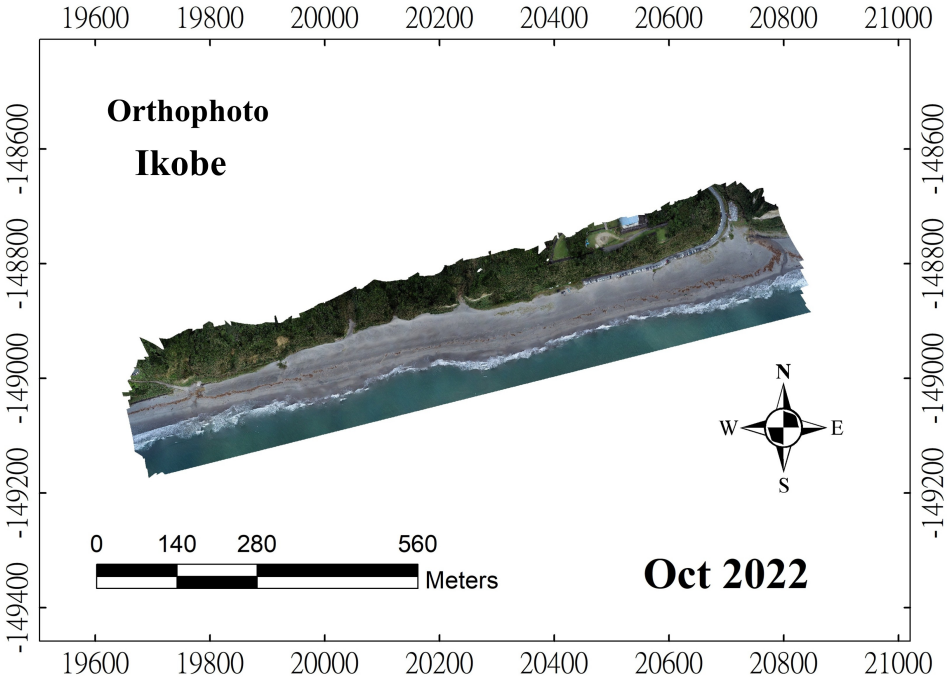

Figure 25: Ikobe Orthophoto 202210

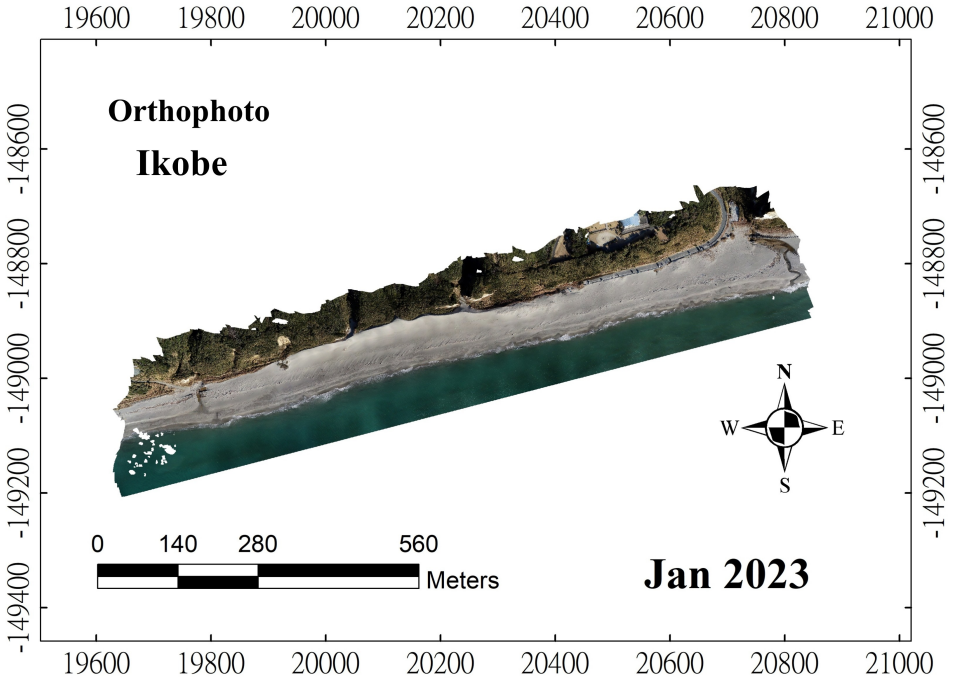

Figure 26: Ikobe Orthophoto 202301

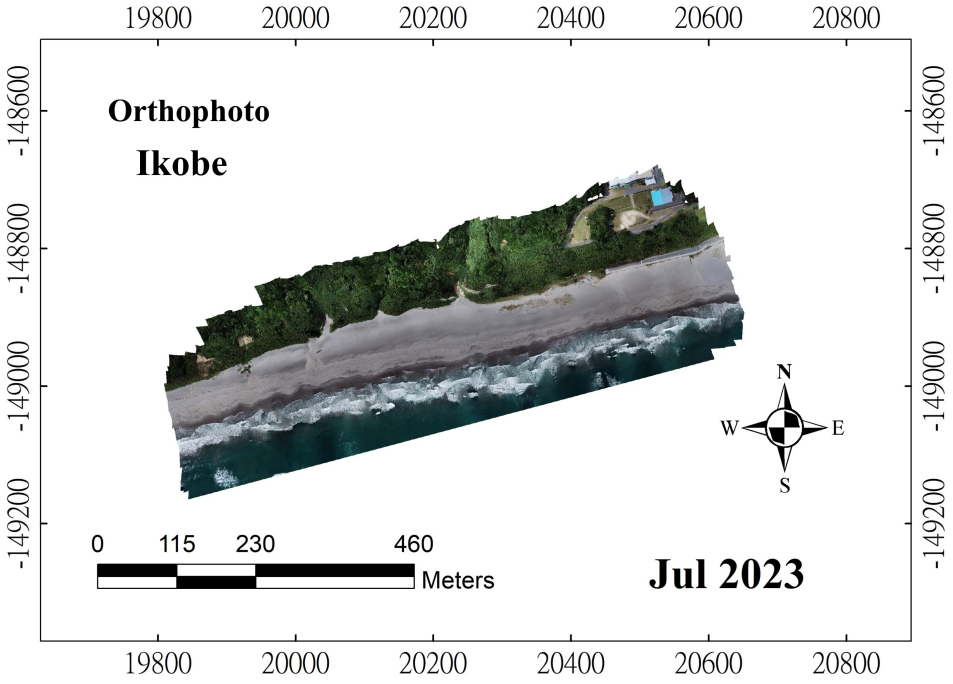

Figure 27: Ikobe Orthophoto 202307

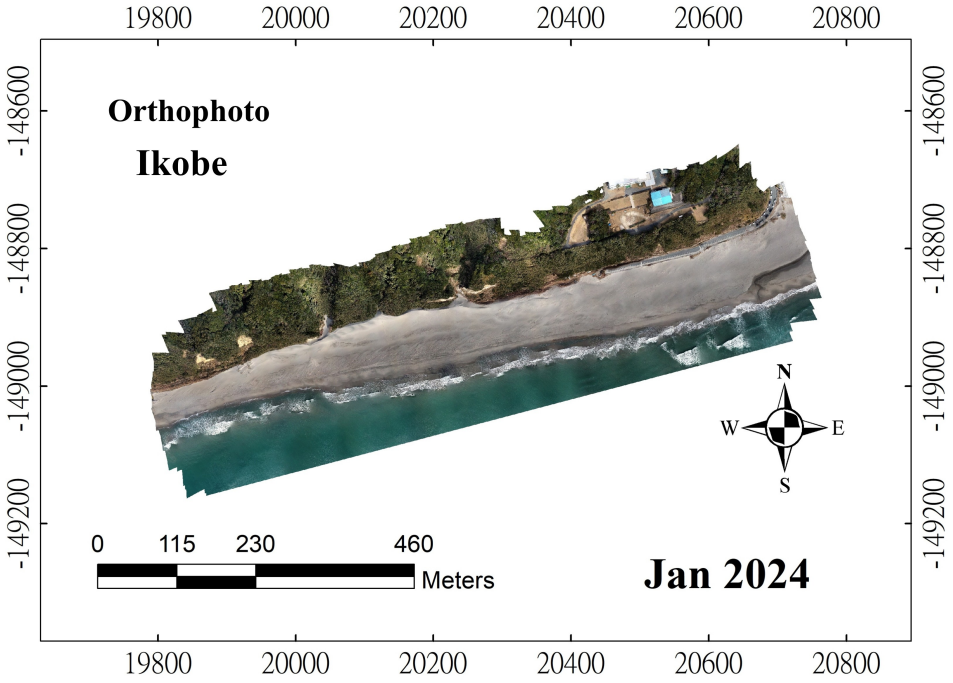

Figure 28: Ikobe Orthophoto 202401

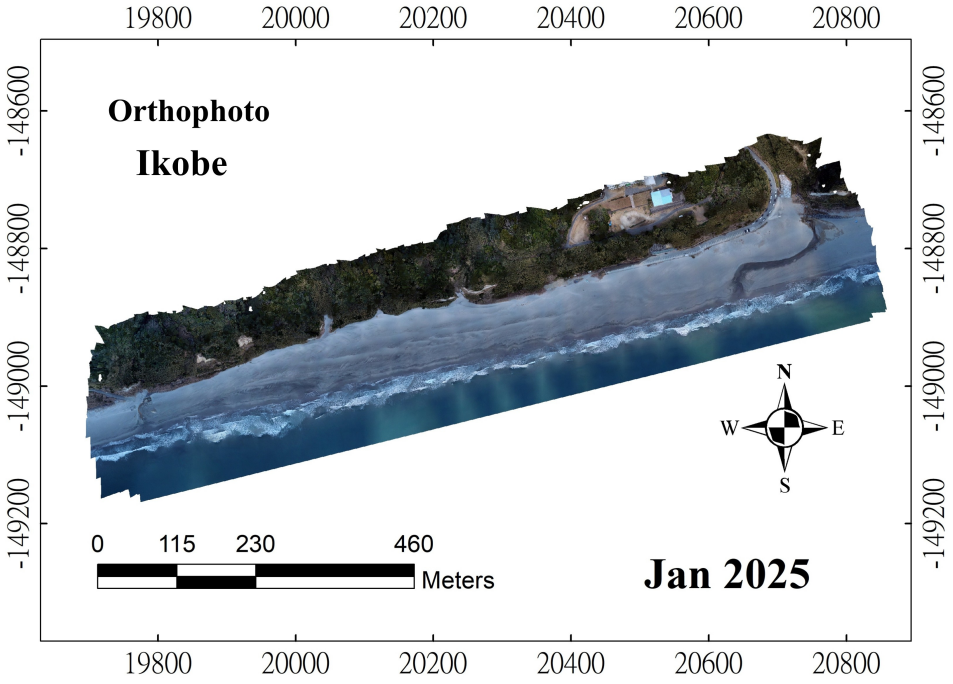

Figure 29: Ikobe Orthophoto 202501

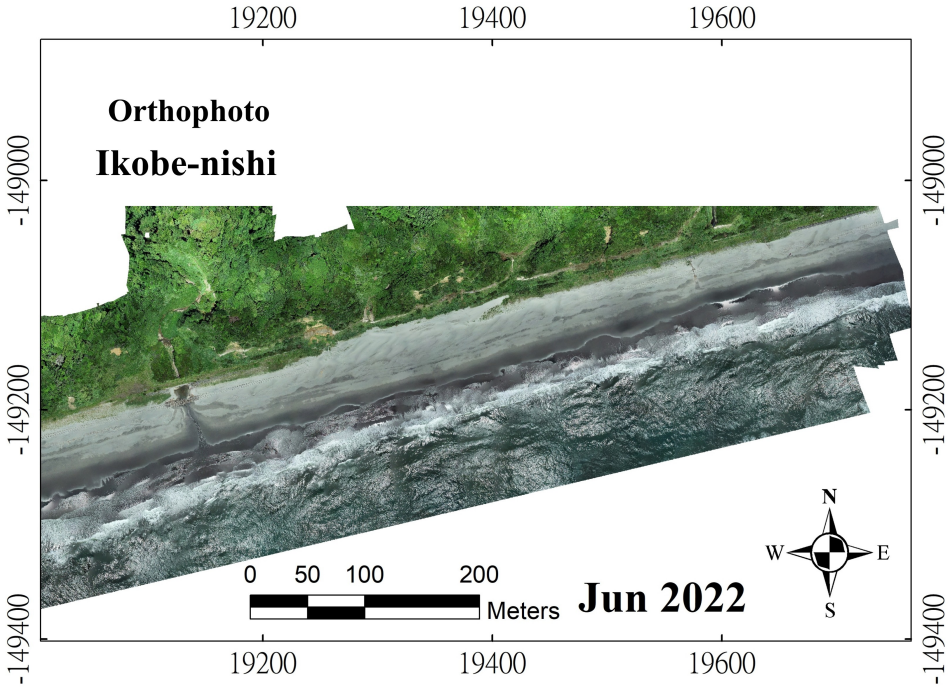

Figure 30: Ikobe-nishi Orthophoto 202206

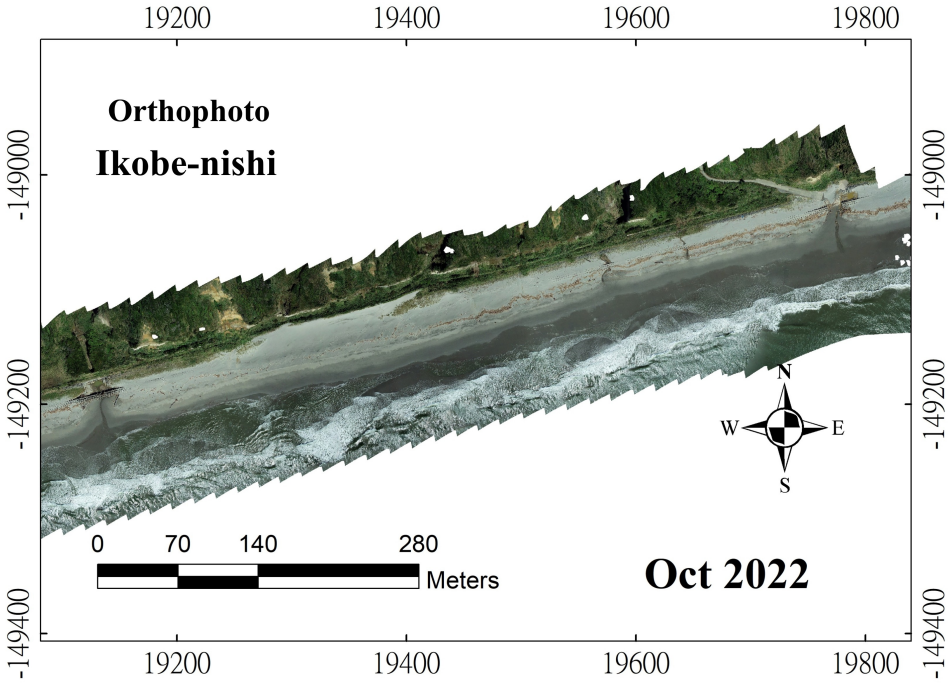

Figure 31: Ikobe-nishi Orthophoto 202210

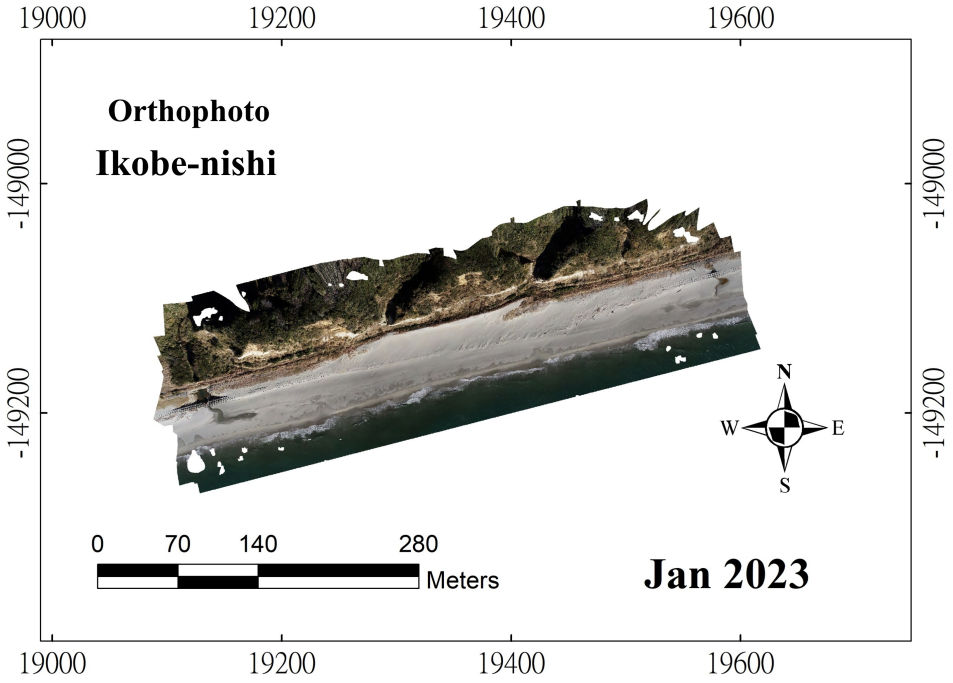

Figure 32: Ikobe-nishi Orthophoto 202301

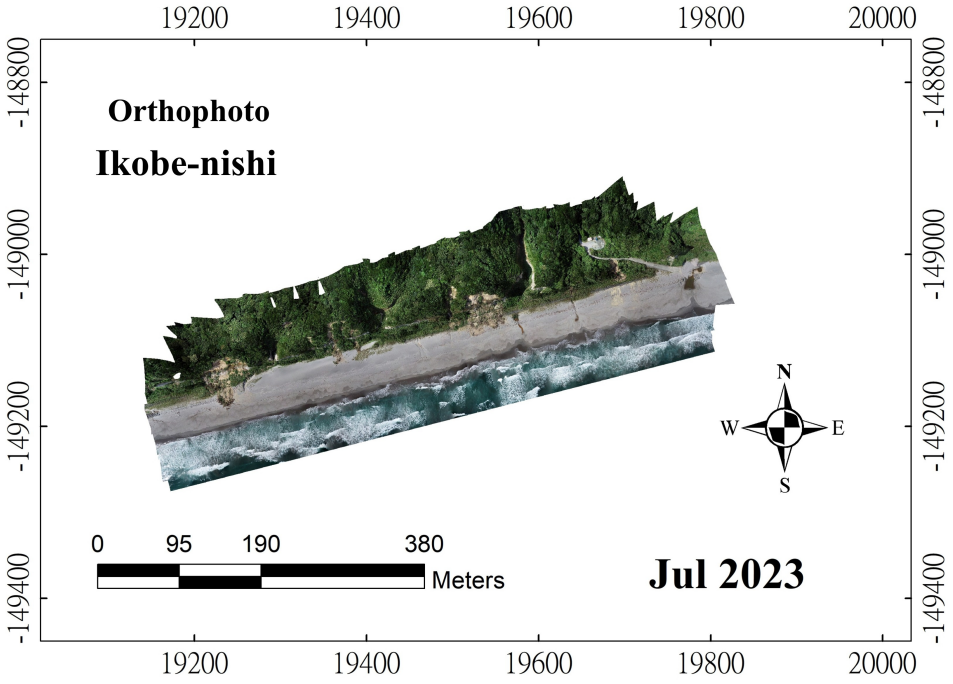

Figure 33: Ikobe-nishi Orthophoto 202307

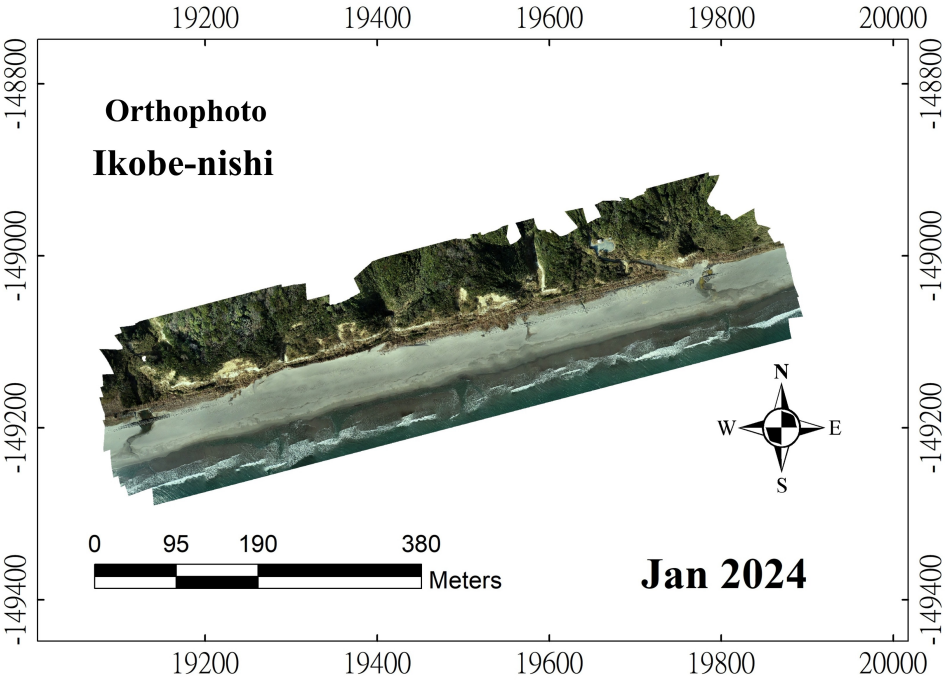

Figure 34: Ikobe-nishi Orthophoto 202401

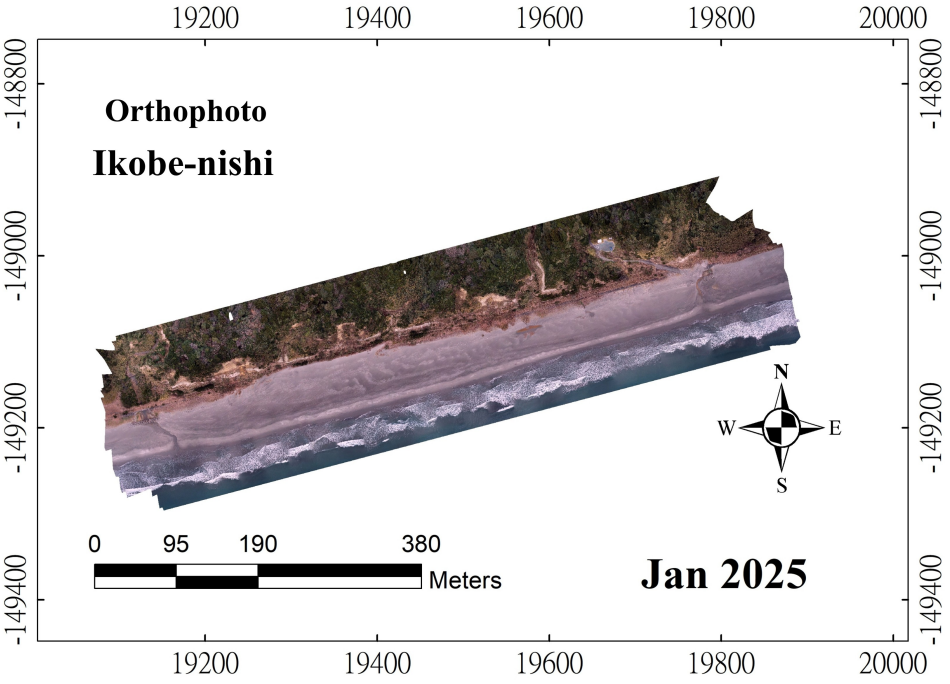

Figure 35: Ikobe-nishi Orthophoto 202501

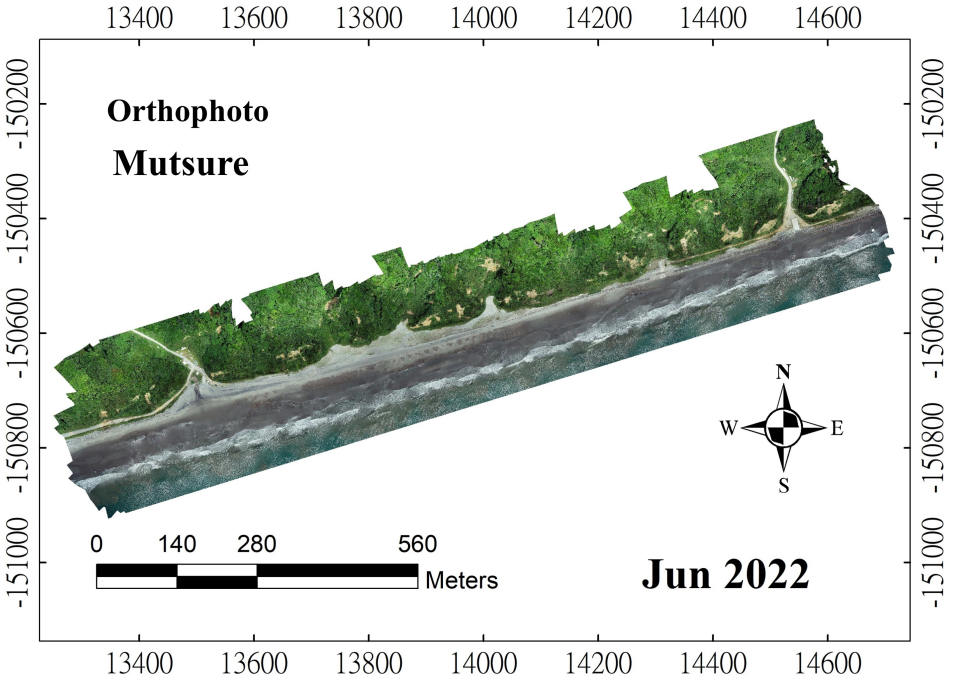

Figure 36: Mutsure Orthophoto 202206

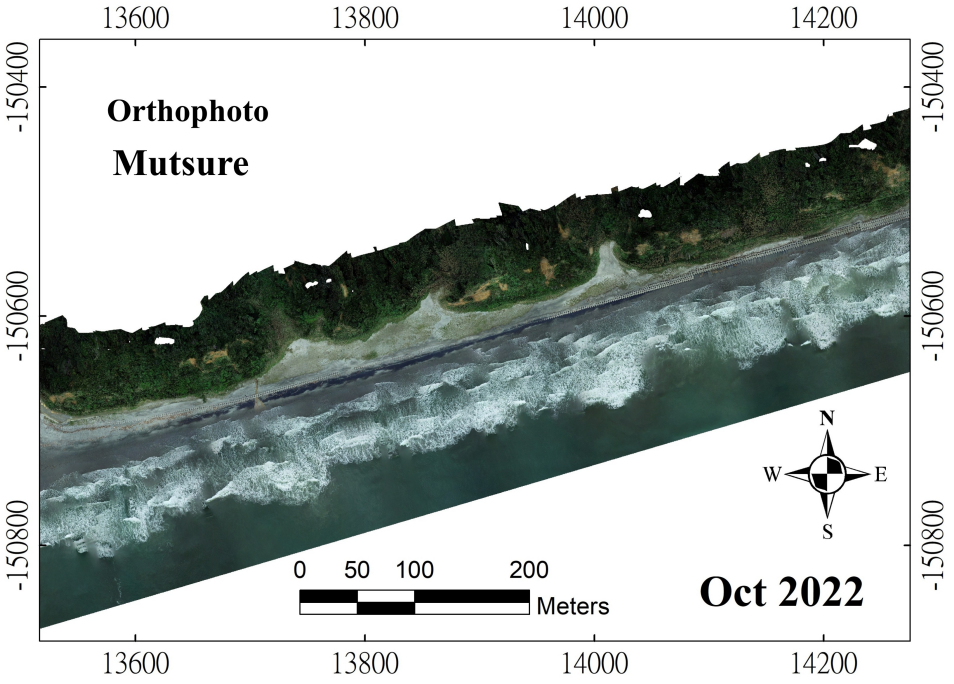

Figure 37: Mutsure Orthophoto 202210

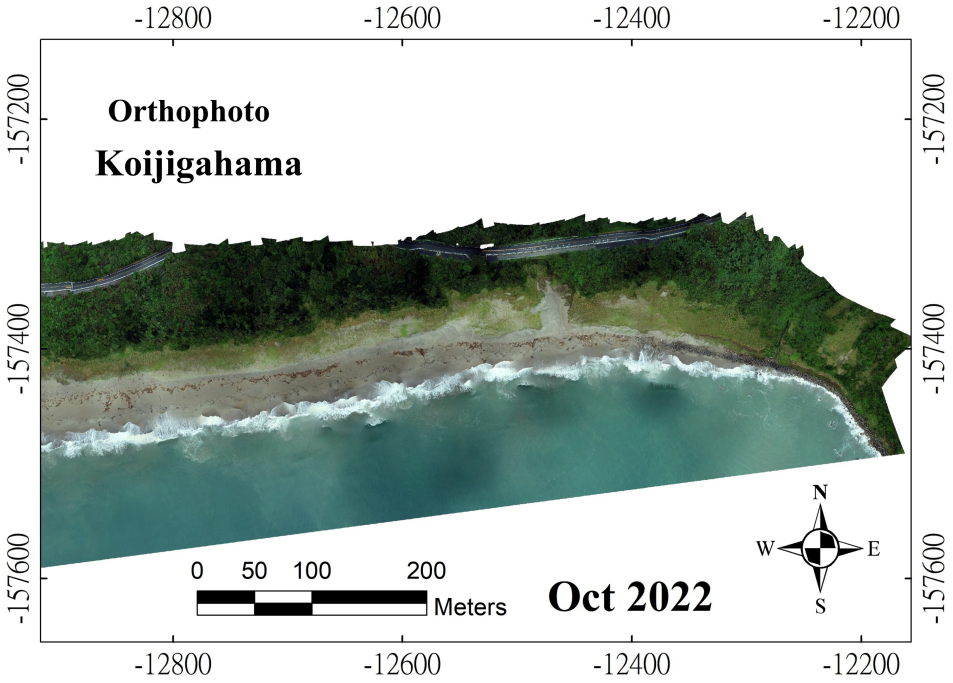

Figure 38: Koijigahama Orthophoto 202210

Elevation Change Figures

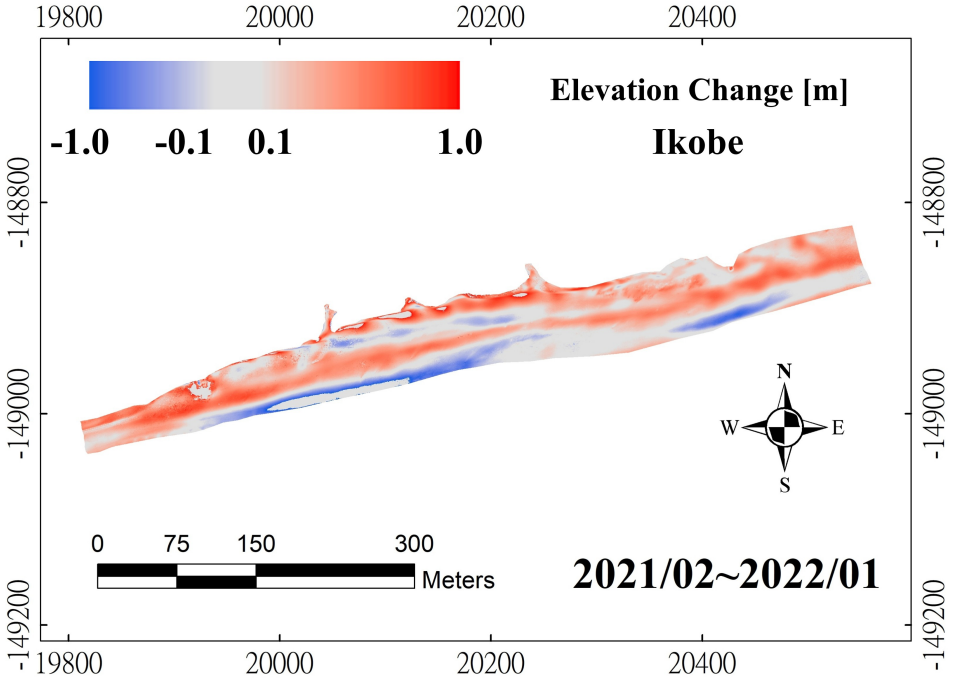

Figure 39: Ikobe Elevation Change 202102-202201

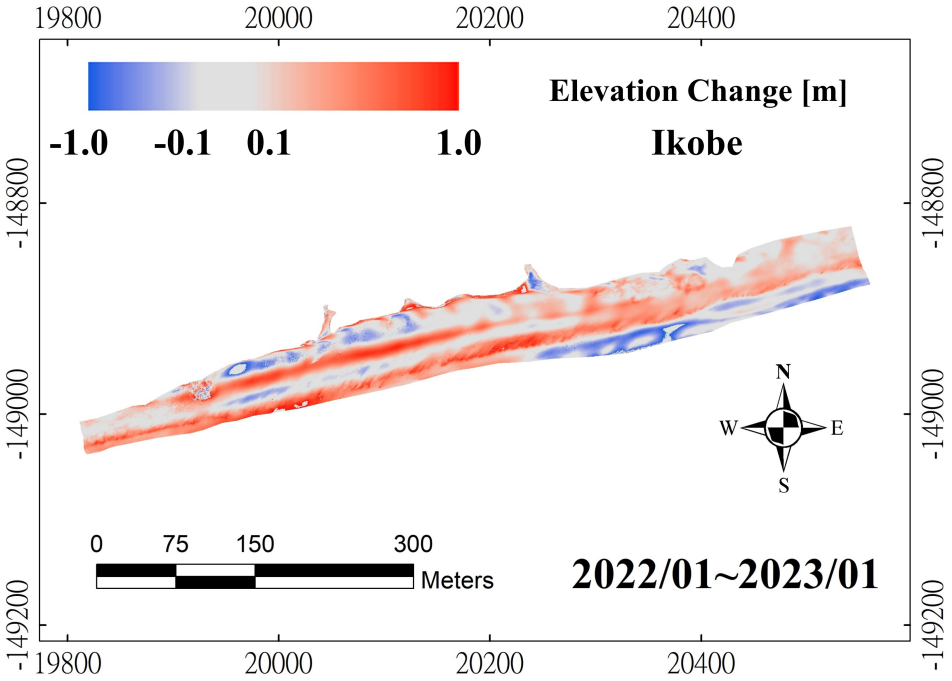

Figure 40: Ikobe Elevation Change 202201-202301

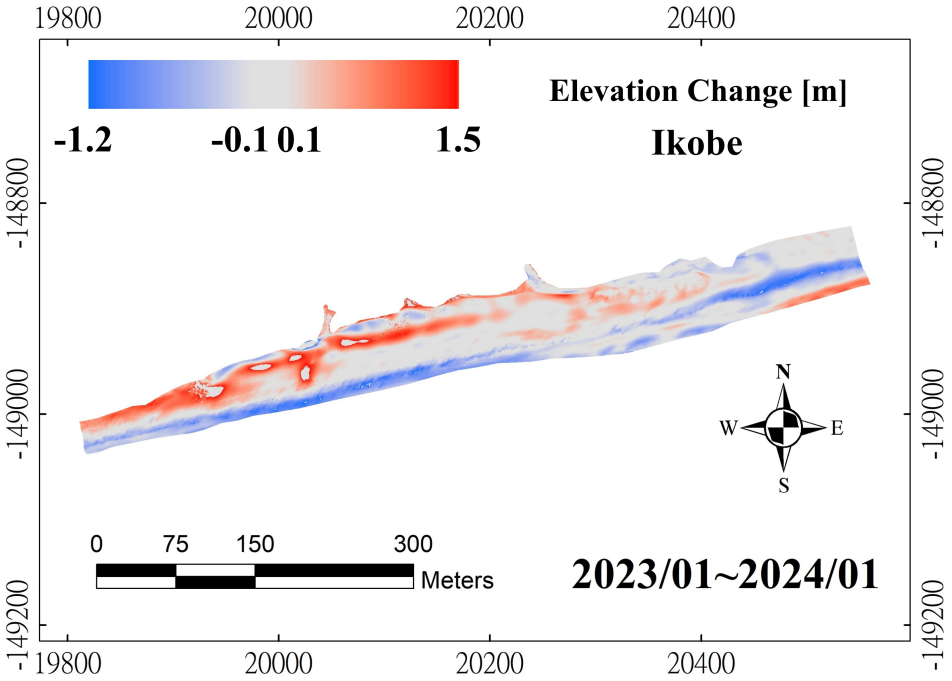

Figure 41: Ikobe Elevation Change 202301-202401

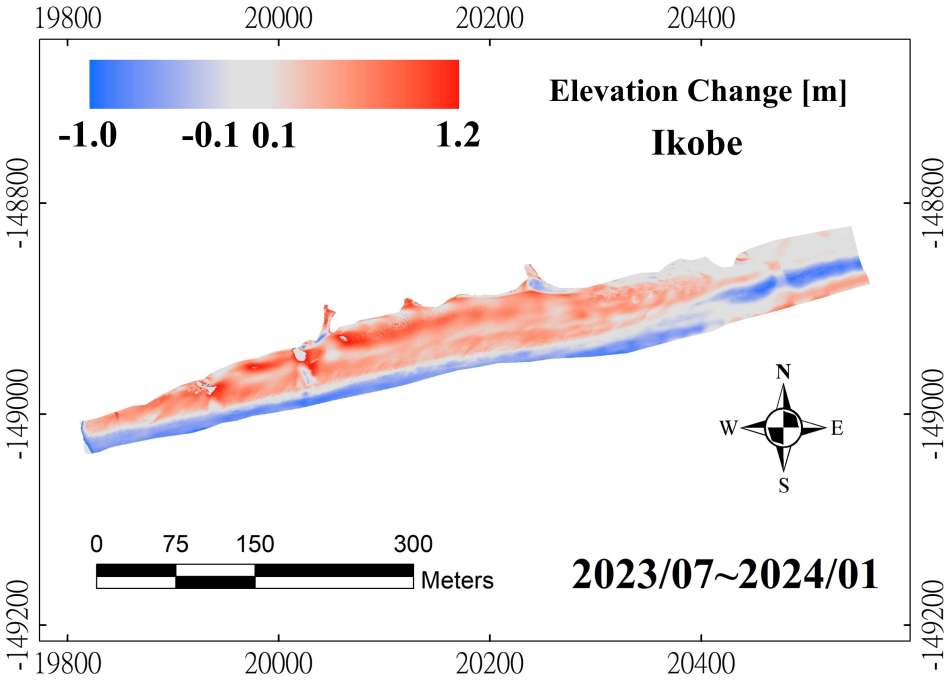

Figure 42: Ikobe Elevation Change 202307-202401

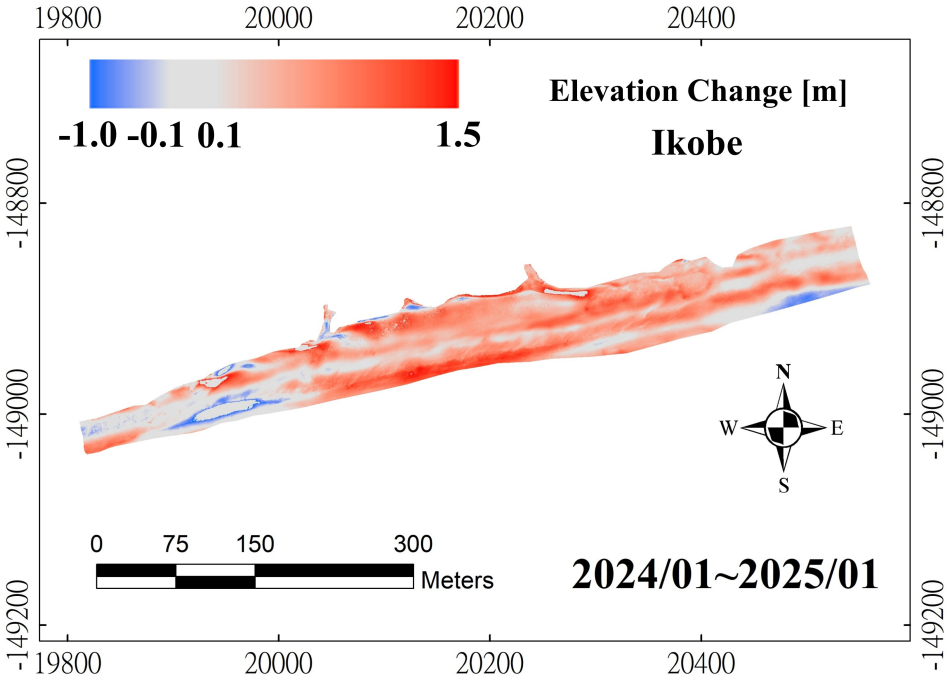

Figure 43: Ikobe Elevation Change 202401-202501

Slope Figures

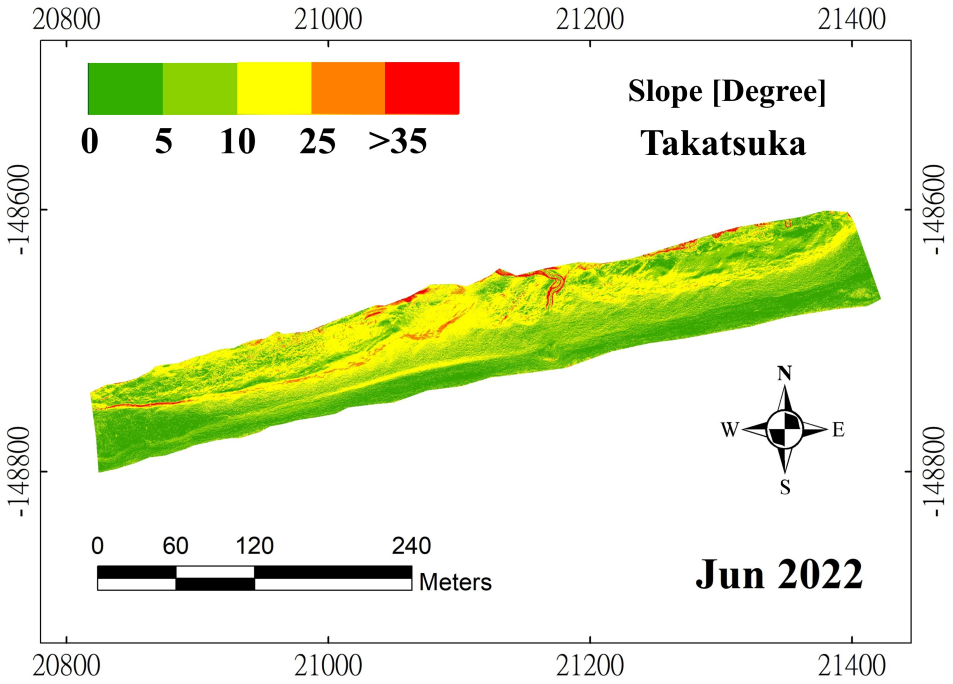

Figure 44: Takatsuka Slope 202206

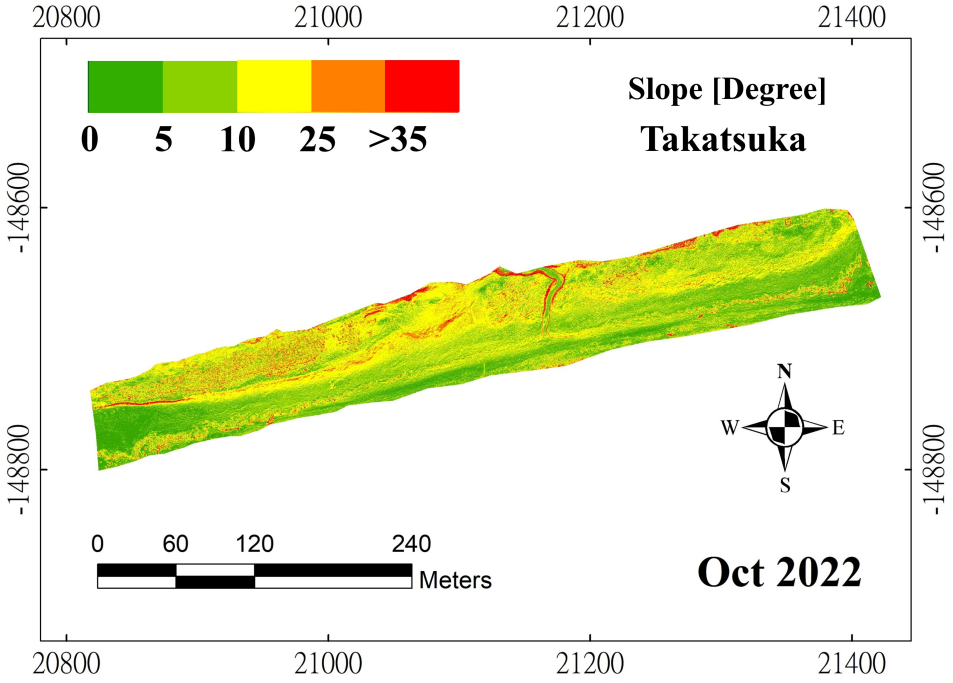

Figure 45: Takatsuka Slope 202210

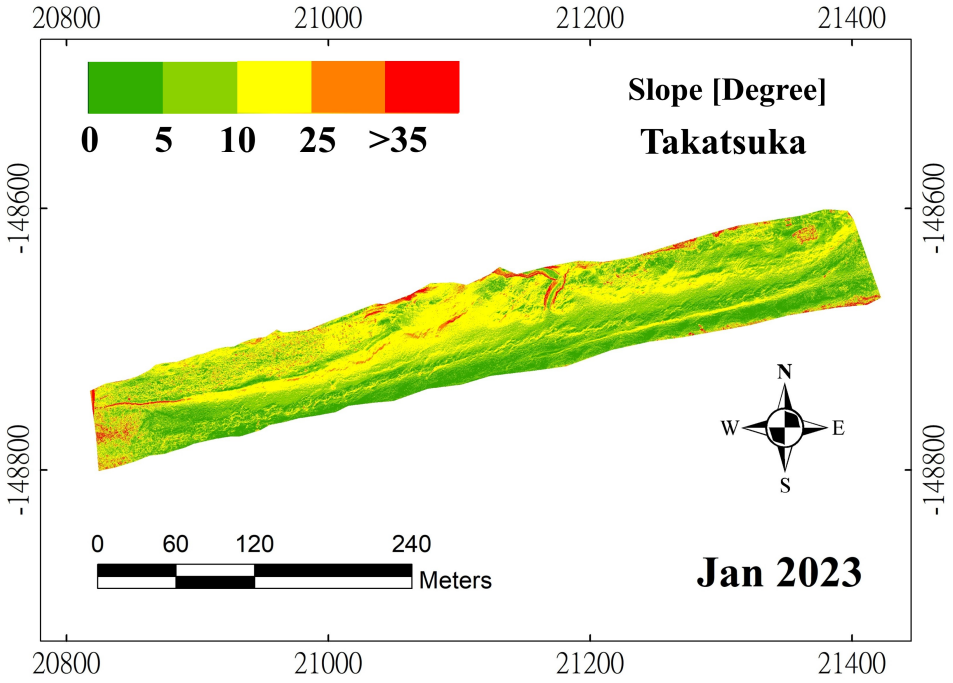

Figure 46: Takatsuka Slope 202301

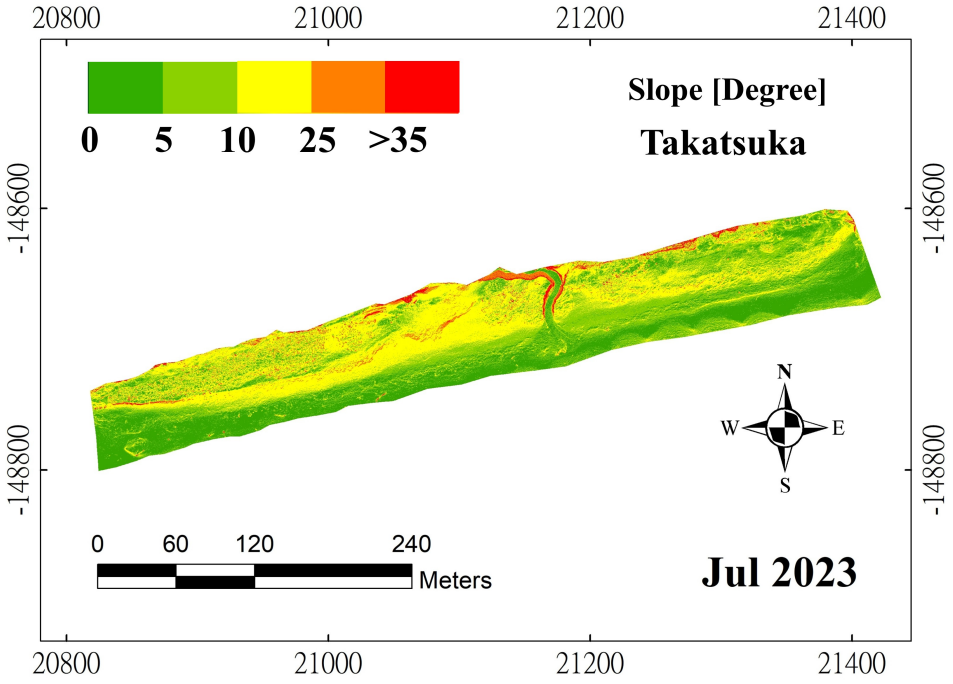

Figure 47: Takatsuka Slope 202307

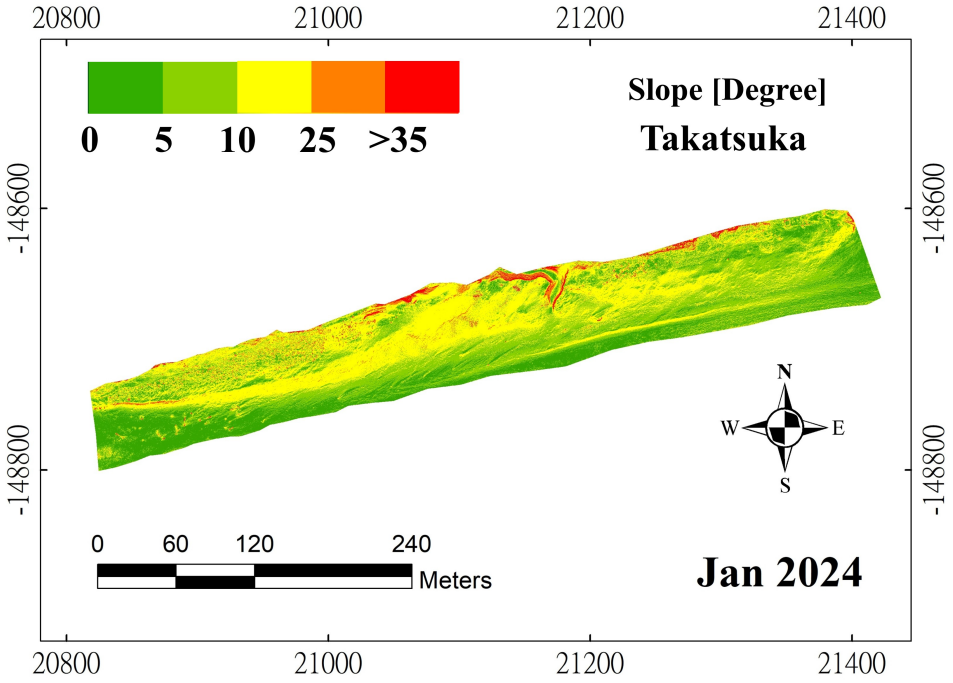

Figure 48: Takatsuka Slope 202401

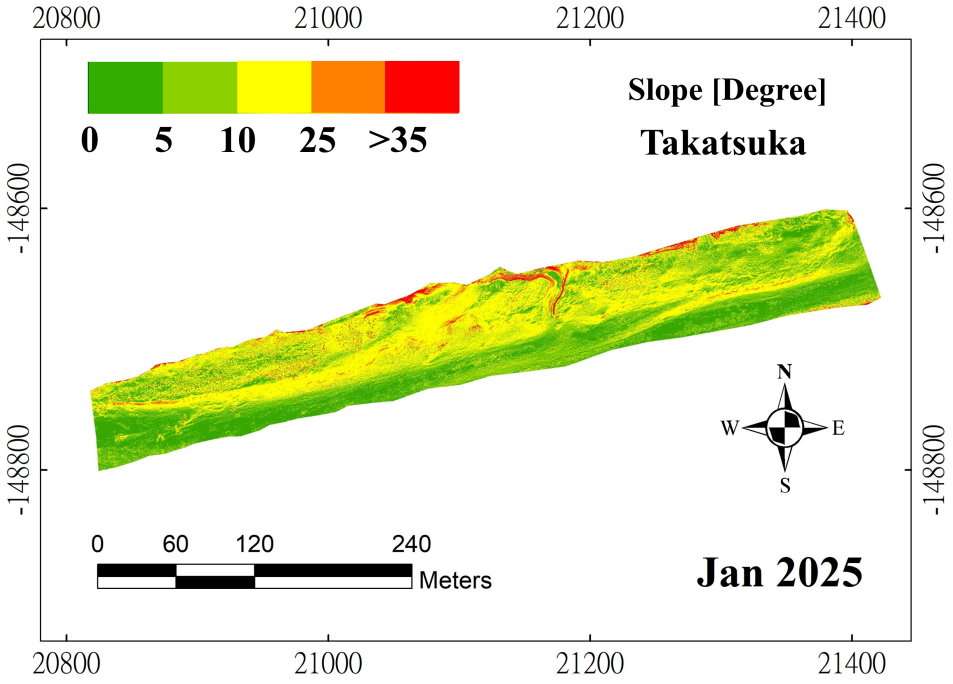

Figure 49: Takatsuka Slope 202501

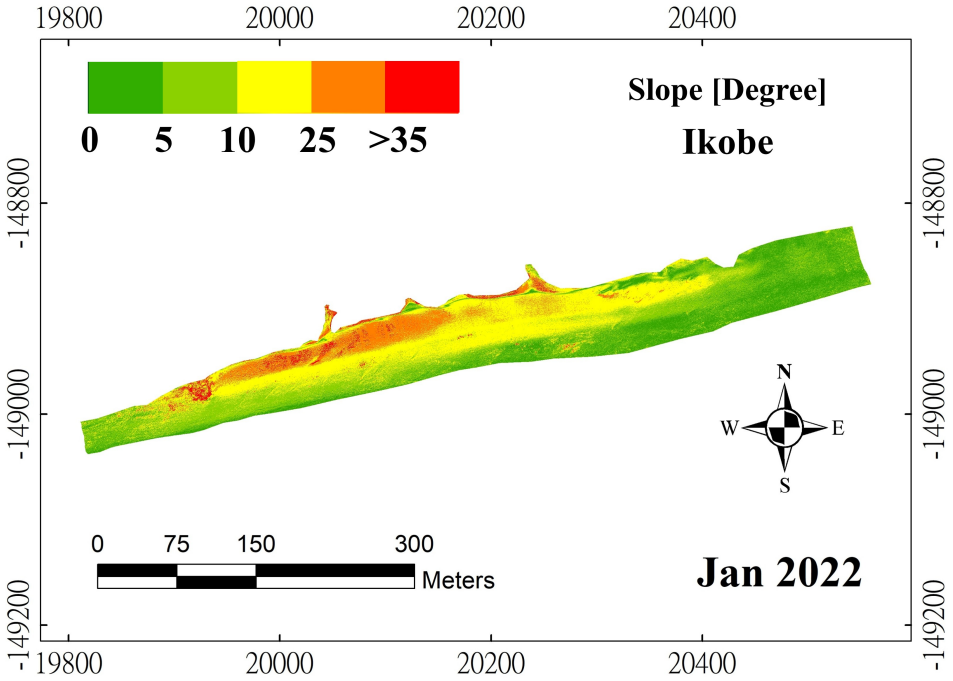

Figure 50: Ikobe Slope 202201

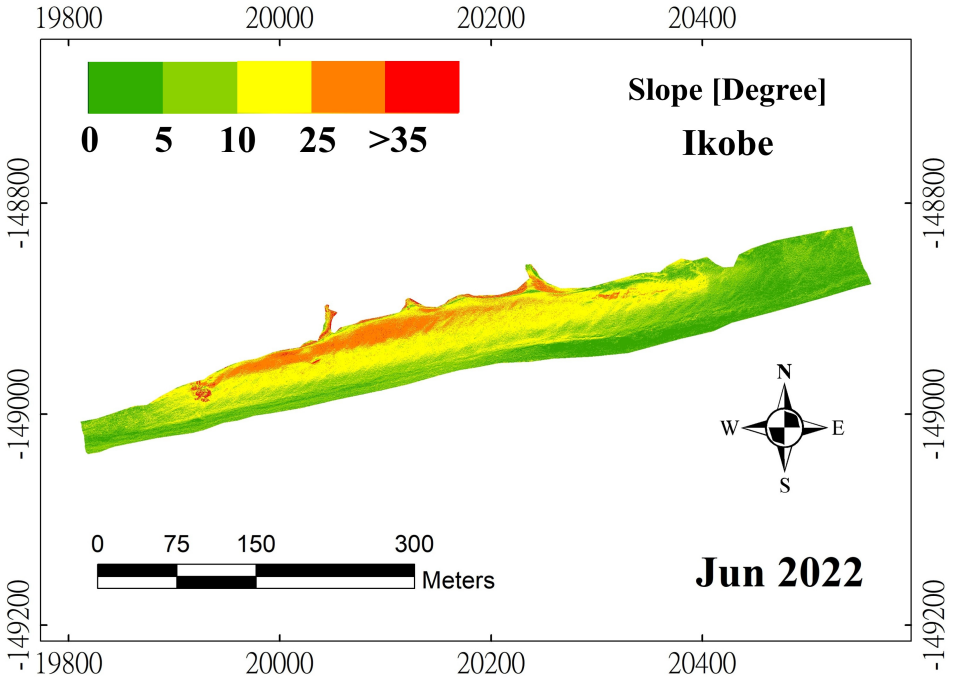

Figure 51: Ikobe Slope 202206

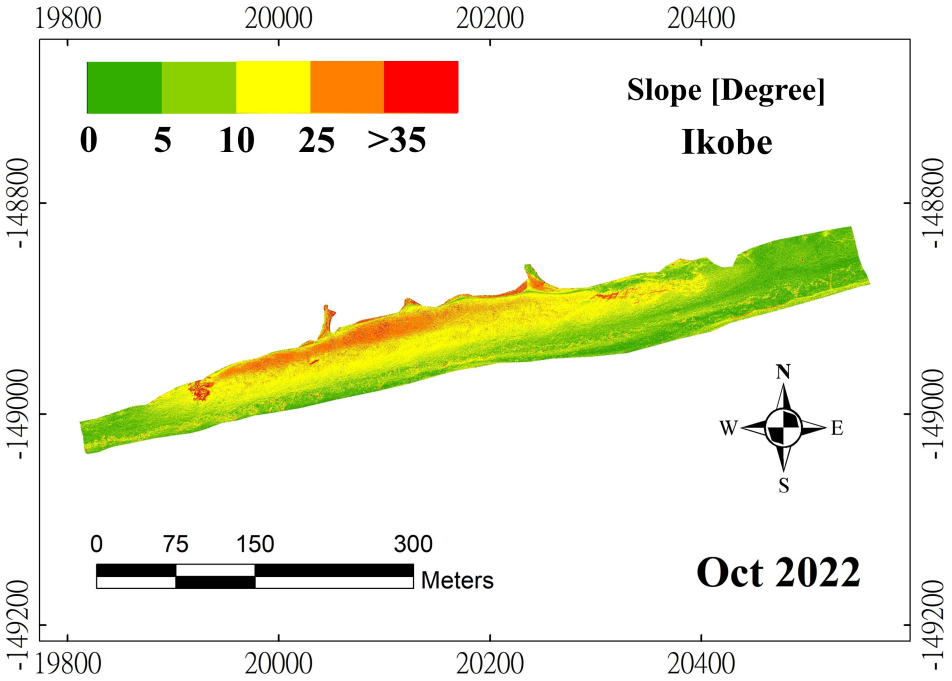

Figure 52: Ikobe Slope 202210

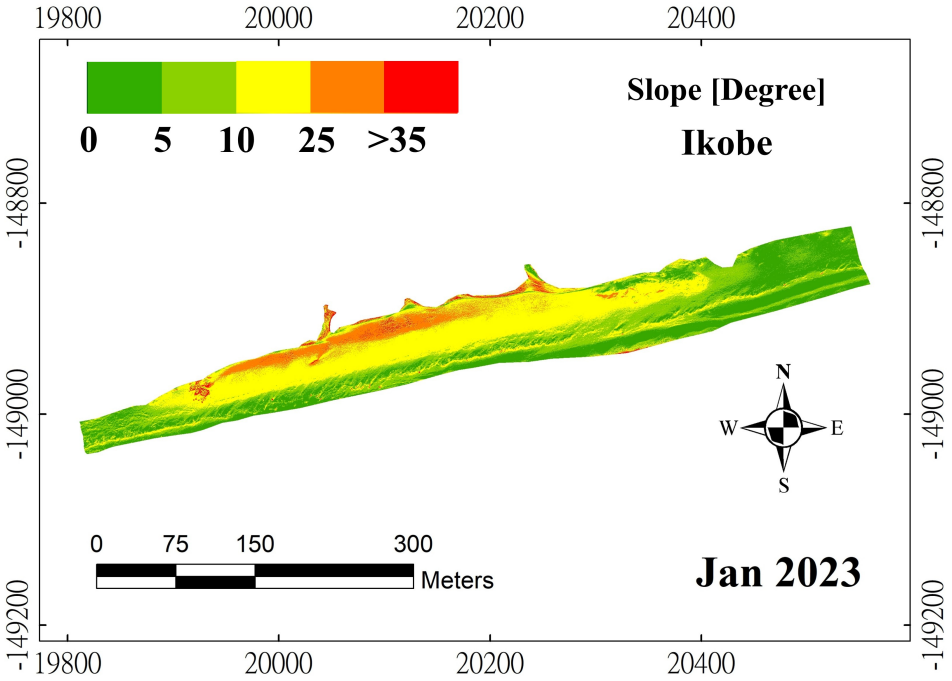

Figure 53: Ikobe Slope 202301

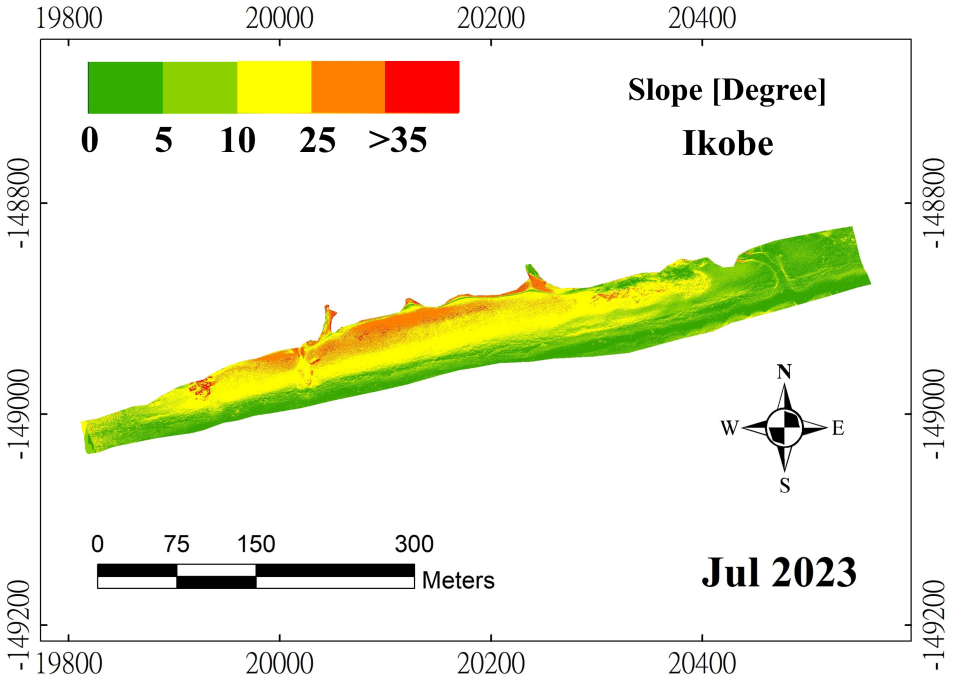

Figure 54: Ikobe Slope 202307

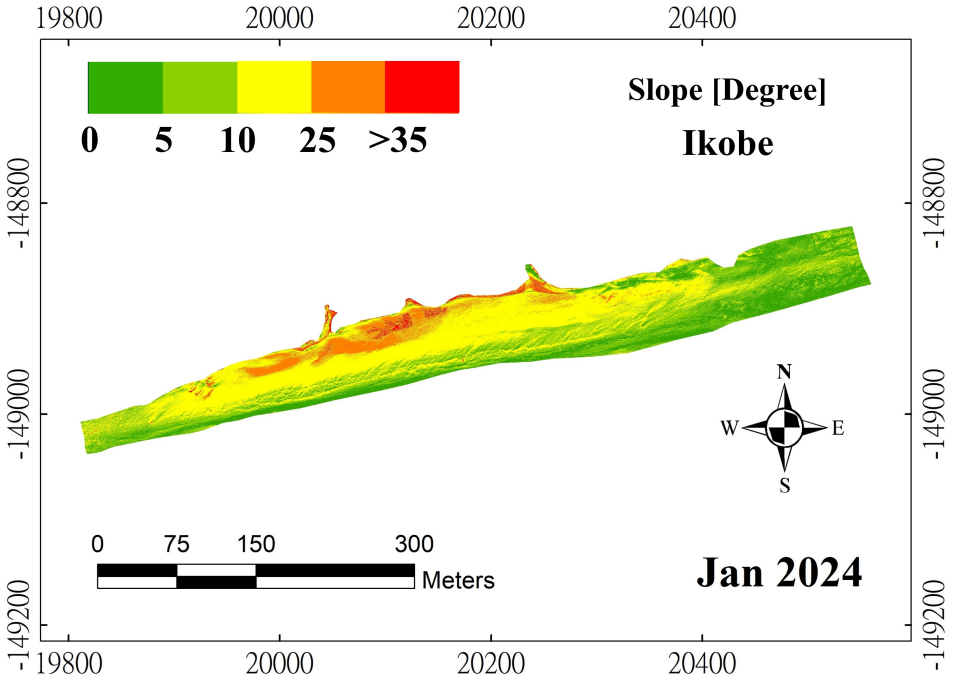

Figure 55: Ikobe Slope 202401

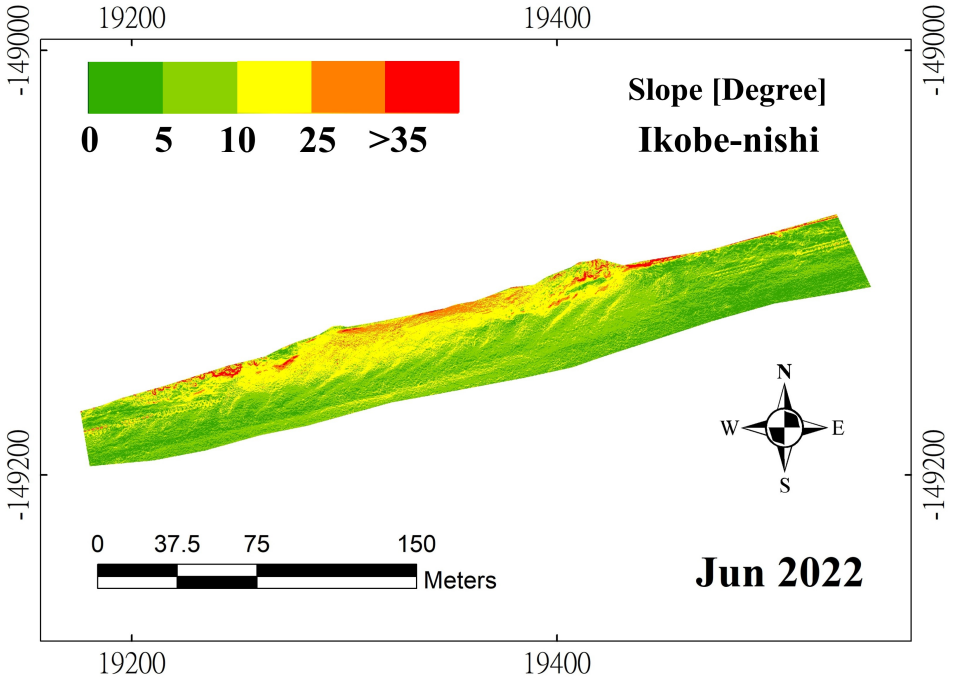

Figure 56: Ikobe-nishi Slope 202206

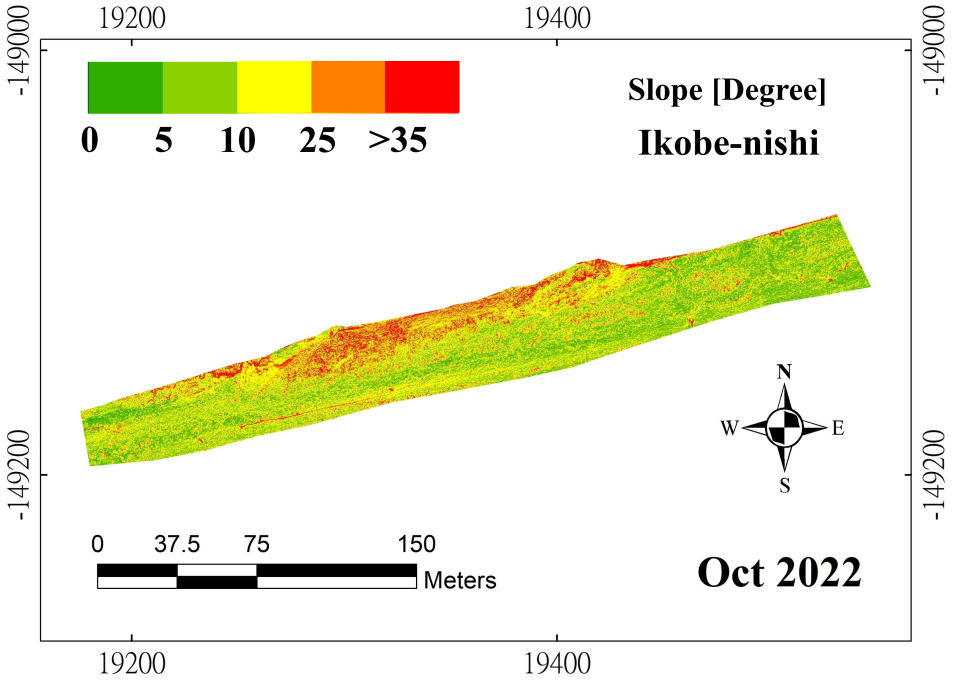

Figure 57: Ikobe-nishi Slope 202210

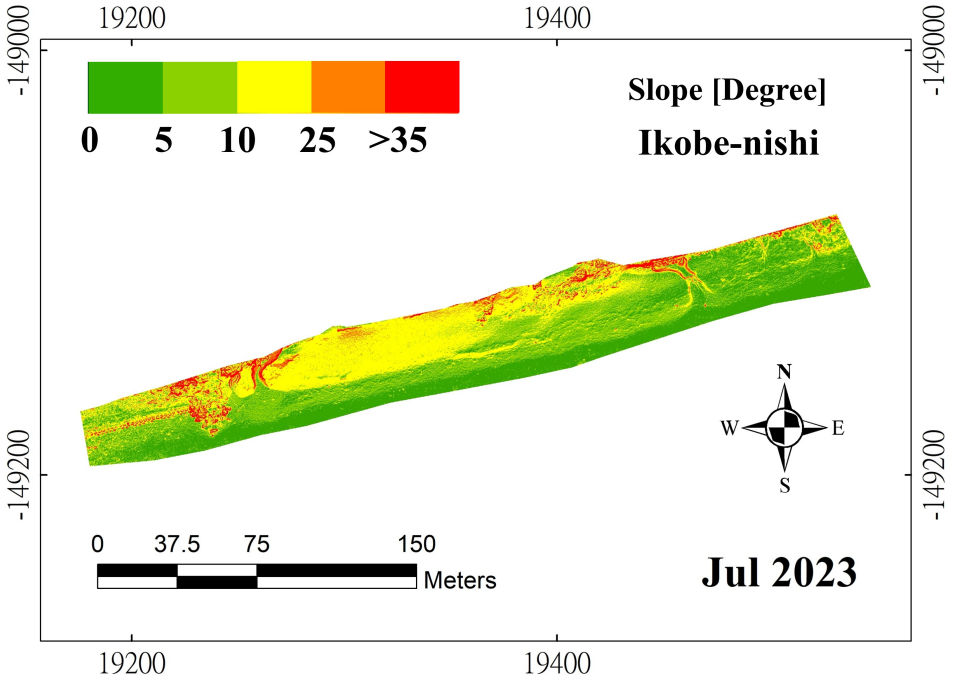

Figure 58: Ikobe-nishi Slope 202307

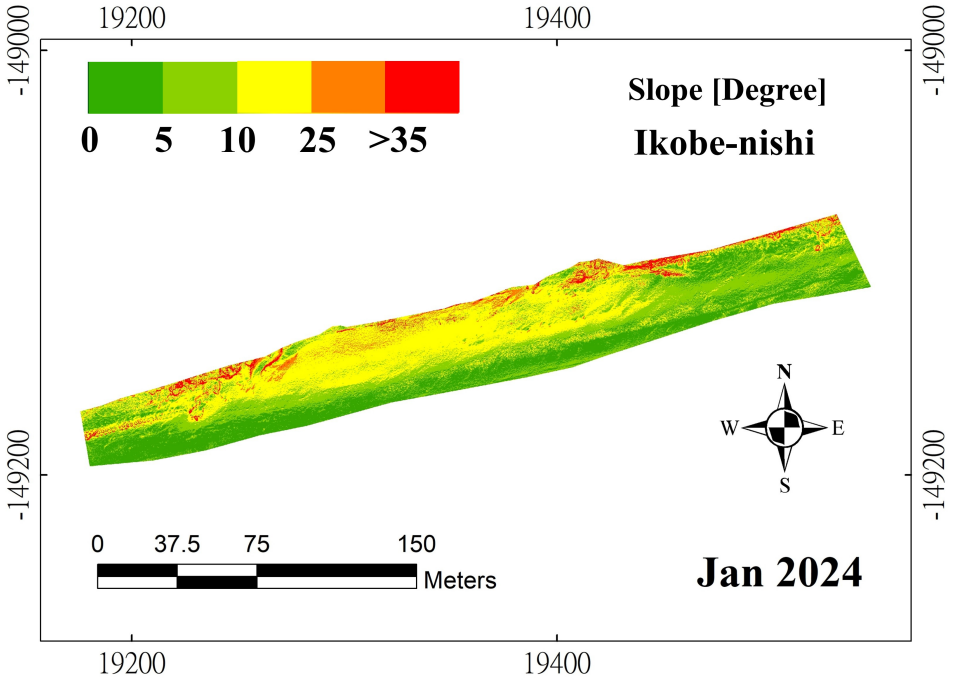

Figure 59: Ikobe-nishi Slope 202401

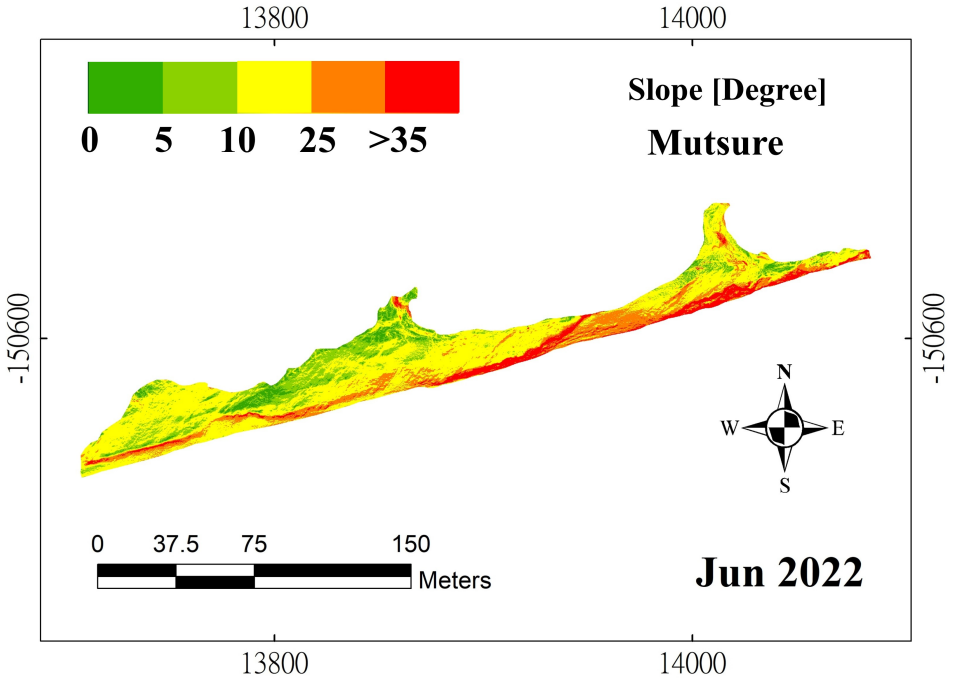

Figure 60: Mutsure Slope 202206

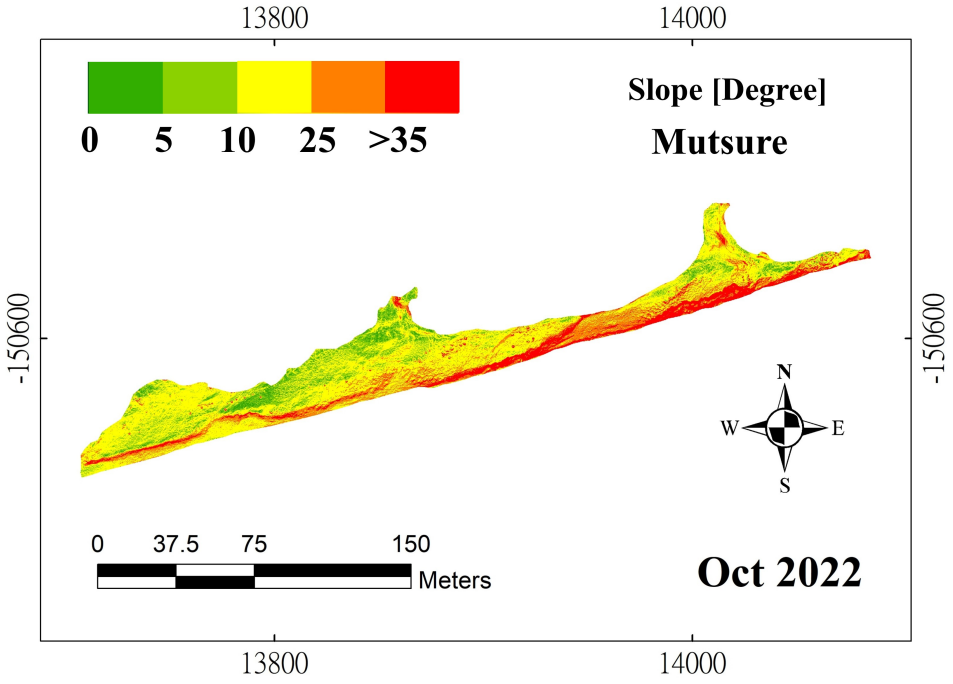

Figure 61: Mutsure Slope 202210

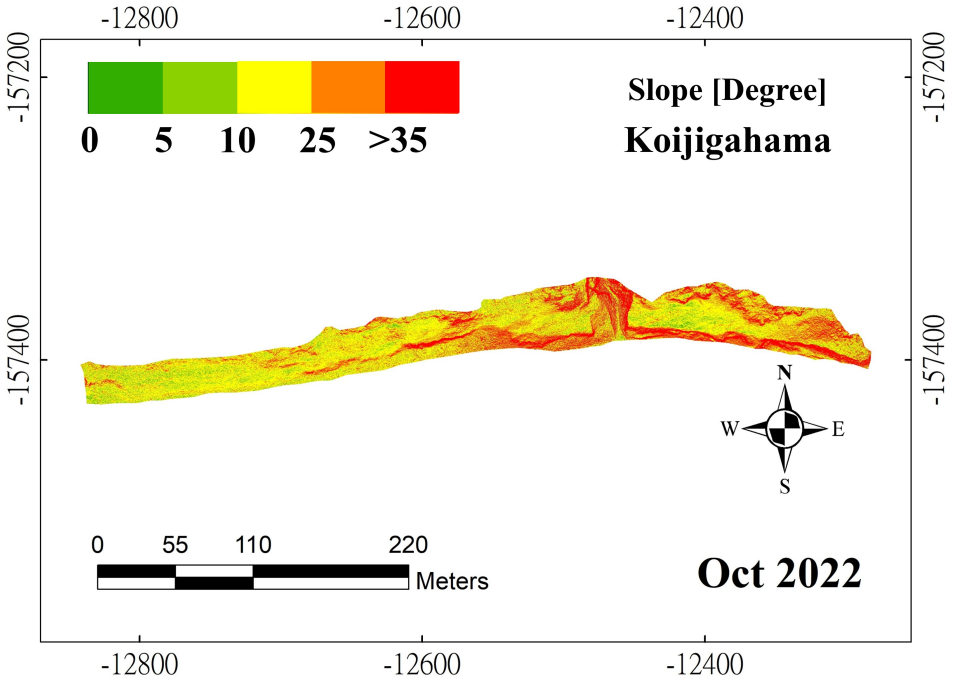

Figure 62: Koijigahama Slope 202210

References

Aichi Prefecture. Enshunada coastal conservation master plan, 2003. in Japanese.

Aichi Prefecture. Revised enshunada coastal conservation master plan, 2011. in Japanese.

Aichi Prefecture and Shizuoka Prefecture. Revised enshunada coastal conservation master plan, 2015. in Japanese.

Hamzah M. Al-Hashemi, Hamzah M. Beakawi, and Omar S. Baghapra Al-Amoudi. A review on the angle of repose of granular materials. *Powder Technology*, 330:397–417, 2018. doi: 10.1016/j.powtec.2018.02.003.

Shinichi Aoki, Seiji Sanada, and Hiroyasu Utatsu. Shoreline change and longshore sediment transport west of the tenryu river mouth. *Proceedings of Coastal Engineering, JSCE*, 46:661–665, 1999. in Japanese.

Shinichi Aoki, Hiroshi Kato, Takaaki Uda, and Hajime Osumi. Verification of westward longshore sediment transport west of the tenryu river mouth and associated shoreline changes. *Proceedings of Coastal Engineering, JSCE*, 50:571–575, 2003. in Japanese.

Andreas C. W. Baas and Douglas J. Sherman. Spatiotemporal variability of aeolian sand transport in a coastal dune environment. *Journal of Coastal Research*, 22(5): 1198–1205, 2006.

Ralph Alger Bagnold. The transport of sand by wind. *Geographical Journal*, 89: 409–438, 1937.

Ralph Alger Bagnold. *The Physics of Blown Sand*. Dover Publications, New York, 1941.

Ralph Alger Bagnold. *The Physics of Blown Sand and Desert Dunes*. Courier Corporation, 2012.

Bernard O. Bauer, Robin G. D. Davidson-Arnott, Ian J. Walker, Patrick A. Hesp, and Jeff Ollerhead. Wind direction and complex sediment transport response across a beach–dune system. *Earth Surface Processes and Landforms*, 37(15):1661–1677, 2012.

Bernard O. Bauer, Ian J. Walker, Andreas C. W. Baas, Derek W. T. Jackson, Cheryl McKenna Neuman, Giles F. S. Wiggs, and Patrick A. Hesp. Critical reflections on the coherent flow structures paradigm in aeolian geomorphology. In *Coherent Flow Structures at Earth's Surface*, pages 111–134. Wiley Online Library, 2013.

J. L. Davies and K. M. Clayton. *Geographical Variation in Coastal Development*. Oliver and Boyd, 1972.

Kazumasa Endo, Shusaku Sakakibara, Takaaki Uda, Toshinori Ishikawa, and Kou Koike. Reproduction of shoreline advance and offshore erosion after beach nourishment on the shinohara coast. *JSCE Journal of Civil Engineering, Series B2 (Coastal Engineering)*, 71(2):I_781–I_786, 2015. in Japanese.

Esri. Cell size and resampling in analysis, 2025a. URL https://desktop.arcgis.com/en/arcmap/latest/extensions/spatial-analyst/performing-analysis/cell-size-and-resampling-in-analysis.htm. Accessed: October 2025.

Esri. Resample, 2025b. URL https://desktop.arcgis.com/en/arcmap/latest/tools/data-management-toolbox/resample.htm. Accessed: October 2025.

Esri. How idw (inverse distance weighted) interpolation works, n.d.a. URL https://doc.arcgis.com/en/allsource/1.2/analysis/geoprocessing-tools/spatial-analyst/how-idw-works.htm. Accessed: October 2025.

Esri. How kriging interpolation works, n.d.b. URL https://doc.arcgis.com/en/allsource/1.2/analysis/geoprocessing-tools/spatial-analyst/how-kriging-works.htm. Accessed: October 2025.

Esri. How natural neighbor interpolation works, n.d.c. URL https://doc.arcgis.com/en/allsource/1.2/analysis/geoprocessing-tools/spatial-analyst/how-natural-neighbor-works.htm. Accessed: October 2025.

Esri. How spline interpolation works, n.d.d. URL https://doc.arcgis.com/en/allsource/1.2/analysis/geoprocessing-tools/spatial-analyst/spline.htm. Accessed: October 2025.

Norio Fuji. Coastal dunes of the hokuriku region. *Quaternary Research (Daiyonki-Kenkyu)*, 14(4):195–220, 1975. in Japanese.

Nobuyuki Fujishiro. Tracking the coastline along the pacific side of the atsumi peninsula: Re-evaluating erosion on the omotehama coast, 2021. Unpublished manuscript.

Sylvain Gabarrou, Gonéri Le Cozannet, Eric J. R. Parteli, Rodrigo Pedreros, Etienne Guerber, Bastien Millescamps, Cyril Mallet, and Carlos Oliveros. Modelling the retreat of a coastal dune under changing winds. *Journal of Coastal Research*, (85): 166–170, 2018.

Kohei Hamaguchi, Takashi Harano, Fuminori Kato, Ryuji Nikaido, and Yusuke Igarashi. A study on coastal dune profile and vegetation condition necessary for securing tsunami disaster reduction effect. *Journal of Japan Society of Civil Engineers, Series B2 (Coastal Engineering)*, 73(2):I_595–I_600, 2017. in Japanese.

Masataro Hattori, Ryusuke Suzuki, and Toshio Sato. Beach deformation and littoral drift in the central enshunada coast. *Proceedings of the Coastal Engineering Conference*, 21:127–133, 1974. in Japanese.

I. Henrico, T. Ledwaba, and G. Van Zyl. Measuring the effect of wind-driven processes on coastal dunes: a study of the atlantis and geelbek dune fields along the west coast of south africa. *Spatial Information Research*, 28:569–577, 2020.

Patrick Hesp. Foredunes and blowouts: Initiation, geomorphology and dynamics. *Geomorphology*, 48:245–268, 2002.

Patrick Hesp and Robert Hyde. Flow dynamics and geomorphology of a trough blowout. *Sedimentology*, 43:505–525, 2008.

Patrick A. Hesp. Flow reversal and dynamics of foredunes and climbing dunes on a leeward coast, new zealand. *Zeitschrift für Geomorphologie, Supplementband*, 141: 123–134, 2005.

Siyu Ho, Nozomu Yoneyama, and Tetsuya Hiraishi. Numerical analysis of the wave force exerted by the tsunami over the sand dune in front of the seawall. *Journal of Japan Society of Civil Engineers, Series B2 (Coastal Engineering)*, 78(2):I_241–I_246, 2022. in Japanese.

K. Horikawa, S. Hotta, and S. Kubota. Experimental study of blown sand on a wetted sand surface. *Coastal Engineering in Japan*, 25:177–195, 1982.

Kiyoshi Horikawa, Shintaro Horita, Susumu Kubota, and Soichi Harigai. Studies on blown sand on coasts. *Proceedings of Coastal Engineering, JSCE*, 28:574–578, 1981. in Japanese.

Shintaro Horita, Naoaki Yamaya, Takayuki Kojima, Mikio Nakai, and Yuji Saito. Blown sand transport of coarse grains on coasts. *Proceedings of Coastal Engineering, JSCE*, 42:476–480, 1995. in Japanese.

Shintaro Horita, Susumu Kubota, and Mitsuo Takezawa. Blown sand transport of fine grains on coasts. *Proceedings of Coastal Engineering, JSCE*, 51:551–555, 2004. in Japanese.

S. Hotta, S. Kubota, S. Katori, and K. Horikawa. Sand transport by wind on a wet sand surface. In *Proceedings of the 19th Coastal Engineering Conference*, pages 1265–1281, New York, 1984. American Society of Civil Engineers.

Hsiang Hsin and Shin-ichi Aoki. A method of identifying coastal dunes in front of cliffs by uav mapping—an application to omotehama coast, aichi prefecture, japan. In *International Conference on Asian and Pacific Coasts*, pages 1093–1101. Springer, 2023.

Hsiang Hsin, Shinichi Aoki, and Takumi Okabe. Study on the formation mechanism of a coastal dune in front of a sea cliff. *Journal of JSCE, B2 (Coastal Engineering)*, 78 (2):I_523–I_528, 2022. in Japanese.

Hsiang Hsin, Saeko Kamioka, Shinichi Aoki, and Takumi Okabe. Wind conditions and aeolian transport characteristics around a coastal dune formed in front of a sea cliff. *Journal of JSCE, B2 (Coastal Engineering)*, 79(2):17085–17023, 2023. in Japanese.

Hsiang Hsin, Shinichi Aoki, and Shinpo Araki. Relationship between coastal dune development and nearshore bathymetric changes. *Journal of JSCE, B2 (Coastal Engineering)*, 80(2):17148–17124, 2024. in Japanese.

Mitsuhiro Inoue. From dune research to arid land studies: A centennial review of the dune research institute era. *Sand Dune Research*, 71(1):11–26, 2024. in Japanese.

Yoshinori Ishikawa, Takami Uda, Takahisa Tamura, Hiroaki Kogane, Takuya Yokota, and Yasuo Otani. Effective use of aeolian sand deposits behind the beach for regional sediment management. *Journal of JSCE, Series B3 (Ocean Engineering)*, 77(2): I_841–I_846, 2021.

Masahiko Isobe. Sediment transport system management as a basis for national land management. *Trends in the Sciences*, 13(3):52–53, 2008.

D. W. T. Jackson, J. H. M. Beyers, Kevin Lynch, J. A. G. Cooper, A. C. W. Baas, and Irene Delgado-Fernandez. Investigation of three-dimensional wind flow behaviour over coastal dune morphology under offshore winds using cfd and ultrasonic anemometry. *Earth Surface Processes and Landforms*, 36(8):1113–1124, 2011.

Masatsugu Kainuma, Kazumasa Endo, Shusaku Sakakibara, Takaaki Uda, Toshinori Ishikawa, and Toshiro Sannami. Progressive large-scale offshore erosion in the nourished area off the shinohara coast. *JSCE Journal of Civil Engineering, Series B2 (Coastal Engineering)*, 72(2):I_709–I_714, 2016. in Japanese.

Masatsugu Kainuma, Akihiro Toda, Yasuhiro Tsushima, Takaaki Uda, Toshinori Ishikawa, and Toshiro Sannami. Sediment dynamics along the eastern enshunada coast between the tenryu river mouth and cape omaezaki. *JSCE Journal of Civil Engineering, Series B2 (Coastal Engineering)*, 74(2):I_805–I_810, 2018. in Japanese.

Masatsugu Kainuma, Yu Ohashi, Takaaki Uda, Toshinori Ishikawa, and Toshiro Sannami. Estimation of shoreline change and longshore sediment transport distribution along the western enshunada coast. *JSCE Journal of Civil Engineering, Series B2 (Coastal Engineering)*, 75(2):I_649–I_654, 2019. in Japanese.

Kiyomi Kakuda. Formation and stabilization periods of major coastal dune areas along the sea of japan and the east china sea. *Quaternary Research (Daiyonki-Kenkyu)*, 14 (4):251–276, 1975. in Japanese.

R. Kawamura. Study on blown sand by wind. *Report of the Institute of Science and Technology, University of Tokyo*, 5(4):95–112, 1951. in Japanese.

Satoshi Kawasaki. Development of coastal dunes in tottori prefecture. *Geographical Review of Japan*, 18(4):271–291, 1942. in Japanese.

Yoshiaki Kawata and Minoru Uemoto. Coastal processes of the tenryu river–enshunada coast system. *Proceedings of Coastal Engineering, JSCE*, 45:616–620, 1998. in Japanese.

Toshiaki Maekawa, Yasuo Nihei, and Haruka Nakata. Study on tsunami mitigation effect of coastal dune and fill. *Journal of Japan Society of Civil Engineers, Series B1 (Hydraulic Engineering)*, 69(4):I_1453–I_1458, 2013. in Japanese.

Gerd Masselink, Michał Hughes, and Jasper Knight. *Introduction to Coastal Processes and Geomorphology*. Routledge, 2014.

Akimi Matsuda. Dune utilization research facilities at tottori university. *Tenki*, 37(1): 71–74, 1990. in Japanese.

Hideo Miie. On the formation of coastal dunes. *Quaternary Research (Daiyonki-Kenkyu)*, 4(1):5–12, 1965. in Japanese.

Ikuo Nagashima, Nobuaki Iwasaki, Takaaki Uda, and Junichi Arimura. Erosion characteristics west of the tenryu river mouth along the enshunada coast. *Proceedings of Coastal Engineering, JSCE*, 52:596–600, 2005. in Japanese.

Yuki Nakajima and Kai Suekatsu. Effects of grain size on the amount of blown sand. *Journal of the Japanese Forestry Society*, 60(12):450–455, 1978. in Japanese.

Susumu Naruse and Hideya Ooka. A comparative study on coastal management in various countries. *Proceedings of Coastal Engineering, JSCE*, 47:1251–1255, 2000.

Toshiro Naruse. Coastal dune of fukiagehama in kagoshima prefecture. *Geographical Sciences*, 12:48–57, 1969. in Japanese.

Toshiro Naruse. Coastal dunes of tanegashima island. *Geographical Review of Japan*, 44(10):697–706, 1971. in Japanese.

Toshiro Naruse. Coastal dunes in japan. *Geographical Review of Japan Series A*, 62(2): 129–144, 1989. in Japanese.

Ryuji Nikaido, Shinichi Aoki, Shigeru Kato, and Takumi Okabe. Study on erosion mechanisms of coastal dune and fill by tsunami overflow. *Journal of Japan Society of Civil Engineers, Series B3 (Ocean Development)*, 71(2):I_425–I_430, 2015. in Japanese.

Ryuji Nikaido, Shinichi Aoki, Susumu Araki, Kenichi Tokida, and Others. Erosion mechanisms of coastal dunes using hydraulic model test and numerical simulation. *Journal of Japan Society of Civil Engineers, Series B2 (Coastal Engineering)*, 72(2): I_619–I_624, 2016. in Japanese.

Ryuichiro Nishi and Ryuta Mizukawa. Fundamental study on dune wind erosion and blown sand. *Proceedings of Coastal Engineering, JSCE*, 48:591–595, 2001. in Japanese.

Ryuichiro Nishi, Takaaki Uda, Michio Sato, Yukio Nishihara, and Yoshito Inoue. Long-term variability of shoreline, coastal vegetation and dune forest boundary at fukiagehama coast. *Proceedings of Coastal Engineering, JSCE*, 45:661–665, 1998. in Japanese.

T. Okutani, S. Iwata, and T. Hiraishi. Experimental study on the effect of coastal dune against tsunami action to seawall. *DPRI Annuals*, 64(B), 2021. in Japanese.

Tetsuya Okutani and Tetsuya Hiraishi. Model experiment on deformation of coastal dunes by tsunami. *Journal of Japan Society of Civil Engineers, Series B2 (Coastal Engineering)*, 76(2):I_403–I_408, 2020. in Japanese.

Tadahiro Ono. Study on the formation period of coastal dunes in the westernmost part of honshu. *Geographical Review of Japan*, 36(7):391–411, 1963. in Japanese.

Ayumi Onuma. Sustainable coastal management policies under population decline: Issues of disaster prevention and nature conservation. *Environmental Economics and Policy Studies*, 8(2):11–17, 2015.

Daniel R. Parsons, Giles F. S. Wiggs, Ian J. Walker, Robert I. Ferguson, and Brian G. Garvey. Numerical modelling of airflow over an idealised transverse dune. *Environmental Modelling & Software*, 19(2):153–162, 2004.

Kenneth Pye. Coastal dunes. *Progress in Physical Geography*, 7(4):531–557, 1983.

Kenneth Pye and Haim Tsoar. *Aeolian Sand and Sand Dunes*. Unwin Hyman, London, 1990.

Shinji Sato. Dynamics of sand movement on hamamatsu coast facing enshuu-nada. *Journal of Japan Society of Civil Engineers, Series B*, 64(3):192–201, 2008. in Japanese.

Shinji Sato, Takaaki Uda, Tetsuya Okayasu, and Masumi Serizawa. Sediment transport processes and sediment management in the tenryu river–enshunada system. *Proceedings of Coastal Engineering, JSCE*, 51:571–575, 2004. in Japanese.

Yasumitsu Sato, Atsushi Sugita, Yukiyoshi Hoshigami, Hiroki Ozawa, Shinichi Aoki, and Shigeru Kato. Evaluation of sandy beach restoration by improved submerged breakwaters on the omotehama coast, atsumi peninsula. In *Proceedings of the Coastal Zone Research Conference*, volume 31, pages 7–3, 2018. in Japanese.

Samantha E. Saye, Kenneth Pye, and Lars B. Clemmensen. Development of a cliff-top dune indicated by particle size and geochemical characteristics: Rubjerg knude, denmark. *Sedimentology*, 53(1):1–21, 2006.

Yaping Shao and Hua Lu. A simple expression for wind erosion threshold friction velocity. *Journal of Geophysical Research: Atmospheres*, 105(D17):22437–22443, 2000.

Francis P. Shepard. *Submarine Geology*. Harper and Row, New York, 3 edition, 1973.

Yoko Shibuya, Yuhei Matsubara, Masamitsu Kuroiwa, and Masashi Ide. Investigation of sediment dynamics and the effectiveness of sand recycling at the tottori sand dune coast. *Journal of JSCE, Series B2 (Coastal Engineering)*, 68(2):I_676–I_680, 2012.

Yoko Shibuya, Naoki Tamura, Keigo Ota, Masamitsu Kuroiwa, and Yuhei Matsubara. Effectiveness and stability of large-scale beach nourishment at the tottori sand dune coast. *Journal of JSCE, Series B3 (Ocean Engineering)*, 71(2):I_479–I_484, 2015.

Yuji Sorimachi. Concepts of sediment management in sediment transport systems. *Civil Engineering Journal*, 41(7):38–41, 1999.

M. L. Sweet and Gary Kocurek. An empirical model of aeolian dune lee-face airflow. *Sedimentology*, 37(6):1023–1038, 1990.

Toru Tamura, Kazuaki Watanabe, Naofumi Yamaguchi, Dan Matsumoto, Yoshitaka Kodama, and Yu Saito. Formation process of the tottori sand dune over the past 500 years: Reconstruction using ground-penetrating radar and luminescence dating. In *Abstracts of the 118th Annual Meeting of the Geological Society of Japan and 2011 Annual Meeting of the Mineralogical Society of Japan*, pages 48–48. Geological Society of Japan, 2011. in Japanese.

Kenichi Tanabe. Morphological classification and land use of coastal dunes in japan. *Geographical Review of Japan*, 17(5):373–401, 1941. in Japanese.

Hisao Tanaka, Tadashi Hasegawa, Sumie Kimura, Ikuei Okamoto, and Yoichi Sakai. The geohistory of the formation of the niigata sand dunes. *Quaternary Research (Daiyonki-Kenkyu)*, 35(3):207–218, 1996. in Japanese.

Kikuko Tanino. Environmental conditions for dune formation at shiriyazaki, aomori prefecture. *Quaternary Research (Daiyonki-Kenkyu)*, 39(5):471–478, 2000. in Japanese.

Kunihiro Tomita, Tetsuya Sumi, and Mamoru Watanabe. Project evaluation of river management through sediment flushing and sediment management from dams: Optimization and cost-benefit analysis for integrated sediment management from dam to coast in the yahagi river. *Proceedings of River Engineering, JSCE*, 17:53–58, 2011.

Yoshinori Toyoshima. Coastal dunes of the san'in region. *Quaternary Research (Daiyonki-Kenkyu)*, 14(4):221–230, 1975. in Japanese.

Yoshinori Toyoshima and Saburo Akagi. On the formation of the tottori sand dune. *Research Reports of the Faculty of Education, Tottori University. Natural Science*, 16(1):32–45, 1965. in Japanese.

Gozo Tsujimoto and Yoko Shibuya. Spatiotemporal characteristics of shoreline variations at the tottori sand dune coast. *Journal of JSCE, Series B2 (Coastal Engineering)*, 75(2):I_613–I_618, 2019.

Gozo Tsujimoto and Yoko Shibuya. Characteristics of shoreline and cross-shore profile changes at the tottori sand dune coast. *Journal of JSCE*, 80(18):24–18050, 2024.

Takaaki Uda, Takashi Ishii, Koichi Uchida, Hajime Koga, Yasuhide Kageyama, Kou Koike, and Toshinori Ishikawa. Long-term prediction of coastal morphology and effects of beach nourishment on the enshunada coast. *Proceedings of Coastal Engineering, JSCE*, 53:666–670, 2006. in Japanese.

Takaaki Uda, Shinichi Aoki, Toshiro Minami, Masumi Serizawa, Ko Furuike, and Toshinori Ishikawa. Beach changes around the mouth of the magome river on the enshuu-nada coast and conservation of the nakatajima sand dune. *Journal of Ocean Development, JSCE*, 23:1021–1025, 2007a. in Japanese.

Takaaki Uda, Takachika Yoshizoe, Takuji Yokoyama, Hajime Koga, Kou Koike, Kenta Murai, and Toshinori Ishikawa. Relationship between increased sediment supply from the tenryu river and coastal erosion along the enshunada coast. *Proceedings of Coastal Engineering, JSCE*, 54:596–600, 2007b. in Japanese.

Takaaki Uda, Toshiro Sannami, Toshinori Ishikawa, Yusuke Ito, Shincho Shiraishi, and Junichiro Sato. Influence of crustal movements on beach morphology at the omaezaki coast. *JSCE Journal of Civil Engineering, Series B2 (Coastal Engineering)*, 69(2): I_666–I_670, 2013. in Japanese.

Takaaki Uda, Toshinori Ishikawa, Kou Koike, Yoshihiro Aoba, and Shirou Ooido. Reproduction and future prediction of morphological changes after beach nourishment on the shinohara coast, hamamatsu. *JSCE Journal of Civil Engineering, Series B2 (Coastal Engineering)*, 70(2):I_696–I_700, 2014a. in Japanese.

Takaaki Uda, Toshinori Ishikawa, Toshiro Sannami, Yoshihiro Aoba, and Shirou Ooido. Observed morphological changes after coarse-grained beach nourishment on the shinohara coast, hamamatsu. *JSCE Journal of Civil Engineering, Series B2 (Coastal Engineering)*, 70(2):I_691–I_695, 2014b. in Japanese.

Takami Uda, Toshiro Sannami, Koichi Takahashi, Tetsuyuki Tako, and Yoshinori Ishikawa. Beach morphodynamics driven by sediment budget imbalance and future sediment management: A case study of the shonan coast. *Journal of JSCE, Series B2 (Coastal Engineering)*, 72(2):I_751–I_756, 2016.

Keiko Udo and Satoshi Takewaka. Long-term topographic variability of coastal dunes and its reproduction, 2001. in Japanese.

Naoto Wakae, Shoichiro Shimizu, Mieko Kataoka, and Shinichi Aoki. Short-term and long-term topographic changes of nakatajima dune. *Journal of Ocean Development, JSCE*, 24:1291–1296, 2008. in Japanese.

Ian J. Walker and William G. Nickling. Dynamics of secondary airflow and sediment transport over and in the lee of transverse dunes. *Progress in Physical Geography*, 26 (1):47–75, 2002.

Mami Yanagisawa, Yasuo Nihei, Shimpei Yamaguchi, Shohei Kawabe, and Fumio Tatsuoka. A new type tsunami barrier seawall of sand dune using reinforcing technology. *Journal of Japan Society of Civil Engineers, Series B2 (Coastal Engineering)*, 68(2):I_886–I_890, 2012. in Japanese.

Yoshiyuki Yasumoto, Takami Uda, and Yuhei Matsubara. Investigation of coastal erosion and integrated sediment management: Case study of the right-bank sediment transport system of the sendai river in tottori. *Proceedings of Coastal Engineering, JSCE*, 53: 641–645, 2006a.

Yoshiyuki Yasumoto, Takami Uda, Yuhei Matsubara, and Shinji Sato. Development and implementation of a comprehensive sediment management guideline for the tottori coast. *Journal of Ocean Engineering*, 22:415–420, 2006b. doi: 10.2208/prooe.22.415.

Takuya Yokota, Akio Kobayashi, Takaaki Uda, Masumi Serizawa, Atsunari Katsuki, and Yasuhito Noshi. Model for predicting formation of blowout on coastal sand dune using cellular automaton method. *Journal of Japan Society of Civil Engineers, Series B2 (Coastal Engineering)*, 73(2):I_583–I_588, 2017. in Japanese.

Takuya Yokota, Akio Kobayashi, Takaaki Uda, and Yasuhito Noshi. Relationship between width and direction of a path crossing coastal sand dune and formation of blowout. *Journal of Japan Society of Civil Engineers, Series B3 (Ocean Development)*, 75(2):I_635–I_640, 2019. in Japanese.

Takuya Yokota, Takaaki Uda, Akio Kobayashi, Yukiyoshi Hoshigami, Atsunari Katsuki, and Yasuhito Noshi. Measurement and prediction of coastal dune formation on hamamatsu–shinohara coast. *Journal of Japan Society of Civil Engineers, Series B2 (Coastal Engineering)*, 76(2):I_469–I_474, 2020a. in Japanese.

Takuya Yokota, Takaaki Uda, Akio Kobayashi, Yukiyoshi Hoshigami, Atsunari Katsuki, and Yasuhito Noshi. Prediction of topographic changes on enshunada coast considering effect of both waves and windblown sand. *Journal of Japan Society of Civil Engineers, Series B3 (Ocean Development)*, 76(2):I_240–I_245, 2020b. in Japanese.

Takuya Yoshii and Shinji Sato. Clarification and future prediction of regional sediment dynamics in the tenryu river–enshunada sediment transport system. *Journal of Japan Society of Civil Engineers, Series B (Hydraulic Engineering)*, 66(1):1–18, 2010. in Japanese.